ENERGY SCAVENGING FROM LOW FREQUENCY VIBRATIONS

by

Tzeno V. Galchev

A dissertation submitted in partial fulfillment
of the requirements for the degree of
Doctor of Philosophy
(Electrical Engineering)
in The University of Michigan
2010

Doctoral Committee:

Professor Khalil Najafi, Chair
Professor Noel C. Perkins
Professor Kensall D. Wise
Assistant Research Scientist Rebecca L. Peterson
Christopher A. Apblett, Sandia National Laboratories

This thesis is dedicated to my parents Vania and Vladimir and my grandparents Maria and Tzeno whose unyielding love and support continue to inspire me.

TABLE OF CONTENTS

LIST OF FIGURES

LIST OF TABLES

ABSTRACT

ENERGY SCAVENGING FROM LOW FREQUENCY VIBRATIONS

by

Tzeno V Galchev

Chair: Khalil Najafi

The development of three energy conversion devices that are able to transform vibrations in their surroundings to electrical energy is discussed in this thesis. These energy harvesters are based upon a newly invented architecture called the Parametric Frequency Increased Generator (PFIG). The PFIG structure is designed to efficiently convert low frequency and non-periodic vibrations into electrical power. The three PFIG devices have a combined operating range covering two orders of magnitude in acceleration (0.54-19.6m/s^2) and a frequency range spanning up to 60Hz; making them some of the most versatile generators in existence.

The PFIG utilizes a bi-stable mechanical structure to initiate high-frequency mechanical oscillations in an electromechanical scavenger. By up-converting the ambient vibration frequency to a higher internal operation frequency, the PFIG achieves better electromechanical coupling. The fixed internal displacement and dynamics of the PFIG

allow it to operate more efficiently than resonant generators when the ambient vibration amplitude is higher than the internal displacement limit of the device. The PFIG structure is capable of efficiently converting mechanical vibrations with variable characteristics including amplitude and frequency, into electrical power.

The first electromagnetic harvester can generate a peak power of 163µW and an average power of 13.6µW from an input acceleration of 9.8m/s^2 at 10Hz, and it can operate up to 60Hz. The internal volume of the generator is 2.12cm^3 (3.75 including casing). It sets the state-of-the-art in efficiency in the <20Hz range. The volume figure of merit is 0.068%, which is a 10x improvement over other published works. It has a record high bandwidth figure of merit (0.375%). A second piezoelectric implementation generates 3.25µW of average power under the same excitation conditions, while the volume of the generator is halved (1.2cm^3).

A third PFIG was developed for critical infrastructure monitoring applications. It is used to harvest the very low-amplitude, low-frequency, and non-periodic vibrations present on bridges. The device generates 2.3µW of average power from an input acceleration of 0.54m/s^2 at only 2Hz. The internal volume of the generator is 43cm^3. It can operate over an unprecedentedly large acceleration (0.54-9.8m/s^2) and frequency range (up to 30Hz) without any modifications or tuning.

Chapter 1

INTRODUCTION

As we inch toward, and enter, a new era in human development, one enabled by automation and ubiquitous computing, researchers and engineers around the world are busier than ever solving the daunting technological questions which still remain, including designing smaller, cheaper, and more efficient processors, inventing the necessary physical interfaces, and devising ways of transferring, processing, and storing the immense amount of decentralized data that will result. However, the success of this effort may very well hinge upon the availability of energy: a topic that will be of great consequence in general. It is certainly illogical to provide power through wired means to devices that derive their value through their distribution, in some cases randomly so, and through their mobility. Of course, if a fixed-capacity power source such as a battery is used, the questions of lifetime, maintenance, utility, and cost arise. The answer to this dilemma may in fact lie hidden within the problem itself. Because of the exponential progress in our information technologies to date, these front-end devices will likely require so little energy that they may be able to simply harvest or scavenge it from their ambient – and that is the topic of this thesis.

1.1 MOTIVATION FOR SCAVENGING AMBIENT ENERGY

Energy scavenging has become a popular research topic over the past several years because miniaturization and other technological advances have reduced power consumption and opened the door for powering wireless sensors, implantable devices, and other wireless gadgets using harvested ambient energy. Of course, wireless sensor networks and energy harvesting devices go hand in hand. For sometime now researchers have realized the potential value of implementing wireless sensor networks for use in various applications including infrastructure monitoring, industrial automation, buildings, asset tracking, military applications and many others. The front end of these networks is a 'node' consisting of a sensor, on-board computer processing, and a wireless link. A great deal of research has gone in to miniaturizing, integrating, and making this 'node' energy efficient. At this point as far as energy is concerned, computing power is essentially free with researchers demonstrating extremely efficient processors [1], consuming as low as 30pW during their idle state (the dominant mode of operation in sensor networks). Most of the energy consumed generally goes towards performing the sensing and wirelessly transmitting the data. However, because the physical world around us does not change very rapidly, as far as electronics is concerned, the gathering and dissemination of information can be performed at very large intervals, leading to very low-data rates. Additionally, because sensor networks inherently derive value from having many distributed nodes, using creative network design, the transmit distance can be kept low. These special purpose low-data rate network protocols such as Zigbee and PicoRadio require very little power for transmission, 1mW and 100μW respectively as shown in Figure 1-1.
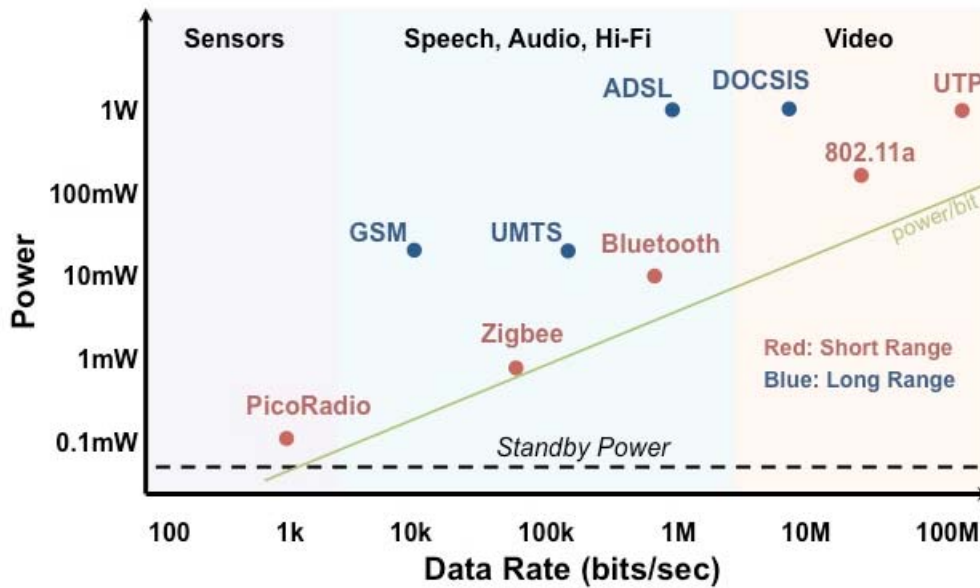
Figure 1-1. Power consumption of various wireless standards. Adapted from [2].

Using the data provided in Figure 1-1, and assuming that at peak power consumption a wireless sensor node consumes between 2-5mW (1mW for the radio transmitter and 2-4mW for sensing and computing), it has a standby power consumption of 50μW, and the node spends 1% of its time at peak power consumption and the rest in idle, then the average power consumption of the sensor node is roughly 100μW. If this node were coupled with a 1cm^3 lithium battery containing 2,880J of energy [3], then the life expectancy of that node would be a little less than one year. This poses a tremendous problem because wireless sensor networks derive their value from being able to monitor many parameters using thousands or hundreds of thousands of sensors, each of which would have to be maintained annually. Compounding that problem is the fact that battery technology cannot be expected to improve in the near future. As shown in Figure 1-2, while the relative performance improvement of computing technology has been exponential over the past couple of decades, battery capacity has improved by about a
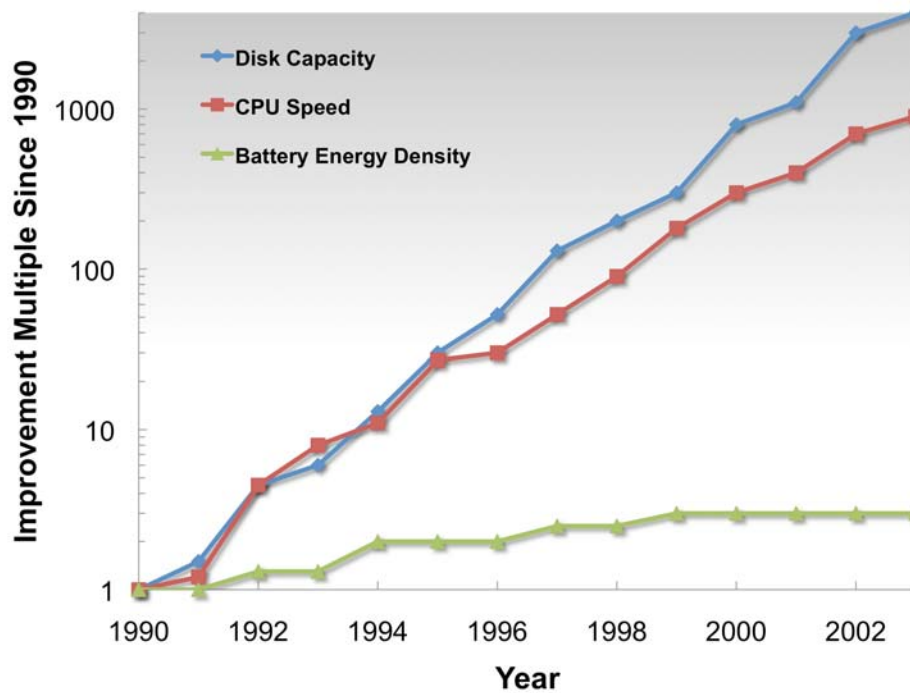
Figure 1-2. Relative performance improvement in computing technology between 1990 and 2003.
Shown is the relatively stagnant improvement in battery technology over that time period. Adapted from
[4].

factor of 3 over that same time period.

The previous example illustrates why energy harvesting has generated so much interest in recent years. Wireless microsystems have become so energy efficient that envisioning a scenario where they scavenge energy from their surroundings is within reason. If this can be done within a practical volume perhaps 1-5 cm^3, at a tolerable cost, then the advantage is that the wireless sensor node in the previous example will have a very long lifetime, in contrast to the 5-year expectancy that it has with a battery of comparable size. One can further speculate that energy harvesting will become an enabling technology, making possible various applications where lifetime is paramount and where having to maintain batteries would inhibit their development.

1.1.1 ENERGY SCAVENGING APPLICATIONS

Possible applications for energy harvesting devices are those that necessitate a long lifetime, and they fall in one of two categories: 1) situations in which the number of deployed devices make battery replacement and disposal a nightmare, such as industrial automation and environmental monitoring, and 2) applications in which it is difficult to gain access to the device, such as infrastructure monitoring and implanted medical devices. A special case is a situation in which using a battery is dangerous and needs to be avoided. An example of this is placing instruments in hazardous environments such as oil drilling, where batteries are known to explode, thereby exposing workers to dangerous gases.

1.1.2 COMMERCIALIZATION OF ENERGY HARVESTING TECHNOLOGY

One aspect of research on this topic that makes it very exciting is that there is a clear market potential and immediate value can be delivered. In fact, over the course of this thesis over 10 companies have begun to offer, or are in the process of developing energy scavenging products. The case to be made for commercialization of energy scavenging products in wireless sensor applications is very simple: they reduce the cost of ownership. Shown in Figure 1-3 is the projected cost of battery maintenance in wireless sensor networks between now and the year 2015. When summed together, this amounts to $1.1 billion dollars that will be spent by wireless sensor users for maintenance between now and then. This number coupled with the cost of the battery, and the cost of disposal gives a first order approximation of the market size for energy scavenging power sources.
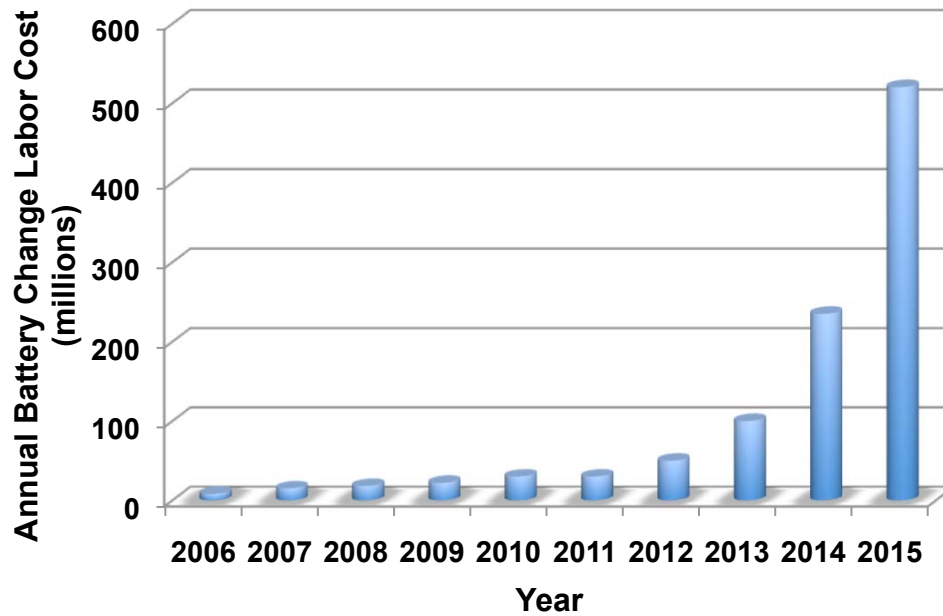
Figure 1-3. Projected annual battery replacement labor cost for wireless sensor networks until 2015, $1.1 billion in total [5].

Shown in Figure 1-4 is the likely market penetration scenario for harvester technology. These devices are already beginning to be used in industrial applications where they can generate significant value and at the same time the technical challenges are not very large because the availability of energy can be exactly quantified and designed for. As scavenging technology begins to mature, it will gain wider acceptance in more heavily regulated markets such as automotive and military applications, as well as lower-end consumer applications such as building automation. Medical applications are likely to come last because of the heavy regulation and safety trials associated with that market. It should be noted that many applications for this technology are likely to surface that are not on that list.

6
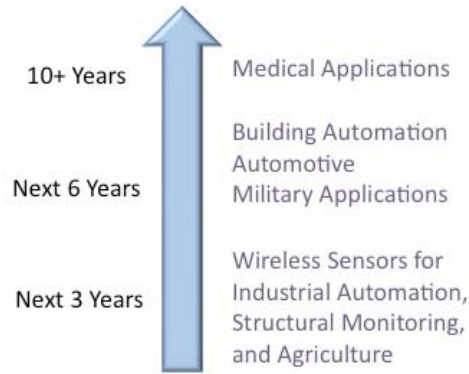
Figure 1-4. Likely market penetration scenario of energy harvesting devices.

1.2 SURVEY OF ENERGY HARVESTING TECHNOLOGY

This section entails a brief survey of various potential sources of ambient energy. A brief discussion is provided for each one, outlining the advantages and limitations of the particular energy source. Additionally, the state-of-the-art in building micro scale harvesters to convert the various energy sources is discussed. Table 1-1 is a summary of energy sources that can be used to power long-lifetime wireless electronic devices. The values in the table are compiled from published work and theory.

Table 1-1: Comparison of energy scavenging sources with a few fixed capacity energy storage methods.

Energy Source	Power (μW/cm^3)	Energy (Joules/ cm^3)	Power (μW/cm^3/yr)	Notes
Battery	-	2,880	90	
Micro Fuel Cell	-	3,500	110	
Ultracapacitor	-	50-100	1.6-3.3	
Heat Engine	10^6	3,346	106	
Radioactive (^{63}Ni)	0.52	1,640	0.52	
Solar (Outdoors)	15,000	-	-	Measured in Power/cm^2
Solar (Indoor)	10	-	-	Measured in Power/cm^2
Temperature	40	-	-	ΔT=5°C, Measured in Power/cm^2
Ambient RF	1	-	-	Away from transmitter
Air Flow	380	-	-	Air velocity 5m/s, and efficiency is 5%
Pressure Variation	17	-	-	Based on 1 cm^3 He undergoing ΔT=10°C per day.
Vibrations	375	-	-	

1.2.1   SOLAR ENERGY

With 120,000TW of solar power hitting the earth's surface at any given time, it is hard to believe that any other source of energy would ever be necessary, however converting this into cheap electrical power is difficult. Further when dealing with powering small distributed unmanned microsystems, the challenges become even more daunting.

Solar cells exploit the photoelectric effect, to generate current from incident light. These devices actually pre-date modern electronics and the transistor, with the first solar cell being developed by Charles Fritts in 1884 [6]. This device had an efficiency of 1%. The first patent for the modern solar cell was awarded to Charles Ohl and Gerald Pearson of Bell Laboratories in 1946 [7]. Today commercially available solar cell made out of Si have efficiency between 20-30%. If we assume a solar irradiance of $1000W/m^2$, which is approximately the amount of solar energy available on a clear sunny day, then these commercial solar cells can provide around $30mW/cm^2$.

Photovoltaics are currently experiencing a renaissance due to the ongoing concerns about climate change, and more importantly the access to cheap, clean energy. Many types of technologies are being investigated. On the one had, lower-efficiency but low-cost solar cells made out of amorphous materials are being researched. On the other side of the spectrum, researchers are trying to maximize efficiency. Two of the main approaches are to use multiple junctions as shown in Figure 1-5a, and solar concentration, which is shown in Figure 1-5b. Multiple junction devices allow for different bandgap semiconductors to capture more of the solar spectrum. These can be coupled with optics designed to concentrate the sun's light by factors of 100–10,000x. The highest reported efficiency so far is 40.7% [8], with researchers having announced

plans for a 50% efficiency solar cell in the near future [9]. These devices could raise the available power output to 100mW/cm^2.
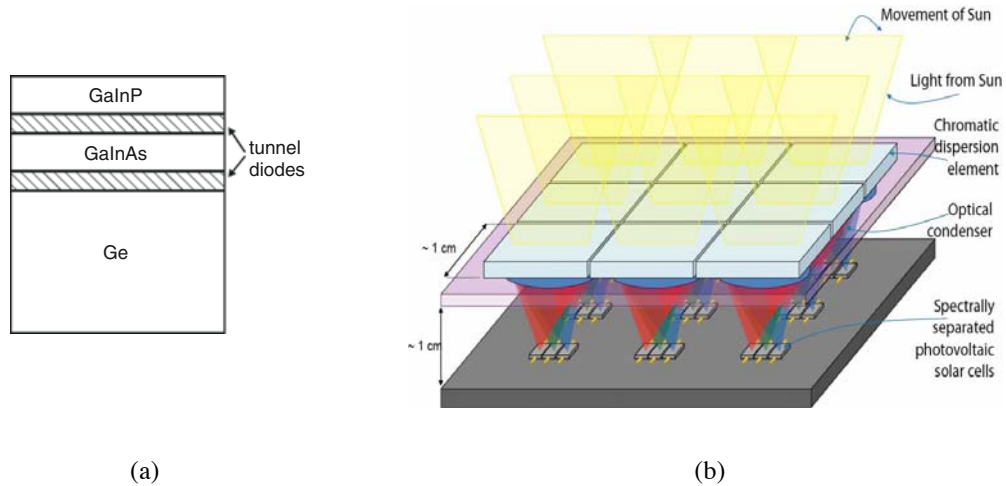
Figure 1-5. a) Outline of an epitaxial triple junction solar cell, the most energetic photons are absorbed in the top cell and subsequently the least energetic are absorbed in the semiconductor at the bottom [8]. b) Shown is a lateral solar cell approach. The concept is the same as the multiple junction device, however here the photovoltaic cells are laterally distributed. A set of optical elements is used to both concentrate the solar radiation and disperse appropriate wavelengths to the solar cells below [9].

The challenges associated with using solar cells to replace fixed-capacity power sources in long-lifetime applications are two. First, solar cells may only be useful outdoors. The available power indoor is 1000-2000x less than when exposed to direct sunlight. Second, when photovoltaic power sources are used outside, they have to be able to overcome challenges such as cloudy days, debris obstructing their line of sight (for example snow, dust, etc.), and adequate storage capacity to accommodate these occasions. One has to remember that unlike large power-plant operations, the applications that can benefit from scavenging energy are typically unmanned.
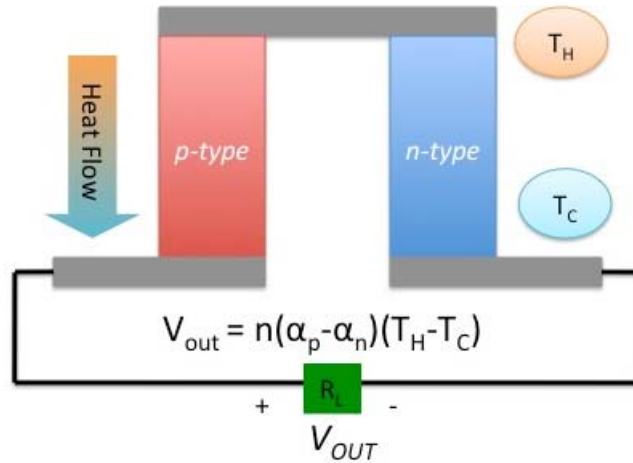
Figure 1-6. Illustration of the operation principle of thermoelectric generators based on the Seebeck effect.

1.2.2 THERMAL ENERGY

Variations in temperature offer another opportunity for scavenging energy. Despite their high cost and low efficiency, thermoelectric generators offer an interesting energy alterative because of their reliability and lack of moving parts. One of the first commercial energy scavenging devices was a thermoelectric generator built inside a Seiko watch released in 1999 [10].

Thermoelectric generators utilize the Seebeck effect where a voltage is created when there is a temperature difference between two different metals or semiconductors. A simple set of relations governs their behavior and they are shown in equations (1.1)-(1.2).

$$V = \alpha N (T_h - T_c),$$
<div align="right">(1.1)</div>

$$Power = \frac{V^2}{R_g} = \frac{\alpha^2 N^2 (T_h - T_c)^2}{R_g}.$$
<div align="right">(1.2)</div>

Here α is the Seebeck coefficient of the material, N is the number of thermopiles, T_h and T_c are the hot and cold side temperatures respectively, and R_g is the internal

resistance of the generator. Figure 1-6 shows a graphical representation of a thermocouple and the associated circuit. Ultimately the efficiency of thermoelectric conversion is governed by the Carnot cycle, which suggests a maximum efficiency of $\Delta T/T_h$. The meaning of this result is that for small temperature gradients, the efficiency of thermoelectric conversion is low.
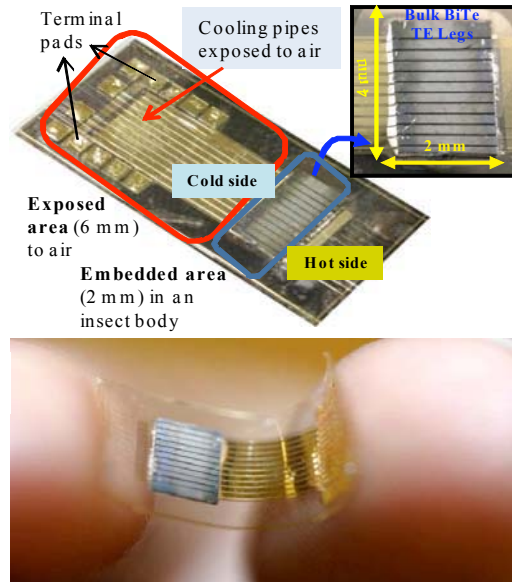
Figure 1-7. Photograph of a flexible thermoelectric generator designed for implantation into insects [11].

The design of thermoelectric generators is an optimization in the number of thermocouples relative to the internal resistance that is generated. To aid in this process materials with a high figure of merit *ZT* are chosen. The figure of merit takes into account the Seebeck coefficient, electrical resistivity, and thermal conductivity. By utilizing bulk Bi_2Te_3/Sb_2Te_3 (*ZT* of 0.8, compared with thin film *ZT* of 0.3-0.4) a flexible micro thermoelectric generator has been designed here at the University of Michigan which gives $0.9\mu W/cm^2 K$ [11]. This result is among the top echelon of reported thermoelectric results and a photograph of the device is shown in Figure 1-7. To generate a large thermal gradient, thermal isolation is very important, and this makes thermoelectric generators

prime candidates for miniaturization where they can exploit the micro scale to generate large thermal impedances. The best performing thermoelectric generator to date is designed by Thermo Life Energy Corporation, and gives a performance of ~15μW/cm²K, it has a diameter of 9.3mm, a mass of 230mg, and a thermal impedance of 43K/W, however its performance below ΔT = 5°K degrades rapidly [12]. As far as the author can ascertain this device utilizes thin film Bi_2Te_3.

The main drawback to utilizing thermoelectric generators is the absence of practical applications where a large enough temperature gradient can be formed to generate appreciable amounts of power.

1.2.3   AMBIENT RF AND COUPLED ENERGY

Given that in urbanized areas we are bombarded by background radio signals of all sorts, it would seem logical to consider taping into this stockpile of wasted energy. The problem is that the efficiency of tapping into this energy source is very small, and to design a system for the purpose of scavenging some of this energy requires a large collection area or extreme proximity to the radiating source. A crude analysis of this energy scavenging method approximates the power density a receiving antenna produces as E^2/Z_o, where Z_o is the radiation resistance of free space (377 Ohms) and E is the local electric field strength measured in Volts/meter [13]. This means that an electric field of 1V/m can produce 0.26μW/cm². The troubling aspect of this result is that an electric field of 1V/m is difficult to find, and even a few volts per meter are rare except when close to a
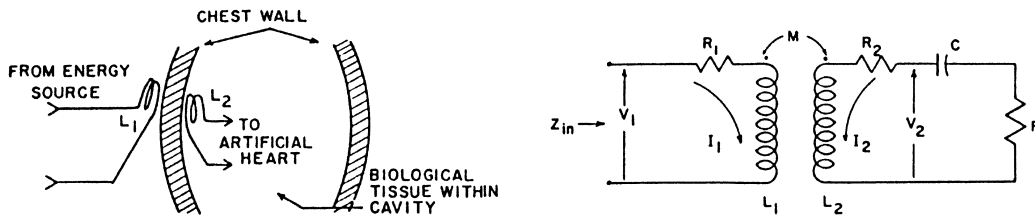
Figure 1-8. Inductively coupled power transfer model for implanted systems. On the left, one can see an illustration of the system, where one coil outside of the body is used to broadcast energy to another one implanted inside. On the right the electrical representation of the system is shown. Figure from [14].

powerful transmitter. This makes this source of ambient energy impractical for powering electrical devices.

A similar idea to using ambient radio signals is the idea of wirelessly transmitting energy for the purpose of coupling a part of it to power electrical devices. The first work in this area was done by Nicola Tesla who first patented the idea of long distance power transfer by means of inductive coupling 1900 [15]. This technology is now widely used to power medical devices and passive radio frequency identification devices (RFIDs). The basic principle is the same as a transformer where two coils are used in proximity to each other, and a magnetic field in one coil produced by an applied current, induces current in the second coil. This scheme was first designed to power an implanted artificial heart, and the first successful experimental validation occurred in 1960 using a coil which was surgically implanted in a dog [14] and is shown in Figure 1-8. Similarly, power transfer can be accomplished using capacitive or direct coupling. The problem is that the efficiency of this type of omnidirectional power transfer is very low and requires the transmitter to be very close to the receiver; otherwise most of the energy spreads out and is wasted. Alternatively a direct unidirectional approach can be used, for example by using a laser, however this type of system requires uninterrupted line of sight. Recently,

researchers at MIT have improved the efficiency of inductively coupled systems and were able to power a 60W light bulb over 2 meters with a 40% efficiency [16]. They achieve this by means of two self-resonant coils on both the source and receiver end. A start-up company called Powercast is currently working to commercialize similar technology whereby they wirelessly transmit energy, up to several meters, to power various receivers in a room. Their technology is tunable in the 40MHz-5.8GHz frequency span, however it is not publicly available how much power can be coupled at what distance and with what efficiency. Nevertheless, these types of systems that transmit energy will remain limited to several meters because the required transmitter power quickly exceeds the approved FCC safety levels.

1.2.4   AMBIENT ACOUSTIC ENERGY AND PRESSURE VARIATIONS

Machines, humans, and the environment cause acoustic noise to varying degrees and it would seem logical that this stray energy could be captured and utilized; however, very little energy is available. One author estimated that $0.003\mu W/cm^3$ is available at 75dB and $0.9\mu W/cm^3$ at 100dB [17]. This limits scavenging acoustic energy to some niche applications in very loud environments. This is perhaps the reason why very little work has been done in this area. One group has developed a method to scavenge acoustic energy by using a Helmholtz resonator [18] (Figure 1-9). The authors are able to generate 30mW from a sound pressure level of 160dB. It is unclear how large the device is. As a point of reference a rock concert is 120dB and at 160dB mammals will get tissue damage in their ears.
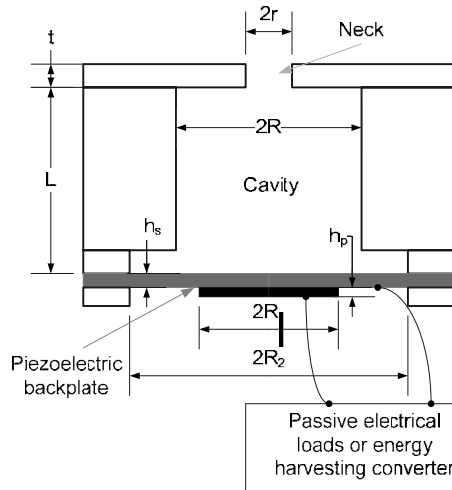
Figure 1-9. Shown is the configuration for a Helmholtz resonator for acoustic energy scavenging. A diaphragm with a laminated piezoelectric material is suspended under a Helmholtz cavity [18].

Devices that seek to scavenge energy from pressure variations similarly have limited application due to the lack of practical environments where large enough, or alternatively, rapidly varying pressure variations can be found. That being said, a start-up company, which seeks to develop energy scavenging solutions for automobile tire pressure sensors, has filed a patent [19] that targets the use of pressure variations in tires. The device is configured as a standard differential pressure sensor, featuring a round diaphragm with a piezoelectric material adhered on top. The authors have performed measurements that show that $5\text{-}10\text{x}10^{-3}$psi pressure variations occur in tires when an automobile is moving. When looking at the frequency response, several peaks occur in the band 0-100Hz. They claim that 138mW/mm^2 can be generated from these pressure variations. A publicly available product is not available as of the writing of this thesis. Another effort seeks to scavenge energy from the expansion and contraction of a blood artery [20]. A typical blood pressure waveform has systolic/diastolic pressures of 115/80 mmHg and a pulse of 60 beats per minute. This can cause the typical distal abdominal aorta to vary from 15.8mm to 17.3mm in diameter. The authors have placed a Polyvinylidene Fluoride

15

(PVDF) flexible polymer piezoelectric material around a mock artery. Using a device volume of 0.25cm^3 they were able to generate 16nW.

1.2.5   RADIOACTIVE ENERGY HARVESTING

A new energy scavenging source deals with capturing the emitted energy of various radioisotopes that emit low-energy beta particles. These particles are essentially high-energy electrons, which do not pose the health concerns typically associated with radiation. For example 1 to 10 millicuries of nickel-63 or tritium can be blocked by plastics, metal, or semiconductor 25-100μm thick, as well as by the top layer of dead skin on humans. This work is promising if researchers can get over significant efficiency, safety, cost, and public relations hurdles. Compared to chemical fuels, radioisotopes have much higher energy density, 10^5kJ/m^3, and because the half-life of certain isotopes can be as large as hundreds of years, they can supply energy for a very long time. Unlike the large isotope powered generators used by NASA in satellites, which convert the radioactive decay into thermal energy before converting it to electrical, the micro-scale generators being developed either first generate mechanical motion, or generate electrical current directly from the emitted particles. In the case of direct conversion, a sample of nickel-63 is placed in proximity to a p-n junction. As the emitted beta particles ionize the diode's atoms, they produce electron-hole pairs in the vicinity of the junction, producing current [21]. These betavoltaic devices operate with efficiencies of less than 0.5%, and are unlikely to yield reliable devices due to long term impact damage of the semiconductor material. Alternatively, researchers are able to deflect a cantilever beam by means of an electric field developed between the cantilever and the decaying isotope [21, 22] (Figure 1-10). As electrons from the isotope are emitted, they collect at the tip of

the cantilever, pulling it towards the radiation source, until it touches and discharges –

releasing the beam to resonate at its natural frequency. A piezoelectric material attached

to the beam can be used to convert the mechanical motion into electrical power. A

microfabricated 1cm long silicon device with a sol-gel PZT layer is able to generate a

peak of 1.13μW [23]. However, depending on the beam stiffness and gap to the isotope,

the reciprocation period can be quite large (several hundred seconds), making the average

power generated very small. Currently these devices operate with an efficiency of less

than 5%, however researchers feel they can improve that to 20% in coming years.
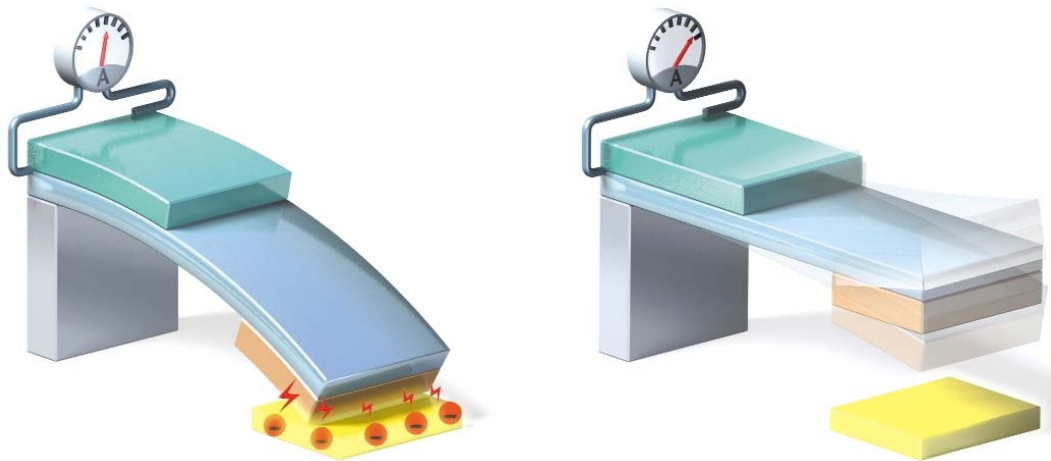
Figure 1-10. A beam with a piezoelectric element is shown to deflect after an electric field is generated
between a radioisotope sample on the bottom and a collector place on the beam. After the beam touches
down and discharges, it is released to resonate at its natural frequency [21].

1.2.6   HARVESTING ENERGY FROM AMBIENT AIR/FLUID FLOW

The first of a series of examples of energy harvesting from motion is the use of

kinetic energy due to airflow (and other fluids). Compared to other sources of kinetic

energy, airflow has received the least attention. Of course, this is only true as far as

miniaturization is concerned. The windmill, invented in Persia in the 9th century, is

perhaps the second energy-harvesting apparatus ever devised by mankind. Today, wind-

farms are becoming increasingly popular due to the cheap clean energy that they produce, and at the same time wind turbine technology is quickly being refined.

The kinetic energy of a flowing fluid with speed U and fluid density ρ is $0.5\rho U^2$, resulting in a power flow of $0.5\rho U^3$ per unit area normal to the fluid motion [24]. Needless to say, not all of that power can be extracted because then the fluid would stop moving. Thus, the power extracted by a device of area A, and "coefficient of performance" C_p ($0 < C_p < 1$) is given in equation (1.3).

$$P_{out} = \frac{1}{2}C_p\rho AU^3 \tag{1.3}$$

The ideal maximum value of C_p is 0.593, and this is called the Betz limit [25]. Modern wind turbine rotors achieve a C_p value between 0.4 and 0.5. On the other hand, efforts to miniaturize airflow generators have yielded a maximum C_p of around 0.1. This illustrates one of the main difficulties in harvesting airflow energy: effective miniaturization [26-30]. Furthermore, all of these devices are still quite large because they operate on the same principle as the wind turbine. Only one effort has led to a device that utilizes micromachining and it is shown in Figure 1-11 [27, 29]. It comprises a 12mm diameter rotor made out of SU8 using laser ablation. Although this device was not tested in free-stream, 1mW was generated in a duct test using 35l/min volume flow. The turbine created a pressure drop of 8.4mbar. Although it is an impressive first result, this device requires free stream flow rates that are impractical (40m/s). Practical airflow powered harvesters will have to operate in the 1-5m/s speed range, and they will have to overcome issues like high viscous drag at low Reynolds numbers, as well as increased friction losses. However, if they can reach even a C_p of 0.1, Eq. 2-3 predicts that 750μW/cm^2 can be obtained at 5m/s decreasing to 6μW/cm^2 at 1m/s.
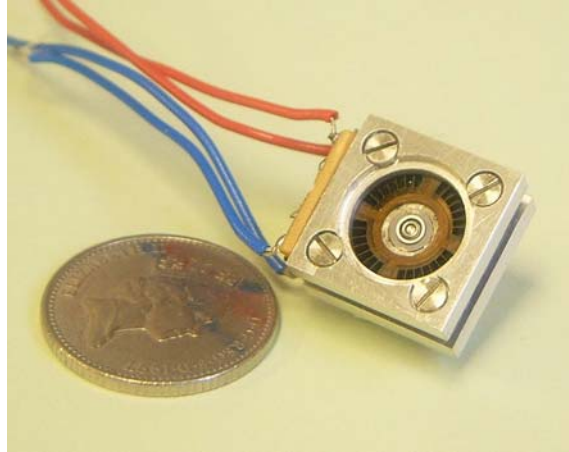
Figure 1-11. An axial flow permanent magnetic micro-turbine generator designed to convert ambient air flow to electrical power shown next to a 5 pence coin [29].

1.2.7 DIRECT FORCE SCAVENGERS

Direct force application constitutes a special case of energy scavenging from motion. In these devices somebody or something typically applies a force inducing mechanical motion that is then converted into electrical energy. A couple of old examples of this are either self-powered flashlights, which can be powered by repeatedly squeezing and releasing their handle, or AM/FM radios which could be powered by turning a crank. Additionally, direct force scavengers can be either designed to work "passively," for example shoe soles which have embedded mechanisms to scavenge energy from human walking, or they can work actively, such as a push-button designed to generate enough power to perform some specific task. The engineering considerations with these scavengers are different from completely passive devices, because they seek to maximize the imparted kinetic energy versus the ability of the device to convert this energy to electricity. Further, they have almost complete control over where the load is applied, which can allow them to be more effective.
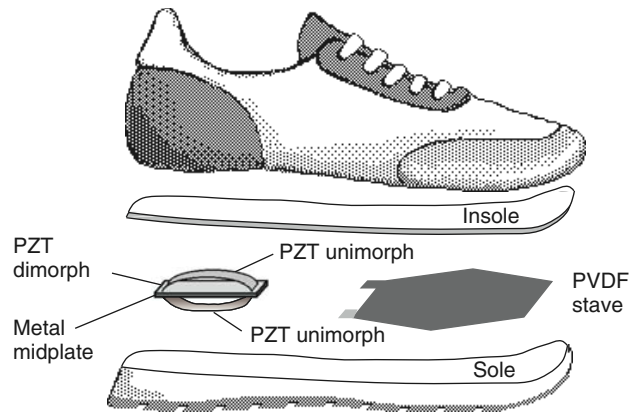
Figure 1-12. Shown are the two ways of scavenging energy, developed to use the d_{31} piezoelectric mode: A PZT unimorph or dimorph under the heel and a PVDF stave under the ball of the foot [31].

The first example was developed at MIT in the late 90's. Researchers sought to harvest energy from walking by means of an embedded piezoelectric element in the sole of a shoe [31, 32]. As shown in Figure 1-12 they utilized two different approaches, a pre-bent lead zirconate titanate (PZT) unimorph is flattened out against a back plate causing compression/tension about the neutral axis when the heel comes in contact with the ground, and a PVDF laminate is placed in the front of the shoe such that when the center bends, the outside corners are pulled in causing strain. An analysis done by the authors suggests that not enough energy is available to effectively use the d_{33} mode, so both of these devices utilize the d_{31} polling direction The device embedded in the heel produced about 2mW of average power, and the PVDF stave produced about 1mW.

The same group at MIT has also developed a push-button device integrated with an off-the-shelf RF transmitter which consumes 7.5mW and can broadcast a signal over 50 feet [33]. A piezoelectric element from a commercially available lighter was used. The device has a deflection of 3.5mm at a force of 15N. They generated enough energy to power the transmitter over 20ms using a single actuation. A similar effort at the

University of Michigan sought to generate power from a beetle flapping its wings [34]. Piezoelectric beams were attached such that the beetle would actuate the tips during flight. The authors generated 11.5μW and 7.5μW in device volumes of 11mm^3 and 5.6mm^3 respectively. They predict that an optimized device, utilizing a coiled beam (one attached to each wing) could in the future generate 101.6μW total. It is important to note that the most successful commercial energy scavenging product to date comes from this category of energy harvesters [35]. A spin off from Siemens, called EnOcean, has commercialized a wireless light switch, which generates energy from the pushing of the switch button, to transmit an on/off signal for operating building lighting. The device works electromagnetically, whereby the push of a button generates oscillation in a magnet encircled by a coil winding.

Direct force scavengers are not limited to human or animal power. One group has performed a theoretical analysis as well as preliminary test to utilize piezoelectric elements to generate power from raindrops [36, 37]. Using a piezoelectric element which is 7.5mm^3, they predict a peak power output of 0.8μW from a 1mm diameter raindrop traveling at 2.8m/s, and 12.5μW from a 5mm diameter raindrop traveling at 5.7m/s using a slightly larger device. Laboratory experiments have yielded 73μW (3mm diameter traveling at 4.5m/s) and 8μW (1.6mm diameter traveling at 3.2m/s).

BODY HEAT 2.4-4.8 W
(CARNOT EFFICIENCY)

EXHALATION 0.40 W
(1.0 W)

BLOOD PRESSURE 0.37 W
(0.93 W)

BREATHING BAND 0.42 W
(0.83 W)

ARM MOTION 0.33 W
(60 W)

FINGER MOTION 0.76-2.1 mW
(6.9-19 mW)

FOOTFALLS 5.0-8.3 W
(67 W)
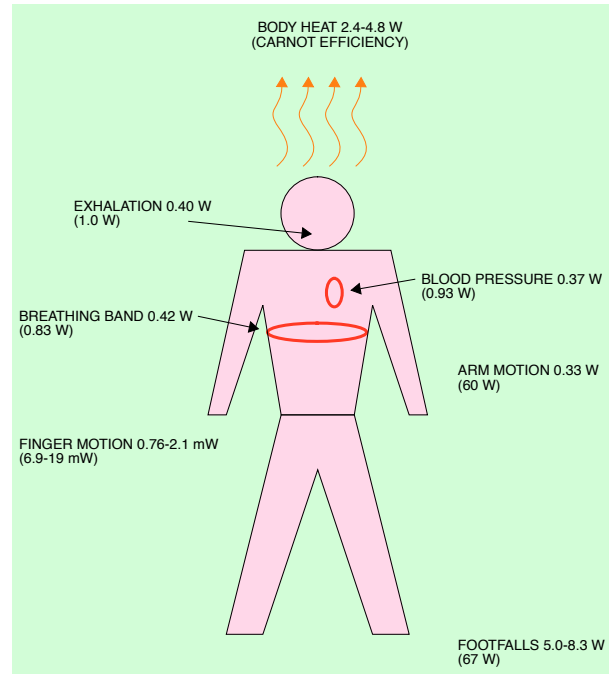
Figure 1-13. Power available from body driven sources. In parenthesis is the total power the body requires for each action [38].

1.2.8   HUMAN POWERED ENERGY HARVESTING

A great deal of consideration has gone into devising ways to scavenge waste energy generated by humans and the human body. In many ways the previous section is a good lead in to this topic, because force application as well as motion are some of the most important methods. Interest in this area has been generated by people seeking to develop wireless body networks of sensors and actuators, those developing new ways to power advanced implantable devices and prosthetics, and people wanting to use harvested energy to recharge mobile gadgets. A thorough analysis of various energy sources has been done [38], and the available energy is shown pictorially in Figure 1-13. Many of the methods to convert this energy have already been outlined. The values in Figure 1-13 constitute the total amount of power available, of course only a portion could

22

possibly be harvested in practice. For example, if one wanted to convert all of the wasted head the body gives off, the entire human would have to be wrapped up in thermocouples. Thus, one of the engineering challenges associated with harvesting waste human power is to do so unobtrusively. The ideal source of wasted energy produced by humans, which is the most abundant and at the same time is easily utilized without being intrusive, is kinetic energy. This is one of many reasons why vibration scavenging has garnered the most interest out of all of the energy scavenging mechanisms and will be covered in detail in this section.
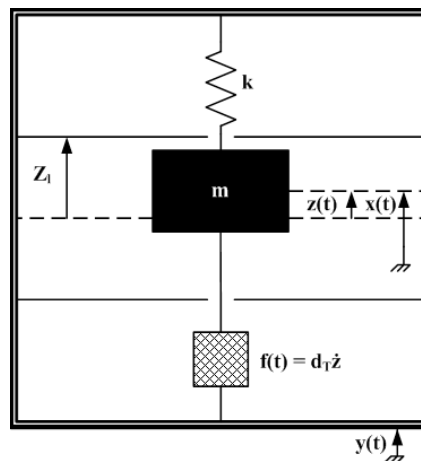
Figure 1-14. Generic model of an inertial micro power generator.

1.3 SCAVENGING ENERGY FROM AMBIENT VIBRATIONS

1.3.1 BASIC THEORY OF VIBRATION SCAVENGING

Vibration-driven scavengers can be analyzed using a generic model shown in Figure 1-14. For the sake of analysis it can be assumed that the vibration source has infinite power, meaning that it is unaffected by the movement of the generator. A typical generator consists of a rigid casing with a seismic mass suspended inside. The mass

moves relative to the casing in response to an externally applied displacement. During this motion, it performs work against a damping force f opposing the movement of the mass, thereby generating energy. The damping force f is generated in response to a disturbance in an applied electric or magnetic field. The purpose of the suspension is to constrain the mass, but typically it is also used to generate a resonant response. The displacement of the mass relative to the frame is denoted by $z(t)$. The absolute motion of the mass $x(t)$, is given by the sum of the source motion $y(t)$ and $z(t)$, $x(t) = y(t) + z(t)$. For simplicity the source motion will be considered harmonic $y(t) = Y_o cos\omega t$, Y_o being the source motion amplitude. Lastly, the relative mass to frame displacement will be denoted by Z_o and the maximum such displacement for a particular device is referred to as Z_l.

Summing the dynamic forces on the mass gives the differential equation of motion for a typical generator and is shown in Eq. (1.4).

$$m\ddot{z}(t) + d_T \dot{z}(t) + kz(t) = -m\ddot{y}(t) \tag{1.4}$$

The equation is normalized using the damping factor $\zeta = d_T/2m\omega_n$, where ω_n is the natural frequency $\omega_n = \sqrt{k/m}$, and the Laplace transform is taken to give the transfer function $Y(s)/Z(s)$ shown in Eq. (1.5).

$$\frac{Z(s)}{Y(s)} = \frac{-s^2}{s^2 + 2\zeta\omega_n s + \omega_n^2} \tag{1.5}$$

The magnitude of this transfer function is given by

$$\frac{Z_o}{Y_o} = \frac{\eta^2}{\sqrt{(1-\eta^2)^2 + (2\zeta\eta)^2}}, \tag{1.6}$$

where $\eta = \omega/\omega_n$. The energy dissipated in the damper every cycle is equivalent to the work performed on the damper, given by integrating the damping force $f = d_T\dot{z}$ over a full

24

cycle and shown in Eq. (1.7):

$$W_d = \oint f dz.$$

(1.7)

This analysis assumes viscous damping, which is true for electromagnetic and piezoelectric generators. Electrostatic generators can be modeled as coulomb damped devices and result in non-linear systems that must be treated separately. Assuming a steady state displacement and velocity of

$$z = Z_o \sin(\omega t - \phi)$$
$$\dot{z} = \omega Z_o \cos(\omega t - \phi).$$

(1.8)

the energy dissipated per cycle in Equation (1.7) becomes

$$W_d = \oint d_T \dot{z} dz = \oint d_T \dot{z}^2 dt = d_T \omega^2 Z_o^2 \int_0^{2\pi/\omega} \cos^2(\omega t - \phi) dt = \pi d_T \omega Z_o^2.$$

(1.9)

Multiplying the energy by the period and substituting an expression for Z_o defined in Eq. (1.6) gives the power dissipated in the damper to be

$$P = \frac{\zeta \eta^3 Y_o^3 \omega^3 m}{\left[1 - \eta^2\right]^2 + \left[2\zeta\eta\right]^2}.$$

(1.10)

This equation predicts that the generated power can increase without bound at resonance ($\eta = 1$). Mathematically this happens because the source is assumed to have infinite power, no internal displacement limit is taken into account, and parasitic dissipative forces have not been considered.

To determine the maximum obtainable power, one first has to find the optimal damping factor ζ_{opt}, given by the point at which $dP/d\zeta = 0$,

$$\zeta_{opt} = \frac{1}{2\eta}\left|\eta^2 - 1\right|. \tag{1.11}$$

This leads to the maximum power, P_{max}, by substituting Eq. (1.11) into Eq. (1.10)

$$P_{max} = \frac{\eta^3 Y_o^2 \omega^3 m}{4\left|\eta^2 - 1\right|}. \tag{1.12}$$

The main problem with Eq. (1.12) is that it can violate physical constraints imposed on the system, namely the displacement limit. A typical displacement for a micromachined generator could be as low as several microns and for larger centimeter-scale devices it would likely be in the range of a few millimeters. The internal displacement is given by rearrangement of Eq. (1.6)

$$Z_o = \frac{\eta^2 Y_o}{\sqrt{(1-\eta^2)^2 + (2\zeta\eta)^2}}. \tag{1.13}$$

This means that for devices designed to operate at resonance, the maximum power is generated when the damping is designed such that Z_o is equal to but does not exceed Z_l. The new constrained ζ_{opt} can be computed by rearranging Eq. (1.13)

$$\zeta_{opt} = \frac{1}{2\eta}\sqrt{\eta^4\left(\frac{Y_o}{Z_l}\right)^2 - (1-\eta^2)^2}. \tag{1.14}$$

Using this constrained optimal damping, a more realistic measure of the maximum power can be computed by substituting Eq. (1.14) into Eq. (1.10)

$$P_{max} = Y_o^2 \omega^3 m \frac{1}{2\eta}\left(\frac{Z_l}{Y_o}\right)^2 \sqrt{\eta^4\left(\frac{Y_o}{Z_l}\right)^2 - (1-\eta^2)^2}. \tag{1.15}$$

Finally, the power which can be generated at resonance is simply Eq. (1.15) with $\eta=1$

$$P_{res} = \frac{1}{2}\omega^3 m Y_o Z_l. \tag{1.16}$$

So far the analysis has assumed that there are no parasitic losses in the system. Of course, that is not realistic, and when the parasitic damping is comparable in scale to the electrical damping of the system it must be included in the analysis. This means that the damping coefficient $d_T = d_p + d_e$, where d_p is the open circuit parasitic mechanical damping and d_e is the electrical damping of the transduction mechanism. It follows that $\zeta_T = \zeta_p + \zeta_e$ and that the quality factor of the system, which in total is equal to $Q_T = \omega_n m / d_T$, will be given by

$$\frac{1}{Q_T} = \frac{1}{Q_p} + \frac{1}{Q_e}. \tag{1.17}$$

A modified equation giving the maximum power at resonance having taken parasitic damping into account is given by:

$$P_{max,e} = \frac{\zeta_e m Y_o^2 \omega_n^3}{4(\zeta_e + \zeta_p)^2}. \tag{1.18}$$

Maximum power is delivered to the electrical domain when $\zeta_p = \zeta_e$, meaning that the damping arising from the electromechanical transduction should be equivalent to the mechanical losses. Before the power predicted by Eq. (1.18) can be delivered to a load, more losses can be expected in the electrical domain, and as such Eq. (1.18) still contains idealities that in practice will need to be addressed. These losses are specific to the different transduction methods, but one example is the internal impedance in electromagnetic devices.

1.3.2   TRANSDUCTION MECHANISMS

Once mechanical motion is coupled into the generator a transduction mechanism is required to convert this energy into electricity. Typically, this mechanism utilizes the generated strain or relative displacement within the system. In the case of displacement, either the position (electrostatic generators) or velocity (electromagnetic generators) can be used. Alternatively, by utilizing an active material, such as a piezoelectric, deformations in the mechanical system can also be utilized for transduction. Each mechanism has its own damping characteristics, as well as a variety of design constraints, which should be considered when determining which one should be utilized for a particular device. Many authors have examined the overall merits of using one transduction type over the other [39-43], and a summary will be presented at the end of this section.

1.3.2.1 Electromagnetic Implementation

In a typical electromagnetic generator the damping mechanism is implemented with a moving magnet linking flux to a stationary coil. Although it is possible to implement this type of generator with a stationary magnet and moving coil, the other case offers the advantage that electrical connections are not needed to the moving parts, and also the magnet mass can be utilized (although magnets are typically not very dense materials). The operating principle is that voltage is induced in the coil due to the varying flux linkage of the moving magnet (or vice versa) in accordance with Faraday's law. The resultant current causes a force to develop which opposes the relative motion between the coil and the magnet. In the simplest case, where a coil moves through a constant magnetic field the damping coefficient is given by Eq. (1.19)

$$d_e = \frac{(NlB)^2}{R_{load} + R_{coil} + j\omega L_{coil}}, \tag{1.19}$$

where N is the number of coil turns, l is the side length of the coil (assuming a square), B is the flux density, R_{load} is the load resistance, and R_{coil} and L_{coil} are the parasitic resistance and inductance of the coil. This equation is a rough approximation, which assumes that the coil moves from a constant high magnetic field region to a zero field region. If the gradient of the magnetic field *(dB/dz)* is constant across the plane of the coil and equal to *B'*, then the numerator in Eq. (1.19) can be changed to *(NAB')²* where A is the area of the coil. As already mentioned in the last section, power is optimally delivered to the load when $d_p = d_e$, and so using Eq. (1.19), the optimum value of R_{load} can be determined, or alternatively given an R_{load} an optimum damping coefficient can be designed. Combining Eq. (1.19) and Eq. (1.18) and rearranging the terms gives the optimal R_{load} value as well as the maximum attainable power

$$R_{load} = R_{coil} + \frac{(NlB)^2}{d_p}, \tag{1.20}$$

$$P_{em,\max} = \frac{m\omega_n^3 Y^2}{4\zeta_p}\left(1 - \frac{R_{coil}}{R_{load}}\right). \tag{1.21}$$

1.3.2.2 Piezoelectric Implementation

Certain types of crystals become electrically polarized when subjected to a mechanical strain, and conversely they can deform due to an applied electric field. These types of materials are referred to as being piezoelectric and have been used to convert electrical energy into mechanical and vice versa for quite some time. The constitutive

equations for piezoelectric material, which describe the mechanical and electrical behavior, are given by

$$\delta = \frac{\sigma}{Y} + dE, \tag{1.22}$$

$$D = \varepsilon E + d\sigma, \tag{1.23}$$

where δ is the strain, σ is the stress, Y is the Young's modulus, d is the piezoelectric strain coefficient, D is the charge density, ε is the materials dielectric constant, and E is the electrical field. Piezoelectric materials typically exhibit anisotropic characteristics, meaning that the properties of the material are different depending on the direction of the applied force and the orientation of the polarization and electrodes. To distinguish between these various scenarios a system of notations is used. Each material property is given a set of subscripts, ij, where i represents the direction of the excitation and j is the direction of the system response. For example, d_{33} gives the strain coefficient when the electric field and the applied strain are along the polarization axis, and conversely d_{31} means that the electric field is in the same direction as before, but the strain is orthogonal to the polarization axis. These are the two most commonly used modes in energy harvesting applications. This naming convention is described Figure 1-15, which shows the two commonly used modes, as well as the general renaming of the *x, y,* and *z* axes with the directions 1, 2, and 3. As far as the symbol itself, the piezoelectric strain constant, *d*, can be defined as the strain developed per applied electric field (1/V) or conversely the short circuit charge density per applied stress (C/N). An additional important material constant is the coupling coefficient, *k*, which gives the efficiency with which energy is converted between the electrical and mechanical domains. This is

defined such that $k_{ij}^2 = W_{i,e}/W_{j,m}$ where $W_{i,e}$ is the electrical energy stored in the i axis, and $W_{j,m}$ is the mechanical input energy in the j axis.
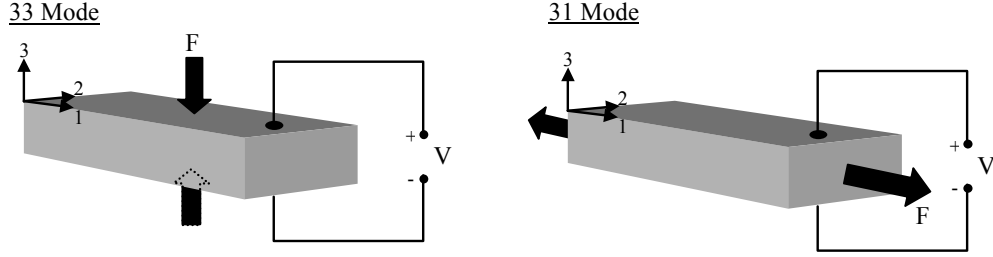
Figure 1-15. Illustration of the naming conventions for piezoelectric material properties, by using the 33 and 31 modes of operation as examples.

Since the damping effect of piezoelectric materials can also be modeled as being proportional to velocity, an expression for the mechanical damping coefficient has been derived in [17] and can be expressed as

$$d_e = \frac{2m\omega_n^2 k^2}{2\sqrt{\omega_n^2 + \left(1\Big/\left(R_{load}C_{load}\right)^2\right)}},$$ (1.24)

where k is the coupling coefficient, and C_{load} is the load capacitance. Once again an optimal load can be chosen to optimize the electrical damping. The optimum resistance is given by

$$R_{load} = \frac{1}{\omega_n C}\frac{2\zeta_p}{\sqrt{4\zeta_p^2 + k^4}},$$ (1.25)

and is a function of the parasitic mechanical damping.

1.3.2.3 Electrostatic Implementation

Electrostatic generators have to be modeled differently then either electromagnetic or piezoelectric because they are nonlinear, and also the damping force is constant and

31

opposes motion. In other words, the generator has to be modeled as being Coulomb damped, which is typically used to model friction. Electrostatic generators are essentially comprised of a capacitor whose plates can move. As the conductors move relative to each other, the energy stored in the capacitor changes. The fundamental definition of capacitance C, is $C = Q/V$, where Q is the stored charge and V is the electric potential between the plates. Likewise, for a parallel plate capacitor $C = \varepsilon A/g$, where A is the overlapping area of the plates, and g is the gap. Work can be done by either constraining the charge Q or constraining the voltage V, and varying capacitance. In addition, there are two ways to typically vary capacitance, one is to vary the overlapping area of the plates, in other words the plates move in parallel to each other, or by varying the gap by moving the plates perpendicular to each other. The energy stored in a capacitor is given by

$$E = \frac{1}{2}QV = \frac{1}{2}CV^2.$$
(1.26)

The damping force is defined by considering the change in energy per change in displacement (dE/dz). In the case of a varying gap capacitor this gives a force

$$F = \frac{Q^2}{2\varepsilon A},$$
(1.27)

when the charge on the plates is held constant, and

$$F = \frac{\varepsilon A V^2}{2g^2},$$
(1.28)

when the voltage on the plates is held constant.

The work performed against the electrostatic forces given in Eq. (1.27) and Eq. (1.28) represents the harvested energy. The energy dissipated and hence the power is given by

finding the force-distance product [43], where $U = sin(\pi/\omega_c)/[1 + cos(\pi/\omega_c)]$

$$P = \frac{4Y_o F \omega \eta^2}{2\pi} \left[\frac{1}{1-\eta^2} - \left(\frac{F}{mY_o\omega^2\eta}U \right)^2 \right]^{1/2}.$$
(1.29)

The optimum damping force can also be found and is given by

$$F_{opt} = \frac{y_o\omega^2 m}{\sqrt{2}} \frac{\eta}{\left|(1-\eta^2)U\right|}.$$
(1.30)

The derivation of these equations as well as their practical application is very involved and is discussed in more detail by Mitcheson *et al* [43].

1.3.3 COMPARING THE DIFFERENT TRANSDUCTION METHODS

There are several things that need to be considered before selecting one of the three conversion mechanisms including the inherent energy density of each one, material and practical limitations, and system limitations.

The relative energy density of the three mechanism has been analyzed and compared by Roundy [17]. The energy density of a dielectric material is given by $0.5\varepsilon E^2$ (J/m^3). Likewise, the energy density of an electromagnetic device is given by $0.5B^2/\mu_o$, where μ_o is the magnetic permeability of free space, which is 1.26 x 10^{-6} H/m. To derive the energy density equation for piezoelectric materials requires reducing Eq. (1.22) to its open circuit condition such that $D=0$. Solving for E and substituting that into the energy density equation for a dielectric material gives the following energy density for piezoelectric materials:

$$\frac{\varepsilon E^2}{2} = \frac{\sigma^2 d^2}{2\varepsilon}.$$ (1.31)

This can be rewritten more intuitively by using the coupling coefficient, which is a measure of efficiency between 0 and 1, where the relationship between d and k is $d = k\sqrt{\varepsilon/Y}$. Substituting this expression into Eq. (1.31) gives the alternate equation for energy density:

$$\frac{\varepsilon E^2}{2} = \frac{\sigma^2 k^2}{2Y}.$$ (1.32)

Substituting the yield strength of PZT (safety factor of 2), and some common piezoelectric material properties, gives an energy density of 335mJ/cm^3. The same analysis for electrostatic devices, assuming the permittivity of free space ε_o, and a gas breakdown field of 100MV/m, gives an energy density of 44mJ/cm^3. Lastly, for a magnetic field of 1T, the energy density of electromagnetic transduction is 400mJ/cm^3.

Mitcheson et al [24, 41, 43] have performed a detailed theoretical study related to the design of the overall energy harvesting system. They conclude that for large devices (high Z_l) and for low source amplitudes (small Y_o), which can be summarized generally as having $Z_l/Y_o > 0.1$, resonant operation is preferred. An exception to this is when the operating frequency is less than half of the resonant frequency, in which case a non-resonant mode of operation should be sought. For devices operating at resonance, electrostatic devices provide superior performance when the operating frequency is close to but below the resonant frequency of the device. Alternatively for devices operating above the resonant frequency, piezoelectric and electromagnetic transduction offers a better alternative. For a device operating at resonance, all three transduction methods are

said to produce similar results.

In addition to system related issues, one has to also consider the many practical constraints that are imposed by the properties of the various transduction schemes. Electromagnetic devices are likely to be the most reliable scheme: they do not age as quickly as piezoelectric and they have been shown to have a higher power density than electrostatic. However, it is difficult to generate strong damping forces in small geometries or at low frequencies since it is challenging to achieve the rapid flux changes necessary. Similarly, it is hard to scale this transduction scheme because integrated approaches would be limited in the number of coil turns. On the other hand, electrostatic devices are impractical and inefficient in large systems and are best suited to the micro-scale where they can exploit various physical properties to their advantage, they can readily be bulk micromachined, and can be easily integrated into complex systems. Voltage constrained devices are said to offer better performance than charge constrained [24], however in either case a pre-charge source is necessary. Using an electret can eliminate the need for this source. On the other hand, because the damping force is proportional to the pre-charge voltage, it can be actively tuned for optimum operation when the pre-charge voltage is not fixed. It could be argued that the third possibility of using piezoelectric materials has the highest practically achievable energy density in miniature power generating devices. However, piezoelectric materials are expensive, difficult to integrate (especially some of the better performing ones), and in some cases are toxic. Many of the piezoelectric materials used to date are ceramics, which limits the amount of strain/deflection they can undergo, and a lever mechanism may be required to combine them with devices that undergo significant displacements. In the end, the

engineer has to weigh all of these issues against application, size, and cost to determine which one is best suited to their needs.

1.3.4 VIBRATION SCAVENGER PERFORMANCE METRICS

In order to discuss inertial energy harvesters, and to determine the relevant issues that have yet to be addressed in this field, metrics for performance have to be developed and standardized. This is easier said than done, because unlike a fixed capacity energy source (e.g. battery), where one simply has to give the power density and the current drain capability of the device, energy harvester performance is a strong function of the available ambient energy and its characteristics. Various metrics have been proposed including power density, normalized power density [44], and two measures of efficiency [43, 45]. The simplest metric, to compute the power density, gives almost no meaningful information. For this reason a more universal metric has been proposed, which normalizes the power density by dividing by the source acceleration amplitude squared. This approach has two big drawbacks: 1) power is proportional to acceleration squared divided by frequency and so the source has not been completely normalized out, and 2) power is also a function of mass times internal displacement range (i.e. volume$^{4/3}$), and so dividing by volume still gives an unfair advantage to larger generators.

Two metrics of performance have been proposed [43] that take into account all of the aforementioned complications when dealing with energy harvesting. They are based on work done by Roundy [45]. The first is the harvester effectiveness

$$E_H = \frac{Useful\,Power\,Output}{Maximum\,Possible\,Output} = \frac{Useful\,Power\,Output}{\frac{1}{2}Y_o Z_l \omega^3 m} \, .$$

(1.33)

The Harvester Effectiveness is a measure of how close a given design is to its ideal performance (0-100%). It does take into account the source energy, and although it does give a one to one measure of device performance, it needs to be accompanied by size, because that is not taken into account. For this reason the same authors introduced a metric called the Volume Figure of Merit (FoM_v), which aims to compare device performance as a function of their overall size [24]:

$$FoM_v = \frac{Useful\,Power\,Output}{\frac{1}{2}Y_o\rho_{AU}Vol^{4/3}\omega^3}.$$ (1.34)

Here the mass (m) and maximum displacement range (Z_l) are substituted with parameters for an idealized device with cubic geometry, having the same volume, but with a proof mass made of gold (one of the densest materials used in micromachining) occupying half of this volume, and space for displacement occupying the other half. A real device cannot reach 100% in practice, because some space must be taken up by the frame, suspension, and transducer components. Lastly, in order to account for bandwidth a further modification is proposed called the Bandwidth Figure of Merit

$$FoM_{BW} = FoM_v \times \frac{BW_{3db}}{\omega},$$ (1.35)

which is simply the volume figure of merit multiplied by the fractional bandwidth (i.e. 3dB bandwidth divided by the center frequency).
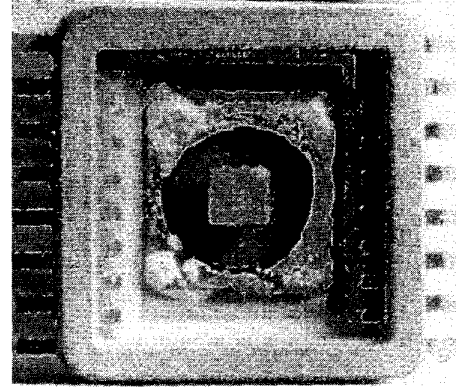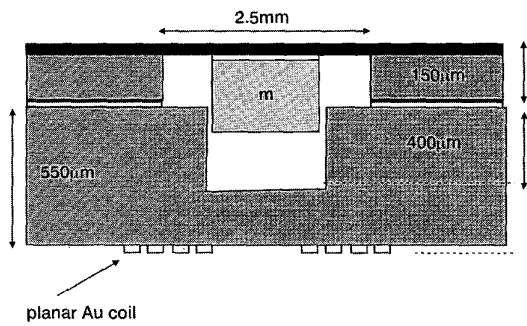
Figure 1-16. *left*. Pictorial representation of the first inertial micro generator developed by Williams, Shearwood, and Yates [46, 47]. *right*. Photograph of the assembled device.

1.3.5 STATE-OF-THE-ART IN VIBRATIONS HARVESTING

This section provides an overview of the state-of-the-art in vibration harvesting technology. A few research efforts for each transduction type have been selected and reviewed in greater detail. The selection was based upon the novelty and impact of the effort at the time at which it was published.

In addition to developing the design methodology for inertial micro-generators, which would be used by all researchers from that point forward, Shearwood, Williams, and Yates also micro-fabricated an electromagnetic micro-generator (Figure 1-16) [46, 48, 49]. A GaAs wafer was coated with 7μm of polyimide, and then wet etched to form circular diaphragms. A Samarium-Cobalt (SmCo) magnet (B_r=0.9T, m=2.4mg) was attached to the membrane. This substrate was bonded to a second substrate, with an etched recess, using epoxy. Additionally, a planar coil is deposited on the back of the second substrate (thickness=2.5μm, 13 turns). The micro-generator was tested both in vacuum and in air, and produced 0.3μW at a resonant frequency of 4.4kHz. Although this particular device was far from being practical, it validated the design methodology, as the

38

authors were able to predict its behavior with great success, and it demonstrated the possibility of generating useful power levels in the future.
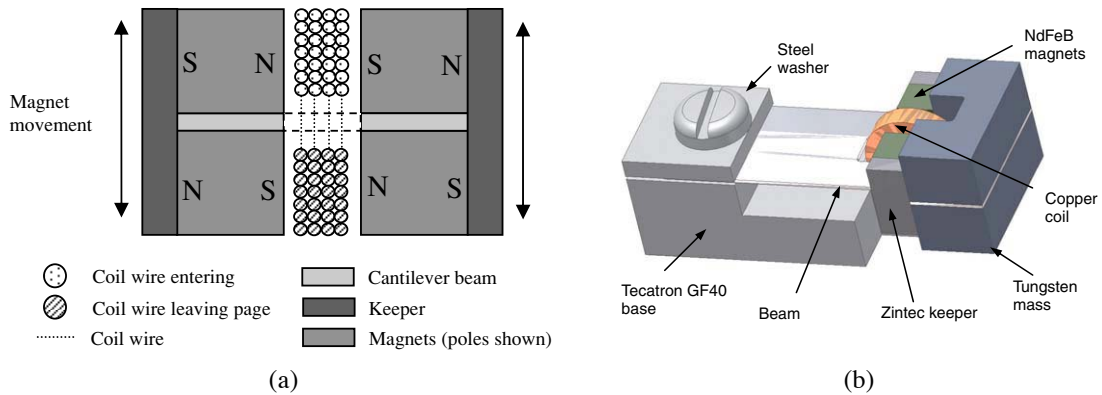
Figure 1-17. a) Cross section of four magnet arrangement developed by Beeby *et al*. b) Illustration of micro cantilever generator [44].

For several years, researchers at the University of Southampton have been working on increasing the efficiency of inertial electromagnetic generators. The main innovation underlying their work was a 4-magnet configuration shown in Figure 1-17a, producing a concentrated flux gradient through a center coil as the magnets move. Their work led to the generator shown in Figure 1-17b [44]. It is able to produce 46μW from a 0.59m/s^2 acceleration at 52Hz, and occupies a volume of 0.15cm^3. Additionally, with the increased electromagnetic coupling, due to the 4-magnet arrangement, the generator produces a 428mV$_{rms}$ signal that can be rectified by conventional means. Overcoming the low voltage levels produced by electromagnetic conversion is one of the main practical challenges of using this transduction approach. The cantilever spring was initially fabricated out of 50μm thick silicon wafers, however those devices were found to be quite brittle and difficult to assemble. The alternative was to use beryllium copper (BeCu) and stainless steel type 302. Those cantilevers are formed through lithography and subsequent spray etching of the metal substrate. The thickness is again 50μm. A finite

element analysis determined that the optimum NdFeB magnet size would be $2.5x2x1.5mm^3$, and a coil is wound from 12μm diameter enameled copper wire. The generator has a volume of $0.15cm^3$.

Roundy *et al* at UC Berkeley performed one of the first few research efforts into energy scavenging [50]. They did a comprehensive study of the available vibration energy in common locales. Their goal was to design a device that would produce a maximum amount of power in a volume of $1cm^3$. After an analysis of the different transduction methods, they decided to utilize piezoelectric and electrostatic. An electromagnetic generator was ruled out because it was determined that they could not produce a high enough voltage to power a wireless sensor. A piezoelectric generator was modeled, consisting of a bimorph beam with a mass attached to the free end. This model was used to determine the optimal beam and mass dimensions. A prototype built using a commercially available PZT bimorph (Figure 1-18), generated $70μW/cm^3$ from an acceleration of $2.25m/s^2$ at 120Hz. Future prototypes assembled in the same manner were further optimized using numerical methods, and generated 375μW from an acceleration of $2.25m/s^2$ at 120Hz [17]. An RF radio was powered using a combination of a piezoelectric scavenger and a solar cell. This work constitutes the highest harvester effectiveness (efficiency) to date. Although their work on electrostatic generators yielded some interesting mathematical modeling, the results of the manufactured prototypes are not very impressive and the reader is referred to the following reference for more information [17].
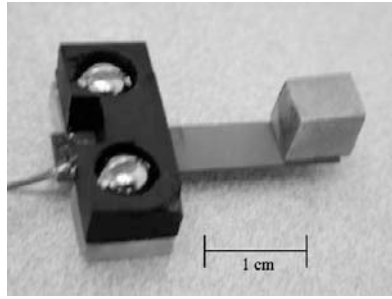
Figure 1-18. Piezoelectric bimorph generator developed by Roundy et al [50].

(a)   (b)
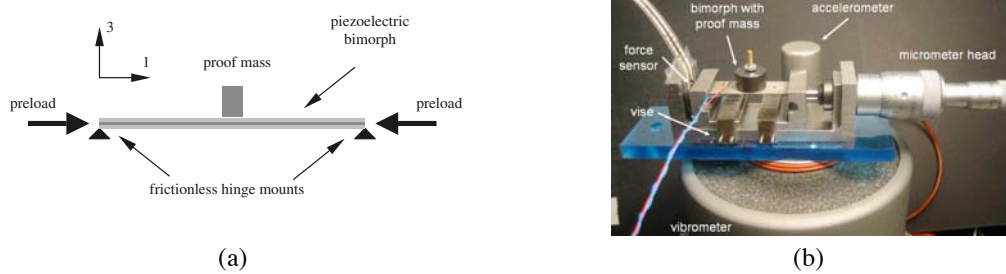
Figure 1-19. a) Schematic of a simply supported piezoelectric bimorph vibration energy scavenger with resonance frequency tunability via axial preload developed by Leland et al. b) Test setup and fabricated device [51].

Recognizing that bandwidth is a major concern in developing a practical scavenger, Leland *et al* investigated the use of an axial preload as a means to tune the resonance frequency of the scavenger [51]. They developed the theory and experimented with a doubly clamped PZT bimorph with a proof mass in the middle (Figure 1-19). The axial load is applied using a vice, which compresses the bimorph from both ends. They were able to tune the resonance frequency of a simply supported bimorph to 24% below the nominal. At frequencies that were 19-24% below the nominal, power values dropped by 10-35%. On the other hand, by applying a preload, the piezoelectric coupling coefficient could be increased by as much as 25% from 0.37 to 0.46. The maximum applied load was 65N. Power values between 300-400μW were generated from 9.8m/s^2 vibrations at frequencies between 200-250Hz.

41
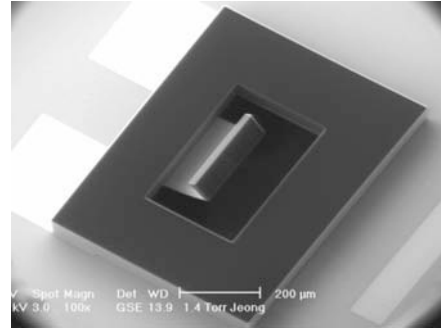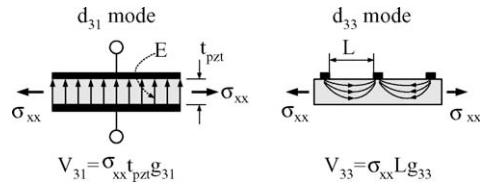
Figure 1-20. a) A comparison of the two modes of piezoelectric conversion, d_{31} mode which is conventionally used, and the d_{33} mode used by Jeon et al by patterning interdigitated electrodes on the PZT beam. b) SEM of the fabricated device [52, 53].
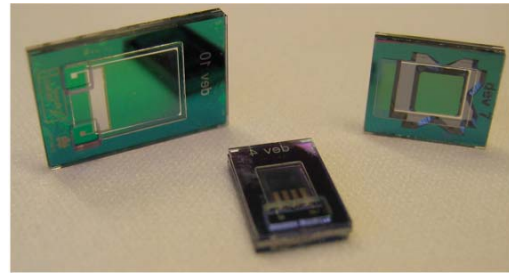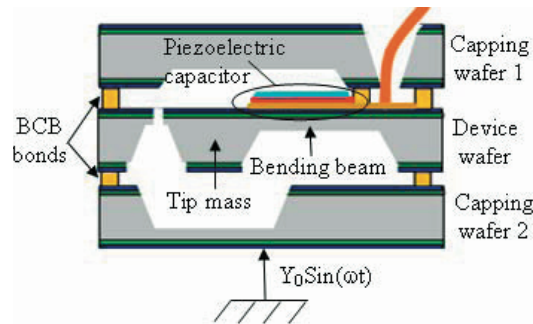
Figure 1-21. *left*. Pictorial description of the integrated piezoelectric generator under development at IMEC Belgium. *right*. Photograph of fabricated devices [54]

In an effort to micromachine piezoelectric scavengers Jeon *et al* developed a thin film sol-gel PZT process (Figure 1-20) [52, 55, 56]. The authors sought to exploit the d_{33} piezoelectric mode, which has a higher coupling coefficient and can generate a 20 times higher voltage than d_{31}. Additionally, the d_{33} mode can be utilized somewhat efficiently in thin film devices by placing interdigitated electrodes on top of the piezoelectric film to create electric field patterns such as the ones shown in Figure 1-20. The authors describe significant efforts to deal with built in stress by adding layers of SiO_2 and SiN_x. The design of the cantilever for power generation is described in more detail in [53]. A 170 x 260μm cantilever, with a resonant frequency of 13.97kHz is fabricated. Using base excitation, 1μW of power is delivered to a 5.2MΩ load. The authors describe the design

of spiral beam shapes, targeting the 100-200Hz frequency range. They predict that $207\mu W$ could be generated from $5m/s^2$ input vibrations.

The best effort to integrate piezoelectric scavengers to date is an ongoing project between IMEC Belgium and Katholieke University in Leuven [54-56]. The functional material is aluminum nitride (AlN), which is more easily integrated than PZT. They form cantilevers, with a tip mass made out of silicon, as shown in Figure 1-21 *left*. Then AlN is deposited on top of the cantilever. Finished devices are shown in Figure 1-21 *right*. Initial devices had a resonance frequency of 1.8kHz and produced $40\mu W$ from a vibration amplitude of 180nm (2.3g). However, more recently they have measured $85\mu W$ from an unpackaged device at 325Hz and 1.75g acceleration [55, 56]. This work has led to the most efficient micromachined piezoelectric vibration power generator to date.

Researchers at MIT investigated MEMS electrostatic harvesters, and reported the first work based on this transduction mode [57-59]. In their papers they describe both the generator and associated power conditioning circuitry. They present the first framework for analyzing electrostatic generators and discuss the merits of operating in constant charge or constant voltage modes of operation. A generator is simulated to give $8.6\mu W$, where $3\mu W$ would be consumed in driving the control and power conditioning circuitry.

Building on this work, Roundy performed a comprehensive theoretical analysis of electrostatic converters grouping them into three types: in-plane variable gap devices, in-plane variable overlap, and out-of-plane variable gap (Figure 1-22) [17]. The three approaches are analyzed using theoretical modeling and in-plane variable gap and variable overlap devices are shown to be capable of equal power generation. Nonetheless, for the variable overlap design this same maximum occurs at high spring deflections,

43

which raises stability issues. Additionally, the authors determine that the variable gap device is less sensitive to the parasitic capacitance. A disadvantage of out-of-plane gap variable devices is the higher loss due to air damping (proportional to $1/z^3$), and high surface force interaction might cause them to stick. In the in-plane version, the authors reason that the minimum gap can be easily controlled using mechanical stops, which are more difficult to fabricate in the out-of-plane scenario. Based on a silicon-on-insulator (SOI) process technology comb drive structure, the three generators are evaluated using reasonable design choices. The in-plane variable gap device is shown to have the highest power density. The authors predict 116μW from a device made out of a 200μm thick wafer with an aspect ratio of 50 and a minimum gap of 0.25μm.

(a) (b) (c)
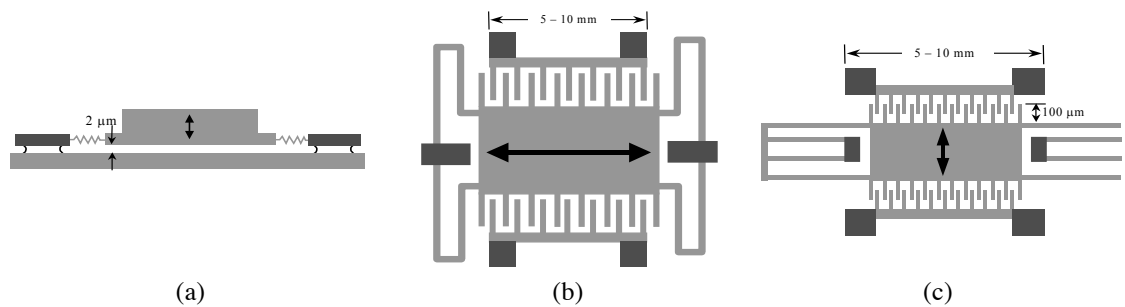
Figure 1-22. Shows the three different electrostatic conversion modes analyzed by Roundy et al. a) Out of plane variable gap, b) in-plane variable gap, and c) in-plane variable overlap [17].

The power density of electrostatic generators has been recognized to be worse than the other transduction schemes. In addition, these devices need a voltage source for pre-charging. Both of these issues can be addressed by adding an electret material. It can serve to both polarize the device, as well as increase the power density. One of the first efforts to utilize an electret was done by Sterken *et al* [58, 59]. Their device is a bulk micromachined variable overlap scavenger and it is shown in Figure 1-23. A silicon wafer is etched using DRIE to form the moving electrodes, and the back is KOH etched

to determine a proof mass. A second Pyrex wafer, with patterned electrodes, is bonded using BCB. Lastly, a third wafer with an insulating layer and an electret material is adhered to the top. Subjecting the device to a 1g acceleration at 500Hz produces 2nW when an external 10V source is used for polarization. When a 100V electret is used, the power output increases to 5μW and the load resistance increases from 1MΩ to 40MΩ.
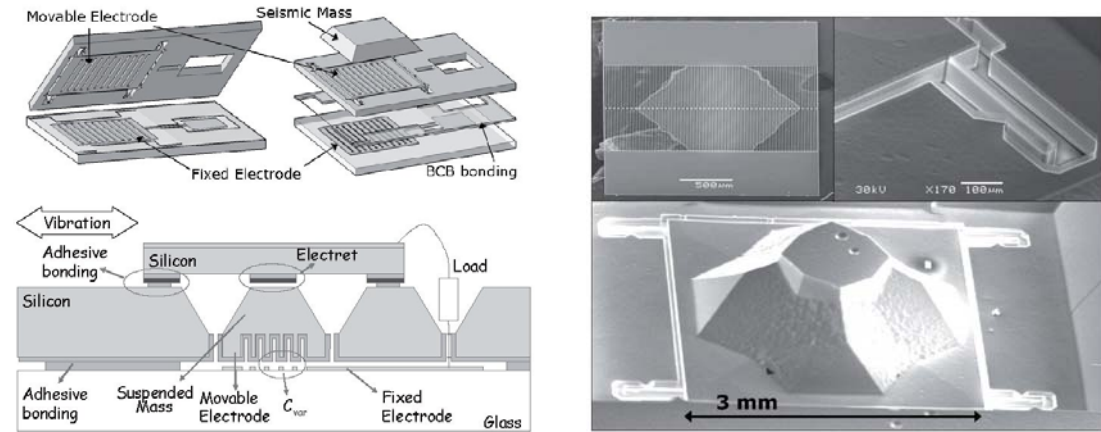
Figure 1-23. *left*. Electret micro generator designed by IMEC Belgium. *right*. SEM images of the seismic mass, movable electrodes, and springs [60, 61].

One of the major energy scavenging efforts has been going on for some time at Imperial College of London. An analysis by those authors shows that when the source motion amplitude exceeds the internal displacement range of the generator by one or more orders of magnitude, a generator which works in the resonant mode is less efficient than a non-resonant, or parametric, device [43]. A device such as this is conceptualized to work in such a manner that there is no spring, and the damping force is always opposite the mass movement, and less than the source induced change in momentum on the mass. The embodiment of their design can be shown in Figure 1-24. The center device is an inertial mass suspended on a low stiffness spring. The bottom structure contains a counter electrode and charging studs, and the top plate has discharge contacts. Initially the moving plate is at its lowest position, resting against the charging studs. At sufficient

acceleration the mass separates from the charging studs, and moves across the gap at constant charge, such that as the capacitance decreases, the voltage increases. Finally the mass discharges into the load circuit. This device has a couple of advantages, including the operation across a broad array of frequencies, as well as the ability to vary the priming voltage such that it can be tuned dynamically. The device shown in Figure 1-24 produced 120nJ per cycle and was tested at 10-100Hz giving repeatable results [62]. The authors predict that they should be able to increase this to 2.6μJ/cycle in the future by reducing the air damping of the device, decreasing the mass susceptibility to movement in unwanted directions, and increasing the starting capacitance.
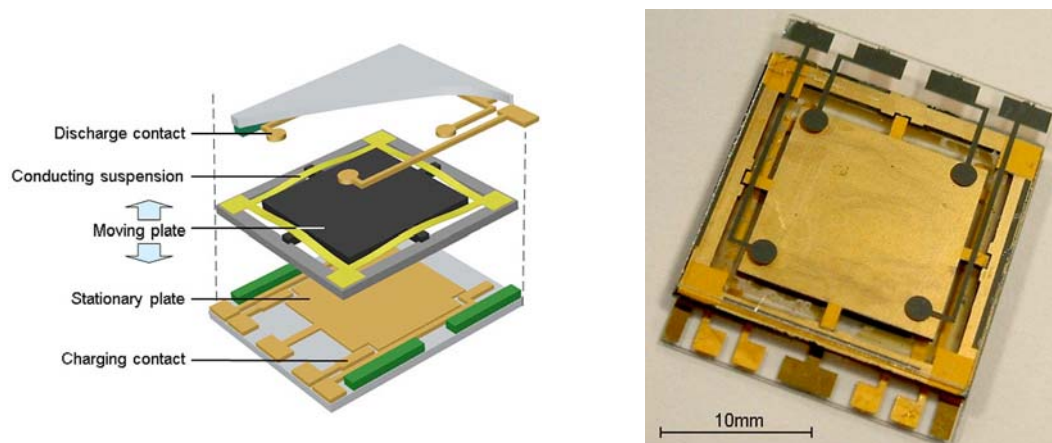
Figure 1-24. *left*. Exploded view of parametric generator developed by Mitcheson et al. *right*. Photograph of the prototype parametric generator [62].

The data included in Table 1-2-Table 1-3 are a summary of the important parameters of reported vibration energy harvesters. This data is only taken from publications that demonstrate experimental results. The three tables are split by transduction method: electromagnetic, electrostatic, and piezoelectric respectively. The projects are listed in no specific order. The last three columns of the tables present data on three of the performance metrics discussed in this section. Not enough data is presented in the published works to be able to fill all fields.

Table 1-2: Comparison of published electromagnetic energy harvesters.

Author	Year	Ref.	Accel (m/s^2)	Freq (Hz)	Mass (g)	Z_l (um)	Vol (cm^3)	Power (not proc) (μW)	Power (proc) (μW)	NPD $(\mu W/cm^3/Accel^2)$	E_H (%)	FoM_V (%)
Li	2000	[63]	28.4	60	0.2	5000	1		100	0.12	1.70	0.077
Li	2000	[63]	113.7	120	0.2	1000	1		100	0.01	1.06	0.009
Ching	2000	[64]	94.9	107			1	1.5		0.00		0.000
Ching	2000	[64]	81.1	104			1	5.0		0.00		0.001
Li	2000	[65]	16.2	64	0.2	1000	1.24		10	0.03	1.46	0.009
Williams	2001	[47]	382.2	4400	0.0	63	0.02	0.3		0.00	0.04	0.0001
El-hami	2001	[66]	102.3	322	0.5	940	0.24	530.0		0.21	1.09	0.142
Ching	2001	[67]	28.4	60			1		680	0.84		0.526
Ching	2001	[67]	95.5	110			1		680	0.07		0.085
Ching	2002	[68]	28.4	60		3000	1		830	1.03		0.642
Ching	2002	[68]	95.5	110		200	1		830	0.09		0.104
Mizuno	2003	[69]	12.4	700	0.5	6.5	2					
Lee	2003	[70]	42.8	85	0.1	7500	7.3	830.0		0.06	6.92	0.021
Glynne-Jones	2004	[71]	53.2	322		360	0.84	37.0		0.02		0.003
Beeby	2005	[72]	19.2	9500	0.0	500	0.1	0.0		0.00	0.00	~0
Beeby	2006	[73]	3.5	9500	0.0	240	0.068	0.1		0.15	0.02	0.0002
Beeby	2006	[73]	3.2	360	0.4	217	0.06	2.9		4.72	0.83	0.140
Beeby	2007	[44]	0.6	60			0.15	10.8		206.97		5.052
Beeby	2007	[44]	0.6	52	0.7		0.15	46.0		883.19		24.853
Saha	2008	[74]	4.9	2	27.0		12.7	300.0		0.99		1.364
Saha	2008	[74]	9.8	2.5	27.0		12.7	1860.0		1.53		3.382
von Buren	2007	[75]			1.4	1800	0.25	25.0				
Serre	2006	[76]	17.4	360	1.6		0.68	0.1		0.00		~0
Huang	2007	[77]	19.7	100	0.0	5200	0.04	1.4		0.09	0.15	0.070
Perpetuum	2007	[78]	0.2	99			131		800	101.80		0.065
Perpetuum	2007	[78]	1.0	99			131		3500	27.66		0.071
Perpetuum	2007	[78]	1.0	99			131		40000	316.13		0.815
Ferro Solutions	2007	[79]	0.2	60			133	800.0		99.50		0.105
Ferro Solutions	2007	[79]	0.5	60			133	3100.0		96.95		0.204
Ferro Solutions	2007	[79]	1.0	60			133	10800.0		84.44		0.356
Ayala	2009	[80]	0.8	45			1.12	200		259		5.14
Chang	2009	[81]	24.7	25	1.28	7k	0.96	400		0.68	2.3	0.9
Wang	2009	[82]	9.8	530			0.014	2E-5		1.7E-5		2E-6
Hoffman	2009	[83]	88.2	390	0.23		0.65	5		1E-3		3.4E-4
Bouendeu	2009	[84]	9.8	98	0.64		4.7	356		0.79		0.06
Wang	2009	[85]	10	280	0.33		0.315	17.2		0.55		0.038

47

Table 1-3: Comparison of published piezoelectric energy harvesters.

Author	Year	Ref.	Accel (m/s²)	Freq (Hz)	Mass (g)	Z_l (um)	Vol (cm³)	Power (not proc) (µW)	Power (proc) (µW)	NPD (µW/cm³/Accel²)	E_H (%)	FoM_V (%)
Glynne-Jones	2000	[86]	0.0	80.1		800	0.53	1.5				
Roundy	2003	[17]	2.3	120	8.5	150	1	80.0		15.47	7.32	0.386
Roundy	2003	[17]	2.3	85	7.5	143	1	207.0	90	17.73	13.95	0.619
Roundy	2003	[17]	2.3	60	8.2	150	1	365.0	180	34.81	34.14	1.740
Wright	2005	[87]	2.3	40	52.2		4.8	1700.0	700	28.20		1.254
Lefeuvre	2006	[88]	0.0	56	228.0	2000	113		10k			
Lefeuvre	2006	[88]	0.0	56	228.0	2000	113		300k			
Tanaka	2005	[89]	1.0	50			9	180.0		20.53		0.257
Fang	2006	[90]	64.4	609	0.0		6E-4	2.2		0.87		1.435
Jeon	2005	[52]	248k	14		2.56	2.7E-5	1.0		0.00		0.001
Ferrari	2006	[91]	0.0	41	82.0				0.27			
Ng	2005	[92]	72.6	100	1.0		0.2	35.5	16.3	0.02		0.0253
Challa	2008	[93]	0.8	26.4	45.8		50	250.0		7.81		0.085
Leland	2006	[51]	9.8	250	7.1			400.0				
Leland	2006	[51]	9.8	195	12.2			650.0				
White	2001	[94]	127.9	60	0.8		0.125	2.0		0.00		0.005
Mide	2008	[95]	9.8	50			40.5		8k	2.07		0.155
Mide	2008	[95]	9.8	150			40.5		1.8k	0.47		0.011
Bayrashev	2004	[96]		30			6.27	80.0				
Marzencki	2007	[97]	3.9	1.4k			1E-3		0.026	1.69		0.064
Renaud	2007	[54]	23.0	1.8k	0.0			40.0				
Zhu	2009	[98]	3.9	67			14	181		0.85		0.027
Elfrink	2009	[56]	19.6	572	0.029	400	0.007	60		22.9	7.35	2.74
Elfrink	2009	[56]	17.2	325	0.057	400	0.029	85		10.1	21.3	2.29
Berdy	2009	[99]	2	49	0.48		0.2322		7.2	8.07		0.69
Woias	2009	[100]	1.5	24				37				
Ardila Rodriguez	2009	[101]	4.9	50	8		1.36	0.1		0.003		3.6E-4
Park	2009	[102]	3.8	528	0.001		0.001	1.1		75.3		7.19
Wischke	2009	[103]	10	567	0.525			420				
Khbeis	2009	[104]	2.5	120	0.95		0.054	145		430		31.2
Renaud	2009	[105]	394	10	0.6		14	600		2.7E-4		0.006

Table 1-4: Comparison of published electrostatic energy harvesters.

Author	Year	Ref.	Accel (m/s^2)	Freq (Hz)	Mass (g)	Z_l (um)	Vol (cm^3)	Power (not proc) (μW)	Power (proc) (μW)	NPD (μW/cm^3/Accel^2)	E_H (%)	FoM$_V$ (%)
Miyazaki	2003	[106]	0.1	45	5.0	30			0.21			
Arakawa	2004	[107]	3.9	10	0.7	1000	0.4	6.0		0.96		0.680
Tsutsumino	2006	[108]	15.8	20				38.0				
Tsutsumino	2006	[108]	9.5	20				280.0				
Tashiro	2002	[109]	0.3	4.76	640.0	19000			58			
Tashiro	2002	[109]	12.8	6	780.0			36.0				
Miao	2006	[62]	17.8	20	0.1	100	0.6	2.4		0.01	17.84	0.017
Despesse	2005	[110]	8.9	50	104.0	90	18	1760.0	1000	0.70	7.66	0.062
Mizuno	2003	[69]	13.9	743	0.7	4.9	0.6	0.0		0.00	0.00	~0
Sterken	2007	[111]	9.9	500				5.0				
Chiu	2006	[112]	253	800	0.038	35						
Miki	2009	[113]	19.6	63	0.1		0.305	1		0.009		5E-3
Wong	2009	[114]	1.5	1400	yE-4			0.1				
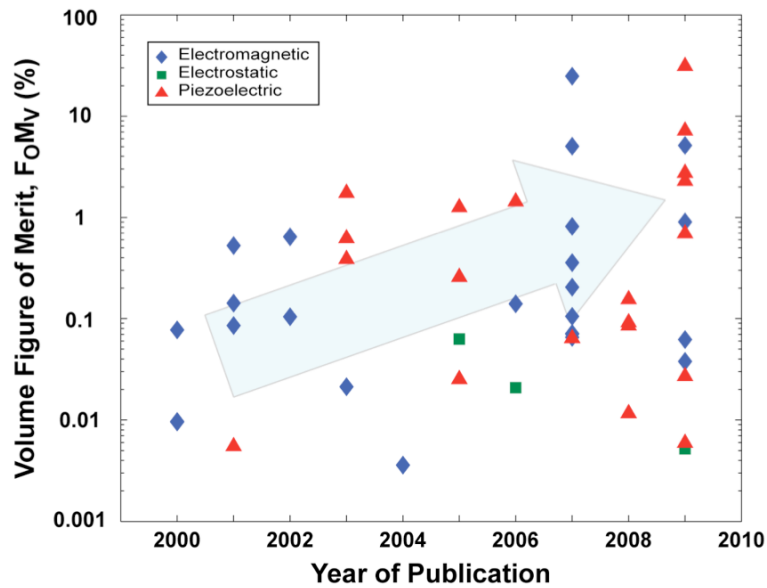
Figure 1-25. Shows volume figure of merit vs. publication year for reported energy harvesters to date.

A thorough analysis of ambient energy sources has shown that vibration is one of the most abundant. This is perhaps the reason why over the past decade, vibration scavenging has attracted the most interest from the research community. Nonetheless, as shown by the results presented in the last section, research in this area can still be characterized as

nascent. Shown in Figure 1-25 is a plot of volume figure of merit against publication year. Although there is a large amount of scatter, a pattern trending upwards can be seen from this plot. The average is below 1%, meaning that significant work has yet to be done and this number can be expected to improve an order of magnitude or so.
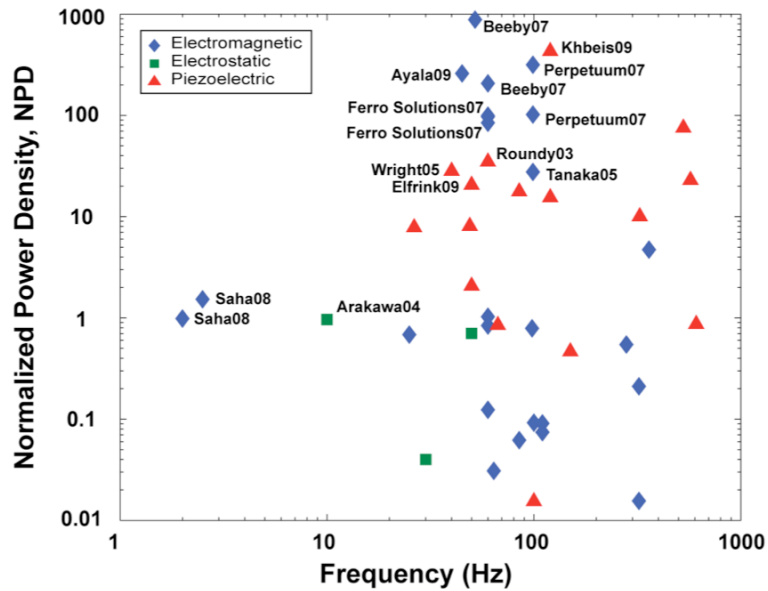
Figure 1-26. Shows Normalized Power Density vs. frequency for reported energy harvesters to date.

A plot of Normalized Power Density plotted against frequency is included (Figure 1-26) in order to be able to add as many research efforts as possible (not enough data is typically published to calculate all of the other performance metrics for every device). While this metric does not eliminate the source vibration dependency completely, and thus is not a complete normalization, it is pretty close. It reveals several trends that will repeat themselves using the other metrics as well. First, electromagnetic and piezoelectric devices have resulted in the most successful generators to date, which is not a surprise given the relative energy density between the three different approaches. Secondly, as the frequency increases, more efficient devices have been reported. Lastly, most of the research has centered on building devices in the 60-120Hz range. The reason for this is

that this frequency range encompasses many automation tasks in industrial applications. Of course, electrical motors typically provide a vibration peak of some magnitude around 60Hz and then associated harmonics. All of the work in this space uses single degree-of-freedom resonant systems. One can see that when using NPD as the performance metric the commercial generators offered by Perpetuum and Ferro Solutions are amongst the most efficient. The reason is that NPD does not completely remove volume dependency and frequency, and although not enough data is available to compute the other metrics for these devices, it is expected that if this were done they would fall lower in the rankings.
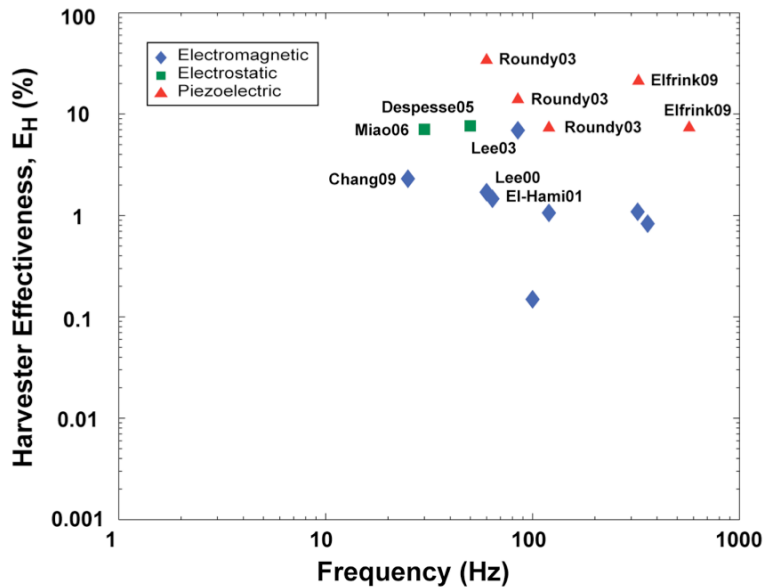
Figure 1-27. Shows harvester effectiveness, E_H, vs. frequency for reported energy harvesters to date.

As previously mentioned two much more normalized performance metrics have been proposed which offer a better comparison and clearer representation of the state-of-the art. Shown in Figure 1-27 is the Harvester Effectiveness (E_H) of reported scavengers to date. Good results have been achieved, with two authors achieving harvester effectiveness (E_H) values over 10% (best value 34%). The same trends can be observed as with NPD, namely the concentration in the 60-120Hz range, and the relative lack of

development in the <60Hz range. The effort with the best E_H to date is the early piezoelectric work by Roundy *et al* [17], however one of the newest efforts by IMEC (Elfrink *et al* [56]) comes very close and is the best performing fully micromachined device.
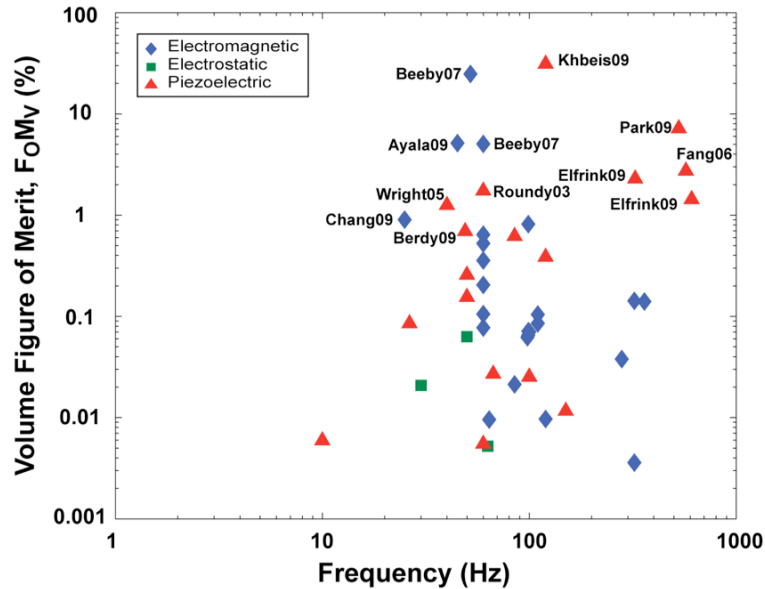
Figure 1-28. Shows volume figure of merit vs. frequency for reported energy harvesters to date.

When looking at the volume figure of merit (FoM$_V$), shown in Figure 1-28, while Roundy's and Elfrink's devices are still among the best performing, two new leaders emerge. The reason for the discrepancy is that while E_H compares the performance of each device relative to the best generator of identical volume and working in the same ambient energy conditions, the FoM$_v$ metric normalizes this by comparing to a generic design. Here the best performing electromagnetic generator is the effort by Beeby *et al* [44] from the University of Southampton in the UK. The piezoelectric effort by Khbeis *et al* [104] is shown to have the highest volume figure of merit. It uses the same approach as Roundy, where a piezoelectric bimorph with a Tungsten mass is actuated at resonance.
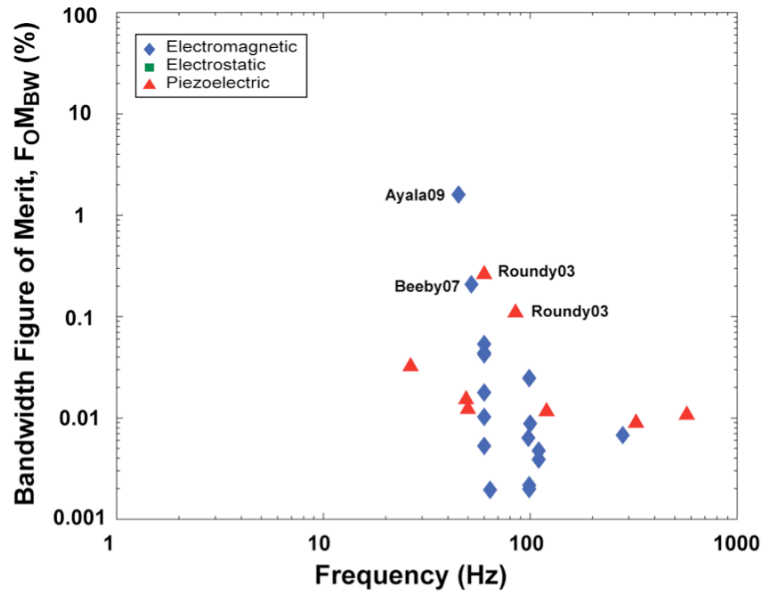
Figure 1-29. Shows bandwidth figure of merit vs. frequency for reported energy harvesters to date.

It is confirmed once again that work in the <60Hz range is very underdeveloped. As one moves down in the frequency spectrum, the ambient vibrations become more dependent on natural or probabilistic phenomenon than, for example, a motor, which is man, made. This means that these vibrations are not periodic and the bandwidth of the harvester becomes an important performance metric. This can be taken into account by calculating the Bandwidth Figure of Merit or F_oM_{BW}. Very few authors have published enough information regarding the bandwidth of their generators, and so this information is not included in the summary Table 1-2-Table 1-3. However, to illustrate how little development there has been with respect to bandwidth, information has been estimated from published data (with generous assumptions for all devices). Using this data the F_oM_{BW} has been calculated and shown in Figure 1-29. The data suggests that all of the reported work is completely inefficient in scavenging vibrations outside of their resonant frequency. The single effort above 1% efficiency is a new device reported by Ayala *et al* [80] where the research group from the University of Southampton have begun to

develop a resonant generator with active tuning. It is similar in principle to Leland [51], however the axial stress is applied magnetically and can be modified on the fly using closed loop monitoring circuitry.

1.4 RESEARCH MOTIVATION

As was shown in the last section a great deal of work has already gone into developing vibration harvesting power generators over the past 10 years. The significant developments that have been attained have even led to the first commercial products on the market. That being said, it was also quite apparent that most of the academic and industrial efforts have focused on scavenging energy from relatively high frequency periodic vibrations. These systems employ resonant operation to utilize the inherent quality factor amplification for maximum power generation. The art of scavenging energy using this type of resonant operation has largely been perfected. Future efforts should, and will likely focus on material improvement and integration in order to attain the highest possible electromechanical coupling by the energy transduction mechanism.

Despite all of the gains in the field, they only apply to one specific type of vibration typically produced by man-made sources such as motors and other machinery. Work in the frequency range below 60Hz is scarce, with maximum Harvester Effectiveness and Volume Figure of Merit values < 0.1% in the < 40Hz frequency range. However, it is at these low frequencies that available vibration energy can be found in many practical applications including environmental monitoring, agricultural automation, structural monitoring, security and military applications, and of course medical and body-worn devices. Figure 1-30 shows the frequency spectra of the ambient vibrations found in a number of environments, and overlaid on top is the F_oM_v of reported scavengers to date.

Looking at this plot the discrepancy is quite evident between the scavenging efforts to date and the many applications and environments in the lowest end of the frequency spectrum, where few efforts have been reported. Furthermore, generated power values typically quote peak power, as opposed to average power values, which skews the E_H and FoM_v data upward, especially for low-frequency devices. Lastly, the aforementioned applications, including environmental, human, etc typically do not provide power at a single fundamental frequency, and so the concept of bandwidth becomes extremely important. The main technology developed to address this issue for high frequency applications is tunability; something that has limited practical application in environments where the vibration frequency could be quite random and not known *a priori*.
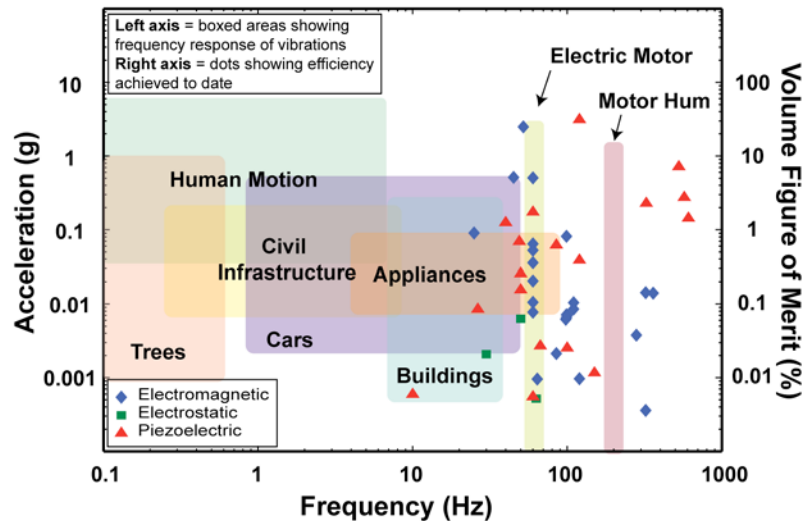
Figure 1-30. Composite plot showing the frequency spectra of the vibrations in typical environments where energy harvesting applications may be found, along with the F₀Mᵥ of vibration scavengers reported to date.

The goal of this thesis was to develop a generator capable of scavenging energy in the low end of the frequency spectrum (<50Hz). This generator was expected to set the state-of-the-art in this design space. Additionally, these environments do not give off steady

and periodic vibrations. Instead, their frequency response constantly changes, meaning that a high bandwidth must be sought. A new generator architecture was developed so that scavenging can be performed in these ambient environments. As a design goal this thesis project sought to exceed all previously reported scavenger efficiencies in the <10Hz frequency range; specifically, highest Volume Figure of Merit values are sought. Low frequency vibrations by their nature have high displacement amplitudes, which is a great impediment to miniaturization. This thesis sought to develop a "dense" architecture suitable for miniaturization into the micro scale. To demonstrate the feasibility and practicality of scavenging energy in such an environment, an energy scavenging system was developed. This system includes the harvester and power management electronics, and it was tested in a realistic environment. The contributions of this thesis span a number of realms including the design and theory of vibration harvesters, technology and process development, and system level implementation and integration.

1.5   THESIS ORGANIZATION

This thesis is organized into six chapters. Chapter II begins with an examination of the challenges associated with scavenging low frequency vibrations. It will discuss the drop in efficiency due to the increased displacement requirement of these generators as well as the weakened electromechanical coupling associated with low frequency operation. Next Chapter II will introduce the Parametric Frequency Increased Generator (PFIG) architecture. A theoretical framework for modeling the generator will be developed, and the chapter will conclude with a discussion of the proper application of this type of device.

Chapter III presents the first electromagnetic PFIG generator. It will begin with the

development and testing of the first generation bench top device. It will discuss its design, fabrication, and testing. Comprehensive test results from this device will be presented. An electromagnetic FEM analysis will be carried out to determine the best way of optimizing the electromagnetic conversion system. The results of this analysis are applied and an optimized electromagnetic device is developed and tested.

Chapter IV discusses the development of a piezoelectric PFIG generator. The chapter begins with a discussion on modeling of the piezoelectric transduction system. It then presents the development and fabrication of the piezoelectric device. Test results are presented and analyzed to determine the effectiveness of this generator and how to improve its performance in the future.

Chapter V details the development of the first parametric generator system for scavenging vibrations on a bridge. It discusses the design requirement for such a device and an analysis of bridge vibrations is carried out. The design, manufacturing, and testing of a bridge harvesting system is reported. A power management circuit is developed to rectify and store the converted energy.

Chapter VI summarizes the results and contributions of this thesis and presents ideas and suggestions for future work.

Chapter 2

PRINCIPLES OF SCAVENGING LOW FREQUENCY PERIODIC VIBRATIONS

At the end of the last chapter the conversion of vibrations into electricity was covered in great detail. One can draw an inference that those same principles would apply to all vibrations irrespective of their amplitude or frequency. In the general sense, this conclusion is correct. However, in Section 1.3.5 it became apparent that the efficiencies achieved when scavenging low-frequency vibrations remain orders of magnitude less than when converting higher frequency vibrations. This chapter aims to explain exactly why this is the case and what further challenges need to be addressed when aiming to harvest low-frequency vibrations. Once the challenges become clear, a new type of non-resonant vibration-to-electricity conversion device is introduced which aims to address some of the difficulties hampering other converters when working in these environments. The merits and operating range of this device will be discussed in detail.
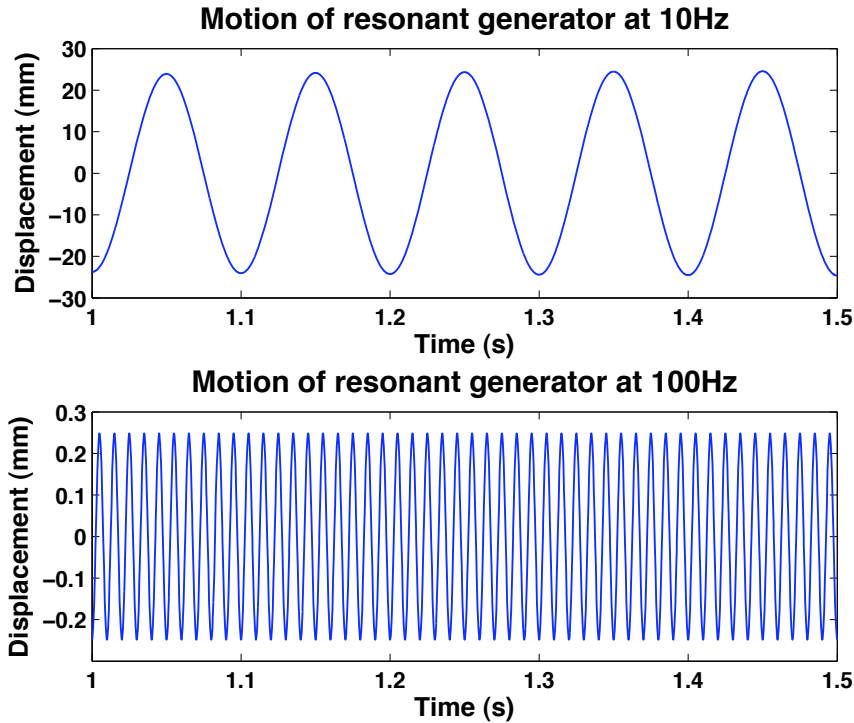
Figure 2-1. Simulated displacement of an inertial generator with a Q of 10 working at steady-state resonance with an applied excitation of 9.8m/s^2 at 10Hz (*top*) and 100Hz (*bottom*).

2.1 DISPLACEMENT CHALLENGE

In this chapter the term "low-frequency vibration" is used quite liberally to mean both the frequency of the vibration as well as to allude to the source of the vibration, spectral content, directionality, etc. While a number of the challenges associated with scavenging low-frequency vibrations stem from the vibration source, in this particular instance the term low frequency is used strictly referring to the physical characteristic of the vibrations. For a given acceleration, the amplitude of the vibration Y_o increases inversely proportional to the square of the frequency, i.e. $Y_o \sim 1/\omega^2$. As was shown in Eq. (1.15) the power which can be generated from vibrations is $P \sim (Z_l/Y_o)$. This means that the internal displacement limit of the generator Z_l has to be at least as large as the vibration

amplitude. Of course, generators to date have all reported $\zeta_T < 1$, meaning that they are underdamped and require Z_l to be significantly larger than Y_o. This is not a coincidence, obviously having a quality factor Q > 1 is also desirable for power generation when working at resonance. For illustration purposes, Figure 2-1*top* shows the displacement of an inertial power generator working at resonance. This generator has an overall quality factor of 10. In this case the proof mass has to have a displacement of 50mm$_{ppk}$. A stark contrast can be seen from Figure 2-1*bottom* where a generator with similar characteristics (mass, Q) is shown working at resonance but at 100Hz. Here only 0.5mm$_{ppk}$ internal displacement is sufficient for operation. There is a 100x increase in the required linear dimension of the generator casing simply to provide room for the mass to move. This presents a big barrier to the scalability of these types of generators, especially when their dimensions reach the micro-scale range where typical displacements are constrained to 1-100µm. In addition, the increased displacement range is a direct impediment to higher efficiency as it means that a larger volume is needed. In these simulations the mass is assumed to be the same, and so the increase in Z_l directly contributes to dead volume. One way of defining what constitutes "low-frequency vibration" is to say that any time an input vibration has amplitude, Y_o, that is larger than the desired volume, and by extension the Z_l of the power generator, it is low frequency.

2.2 FREQUENCY DEPENDENCE OF ELECTROMECHANICAL COUPLING

As was discussed in Section 1.3.2, electromagnetic and piezoelectric conversion can be exactly approximated by modeling them as viscously damped systems, or ones where the force opposing the motion of the mass is proportional to the velocity of the mass ($f = d\dot{z}$). In general the force for both electromagnetic and piezoelectric generators can be

modeled in the same form [40]:

$$F_{gen} = K^2 \left(\frac{1}{R_{load}} + j\omega C_o \right)^{-1} \frac{dz}{dt}, \tag{2.1}$$

$$F_{gen} = K^2 \left(R_{load} + j\omega L \right)^{-1} \frac{dz}{dt}, \tag{2.2}$$

where Eq. (2.1) applies to piezoelectric and Eq. (2.2) is for electromagnetic conversion. In these equations K is a transformation factor, squared in each instance to account for the forward transformation (mechanical to electrical) and the feedback mechanism back to mechanical. This means that this force f will reduce as $1/\omega$ weakening the electromechanical coupling of the system provided that d stays constant. The physical significance behind this is clear. For electromagnetic generators, the faster the magnetic flux variation becomes, the larger the electromotive force needed to counteract this change is. Similarly, for piezoelectric devices, the faster the strain is changing, the higher the power dissipated in charging and discharging the dielectric capacitor in order to develop a voltage counteracting the strain.

These equations are linearizations, especially with regard to the transformation constant K. In reality, the damping force is a complex quantity to compute, and K itself may vary as a function of position and velocity. It depends on a large number of parameters and their exact configuration. Nonetheless, the general relationships in Eq. (2.1)-(2.2) define the fundamental interaction governing the coupling between the two energy domains.

2.3 TYPICAL APPLICATIONS AND THE BANDWIDTH CHALLENGE

The low-frequency vibrations found in various scavenging applications are predisposed to being created from natural and environmental sources, rather than being created by machinery or other man-made means. Examples include human motion, tree branches swaying from the wind, car vibrations caused by the road and its dynamics, and bridge vibrations due to moving traffic. It follows that applications for energy harvesting which exhibit low-frequency vibrations are not likely to produce periodic motion. Many of these natural vibrations sources relay on random or semi-random phenomenon and their energy is spread over a certain band, for example transportation and car vibrations (<20Hz), human motion (<10Hz), guard rail on the street (<50Hz), etc. This data is found in Paci *et al* [115], however a number of other studies have been published characterizing the vibrations in various locations and provide more examples [116, 117]. Also, Chapter 5 will discuss in detail the vibrations found on two types of bridges. This means that almost inevitably, scavenging low-frequency vibrations will also mean that a certain bandwidth requirement must be met.

As the research field in vibration scavenging technology has progressed, the concept of bandwidth has been gaining significant importance. Two general approaches have been proposed to deal with the issue of bandwidth: 1) passive or active tuning [51, 91, 118, 119], and 2) combining a number of resonators with closely spaced natural frequencies to effectively achieve a greater bandwidth [120]. These approaches unfortunately do not provide much value in this applications space. Including a number of scavenging elements in order to increase the bandwidth is not a practical solution. Low-frequency scavengers are already big enough due to their large mass and

displacement limit Z_l. The approaches to tuning the generators can be split into two categories, active, where an internal mechanism is used to continuously vary either the stiffness (typical case) or the mass of the generator. It is unclear if active tuning results in a net gain in energy [118]. Passively tuned devices utilize the same approach to tuning, by varying the mass or the stiffness, but this is a permanent augmentation made during installation. This means that the resonant frequency has to be known and should not shift, something which cannot be expected in practical low-frequency applications. Lastly, it should be noted that these tuning approaches require that the input vibration will have some identifiable frequency peak. If it is broadband like many of the examples above, then tuning does not serve any purpose.
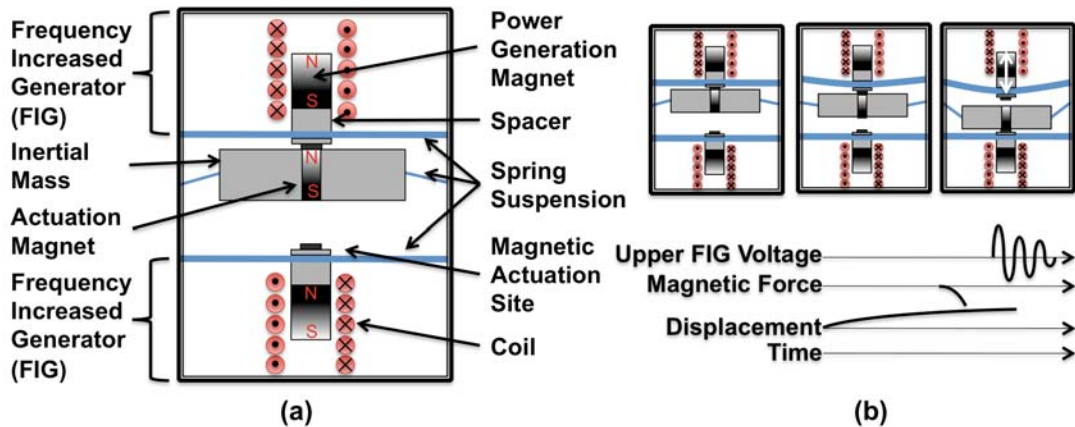
Figure 2-2 a) Parametric Frequency Increased Generator (PFIG) architecture b) Illustration of the method of operation.

2.4 PARAMETRIC FREQUENCY INCREASED GENERATOR

To address the challenges outlined in the previous sections, a novel, non-resonant generator architecture is designed. The Parametric Frequency Increased Generator (PFIG), shown in Figure 2-2a, is designed to accommodate the large amplitudes associated with low-frequency vibrations, and because it works in a non-resonant fashion,

the PFIG is able to operate over a wide band of frequencies. The PFIG utilizes a large inertial mass to couple kinetic energy from the ambient, into the generator structure, and pass a portion of it to one of two Frequency Increased Generators (FIGs), which then convert this mechanical energy to electrical via electromagnetic induction. Two FIGs are placed on either side of the inertial mass, oriented to face each other. Attached to the bottom of the FIG spring is an NdFeB magnet for power generation, while on top, a smaller magnet is used to generate a magnetic force in order to latch the FIG and the inertial mass together. The operation of the PFIG is outlined in Figure 2-2b. The generator operates such that the inertial mass snaps back and forth between the two FIG generators, attaching magnetically. As the inertial mass moves, it pulls the FIG spring along. When the inertial mass approaches the opposing FIG, the magnetic force of attraction begins to increase. As the forces on the FIG/inertial mass system overwhelm the holding magnetic force, the inertial mass detaches and is pulled to the opposing FIG. The freed device now resonates at its high natural frequency converting the stored mechanical energy in its spring to electrical energy. This process is subsequently repeated in the opposite direction.

As previously discussed, one of the factors contributing to the decrease in efficiency associated with scavenging energy from low-frequency vibrations is that the electromechanical coupling is proportional to velocity. The FIG component of the generator gets its name from a concept called frequency up-conversion [121, 122], a method to increase the effectiveness of low-frequency scavengers. This is achieved by implementing a mechanical conversion, such that the internal operating frequency of the generator is increased over the input frequency. The damping force is thereby scaled

proportionately. The FIGs operate at a frequency that is an order of magnitude higher than the ambient vibration. Frequency up-conversion will be discussed in greater detail in Section 2.6.

The PFIG architecture is ideal for two main types of applications: 1) scavenging large amplitude vibrations that exceed the internal displacement of the generator, and 2) applications where the ability to generate a high maximum power at a specific frequency is traded for the ability to generate power over a larger bandwidth to accommodate unpredictable and broader ambient energy environments. The converted energy is linearly proportional to the frequency with which the mechanical vibrations occur because the PFIG is capable of producing a certain amount of energy per cycle, and the more cycles that it undergoes, the higher the power output. The first application space is particularly important for MEMS devices where the reduced displacement range can be accommodated much easier, and various physical properties and advantages of the micro scale can be exploited.

The main design constraint that needs to be considered is the minimum acceleration at which the PFIG will begin operation. This acceleration is the basis for designing the mechanical system, the size of the mass, the latching force, and volume. The next few sections will examine the design of the PFIG in more detail, including modeling, quantitative analysis, and efficiency.

2.5 MODELING OF THE PFIG

The PFIG generator architecture is composed of three mass-spring-damper systems that influence each other through two magnetic latching mechanisms. The attracting force is provided by permanent magnets located on each of the top and bottom FIGs. The overall

system is shown in Figure 2-3. The inertial mass m_i is suspended by a low-stiffness spring k_i, the main purpose of which is to guide its motion. A damping element with constant b_i is included to account for the parasitic mechanical losses associated with the inertial mass. The two FIG devices are represented by mass m_{fx}, spring k_{fx}, parasitic damper b_{fxm}, and electrical damper b_{fxe}. The 'x' in each of these variables is in reference to which FIG the variable belongs to, where the FIG on the bottom is henceforth referred to as FIG1, and the FIG above the inertial mass is called FIG2. The electromechanical coupling is modeled as a viscous damping force with damping constant b_{fxe}.
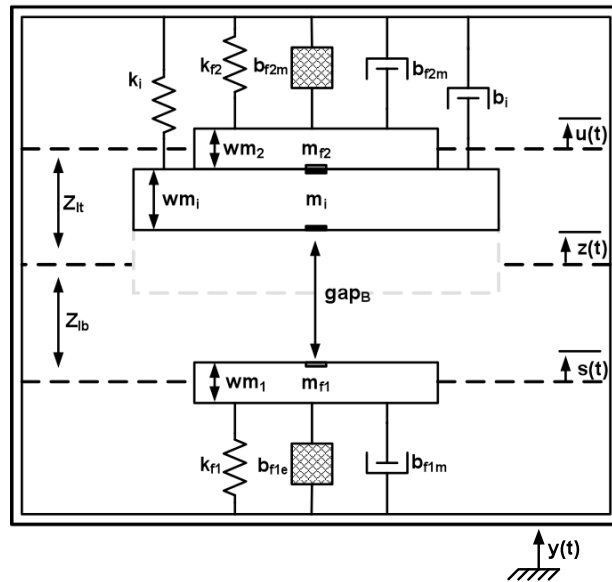
Figure 2-3. Generic model of parametric generator.

The displacements of the inertial mass, FIG1, and FIG2 relative to the frame are denoted by $z(t)$, $s(t)$, and $u(t)$ respectively. A distance of Z_{lb} and Z_{lt} separate the rest positions of FIG1 and FIG2 relative to the equilibrium position of the inertial mass. Lastly, gap_T and gap_B denote the physical distance between the inertial mass and the top of each FIG when the inertial mass is latched on to the bottom and top FIGs respectively. In this model each of the three mass elements is given a width wm_x.

When the generator casing is subjected to a time varying displacement *y(t)*, the components inside will respond in a non-linear fashion because of the magnetic forces and discontinuity of the latching mechanism. This means that a closed form solution for power cannot be computed for the PFIG generator, but rather a dynamic analysis must be carried out. For the purpose of mechanical modeling the PFIG operation is broken down into three distinct cases shown in Figure 2-4 through Figure 2-6. The first case consists of the situation in which the inertial mass and FIG2 are latched together and moving as a single system. Similarly, in a symmetric fashion, case 2 describes the system when the inertial mass is latched with FIG1. Case 3 accounts for the time during which all three systems are moving separately and in relation to one another.
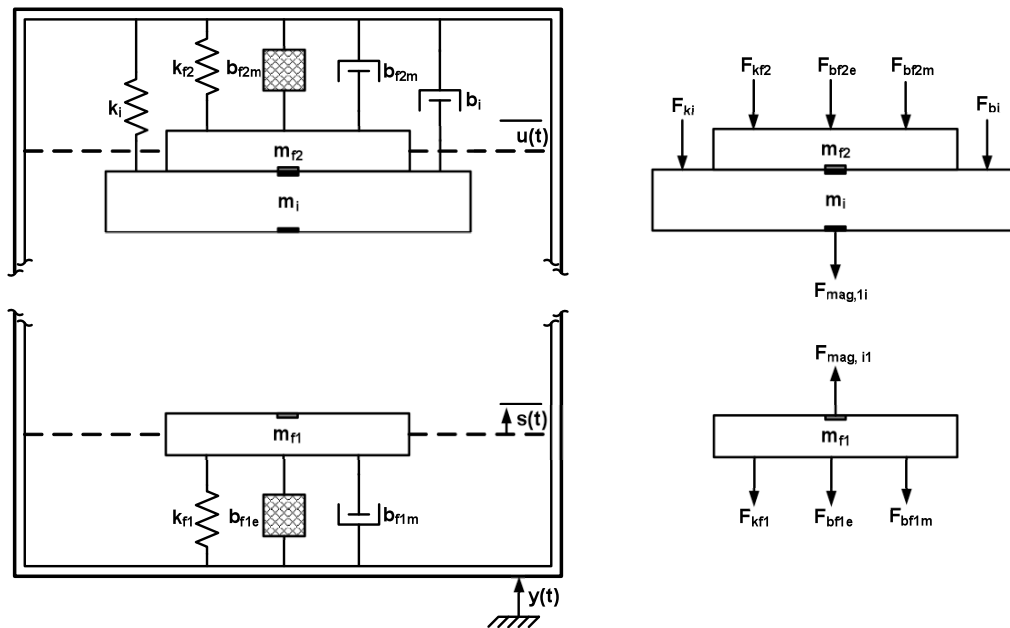
Figure 2-4. Illustration of case 1 when the inertial mass is latched on to FIG2.
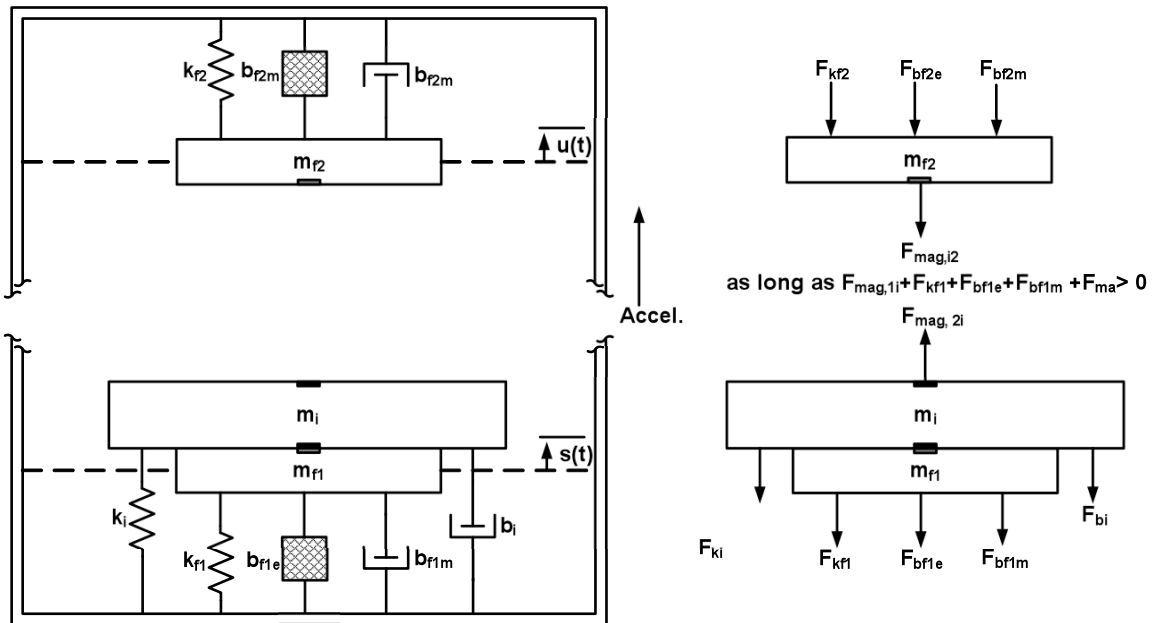
Figure 2-5. Illustration of case 2 when the inertial mass is latched on to FIG1.
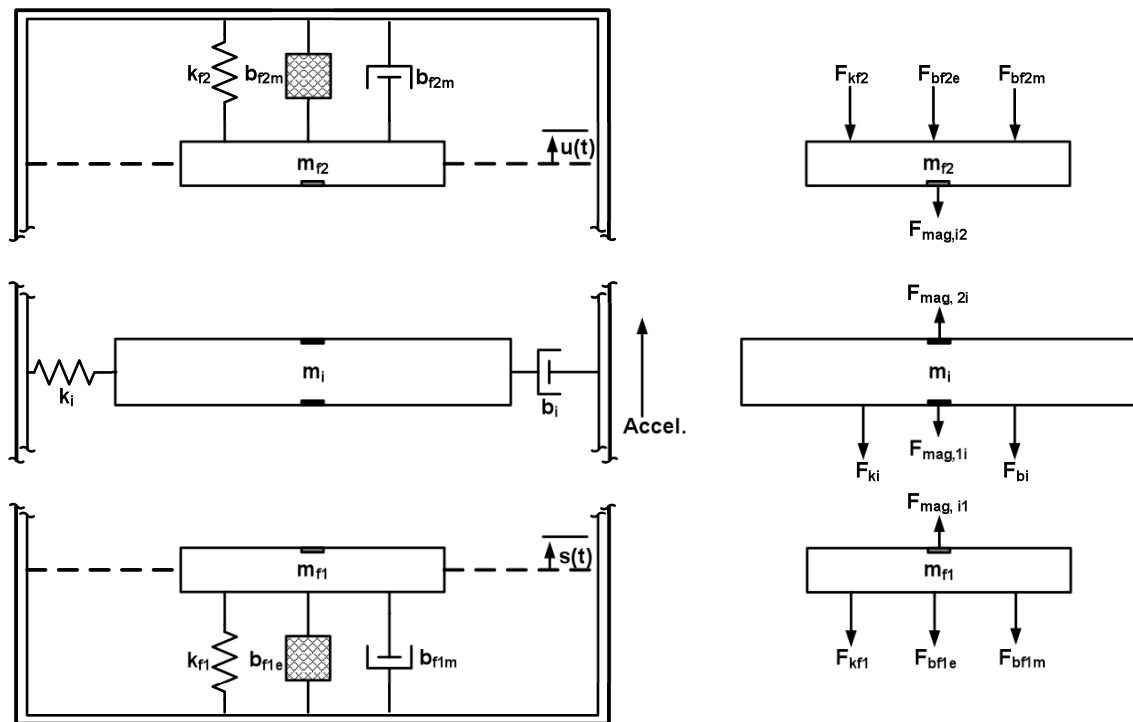
Figure 2-6. Illustration of case 3 when the inertial mass is moving between the two FIG devices.

The two scenarios where the inertial mass is latched on to one of the FIGs, case 1 and case 2, are very similar and it is enough to describe one of the systems mathematically. The other one will be nearly identical, with the exception of a few sign changes because of the physical orientation of the devices. A detailed explanation will be provided considering case 1, and from there case 2 can easily be deduced.

2.5.1 SYSTEM DYNAMICS OF CASE 1

The dynamics of case 1 can be described by two interacting second-order differential equations. The motion of the combined FIG/mass system is given by:

$$(m_i + m_{f2})\ddot{u} + b_{f2e}\dot{u} + b_{f2m}\dot{u} + b_i\dot{u} + k_{f2}u + k_i(u + gap_T) = -(m_i + m_{f2})\ddot{y} - F_{mag,1i}. \tag{2.3}$$

The spring force applied by the inertial mass spring in Eq. (2.3) is augmented to include the gap between the inertial mass and the FIG, because that spring has its equilibrium position when the mass is centered and $z(t) = 0$. The motion of FIG2 during the time when the mass is latched on to FIG 1 is given by:

$$m_{f1}\ddot{s} + b_{f1e}\dot{s} + b_{f1m}\dot{s} + k_{f1}s = -m_{f1}\ddot{y} + F_{mag,i1}. \tag{2.4}$$

The two magnetic forces $F_{mag,1i}$ and $F_{mag,i1}$ in Eq. (2.3) and (2.4) represent the magnetic force that FIG1 exerts on the bottom of the inertial mass and vice versa. These forces are equal and opposite in direction. An approximation to the force between two nearby magnetized surface is given by:

$$F_{mag} = \frac{B^2 A}{2\mu_o}, \tag{2.5}$$

where B is the magnetic flux density, A is the area of each surface, and μ_o is the permeability of free space ($\mu_o = 4\pi \times 10^{-7}$ Tm/A). An estimate of the magnetic flux at a point along the central axis of a rectangular magnet is given by:

$$B = \frac{B_r}{\pi}\left(\tan^{-1}\left(\frac{WL}{2d\sqrt{4d^2 + W^2 + L^2}}\right) - \tan^{-1}\left(\frac{WL}{2(d+T)\sqrt{4(d+T)^2 + W^2 + L^2}}\right)\right). \qquad (2.6)$$

The flux density is computed a distance d from a magnet with length L, width W, thickness T, and residual flux density B_r.

$$d = u - s + \left[Z_{lt} + Z_{lb} - 0.5wm_1 - 0.5wm_2 - wm_i\right] \qquad (2.7)$$

The distance between the bottom of the inertial mass and the top of FIG1, d, is determined by taking into account the positions u and s of the two systems, as well as the physical layout of the PFIG; this includes the distance between the rest positions of the two FIGS with respect to the center of the inertial mass Z_{lb} and Z_{lt}, and the geometrical properties m_{f1t}, m_{f2t}, and m_{it}. The distance d, simplifies to gap_B when u and s are both zero.

While in case 1, $\dot{z}(t) = \dot{u}(t)$ and $\ddot{z}(t) = \ddot{u}(t)$. In order to reflect accurately the position of the inertial mass in terms of $z(t)$ an offset is added such that $z(t) = u(t) + Z_{lt} - 0.5wm_2 - 0.5wm_i$.

While the inertial mass and the FIG are in contact they each exert and equal and opposite contact, or normal, force on each other. This normal force, T, can only be in the direction pointing away from the structure that is applying it. The normal force can never switch directions; it can never be less than zero because that violates the definition of what a normal force is. When the two structures are no longer in contact then the normal

70

force will become zero. The normal force applied to FIG2 by the inertial mass is given by:

$$T = m_{f2}\ddot{u} + b_{f2e}\dot{u} + b_{f2m}\dot{u} + k_{f2}u + F_{mag,2i} \tag{2.8}$$

Equation (2.8) does not work in isolations, but rather is coupled with the remaining statements describing the Case 1 system. The normal force T, can only point up, so when it becomes zero or less, (2.8) is violated and Case 1 is not longer valid.

2.5.2 SYSTEM DYNAMICS OF CASE 2

The second case encompasses the time when the inertial mass is connected to the bottom FIG1 and can be seen in Figure 2-5. It is very similar to case 1 and the main difference that needs to be accounted for is the direction of some of the magnetic forces. The set of equations describing the motion of the two mechanical systems is as follows:

$$\begin{cases} (m_i + m_{f1})\ddot{s} + b_{f1e}\dot{s} + b_{f1m}\dot{s} + b_i\dot{s} + k_{f1}s + k_i(s - gap_B) = -(m_i + m_{f1})\ddot{y} + F_{mag,2i} \\ m_{f2}\ddot{u} + b_{f2e}\dot{u} + b_{f2m}\dot{u} + k_{f2}u = -m_{f2}\ddot{y} - F_{mag,i2} \\ F_{mag} = \dfrac{A}{2\mu_o}\left[\dfrac{B_r}{\pi}\left(\tan^{-1}\left(\dfrac{WL}{2d\sqrt{4d^2 + W^2 + L^2}}\right) - \tan^{-1}\left(\dfrac{WL}{2(d+T)\sqrt{4(d+T)^2 + W^2 + L^2}}\right)\right)\right]^2 \\ d = u - s + \left[Z_{lt} + Z_{lb} - 0.5wm_1 - 0.5wm_2 - wm_i\right] \end{cases} \tag{2.9}$$

The conditions for separation are very similar to case 1. Once again to completely define the system a normal force condition is imposed:

$$T = F_{mag,1i} - m_{f1}\ddot{s} - b_{f1e}\dot{s} - b_{f1m}s - k_{f1}s. \tag{2.10}$$

The inertial mass will separate when the normal force applied by the inertial mass on the FIG is >=0.

2.5.3 SYSTEM DYNAMICS OF CASE 3

Once the inertial mass leaves either the top or bottom FIG all three devices are free to move independently. However, the magnetic forces do influence their motion significantly specially when the inertial mass is in close proximity to either of the FIGs, right after separation, or just before attachment. The motion of the two FIGs and the inertial mass are given in equations (2.11)-(2.13).

$$m_{f2}\ddot{u} + b_{f2e}\dot{u} + b_{f2m}\dot{u} + k_{f2}u = -m_{f2}\ddot{y} - F_{mag,i2} \tag{2.11}$$

$$m_{f1}\ddot{s} + b_{f1e}\dot{s} + b_{f1m}\dot{s} + k_{f1}s = -m_{f1}\ddot{y} + F_{mag,i1} \tag{2.12}$$

$$m_i\ddot{z} + b_i\dot{z} + k_i z = -m_i\ddot{y} + F_{mag,2i} - F_{mag,1i} \tag{2.13}$$

The magnetic force between the three systems can again be computed as shown in Eq. (2.5). However, the distance between the FIG magnet and the inertial mass will be different for FIG 1 and for FIG 2. The two distances are a function of the current position of all three systems and are given by:

$$d_{2-i} = u - z + \left[Z_{lt} - 0.5wm_2 - 0.5wm_i\right], \tag{2.14}$$

$$d_{1-i} = z - s + \left[Z_{lb} - 0.5wm_1 - 0.5wm_i\right]. \tag{2.15}$$

Equations (2.14) and (2.15) can now be used in conjunction Eq. (2.6) to calculate the magnetic flux density at any given point in time.

Case 3 is valid as long as the inertial mass does not make contact with either of the two FIGs. If $z(t) = u(t) + Z_{lt} - 0.5wm_2 - 0.5wm_i$ or $z(t) = s(t) - (Z_{lt} - 0.5wm_2 - 0.5wm_i)$ then case 3 is no longer valid and the system has transitioned to one of the combined modes. When the inertial mass makes contact with each of the FIG devices some energy

is lost because of the ensuing collision. The impact between the inertial mass and the FIG is modeled as an elastic collision and Eq. (2.16) and (2.17) determine the initial and final velocities of the two colliding masses.

$$V_{i,final} = \frac{(C_R + 1)m_{fx}V_{fx} + V_i(m_i - C_R m_{fx})}{m_i + m_{fx}} \tag{2.16}$$

$$V_{fx,final} = \frac{(C_R + 1)m_i V_i + V_i(m_{fx} - C_R m_i)}{m_i + m_{fx}} \tag{2.17}$$

Here, C_R is the coefficient of restitution of the materials coming into contact, V_i and V_{fx} are the initial velocity of the inertial mass and the appropriate FIG device respectively, and m_i and m_{fx} are the inertial mass and the appropriate FIG mass respectively. The ensuing velocities of the inertial mass and the FIG can now be used to determine the initial velocity condition for the combined system in case 1 or 2. This is done in such a way as to conserve linear momentum.
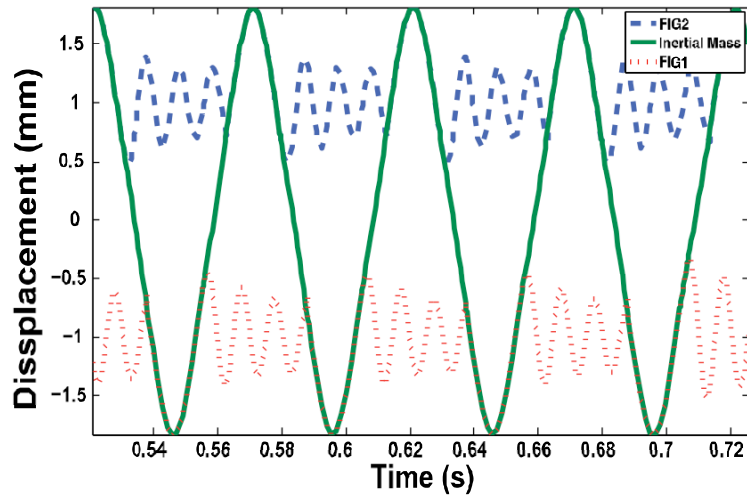
Figure 2-7. Simulated displacement of the three components of the PFIG generator. Shown in green is the movement of the inertial mass. The corresponding actuation of the FIG devices is shown in red and blue.

The PFIG system is simulated using the software tools MATLAB and SIMULINK. A separate SIMULINK model is built for each of the three cases. The

73

interaction between the three cases, determining the transition points, providing the appropriate initial conditions, and saving the data is performed using a controlling script in MATLAB. Shown in Figure 2-7 is a plot of displacement generated with the developed simulation tool. The motion of the inertial mass is plotted in green along with the corresponding FIG1 and FIG2 movement in red and blue respectively. The various parameters, mass, spring constants, electromechanical coupling coefficients and so on, used in the simulation correspond to a system discussed in Appendix A. In this plot the width of the three masses has been subtracted out from the position coordinates in order to better illustrate the combined motion of the inertial mass and the FIGs.
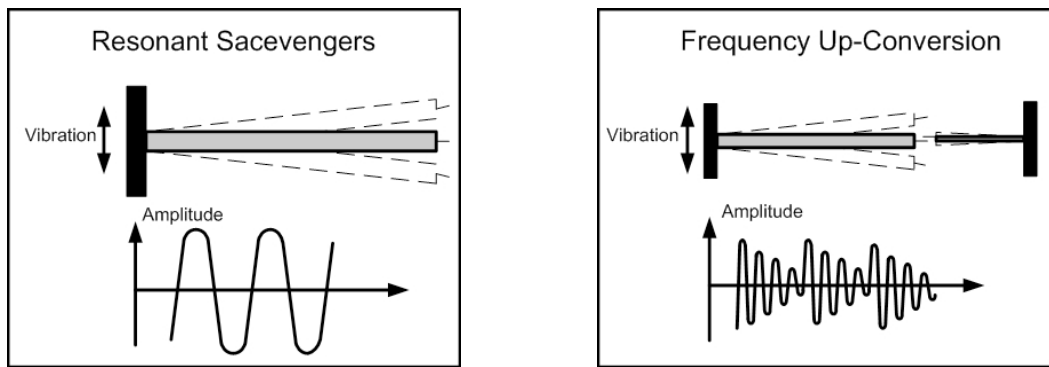
Figure 2-8. Illustration describing the frequency up-conversion principle where a low-frequency large displacement motion is mechanically converted to a higher frequency, lower displacement motion.

2.6 FREQUENCY UP-CONVERSION AND THE PFIG POWER GENERATION CAPABILITY

As discussed in Section 2.2 the electromechanical coupling of velocity-damped generators, such as the PFIG, is linearly dependant on the frequency of operation. In order to increase the operating frequency of the PFIG and decouple it from the low ambient frequency, a mechanical transformation is employed where energy is transferred from the inertial mass to the FIGs. This concept is knows as frequency up-conversion and

was developed at the University of Michigan [121, 122]. The general principle is illustrated in Figure 2-8. One element, designed in such a way as to be sensitive to mechanical excitations within a range of low frequencies, is excited by displacement at its base. The motion of this low-frequency resonator can then be used to actuate a second higher frequency resonant element (or array of elements). The purpose of this mechanical transformation is to convert the low frequency, large displacement motion to a higher frequency, lower displacement motion, for the purposes of increasing the efficiency with which the mechanical energy can then be transformed into electricity. Once energy is stored in the high frequency mechanical spring, the device is released. While undergoing free vibration, the stored mechanical energy is converted to electricity. The motional transformation can be achieved in one of several ways: the low frequency element can exert either a magnetic force; it can mechanically contact and actuate the higher frequency element; or an impulse can be provided by a collision between the two devices. In the PFIG, the transformation is performed using magnetic latching between the inertial mass and the FIGs. While it is not certain which of the three methods is more efficient in transferring energy, magnetic latching is least susceptible to wear. An additional benefit of the frequency up-conversion is that in addition to increasing the conversion efficiency, it decouples the operation frequency of the transducer from the input vibration motion. In this way, the PFIG is able to operate without tuning over a large frequency range, enhancing its bandwidth and versatility.

Calculating the energy converted by the PFIG using the frequency up-conversion method can be performed in the same way as was done for resonant generators in Section 1.3.1. The mechanical energy transformed into electricity is equivalent to the energy

dissipated per cycle by performing work against the transduction mechanism. This is equivalent to taking the distance integral of the damping force $b_{fe}\dot{u}$ over a full FIG cycle:

$$W_{perFIG} = \oint b_{fe}\dot{u}du = \oint b_{fe}\dot{u}^2 dt = \int_0^{2\pi/\omega} b_{fe}\dot{u}^2 dt.$$ (2.18)

In Eq. (2.18), b_{fe} and $\dot{u}$ are the electrical damping coefficient and the velocity of the top FIG as a function of time (the equivalent parameters can be substituted for the bottom FIG as well). Once the change of variables is made, the integral is taken over the period of the ambient source vibration, to take account of the entire time in which the FIG is oscillating after having been actuated. The velocity of the FIG can be represented as

$$\dot{u}(t) = -U_{act}\omega_{nf}\frac{e^{-\zeta_{fT}\omega_{nf}t}}{\sqrt{1-\zeta_{fT}^2}}\sin(\omega_d t),$$ (2.19)

where U_{act} is the initial FIG displacement just after release from the inertial mass, ω_{nf} is the natural frequency of the FIG, ζ_{fT} is the combined electrical and parasitic damping ratio of the FIG, and ω_d is the damped natural frequency of the FIG:

$$\omega_d = \omega_{nf}\sqrt{1-\zeta_{fT}}.$$ (2.20)

Taking the integral in Eq. (2.18), dividing by the period of the ambient vibration, and multiplying by two to account for the fact that each FIG will be actuated once per cycle, gives the equation for total power converted by the PFIG:

$$P_{total} = \frac{m_f \zeta_{fe}\omega\omega_{nf}^3 U_{act}^2}{1-\zeta_{fT}^2}\left[\frac{1-e^{-4\pi\zeta_{fT}\omega_{nf}/\omega}}{2\zeta_{fT}\omega_{nf}} - \frac{e^{-4\pi\zeta_{fT}\omega_{nf}/\omega}\left(2\omega_d\sin(4\pi\omega_d/\omega)-2\zeta_{fT}\omega_{nf}\cos(4\pi\omega_d/\omega)\right)}{4(\zeta_{fT}^2\omega_{nf}^2+\omega_d^2)}\right].$$ (2.21)

Assuming that ζ_{fe} (and ignoring parasitics) is large enough such that the FIG can be completely damped per ambient vibration cycle $2\pi/\omega$, P_{total} can be shown to be

$$P_{total} \sim m_f \gamma^2 \omega^3 U_{act}^2,$$ (2.22)

where $\gamma = \omega_{nf}/\omega$. The major optimization goal in the PFIG, and frequency up-conversion schemes in general, is to assure that the reduction in the mass times the reduction in displacement squared is significantly less than the square of the frequency ratio γ. Upon maximizing the initial deflection, U_{act}, to be as high as possible in a given volume, for a given ζ_{fe}, γ can be used to maximize the converted potential energy stored in the FIG spring. Shown in Figure 2-9 is a simulation where normalized power (normalized to $m_i \omega^3 Y_o^2$) is given as a function γ. As shown for a given ζ_{fe}, frequency up-conversion can be used to increase the electromechanical coupling and optimally utilize the potential energy transferred during the motional transformation.
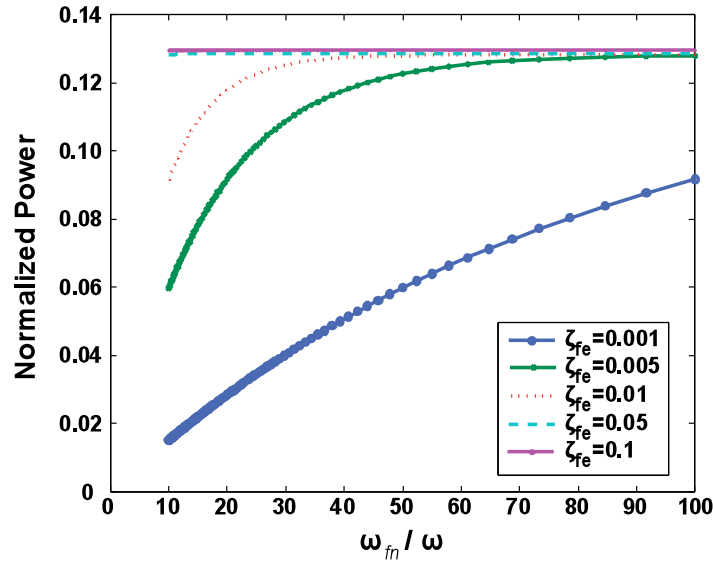
Figure 2-9. Simulated performance of the PFIG as a function of the ratio γ between the natural frequency of the FIG and the ambient vibration frequency ω for different damping ratios. Power is normalized to $m_i \omega^3 Y_o^2$.

2.7 EFFICIENCY AND APPLICATION OF THE PFIG

The PFIG has been specifically designed for applications where the vibration amplitude is very large and/or where a response is needed to a broad range of input frequencies. Just what conditions are implied by this specification can be evaluated by considering the Volume Figure of Merit (FoMv) as defined in Eq. (1.34) for a resonant generator and compare it to the FoMv for the PFIG. Both generators are considered to have a cubic geometry, where one half of the volume is occupied by a mass having a density of 20g/cm^3. The remainder of the space is used for displacement in the resonant generator. When considering the PFIG, the remaining space is used for both displacement and the rest of the hardware. This means that Z_l for the resonant device is set to 1/4 of the linear dimension of the given volume. It is assumed that the PFIG $\text{gap}_T/\text{gap}_B$ will not exceed 1/5 of the linear dimension of the volume in practical applications. The remainder of the space is apportioned equivalently between the two FIGs. The power generated by a resonant generator, ignoring parasitics, and constraining ζ for the maximum displacement condition (Z_l) is given by Eq. (1.15). In comparison, the power generated by the PFIG is given in Eq. (2.21), where U_{act} is ideally equal to $\text{gap}_T/\text{gap}_B$. The FIG parameters are optimized by assuming that the gap $\leq \omega^2 Y_o / \omega_{comb}^2$, where ω_{comb} is the combined resonant frequency of the inertial mass/FIG. In this way, k_f is first set to maximize the gap, and then m_f is set to achieve the desired frequency ratio. The volume of the mass is bounded to 3/10 of the volume of the generator in accordance with the geometric confinement discussed above. If this cannot be achieved, then k_f is adjusted. The damping and frequency up-conversion ratios are chosen so as to saturate the converted energy. The resonant generator is considered at resonance. The damping is automatically adjusted to

be optimal by Eq. (1.34), however as the displacement of the generator exceeds Z_l, the constrained damping factor exceeds 1. This invalidates the analysis that led to Eq. (1.34), because an underlying assumption is that the oscillations are cyclic. For this reason the damping is saturated such that the resonant generator will operate with a minimum quality factor of 1. When Z_l is exceeded, the linear dimension of the generator is increased to accommodate a minimum of $Q = 1$, and the volume is adjusted. Neglecting parasitics, the FoMv of the two generators is compared in Figure 2-10 for an acceleration of $9.8m/s^2$. The dotted line shows the efficiency of the PFIG as a function of Z_l/Y_O, while the solid line shows the efficiency of the resonant generator. Above $Z_l/Y_O = 1$, the resonant generator has an efficiency of 100%, which follows from the way in which FoMv is defined. However, as the input vibration amplitude exceeds Z_l, the efficiency of the resonant generator rapidly drops and it quickly becomes advantageous to use the PFIG. The exact transition point is a matter of some debate because right at the edge of $Z_l = Y_O$ the equations governing the power given by the resonant generator begin violating even more practical considerations than were already assumed during the analysis. A transition region is highlighted in gray. In this region, where $Z_l/Y_O \sim 0.3\text{-}1$, it becomes more advantageous to utilize the PFIG architecture. The vibration frequency where this transition point applies is dependent on the volume of the generator. The red curves, which utilize the right-hand axis, show the frequency as a function of Z_l/Y_O. Assuming a volume of $1cm^3$, one can see that the transition point falls around 6-8Hz for an acceleration of 1g. One important aspect of the PFIG architecture can be seen by comparing the two red curves, for $1cm^3$ and for $1mm^3$, which show that as the volume decreases the transition point happens at an ever-increasing frequency. Thus, the PFIG

architecture becomes very important for the miniaturization of vibration harvesters because the vibration amplitude exceeds the generator dimensions for a much greater portion of the frequency range of interest for most applications.
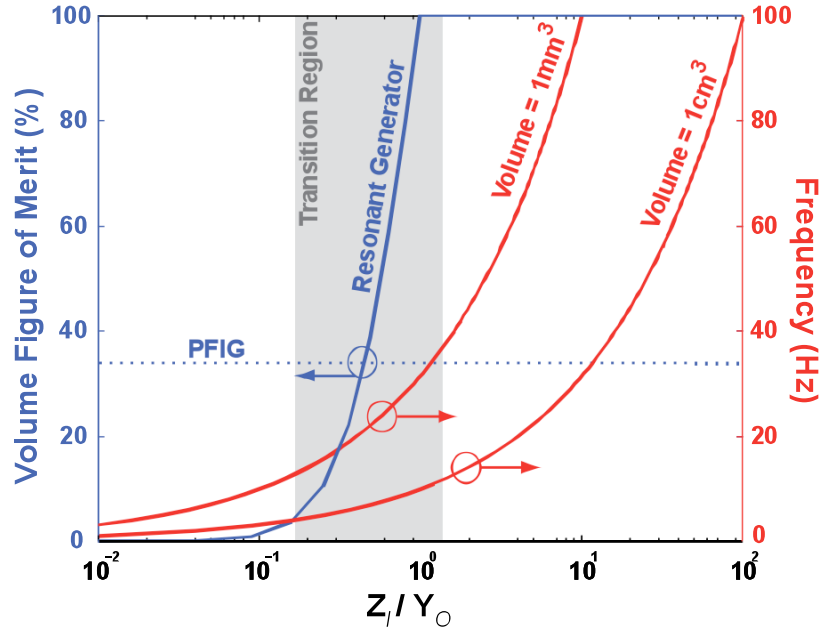
Figure 2-10. Simulated Volume Figure of Merit (FoMv) of a PFIG compared to a resonant generator as a function of Z_l/Y_o. For a given volume and acceleration it becomes more efficient to use the PFIG when Y_o exceeds Z_l. This happens at an ever-increasing frequency as the volume shrinks, demonstrating the importance of the PFIG for microgenerators.

Another important aspect of the PFIG architecture is its wide-band nature. A simulation of the frequency response of the PFIG is shown in Figure 2-11 alongside three different resonant generators working under optimal conditions. When the energy harvesting application calls for it, power can be traded for bandwidth, and the PFIG architecture can be used to scavenge broadband vibrations. The PFIG is shown to work up to 80Hz in this plot because the simplified power analysis does not take into account the dynamic behavior of the system. The exact frequency range that the generator will cover will depend on the design.
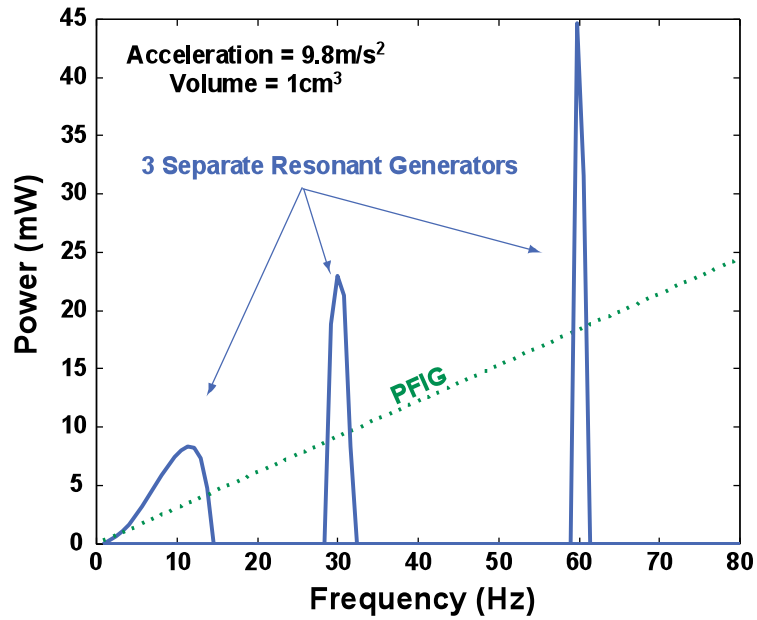
Figure 2-11. Simulated frequency response of the PFIG as compared with three resonant generators working at their optimal conditions. The PFIG has an inherent tradeoff between bandwidth for maximum power. However, this allows the PFIG to operate over a large bandwidth.

2.8 CONCLUSION

This chapter discussed the challenges of scavenging low frequency and non-periodic ambient vibrations. A new vibration harvester architecture called the Parametric Frequency Increased Generator (PFIG) was introduced. A theoretical framework regarding the analysis of the PFIG architecture was presented. The device dynamics are analyzed numerically by considering the structure during three cases of operation that transition between 2- and 3-degree-of-freedom magnetically coupled systems. The theoretical power generating capability of the PFIG was analyzed. Based on this analysis a discussion was carried out about when the use of the PFIG architecture makes sense in terms of efficiency as compared to resonant power generators. It was shown that when the vibration amplitude exceeds the internal displacement limits of a micro generator, implementing the device as a PFIG rather than a resonant generator is more efficient.

Additionally, in situations where a large bandwidth is required at low frequencies, the PFIG can provide the necessary range and versatility without any tuning or other manipulation.

Chapter 3

ELECTROMAGNETIC PARAMETRIC FREQUENCY INCREASED GENERATORS

The previous chapter introduced the new Parametric Frequency Increased Generator architecture that was specifically developed to address the challenges associated with scavenging low-frequency vibrations. A theoretical framework for designing and predicting the performance of the PFIG was developed. The validity of this model was evaluated by using it to design and then test a prototype electromagnetic PFIG bench-top implementation. This device was built in a manner such that many of the model parameters could be modified and studied. The bench-top device is discussed in more detail in Appendix 1. In this chapter the development of the first miniature PFIG is described. First, the design and fabrication of this electromagnetic generator is discussed, and the initial test results are presented. Further FEM modeling is performed to better optimize the electromagnetic transduction mechanism, and based on these optimizations a new improved implementation is built and tested.

3.1 DESIGN OVERVIEW OF ELECTROMAGNETIC PFIG

The main purpose of developing this first electromagnetic PFIG was to show that the concept could feasibly be implemented in a miniature generator. However, the possibility of applying it toward scavenging energy from human motion was kept in mind. The PFIG

83

concept is ideally suited for this type of environment since humans produce large irregular motion. A target acceleration of 1g (9.8m/s^2) was selected for this design. While it is on the high end for many other applications, it has been shown by a number of studies that this is an acceleration level found on the human body [74, 123]. The generator was designed to operate in the range of 0-10Hz.
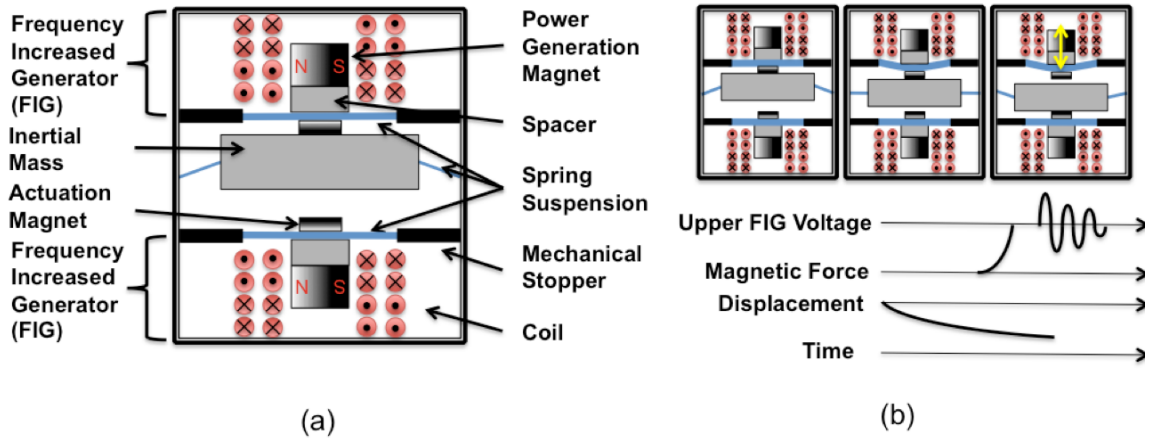
Figure 3-1. a) Electromagnetic PFIG conceptual diagram, and b) theory-of-operation explanation.

The design of the micro electromagnetic generator discussed in this chapter is based directly on the PFIG concept discussed in Chapter 2 and presented in Figure 2-2. In fact looking at Figure 3-1, one can see only a few changes. The first is that a mechanical stopper has been incorporated in order to protect the FIGs from shocks to the generator, or from damage if the device were to operate under excessive acceleration. The second change can be seen in the electromagnetic system of the FIG. The configuration is changed such that two coils are wound in and out of the plane of the page, and a magnet (poled left to right) is moved up and down, parallel to the coils. This generator is a miniaturized version of the proof-of-concept device described in more detail in Appendix 1. For this reason it will be referred to as the second generation, or Gen 2, PFIG in this thesis. While this effort sought to decrease the size of the first generation PFIG, it is not a

fully micromachined device. Instead, a hybrid fabrication approach was used in making this device by incorporating lithographically fabricated parts with discrete components. This way a good balance was struck between being able to exploit the precision and form factor of micromachining, with the significantly superior material properties of bulk magnets and macro coil winding capabilities.

Designing the PFIG is not a trivial matter. As shown in Chapter 2, the system is heavily non-linear. It changes from 2 to 3 degrees of freedom. Lastly, the magnetic forces have an inverse tangent relationship to distance and change rapidly as the distance closes. For these reasons the dynamic behavior of the PFIG can only be studied using numerical methods. An initial hand analysis is carried out to select starting values for many of the parameters. Simplifications are used. The magnetic force was selected based on the availability of a small 1mm diameter magnet that could be ordered without custom manufacturing. From there the inertial mass requirement can be determined such that the inertial force exceeds the maximum magnetic force. Similarly, the FIG spring has to be of a certain stiffness as to ensure that at very low velocities and at the minimum acceleration of 1g, the spring force on the FIG is able to exceed the inertial force, before the gap between the inertial mass and the opposing FIG is reached. After this first order analysis, numerical simulations are carried out to find a stable and reliable configuration for the entire PFIG. Having determined the values for the mechanical parameters, the components themselves can then be designed to meet the specifications that are required of them. The next section is devoted to a description of this process.
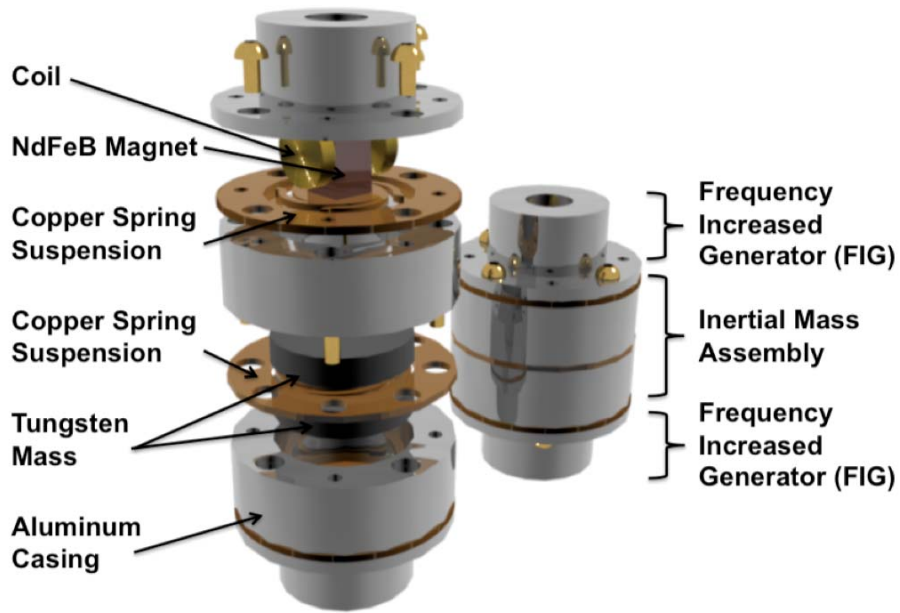
Figure 3-2. Exploded view of the Gen 2 electromagnetic PFIG showing the structure of the device, components, and assembly.

3.2 IMPLEMENTATION, FABRICATION, AND ASSEMBLY

An illustration showing the Gen 2 electromagnetic PFIG is shown in Figure 3-2. The layout mirrors very closely the theoretical implementation of the device presented in Figure 3-1. One can see the FIGs on the top and on the bottom and the inertial mass in the middle. The generator consists of four separate enclosures, bolted together during assembly; the spring suspensions are clamped down in the process.

3.2.1 SPRING DESIGN

Copper is chosen as the material for the spring suspension. A material was sought which would have a low Young's modulus and a high yield strength in order to accommodate high displacements. Additionally, because of the nature of operation, a

86

material with a high fracture limit is necessary. Polymers are avoided because typical energy scavenging applications require materials that are able to withstand harsh conditions. Table 3-1 presents the properties of a number of different spring materials. It can be seen that Copper, although not the best choice, offers a relatively low Young's modulus and acceptable Yield strength. Additionally, copper is easily micromachined and was readily available, so for a first prototype was a good compromise.

Table 3-1: Properties for possible spring suspension materials.

	Density (x10^3 kg/m^3)	Young's Modulus (GPa)	Yield Strength (MPa)	Tensile Strength (MPa)	Poisson's Ratio	Coefficient of Thermal Expansion (x10^{-6} K^{-1})
Aluminum	2.7	68.4	94.4	116	0.33	24.9
Brass	8.48	104	249	441	0.375	20.4
Copper	8.62	117	382	521	0.318	17.8
Nickel	8.45	206	577	884	0.312	14
Parylene C	1.289	3.2	55.2	69		35
Polyimide	1.3	7.54	118	113		24.9
Titanium	4.54	114	977	1060	0.322	9.26
Silicon (SiC)	2.3	185			0.28	3
Stainless Steel	7.81	196	613	870	0.285	15.1

A crab leg design was used for the FIG spring and a meandering fixed-fixed beam was used in the design of the inertial mass spring. The geometry of the beams was approximated first using basic small deflection theory and then fine-tuned using finite element analysis and ANSYS. For a fixed-fixed beam the spring constant is given by:

$$k = \frac{Ewt^3}{l^3}$$ (3.1)

where E is the Young's modulus, and w, t, and l are the width, thickness and length of the beam respectively. A rectangular cross section is assumed. The beams are fixed on both sides and terminate in the middle with a large pad that is assumed to be rigid. This is where either magnets or the inertial mass are attached. In both spring designs this center

region measures 3.5x3.5mm. The crab-leg springs have 4 legs, each of which has two sections of length 5.1mm and 5.8mm. Two designs are simulated, one having a width of 240μm (spring type 1, ST1) and one with a width of 440μm (spring type 2, ST2). Figure 3-3 shows FEM simulations of the stiffness and the stress profile for ST2. As can be seen from the plot considerable stress develops around the edges as the springs deflect. In order to mitigate this stress care is taken to eliminate right angles from the layout, and gradual curves are incorporated in the joints. Two versions of the inertial mass springs are also designed. Each of them has two meandering legs suspending the center region to which the mass is affixed. Both spring designs have a width of 440μm and length of 14.6mm (mass spring type 1, MST1) and 15.8mm (mass spring type 1, MST1).

(a)   (b)
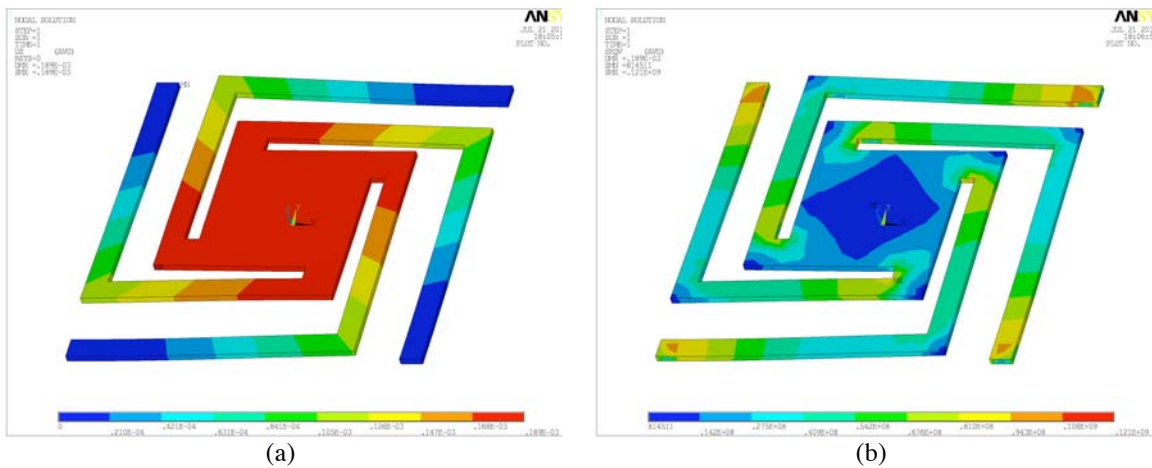
Figure 3-3. FEM results for ST2 a) deflection under a centrally applied force of 0.128N, and b) stress distribution in the structure.

3.2.2   SPRING FABRICATION

The springs for both the FIG and the inertial mass are fabricated out of 127μm thick copper alloy 110. The fabrication process is shown in Figure 3-4left. Copper sheets were mounted on 100mm Si wafers using AZ9260 photoresist. To protect the backside of the

copper foil a 10μm photoresist layer was spun on the copper. Another layer is deposited on the silicon wafer. After allowing the photoresist adequate time to settle, the copper sheet was flipped over on top of the wafer, compressed and soft baked for 30min at 90°C.
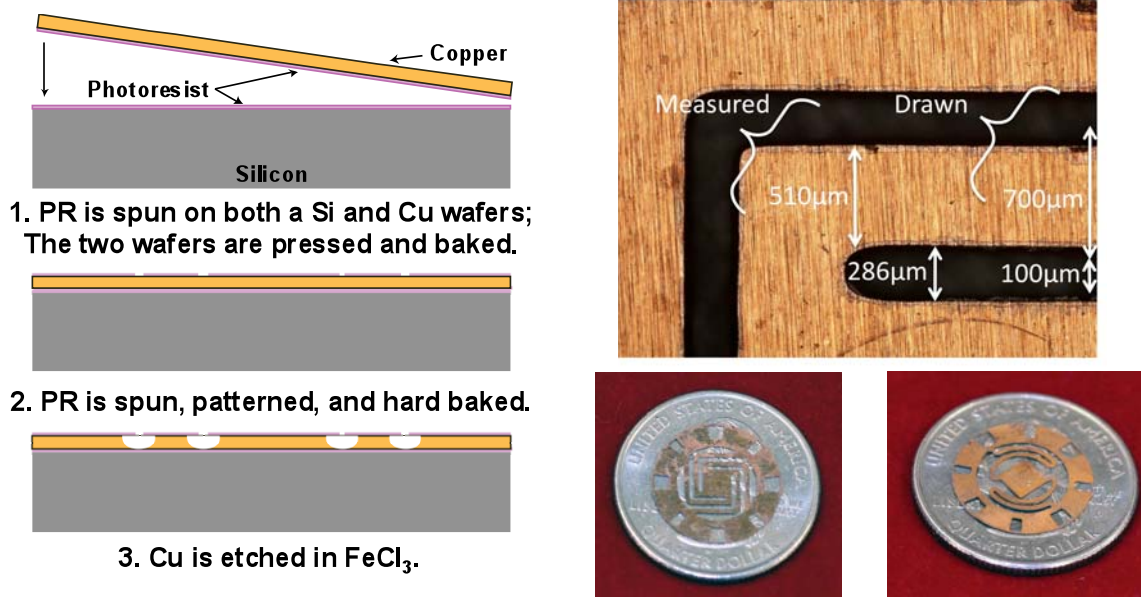
Figure 3-4. *left* Copper spring micromachining process. *right* Close up of a fabricated spring showing the achieved dimensions after wet etching compared with the drawn parameters. Close up photographs of the inertial mass and FIG springs are shown below.

A subsequent layer of the same photoresist is spun and patterned and used for lithography. Because of the long chemical etching time, the elevated temperature, and the corrosive nature of the etchant, a hard bake at 110°C for at least 30min is critical. The springs are etched in iron (III) chloride, or Ferric Chloride, $FeCl_3$ which is heated to 45°C. The wafers are immersed and agitated generously. Figure 3-4*right* shows a microscope close-up of one of the fabricated springs as well as photographs of ST1 and MST1. In order to account for the etch undercut the drawn width was augmented by 260μm. However, the undercut was found to be less than 1:1, in fact closer to 1:0.5. This meant that the resultant features were 10-15% larger than expected. Since stiffness is linearly proportional to width, a variation of the same amount will also exist in the spring

characteristics.

3.2.3   INERTIAL MASS FABRICATION

The inertial mass is made from tungsten carbide, which is a very dense material, 14.7-14.9g/cm^3, and results in a compact mass. A 10mm diameter rod is machined using electric discharge machining (EDM) after which it is ground down for planarization. Two pieces, each of which has a thickness of 3.9mm, are bonded using cyanoacrylate on each side of the spring suspension atop a 1mm spacer. An alignment jig is used to center the mass pieces on the spring.

3.2.4   COIL MANUFACTURING

Coils for the FIGs are wound from 44AWG enameled copper wire. The wire has a diameter of 50.8-55.8μm (53.34-58.34μm including polyurethane nylon insulation). The resistivity is 1.7 x 10^{-8}Ωm. The coils are wound around a plastic core. They have an inner diameter of 1.6mm, an outer diameter of 7mm, and are 1.6mm thick. This allowed for 1000 turns per coil and a resistance of 119Ω.

3.2.5   FIG ASSEMBLY

The FIG assembly is made by bonding a 3x3x3mm rare earth neodymium iron boron, NdFeB, magnet to the spring on top of a 1x1x0.5mm plastic spacer. A cylindrical magnet with diameter 1.15mm and thickness 0.5mm is bonded on the other side of the FIG spring for latching and actuation purposes. The neodymium magnets are grade N42 meaning that they have a residual flux density (B$_r$) of 1.3T. The magnets along with the center part of the spring effectively serve as the FIG mass. NdFeB magnets have a density of

7.4g/cm^3. The coils are placed vertically and opposite each other inside the FIG casing and adhered using epoxy. In this initial implementation the alignment during assembly was done by hand.
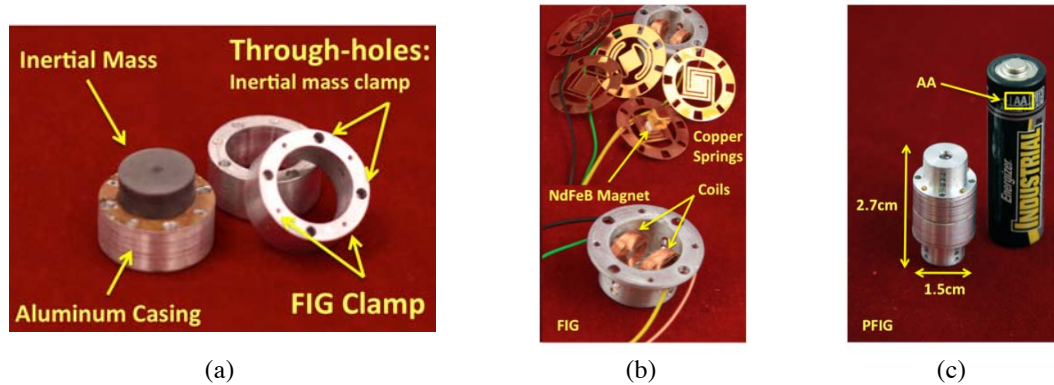
Figure 3-5. Photographs of the fabricated PFIG. a) Shows the inertial mass/spring assembly as well as casing components, b) shows a close-up of one of the FIGs along with an assortment of etched copper springs, and c) the PFIG device is compared with a standard AA battery.

3.2.6 CASING AND ASSEMBLY OF PFIG

The generator casing is milled out of aluminum. It has a 1mm sidewall running throughout. The most intricate parts are the inertial mass enclosures, which contain all of the taps and bore used to secure and fasten the entire generator together. Two types of 000-120 bolts are used: 6.3mm long bolts go though the two separate inertial mass enclosures and clamp its spring suspension into place, and 3.2mm long bolts attach the FIGs to the generator body. The FIG springs have the same outer diameter as the generator body. This way the outer edge of the FIG casing can be used for alignment. The bolt holes serve to orient the spring and the bolts act as alignment pins. Figure 3-5a shows the inertial mass as well as the generator casing components. In, Figure 3-5b one can see the inside of one of the FIGs along with an assortment of etched copper springs. Figure 3-5c shows the assembled PFIG next to a standard AA-size battery.

3.3 TEST SETUP AND GENERATOR RESULTS

The PFIG generator is tested using an Unholtz-Dickie 5PM electrodynamic shaker. A power amplifier UD TA-30 that is controlled by a UD MA-630 transducer calibration control system drives the shaker. Feedback is provided using a UD 8B6 accelerometer. The shaker can apply acceleration of 0.1-2g in the frequency range of 10-10kHz. Only sinusoidal tests can be performed with this test setup due to limitations of the controller. A mounting base plate was machined out of steel and fixed to the shaker table. It has a number of tapped holes that can be used to mount various devices. The FIGs and the PFIG shown in Figure 3-5 are glued using epoxy to an acrylic base that is screwed onto the shaker base plate. In order to extract important parameters after manufacturing, the FIGs are tested before the full generator is assembled. This testing is performed in the y-axis (vertical direction). The PFIG generator is tested in the x-axis (horizontal direction). This initial design does not account for gravity and in order to eliminate this bias the shaker table is inclined by 90°.
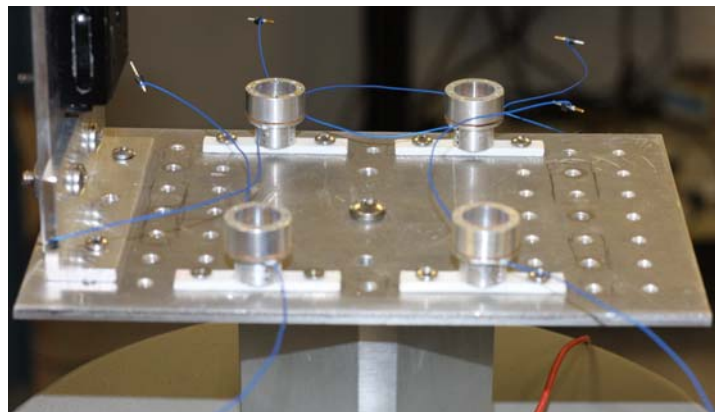
Figure 3-6. FIGs mounted on shaker table for testing.
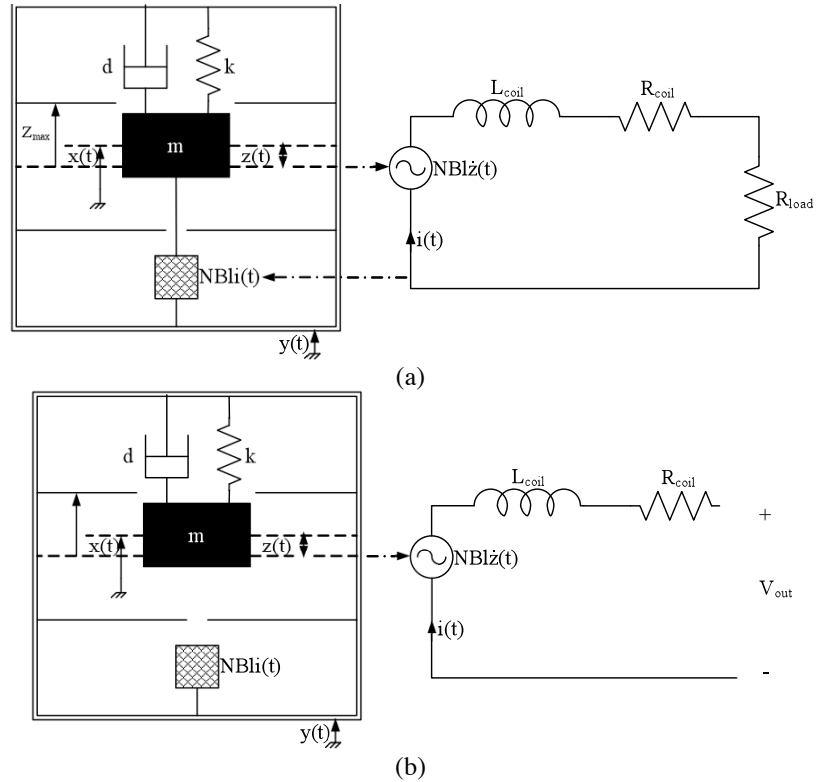
Figure 3-7. a) Resistively loaded electromechanical model of each FIG. b) Open circuit electromechanical model of each FIG.

3.3.1   FIG CHARACTERIZATION

Initial testing was performed to characterize the FIG devices. Each FIG was mounted on the test setup as shown in Figure 3-6. Many important parameters of the generator can be extracted using simple vibration and resonance testing. This is necessary to see how the manufactured characteristics of the device compare from the designed parameters. It is very challenging to predict some things like mechanical/parasitic damping, as well as the electrical damping itself. Accurate mathematical modeling of these things is very involved and in the end will likely still result in significant deviation from practice. For this reason it is imperative that these parameters be extracted experimentally in order to compare the devices performance to theory. To determine damping, the quality factor of

the devices needs to be measured. Using equation (1.17) one can determine the electrical quality factor Q_e having first obtained the loaded Q_T, and open circuit, Q_m, quality factors. Figure 3-7a shows the full electromechanical model of the FIG loaded with a resistor. By measuring the output voltage, V_{out}, the total quality factor Q_T can be computed. Similarly, in Figure 3-7b the electromechanical model of the FIG is shown when the generator circuit is open and no current can flow (consequently no damping force can be applied on the mass from the electromagnetic system). This eliminates the electrical system and by measuring V_{out} one can determine Q_m.

There are two different methods to calculate Q from the output voltage waveform. The first is to actuate the FIGs at their resonance frequency using some small acceleration (0.1g in this case). By examining the decay of the voltage waveform immediately after the shaker table is switched off, one can determine the parasitic and electrical quality factors [44]. The damping ratio can be calculated as

$$\zeta = \frac{1}{2\pi\Delta t f_0} \ln\frac{V_1}{V_2},\tag{3.2}$$

by measuring the peak voltage amplitude at two instances of time. This process is illustrated in Figure 3-8a where a voltage trace from one of the FIGs is shown. This method is used to measure Q for the Gen2 PFIG; it is later replaced using a different technique. The problem with studying the decay is that, as shown in Figure 3-8a, depending on where the voltage points are taken, the calculated quality factor can vary. This implies that the damping is somehow related to the amplitude of the movement, and as the oscillation of the FIG decays the damping constant changes. The most likely causes are damping from internal friction and support loss, both of which likely change

94

with amplitude. When this method is used, in order to make repeatable measurements, the voltage is measured around the 'knee' of the decay plot, where the second arrow is pointing in Figure 3-8a.
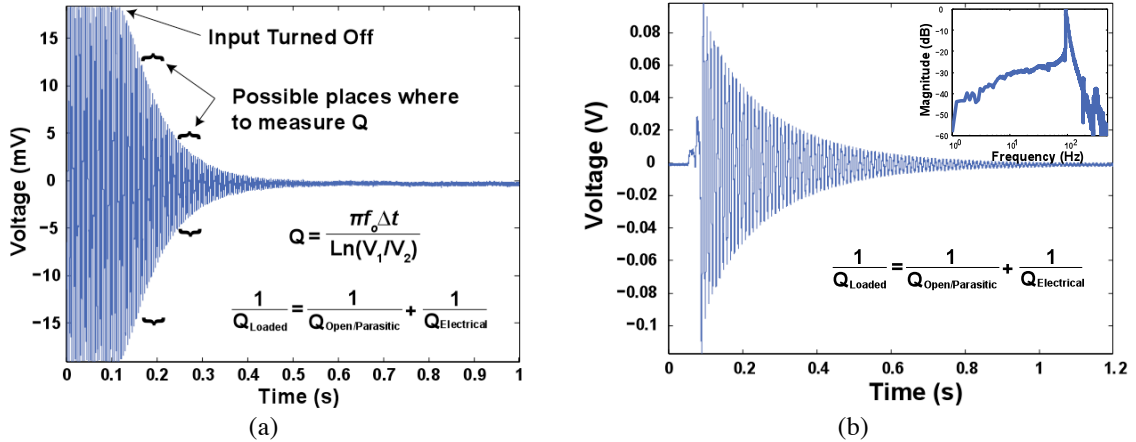
Figure 3-8. a) Plot of voltage signal from FIG illustrating how to measure the quality factor using by analyzing the decay. b) Decaying oscillation of the FIG resulting from a force impulse provided to the spring and used to calculate the quality factor.

A second method to measure the quality factor exists. By providing an impulse to the area for magnetic actuation, the FIG spring is displaced. Waveform traces of the generated output voltage are used to determine the natural frequency of the device, as well as to investigate the parasitic damping and electromechanical coupling of the system. Figure 3-8b shows one such dataset. The frequency response is computed by taking the Discrete Fourier Transform of the voltage signal and the quality factor can then be determined by finding the -3dB bandwidth and the center frequency. This method, although likely averaging the damping factor variation with respect to amplitude, provides more consistent results and is used throughout this thesis unless noted otherwise. The process of finding the damping, regardless of which method is used, also gives the resonant frequency of the FIG. Having measured the exact mass of the FIG using a scale, the spring constant can then be calculated quite accurately.

3.3.2 COIL WIRING AND TESTING CONSIDERATION

As mentioned before, the FIG contains two coils. Each coil has 1000 turns. Their resistance is 120Ω. There are two ways to extract power from the device. Either each coil can be used separately or they can be combined. Obviously, using each one separately means that the PFIG generator would have 4 different signals that need to be rectified, stored, and so on. This is not very practical. In order to alleviate this problem, the two coils in each FIG are wired in series, in such way (taking account of their winding direction and the magnet pole facing them), so that the generated electromotive force would add. From the Gen 1 device it was noticed that when the FIGs were actuated using the shaker table, the voltage that was produced when they were connected in series was less than the sum of the voltages when recorded separately. In other words, connecting the coils separately would result in higher power generation. One of the problems with these coils is that they are uneven due to the manual winding that was used. For future designs a mechanical system is used for coil winding and improves coil reproducibility.
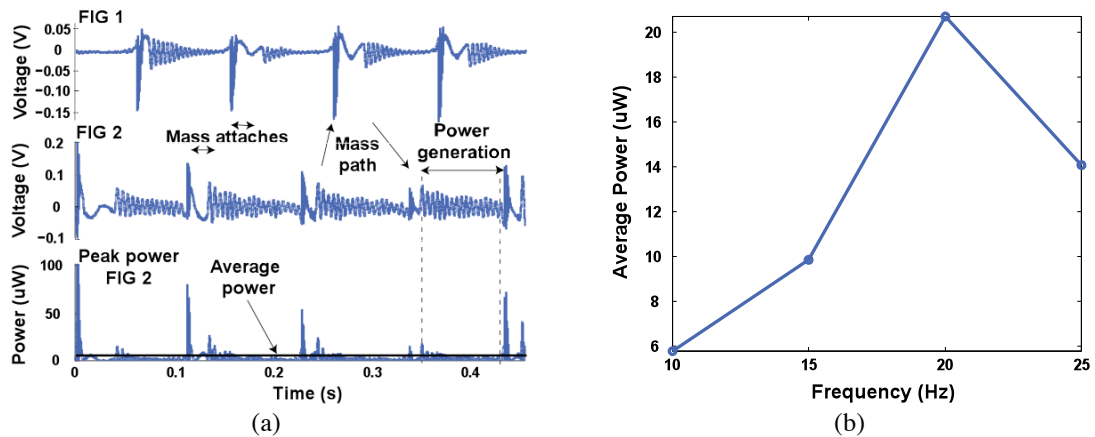
Figure 3-9. a) Oscilloscope trace showing the parametric generator operation from an external acceleration of 1g at 10 Hz. b) Measured frequency response of the PFIG generator. The cut-off frequency is determined by the inertial mass/spring suspension natural frequency.

3.3.3 PFIG TESTING

The PFIG is assembled, and tested at 1g, the acceleration level for which it was designed. The minimum frequency at which the generator can be tested accurately is 10Hz due to limitations associated with the vibration test system. Each FIG is loaded with a 240Ω resistor. Figure 3-9a shows the operation of the PFIG. The top two plots show the voltage generated by each FIG across the load, and the bottom plot shows the instantaneous power from FIG 2. By looking at the voltage waveform it becomes evident where the inertial mass attaches to each FIG, and where the mass detaches and travels to the opposing device. The bandwidth of the PFIG is dominated by the resonant frequency of the inertial mass and its spring suspension in this case. It was found that the generator could function up to a frequency of 20Hz. After 20Hz it would skip latching from time to time, signifying that the frequency was getting too high. The power output reduces from there, and past 25Hz the generator ceased to operate as intended. The device parameters and performance are summarized in Table 3-2.

Table 3-2: Gen2 PFIG Summary

FIG Mass	0.25g	Inertial Mass	9g
FIG Suspension*	614N/m	Inertial Mass Suspension*	135N/m
FIG Natural Frequency	208Hz	Actuation Magnet	Dia. 1.15mm, Thick. 0.5mm
FIG Coil Turns	2000	Internal Volume	2.12cm3
FIG Coil Resistance	240Ω	Total Volume	3.74cm3
FIG Electrical Q-factor	97	Min. Acceleration	0.9g
FIG Parasitic Q-factor	50	Max. Power (1g, 10Hz)	288μW
FIG Magnet	3x3x3mm	Avg. Power (1g, 10Hz)	5.8μW
FIG Displacement Limit	0.5mm	Bandwidth	20Hz

*Simulated Value

The initial PFIG results exceed the state-of-the-art in low-frequency scavengers. This device has the highest power density (under similar input conditions) than any other work reported in the frequency range of interest (≤10Hz). A more extensive discussion of

performance is presented at the end of the chapter. However, as one can see from Figure 3-9a the device is clearly not performing optimally. Further optimizations are needed in three areas: 1) space optimization of the electromagnetic system – thinner coils, larger magnets, and increased flux density through the coils, 2) better magnetic actuation/latching, because as Figure 3-9a shows, the two FIG device are not equally effective, and 3) optimized spring design and fabrication, because they are allowing the FIGs to resonate in more than one mode. So far the electromagnetic transduction system has not been a focus. Future work will be needed to optimize the electromagnetic transduction system to make sure that all of the energy that is transferred to the FIG is utilized. Of course this electromagnetic arrangement does not really utilize the magnetic flux well because it is allowed to spread out. This issue will begin to be addressed in the next section. The second problem which can be seen in Figure 3-9a is that the latching/unlatching and actuation of the FIGs is highly asymmetric. One reason for this is likely the different amounts of parasitic damping. It is clear from Figure 3-9a that FIG1 has much higher damping than FIG2. The most likely cause is that the magnet is contacting the coils and there is a frictional force added to the system. A better positioning and assembly technique is needed to prevent this from happening. Lastly, one can see the significant non-linearity in the oscillations of FIG2. This is likely caused by one of two things: either there is a stress gradient in the spring, or a secondary mode is being induced. It could be that the spring is clamped down unevenly inside the generator. Care was taken to minimize this by carefully securing all bolts in a star pattern. Also, because of the thin width of the long spring beams, the first torsional resonance mode was inevitably very close, only within a few hundred Hertz of the primary mode induced

during the latching.

3.4 ELECTROMAGNETIC OPTIMIZATIONS

Electromagnetic generators relay on the basic law of electromagnetism as described by Michael Faraday, where the induced electromotive force in any closed circuit is equal to the time rate of change of the magnetic flux. Magnetic flux is defined as

$$\varphi = \int_A B dA,$$
(3.3)

where A is the area enclosed by the wire loop and B is the magnetic flux density. From here, the electromotive force, or voltage, induced in the current carrying loop is given by

$$\varepsilon = -\frac{d\varphi}{dt} = -\left(\frac{dA}{dt}B + \frac{dB}{dt}A\right) = -\frac{d\varphi}{dx}\cdot\frac{dx}{dt},$$
(3.4)

where x signifies the position coordinate. Of course, this becomes a very complicated three-dimensional problem to solve. The vast majority of authors, including this one, use a simplification by assuming that the magnetic field is constant. By assuming that a conductor of length l is moving through a constant magnetic field, $d\varphi/dx$ simplifies to the form presented in Eq. (1.19) where

$$\varepsilon = -N\cdot(B\times l)\cdot\frac{dx}{dt}.$$
(3.5)

Designing and optimizing a given electromagnetic transduction configuration means solving and optimizing Eq. (3.4). If multiple designs are considered, this task has to be accomplished for each one. It is a daunting challenge, which nevertheless has been undertaken by one group [124]. They numerically compared a number of different

coil/magnet arrangements used by various authors in the field.

In this study finite element computer aided modeling was used to develop a more optimized design of the electromagnetic transduction system. A number of different topologies were evaluated using simple 2D modeling in Ansoft Maxwell. In this study only single coil/magnet configurations were considered. While using different orientations, the magnet and coil were displaced relative to each other. The magnet poles were arranged parallel to the plane of the coil or perpendicular. The scenario where the magnet rotates was also evaluated. These simplified simulations revealed two topologies where the magnetic flux density had the highest change per given displacement, measured at predetermined locations within the coil. These two topologies were then used for more accurate and sophisticated three-dimensional modeling. They are shown in Figure 3-10.
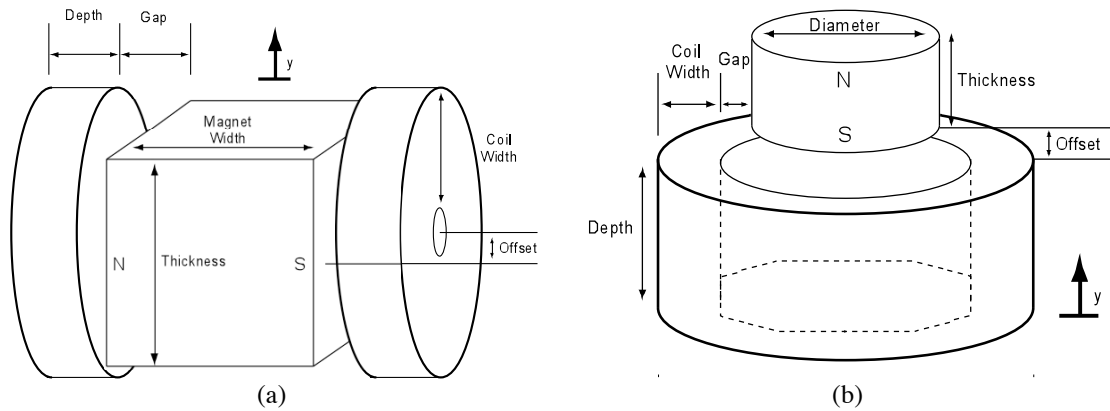
Figure 3-10. Coil/magnet arrangements evaluated using FEM for optimal Gen2 design. a) Parallel configuration: the magnet is displaced parallel to the plane of the coil. b) Perpendicular configuration: Magnet is displaced perpendicular to the plane of the coil. In both topologies the magnet poles are oriented 90° to the plane of the coil

The parallel configuration shown in Figure 3-10a is the topology used in the very first PFIG device (Appendix 1) and the Gen 2 device described in this chapter. Transient 3D simulations were performed on both topologies. A nominal configuration was chosen for

each topology, depth, gap, offset, and magnet dimensions. Each of these parameters was then varied one at a time to determine their influence on the induced voltage. The nominal configuration was chosen based on the Gen 1 and Gen 2 devices' physical dimensions and simulated values such as displacement and velocity were calculated. A 4.75mm cubed magnet was used; the coil had a 2mm depth and a coil width of 3.175mm. The coil was modeled by creating a volume that was specified to have 2000 turns. The gap between the magnet and the coil was initially set to 0.5mm and they were centered such that the offset was zero. The coil resistance was set to 240Ω, and the magnet was given a sinusoidal displacement of 0.4mm at a frequency of 200Hz. The parallel topology induced significantly lower voltages than the perpendicular arrangement. Increasing the magnet dimensions (both thickness and width/depth), led to a higher induced voltage. Making the coil depth thinner increased the voltage, as did increasing the coil width. These results point to the fact that having a coil with a large fill factor (ratio of winding turns to coil volume) is beneficial for inducing a higher voltage. However, the simulation is not sophisticated enough to understand that having a coil with a larger radius will lead to a higher parasitic resistance, nor does it factor into account the fact that a coil with a smaller depth means using thinner, more resistive wire. The optimal physical arrangement was shown to occur when the magnet position was offset by one coil radius such that the bottom of the magnet was lined up to the top of the coils.
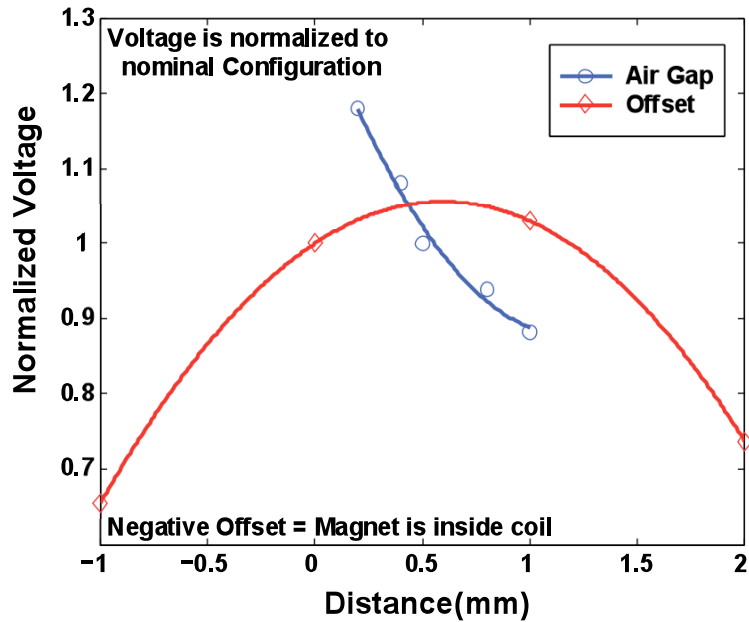
Figure 3-11. Perpendicular coil arrangement simulations using Maxwell 3D. The normalized induced voltage (normalized to nominal configuration) is shown as a function of coil/magnet offset and air gap.

Since the perpendicular configuration, Figure 3-10b, produced much higher induced voltages, it was studied in greater detail. Once again a nominal configuration was augmented, parameter by parameter, to study their influence. The magnet in this case was cylindrical with a diameter of 3.175mm and a thickness of 4.75mm. The coil had a width of 2mm and a length of 3.175mm (notice the change of orientation of the terminology associated with the coil geometry, see Figure 3-10). The gap was once again 0.5mm nominally. The magnet was initially positioned with an offset of zero, such that it was right on top of the coil plane. The magnet displacement and frequency were the same as in the parallel configuration. Once again increasing the size of the magnet yielded higher voltages, as did increasing the coil depth and decreasing the coil width. Figure 3-11 shows results of simulations varying the coil/magnet air gap and offset parameters. The induced voltage is normalized to the nominal configuration in order to show the relative importance of these parameters. The data is fitted using second order polynomials.

Changing the air gap from 0.2 – 1mm reduced the voltage by 34%. Additionally, changing the offset by setting the magnet +/-1mm from its optimal position also yielded >30% reduction in voltage. The most unexpected result was that the optimal position was slightly above the coil plane at 0.6mm (when using the nominal values for the other parameters).

Table 3-3: Optimal values and predicted induced voltages for the parallel and perpendicular coil/magnet topologies.

Parallel Configuration		*Perpendicular Configuration*	
Simulated Peak Voltage	0.568V	Simulated Peak Voltage	1.27V
Coil Turns	2000	Coil Turns	2000
Coil Resistance	240Ω	Coil Resistance	240Ω
Magnet Displacement	0.8mm$_{ppk}$	Magnet Displacement	0.8mm$_{ppk}$
Magnet Frequency	200Hz	Magnet Frequency	200Hz
Magnet	4.75x4.75x4.75mm	Magnet	4.75x4.75x4.75mm
Coil Width	2mm	Coil Width	2mm
Coil Depth	3.175mm	Coil Depth	3.175mm
Air Gap	0.5mm	Air Gap	0.5mm

The optimized parameters for the two coil/magnet configurations are presented in Table 3-3. The main result is that the perpendicular arrangement is predicted to give a 2x increase in the induced voltage, pointing to a 4x increase in generated power. Given a certain volume, optimizing the offset and relative arrangement of the coil and magnet is the most important design aspect. Once satisfied the coil fill factor should be maximized while allowing for the largest possible magnet.

3.5 DEVELOPMENT OF AN OPTIMIZED GEN 2.5 ELECTROMAGNETIC PFIG

Based on the lessons learned from the Gen 2 implementation discussed so far in this chapter, as well as the electromagnetic optimizations from the last section, a new optimized Gen 2.5 device was designed, implemented and tested. This device has the

same topology and reuses the external enclosures already developed. All of the enhancements are designed to fit the same volume and layout. The same springs are used as well as the same inertial mass weight and geometry. The main developments relate to the FIG. The electromagnetic transducer was changed, different magnets and coil are used, and specialized alignment jigs are used to assemble the FIG and the inertial mass in order to minimize the gaps, while gaining more accuracy in the placement so that frictional parasitics are eliminated.

3.5.1   NEW FIG ELECTROMAGNETIC ARRANGEMENT AND DESIGN

The arrangement of the electromagnetic transducer within the FIG is changed to the perpendicular orientation discussed in Section 3.4. The geometry was built around the availability of parts and predetermined casing space and layout. The largest NdFeB magnet that could fit inside the FIG while still leaving room for the coil had a diameter of 4.75mm and was 2.4mm thick.

The remaining space inside the FIG was used for the coil. The coil was wound on a specially designed and manufactured bobbin. The bobbins were manufactured out of aluminum using a computer-controlled mill. A sidewall thickness of 300μm was achieved. Of course, the sidewall thickness adds to the coil/magnet gap and should be minimized. The aluminum bobbins were unfortunately found to produce an unwanted side effect. Micro-scale topology left on the surface by the milling process penetrated the enamel of the wire during coil winding and produced shorting between the coil and the generator body with impedances ranging from several tens of MOhms to, in some cases, tens of Ohms. This issue was resolved in two ways. The first was to coat the bobbin with a 2-3μm layer of paralyne. This was the preferred solution and resulted in usable devices

however it was slower and more expensive. For this reason future bobbins were milled out of polyvinyl chloride (PVC). While the same sidewall of 300μm was achieved using the milling process, the manufacturing was quite complicated and less reproducible. In addition, as the thickness of the sidewall decreased, the PVC would in some instances warp. This is one of the reasons why the bobbin inner diameter was ultimately increased from 5.11mm to 5.54mm so that this warping did not affect the magnet motion. Figure 3-12a shows one of the bobbins as well as a completed coil.

| (a) | (b) |
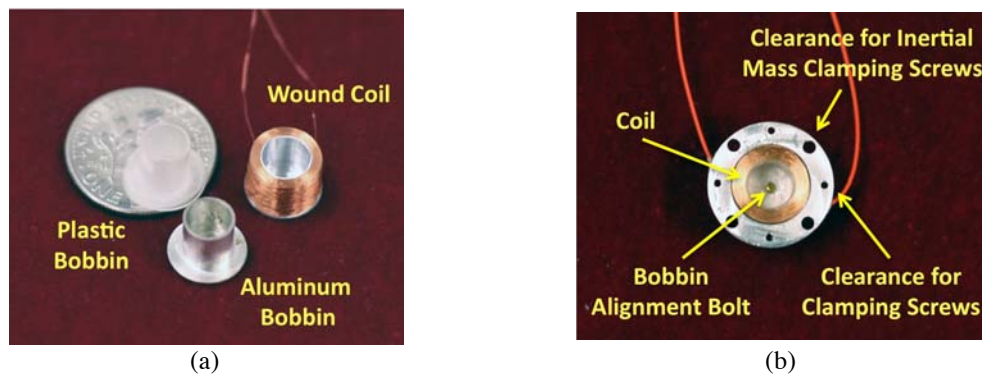
Figure 3-12. a) FIG coil bobbin and finished coil. b) Coil assembled inside FIG.

The coil and bobbin are aligned and fixed inside the FIG using a single 000-120 screw in the center. The clearance for this screw as well as the tap on the FIG casing has to be controlled precisely for proper alignment. While seemingly trivial, because of the double sided processing of both the casing and the bobbin, making these holes centered is not easy. The achieved alignment was +/-50μm. A picture of the assembled bobbin/coil/casing is shown in Figure 3-12b.

3.5.2 SPRING ASSEMBLY

In order to center the magnet with respect to the FIG spring a specialized alignment jig is used, Figure 3-13a. One of the main challenges associated with the new configuration

was eliminating interactions between the power generation magnets and the latching mechanism. Because the magnet is now poled in the direction of the device movement (as opposed to perpendicular in Gen 1/2), it produces a force influencing the latching. For the 2.4mm thick magnets it was found that a spacer of 2mm was needed in order to minimize this interaction. The assembled FIG spring is shown in Figure 3-13b. Due to the spacer, the exact optimal coil/magnet spacing could not be achieved in the given casing while still providing a coil with a significant number of windings. The magnet rests 1mm below where it would optimally be positioned. To study the importance of the position, two coil topologies were manufactured: one that is 3mm tall and one that is 6mm tall. Figure 3-14 shows a photograph of the different FIGs newly developed for the optimized Gen 2.5 PFIG in contrast to the one used in Gen 2.

(a)   (b)
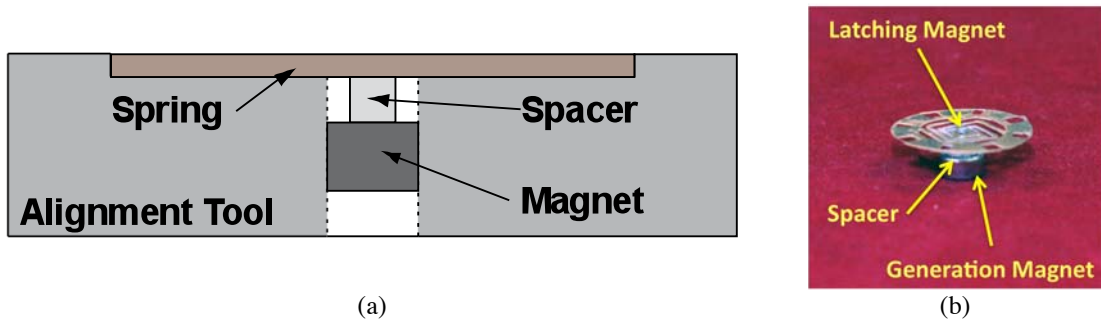
Figure 3-13. a) Spring assembly alignment jig cross-section. b) Assembled FIG spring.
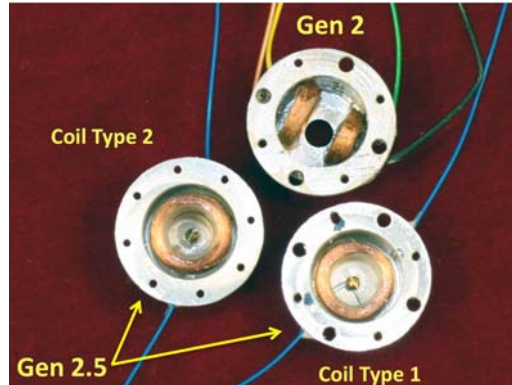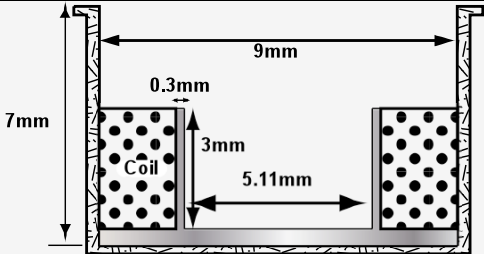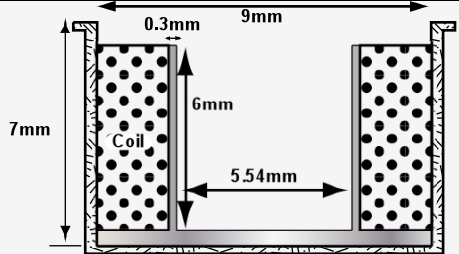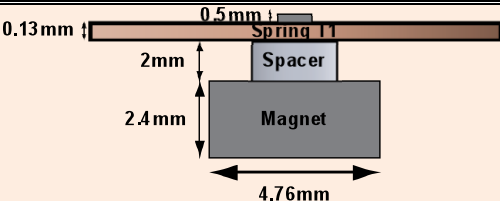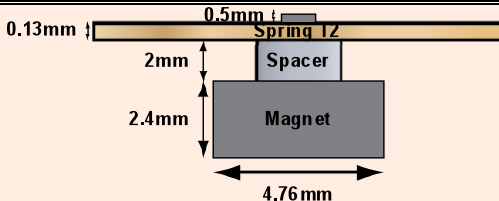
Figure 3-14. Newly designed FIGs for Gen 2.5 compared with layout of Gen2.

3.6 GEN 2.5 TESTING AND RESULTS

Testing of the optimized Gen 2.5 generator was carried out in a similar manner to the previous design. First the FIGs were individually characterized. Their impulse response (open and closed circuit) was recorded and analyzed offline to determine the achieved damping coefficients. After this initial testing was complete, the PFIG was assembled and tested on the electrodynamic shaker using sinusoidal excitation with varying amplitudes and frequency. In summary, there are two types of FIG springs designed for the Gen 2 and 2.5 devices (ST1 & ST2), as well as two new FIG compartments carrying coils with different characteristics (CT1 & CT2). Table 3-4 contains a complete summary outlining the different configurations of the devices, test results from FIG characterization, as well as information about the complete PFIG geometry and parameters.

107

Table 3-4: Summary of Gen 2.5 configurations

FIG Parameters					
Coil Type 1 (CT1)			*Coil Type 2 (CT2)*		
Coil Turns, N	1200		Coil Turns, N	2800	
Coil Resistance	220Ω		Coil Resistance	600Ω	
Spring Type 1 (ST1)			*Spring Type 2 (ST2)*		
Spring Constant, k_f	413N/m		Spring Constant, k_f	612N/m	
Mass, m_f	0.376g		Mass, m_f	0.396g	
Natural Frequency, f_n	165Hz		Natural Frequency, f_n	200Hz	
Magnet Types	NdFeB		Magnet Types	NdFeB	
Actuation Magnet Diameter	1.1mm		Actuation Magnet Diameter	1.1mm	
Actuation Magnet Thickness	0.5mm		Actuation Magnet Thickness	0.5mm	
Generation Magnet Diameter	4.76mm		Generation Magnet Diameter	4.76mm	
Generation Magnet Thickness	2.4mm		Generation Magnet Thickness	2.4mm	
CT1/ST1		*CT1/ST2*		*CT2/ST1*	*CT2/ST2*
Q_T 41.75		Q_T 49.5		Q_T 55	Q_T 57.4
Q_e 83		Q_e 99		Q_e 165	Q_e 200
Q_m 84		Q_m 99		Q_m 82.5	Q_m 67

PFIG	
Inertial Mass, m_i	9.3g
Spring Constant, k_i	150N/m*
Actuation Gap, gap_T/gap_B (ST1)	0.86mm
Actuation Gap, gap_T/gap_B (ST2)	0.35mm
Internal Volume	2.12cm^3
Total Volume	3.75cm^3

*Simulated Value

A direct comparison between CT1 and CT2 reveals that regardless of which spring was used, the electrical quality factor was lower (i.e. higher damping, better electromechanical coupling) for CT1 than for CT2. This result is consistent with the electromagnetic optimization simulations discussed in Section 3.4, which revealed the great importance of the relative positioning between the coil and magnet. While CT1 is likely not optimal due to the geometric constraints, it performs much better than CT2. This is not intuitive because CT2 has more coil windings, has a larger length, width, and volume. CT1 also has a smaller air gap, which while advantageous for the impulse response tests, became detrimental with the larger deflections during PFIG operation, and the result was to have friction once again between the magnet and the bobbin sidewall.

The second noteworthy result is that ST1 has a lower quality factor than ST2 regardless of coil type. The reason for this is covered in more detail in Appendix 1, however the basic principle is that for a given magnetic latching force (and by extension for a given minimum vibration acceleration), the spring constant should be as small as possible while not violating the gap constraint between the inertial mass and the FIG. This allows for the deflection at the instant the inertial mass unlatches to be maximized. A larger deflection in turn has been shown to produce higher electromechanical coupling because it directly translates to increased flux density variation.
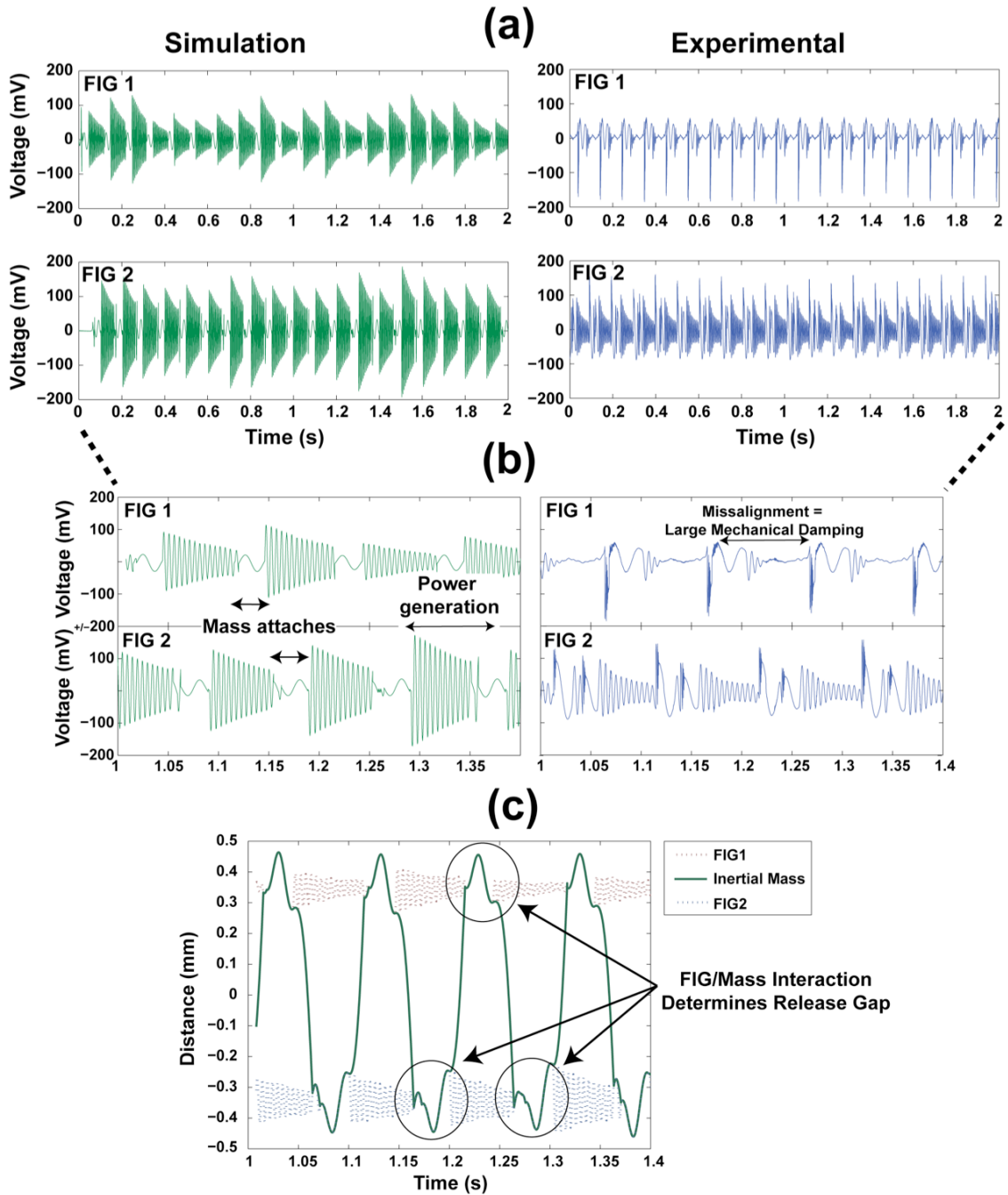
Figure 3-15. Simulated (left side) and experimental (right side) voltage waveforms of from the FIGs showing the PFIG operation from 1g acceleration at 10Hz using CT1/ST2. a) A two second voltage trace. b) Close-up of the simulated and measured voltage waveforms. C) A simulation showing the FIG and inertial mass motion during operation. The complex interaction that occurs during latching/release causes asymmetry of the voltage waveforms during operation.

The Gen 2.5 PFIG is tested with a sinusoidal excitation of 1g at the minimum frequency possible using the Unholtz-Dickie equipment. Having been configured using ST2/CT1, Figure 3-15a-b show voltage waveforms from the top and bottom FIGs. On the left side of the figure, simulation results are shown for a similarly configured device using extracted damping parameters from Table 3-4. On the right side, are the measured waveforms recorded during testing. Figure 3-15b is a zoomed-in view of the waveforms in Figure 3-15a. The simulation results track the experimental performance quite closely. One can see that the decaying oscillations for both the experimental and measured waveforms reach a max/min of +/-100mV$_{ppk}$. Of course, the measured waveforms have voltage spikes each time the inertial mass latches and makes contact, as well as some ringing. The reason for this can be seen in Table 3-4, which shows drawings of the assembled FIG springs. The actuation magnet actually sits above the FIG spring and above the mechanical stopper (see Figure 3-1a). This means that as the inertial mass makes contact it can rapidly compress the FIG spring and suddenly stop when it reaches the mechanical stopper. As the inertial mass stops, the FIG can separate, provided the right conditions, and this results in the ringing in the waveform. The complete effects of the mechanical stopper, as well as the ability to separate into three degrees of freedom after reaching it, are not modeled accurately in the simulations. All of these complex interactions are approximated using an inelastic collision as was discussed in Chapter 2. Nonetheless, these effects are secondary as far as the system is concerned.

The voltage traces Figure 3-15a-b show that the FIGs are not working symmetrically. Heavy mechanical damping in FIG1 causes the large asymmetry in the measured results. This is likely caused by friction between the magnet and the inner sidewall of the coil

bobbin. However, one can see asymmetry between the overall waveforms both from the measured results and the simulations. The reason for this non-symmetric behavior is explained by Figure 3-15c, which shows a simulation of the FIG and inertial mass movement during operation. The middle curve represents the inertial mass. You can see that the release point is heavily depended on the overall system dynamics, the magnetic interaction near the point of release, as well as immediately after. So the gap at which the normal force on the FIG becomes zero will vary each cycle and the FIGs will operate asymmetrically.

(a)   (b)

(c)   (d)
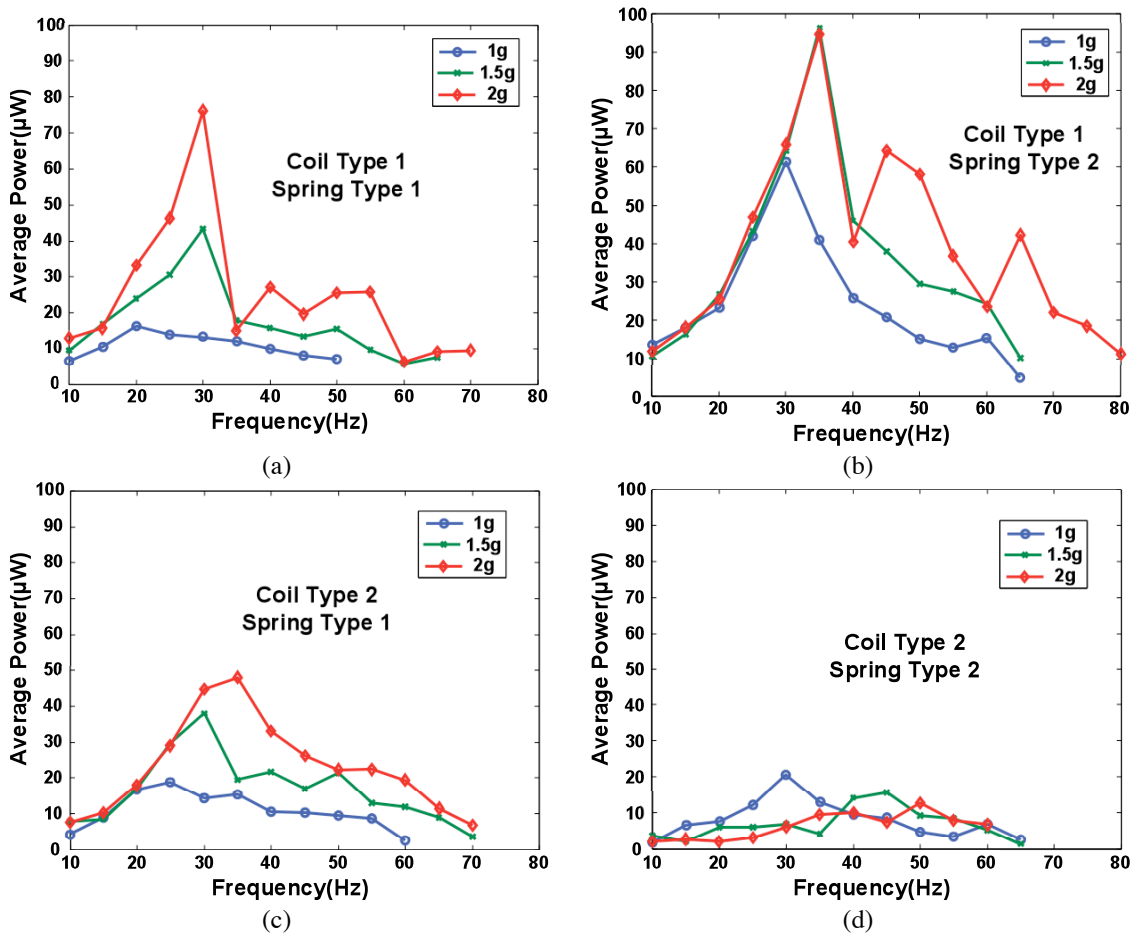
Figure 3-16. Measured frequency response of the PFIG generator at three different acceleration levels for a) CT1/ST1, b) CT1/ST2, c) CT2/ST1, and c) CT2/ST2.

The performance of the PFIG, configured using the various spring and coils types was evaluated over a range of frequencies and accelerations. The minimum acceleration of the PFIG is 1g and the maximum acceleration of the shaker table is 2g. The frequency of the vibration is changed from 10Hz up to when the PFIG ceased to operate as a parametric generator. The maximum average power that could be generated from a 1g vibration at 10Hz was 13.6μW. This is a 2x improvement over the Gen 2 device discussed earlier in the chapter. Additionally, because of an improved gap, alignment, and assembly the dynamics of the PFIG have been improved to the point where it is able to function over a range of 60Hz. Defining bandwidth as the -3dB reduction in power, if the center frequency were considered to be 10Hz, the device shown in Figure 3-16b can be considered to have a bandwidth of 55Hz. As expected, the devices utilizing coil type 1 outperform both of the devices utilizing coil type 2 as can be seen comparing Figure 3-16a-b with Figure 3-16c-d. The interesting result is that the device using spring type 2 in Figure 3-16b performs better than the device using spring type 1 shown in Figure 3-16a.
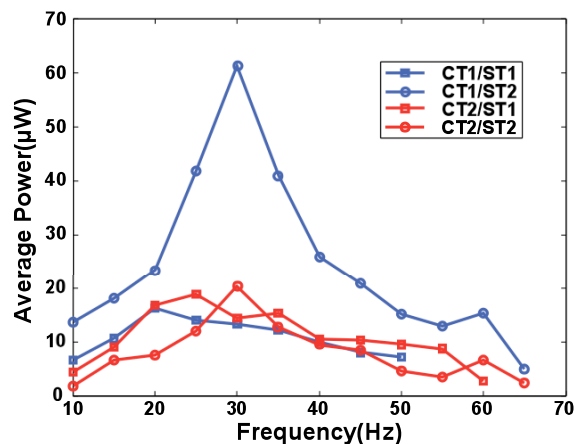
Figure 3-17. Measured frequency response of the PFIG generator for all four configurations, compared at the same acceleration level of 1g.

Figure 3-17 shows a direct comparison between the measured responses of all 4 configurations. Looking at the CT2 plots we can see that ST1 outperforms ST2 as would be expected. The reason this does not happen with the devices using CT1 is that one of them is not functioning correctly. Although both device using CT1 have large mechanical damping due to friction, as was shown in Figure 3-15, the effect is particularly bad in the CT1/ST1 device. In fact, 72% of the power shown in Figure 3-17 is generated by only one FIG. ST1 is particularly susceptible to these problems because those springs are thinner and have more closely aligned resonant modes. Torsional motion can be induced very easily. Combining the effects of 1) misplacement of the actuation magnet, which can causing latching/release forces out of axis, and 2) the large eccentric mass that the spring assembly supports (power generation magnet), it is easy to see why this happens. An additional complication with the ST1 devices is that they have a larger inertial mass/FIG gap ($gap_{T,B}$). A side effect of the lower spring constant is that a larger $gap_{T,B}$ had to be used for this particular design. As already discussed there is interaction between the power generation magnet with the latching mechanism, and because of the more compliant design, the minimum acceleration needed for operation with ST1 changed. A larger gap allowed testing at 1g for direct comparison. The gap can only be tuned with large granularity, since it involves changing physical spacers in the inertial mass assembly. Thus it is larger than it needs to be and it contributes to altering the dynamics of the entire system.

3.7 DISCUSSION

The performance of the Gen 2 and Gen 2.5 devices exceeds in many respects the state of the art in vibration scavenging technology. However, clearly a number of

improvements can be made to future designs of the PFIG architecture. A number of these optimizations are discussed in this section.
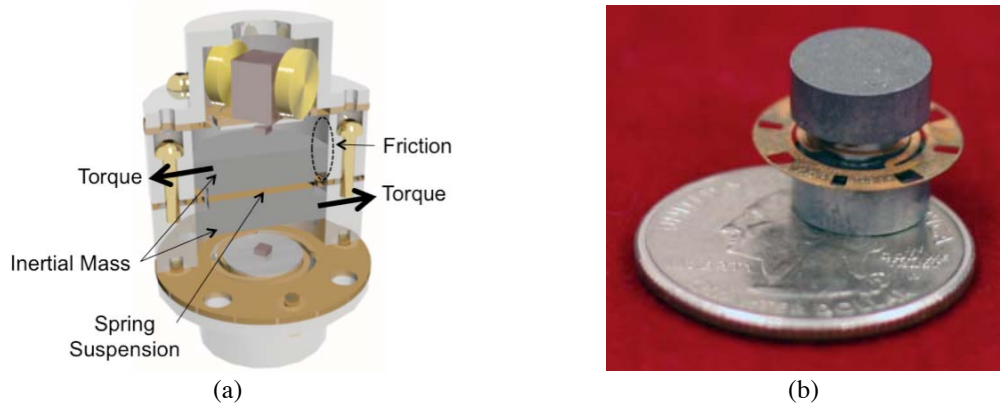
Figure 3-18. a) PFIG cutaway showing the placement of the components, including the inertial mass. Because of its eccentric center mass placement, torsion is easily induced in the suspension, causing friction against the casing sidewall. b) Photo of the inertial mass assembly.

3.7.1 STRUCTURAL IMPROVEMENTS

There are a number of structural improvements that can be made to the PFIG architecture in order to improve the system dynamics, and produce higher output power. A significant amount of energy is being lost to frictional damping. This energy loss both alters the system dynamics and also, when it happens within the FIG, is a direct loss mechanism of the electrical to mechanical conversion mechanism. Figure 3-18a shows a cross-section of the Gen 2 device. One can see the inertial mass is split into two sections with the spring placed in the middle. This design is quite susceptible to torsional motion being induced in the very thin spring supports; complicated by the fact that the PFIG is tested in the horizontal direction (on its side). A photograph of the inertial mass assembly is shown in Figure 3-18b, which shows the scale of the components.

The same issue is present in the design of the FIG spring assembly. The magnet is positioned a certain distance away from the spring. This eccentric mass predisposes the

FIG springs to out-of-axis bending motion. This can happen if the applied force is not exactly centered, which in this design is certainly the case, due to the variability in the motion of the inertial mass as well as possible misalignment in the latching magnet placement.

A related issue is the alignment and placement of the FIG spring relative to the coil and other FIG components. In the current design the spring rests on the top of the FIG casing, however the bolts that clamp it down are on the bottom. This makes alignment of the spring relative to the coil quite complicated. Originally it was thought that the alignment could simply be performed using the clearance holes for the bolts, with the bolts acting like alignment pins, however the tolerances of the various components (especially the ones manufactured by non-lithographical means) made the resolution of this alignment scheme very poor.

These structural issues, although unfortunate, can easily be remedied in the future. Suspending the inertial mass and the FIG magnet from both sides will greatly reduce out-of-axis and bending motion. Alignment of the FIG components can also be improved quite trivially, by simply having the clamping mechanism on the top, such that alignment and clamping can be performed together.

3.7.2 IMPROVED POWER CONVERSION AND EFFICIENCY

The improvements in the electromagnetic conversion system of the Gen 2.5 system led to an improvement in the damping constant by about 17%. If the geometric limitations were not present, and the same FIG case was not reused, perhaps this could have led to a 50-100% improvement. Even a factor of two improvement means going from ζ_e of 0.005 to 0.01. However, even this damping ratio is too low and does not allow the energy to be

116

converted efficiently. A simulation showing average power as the damping ratio is increased (1g acceleration at 10Hz), is shown in Figure 3-19. There is a significant amount of variability in the simulation because the number of latching cycles is limited to 10 per ζ_e simulation point in order to save computation time. However, the trend is clear; increasing ζ_e improves the power output. Because of the non-resonant operation, as well as the transfer of energy from the inertial mass to the FIG, the PFIG is not limited in terms of ζ_e in the same way that a resonant generator is. In fact, the mechanical parasitics should be reduced to an absolute minimum, while ζ_e is increased as much as possible. Of course there are limits on this and they will be discussed in the remainder of the section. Nonetheless, it is highly unlikely that the ζ_e limitation can be met, especially in a confined volume.
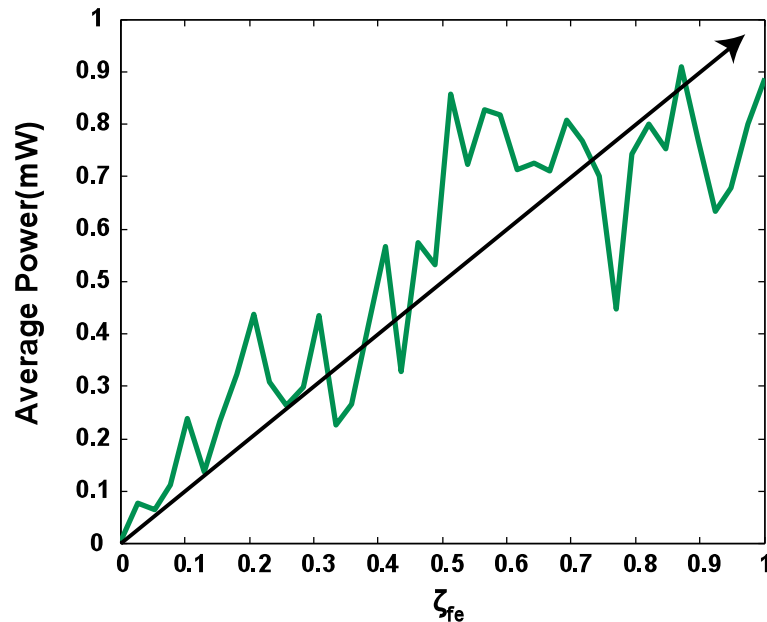
Figure 3-19. Simulation showing average power vs. electrical damping ratio of the FIG.

Increasing ζ_e is not a trivial proposition. More complicated magnetic circuits will have to be developed which confine and route the flux [44, 123] as opposed to letting it spread

out, as is the case for the PFIG implementations of this chapter. In order to further improve the damping ratio, solutions such as combining transduction mechanisms can also be explored.

3.7.3 MINIMUM ACCELERATION AND BANDWIDTH CONSIDERATIONS

The PFIG generator undergoes several distinct modes of operation as shown in Figure 3-20. As the frequency is increased the generator transitions from a velocity limited region, to one where its operation is limited by the physical constraints of the design ($gap_{T,B}$) as well as the latching force, and finally to a cutoff region where the system is too slow to respond to the incoming vibrations. These regions are highlighted in Figure 3-20 and can be identified in both the simulated response curve as well as the measured data. Additionally, the average release gap, or the distance the FIG is actuated before it detaches from the inertial mass is also shown. This is an average over the entire data set of a particular frequency, because variations will occur due to the dynamic behavior of the system. In the velocity limited region, the system response is dictated by the increasing frequency (and hence velocity). As the frequency goes up, little by little the inertia of the FIG increases and counteracts the spring force to push the release gap further and further up. The first resonant peak amplifies this effect by providing more and more energy for the system. The first resonant peak is determined by the inertial mass/suspension natural frequency. Past this first resonance, the effect of the FIG inertia, pushing the release distance higher and higher, saturates, and the unlatching point becomes limited by the FIG spring force exceeding the magnetic latching force. The average power drop is a result of the inertial mass not being able to track the vibration. This means that rather than actuating each FIG once per period, this number becomes

118

lower; its value varies depending on the transient dynamics of the system. The onset of the final phase is governed by the natural frequency of the combined FIG/inertial mass resonator, f_{nc}, which is approximately 45Hz for the system in Figure 3-20. The force transmissibility [125] quickly starts to decrease, and eventually the deflection makes it so the normal force cannot reach zero. Another possible outcome is that the inertial mass releases the FIG, but it can never deflect enough to latch on again.
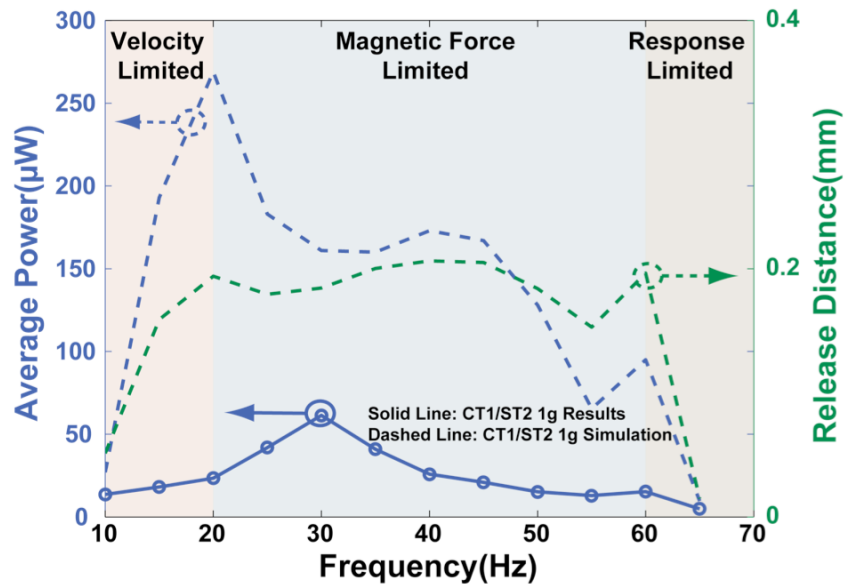
Figure 3-20. Frequency response comparison simulated system (dotted lines) and the performance of CT1/ST2 at 1g. Plot also shows the release distance as a function of frequency.

Optimizing the PFIG system to meet certain technical specifications becomes very challenging because of the many parameters and the dynamics of the system, and can only be performed using numerical optimization techniques. In most realistic applications the technical specifications are clear: extremely small accelerations with the highest possible bandwidth. However, meeting both of these requirements is mutually exclusive in more ways than one. For a given latching force, to achieve operation at a low acceleration requires a larger inertial mass. A larger inertial mass, on the other hand decreases f_{nc} and decreases the bandwidth. To counteract this, one might increase the

inertial mass spring constant, or FIG spring constant, however doing either of those will result in a smaller release distance and lower power output.
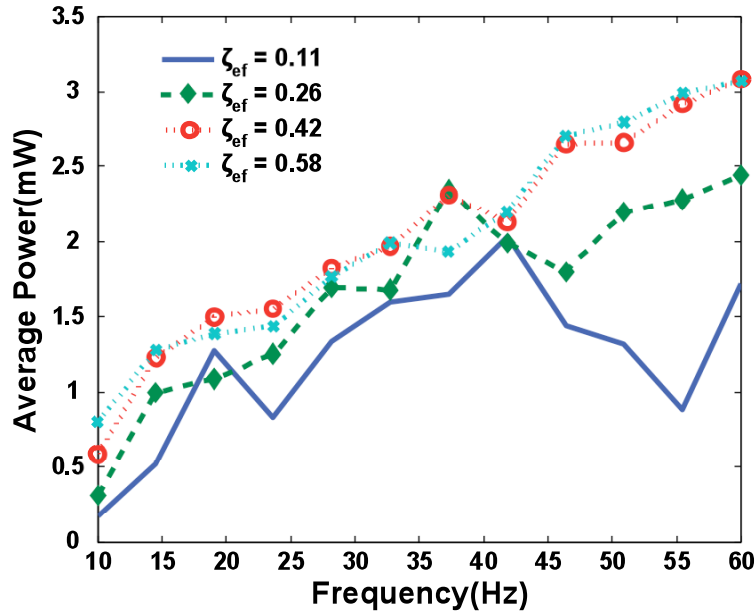
Figure 3-21. Simulation showing average power vs. electrical damping ratio of the FIG.

The one sure way of increasing the bandwidth and the power generation of the PFIG is to increase the electrical damping. Figure 3-21 shows a simulation demonstrating this. Of course, this is, for lack of a better term, "cheating." The bandwidth of the PFIG is not increasing; the mechanical performance remains the same. However, the amount of energy coupled into the FIGs largely goes to waste at higher frequencies, because before the oscillation of the FIG can decay, the inertial mass latches on again. By increasing the electromechanical coupling, more of the energy can be converted before the next cycle. Even though the FIG does not actuate every cycle at higher frequency, there are enough latching events to keep pushing the power output higher. Once again this evidence supports the need for sophisticated electromechanical transduction for proper PFIG operation.

Table 3-5: Summary of generated power by Gen 2.5 PFIGs at 10Hz

	CT1/ST1			CT1/ST2			CT2/ST1			CT2/ST2		
	1g	1.5g	2g	1g	1.5g	2g	1g	1.5g	2g	1g	1.5g	2g
Avg. Power (μW)	6.65	9.6	13	13.6	10.7	11.9	4.4	7.9	7.7	1.7	3.6	1.94
Peak Power (μW)	189	399	449	163	294	460	163	185	261	71	101	123

3.8 GEN 2-2.5 PERFORMANCE

The power output of the Gen 2.5 device is summarized in Table 3-5. Due to the nature in which the PFIG operates, producing decaying oscillations, this chapter has mainly dealt with average power over large samples of collected data, in most cases over 5 seconds. However, the peak power levels generated during operation are also important and are included in the table. Most authors benchmark their device's peak power generating capability. That makes sense if the devices were operating resonantly and producing symmetric periodic output voltage waveforms. Then, the peak power is close enough to the RMS power, and this benchmarking is appropriate. In many other cases, including the PFIG, it would be more appropriate to use average power, or perhaps even some metric that computes converted energy per cycle.
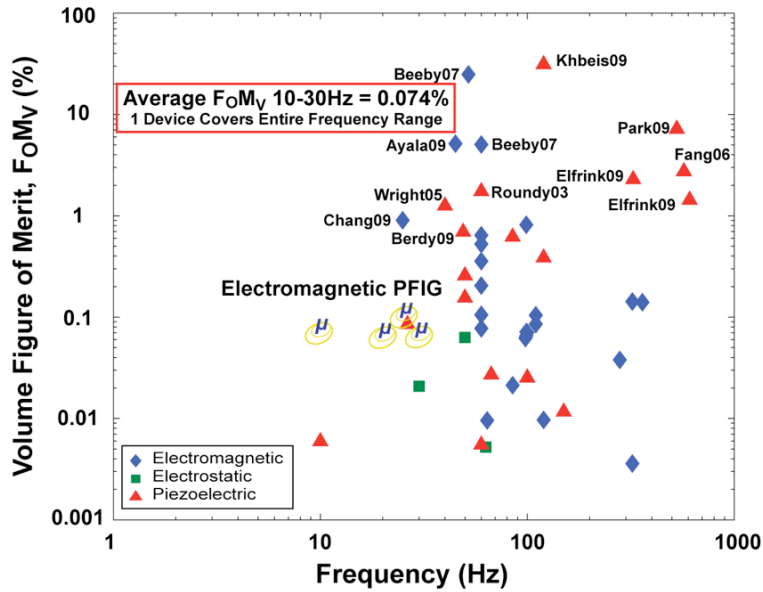
(a)
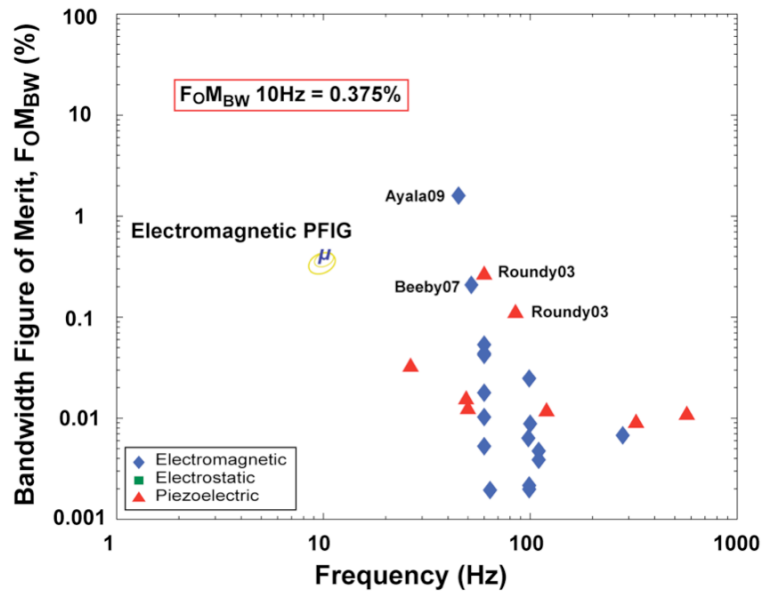
(b)

Figure 3-22. a) Volume Figure of Merit (FoMv) comparison of the PFIG generator to the state-of-the-art in vibration scavengers. b) Bandwidth Figure of Merit (FoMBW) comparison of the PFIG generator to the state-of-the-art in vibration scavengers.

The Gen 2/2.5 generator is benchmarked to the state-of-the-art in vibration scavengers using its average power performance. The Volume Figure of Merit (FoMv), Eq. (1.34), is computed for a few of the recorded operation frequencies and it is shown in Figure 3-22a. The PFIG generator constituted a significant improvement in efficiency for low-

frequency (<20Hz) scavengers. The FoMv metric compares the power output to that of an idealized vibration generator, of the same volume, working under the same conditions. The large operating range of the PFIG is unprecedented. This is not an aspect which is illuminated by the FoMv plot. For this reason the Bandwidth Figure of Merit (FoMBW), Eq. (1.35) is computed and plotted along with the state-of-the-art in Figure 3-22. This metric is simply the FoMv multiplied by the 3db bandwidth as a fraction of the center frequency. This figure better captures the performance aspects of the PFIG as it takes into account its bandwidth. The center frequency used for the calculations is the main frequency of interest, which in this case is the lowest frequency at which the PFIG can operate. It should be noted that bandwidth data is not readily available in publications. As discussed in Chapter 1, for many of the published works, the bandwidth of the generator was estimated from publication figures and other data, in each case giving significant benefit of the doubt to the device in question. This metric is very nice because it normalizes to the center frequency of operation. Of course, the higher the center frequency, the easier it is to make large bandwidth adjustments with small parameter variation. Achieving a wide bandwidth at lower frequencies is much more challenging. The Gen 2/2.5 PFIG has the best FoMBW of all vibration harvesters published to date, except for one that uses active frequency tuning.

3.9 CONCLUSION

This chapter reported on the design, fabrication, and testing, of the first miniature PFIG power scavenger. This generator is ideal for operation in environments with low frequency, large displacement vibrations. The design of the PFIG was discussed in detail. After an initial prototype was developed, a number of improvements were made, most

notably in the electromagnetic transduction topology. A discussion regarding the optimization of the coil/magnet arrangement was carried out. Based on the initial prototype, and incorporating the improved FIG topology, four new generators were built and tested. These four PFIGs had different configurations, and the merits of each was compared and discussed. The average power that could be generated from an input acceleration of 1g applied at 10Hz was 13.6μW. The device is able to operate over a large frequency range and has a 3db bandwidth of 55Hz. A Volume Figure of Merit of 0.068% is achieved at 10Hz, and a Bandwidth Figure of Merit of 0.375% with a center frequency of 10Hz. These results set the state-of-the-art in the field when considering very low (<20Hz) vibration scavengers. In fact, the Volume Figure of Merit achieved is an order of magnitude higher than any other published result for a miniature self-contained generator, and the bandwidth performance is one of the best ever reported. The measured results were compared with the dynamic computer modeling of the PFIG system, and shown to have high agreement. A number of future possible improvements were identified. Two important categories exist: 1) a number of structural changes for better mechanical design have been suggested, and 2) a significant improvement in the electromechanical transduction system is needed in order to achieve electromechanical coupling that is at least an order of magnitude better.

Chapter 4

PIEZOELECTRIC PFIG

Up to this point the PFIG devices were all implemented utilizing electromagnetic transduction. In many ways, the PFIG type of vibration generator is ideal for piezoelectric materials because of its fixed and limited internal displacements. Typically piezoelectric materials are brittle ceramics that cannot withstand large deflections. In addition, it became apparent in Chapter 3 that higher electrical damping needs to be achieved to increase efficiency. One potential way of achieving better electromechanical coupling in a confined area is by using piezoelectric materials. This type of transducer can easily be integrated with an electromagnetic one, providing an even higher damping force. This chapter presents the design, fabrication, and testing of a piezoelectric PFIG. The design of such a transducer is explored, and a new PFIG is fabricated and tested.

4.1 PIEZOELECTRIC PFIG DESIGN

The goal of this study is to demonstrate the feasibility of implementing a PFIG device while using piezoelectric transduction. For this reason, the system level configuration that was designed for the electromagnetic Gen 2 and 2.5 devices is reused and modified as needed to accommodate the Gen 3 piezoelectric components. Figure 4-1 shows a rendering of the Gen 3 PFIG. It can be seen that the majority of the hardware is reused

from before, including the inertial mass, the associated suspension, and the outer casing for the generator. Only the FIGs are changed. The piezoelectric FIG is designed as a clamped-clamped bimorph beam operating in the 31-mode. While piezoelectric materials typically offer higher coupling coefficients in the 33-mode, where displacement is coaxial to the electric field, the 33-mode operation results in small deflections and very high resonance frequencies because piezoelectrics are very hard materials. For this reason most piezoelectric generators operate in the 31-mode where the displacement and the electric field are perpendicular to each other. This mode of operation offers weaker coupling coefficients: however, larger strains can be achieved with a weaker force because of the more compliant configuration. The piezoelectric material is typically used in conjunction with a leveraging mechanism, such as a cantilever beam, which can turn large deflections at its tip into high strains along the surface (maximum at the base).

Figure 4-1. Rendering of the piezoelectric PFIG, showing the layout and the different components.

The piezoelectric FIG is designed as a clamped-clamped beam rather than being free in the middle, in order to keep the orientation of the latching magnet rigid. That way the

connection between the inertial mass and the FIG is reliable. The configuration of the device can be seen in Figure 4-2. Clamping the beam on both ends makes it even more challenging to generate compliant structures out of ceramic piezoelectric materials. Since the spring constant is inversely proportional to the cube of the length of the structure, lengthening the beam is the single best way to reduce the stiffness. The challenge of creating a long beam within the confined generator area, previously defined in the Gen 2 implementation, is solved using a spiral geometry. This way long beams can be generated within a small footprint.
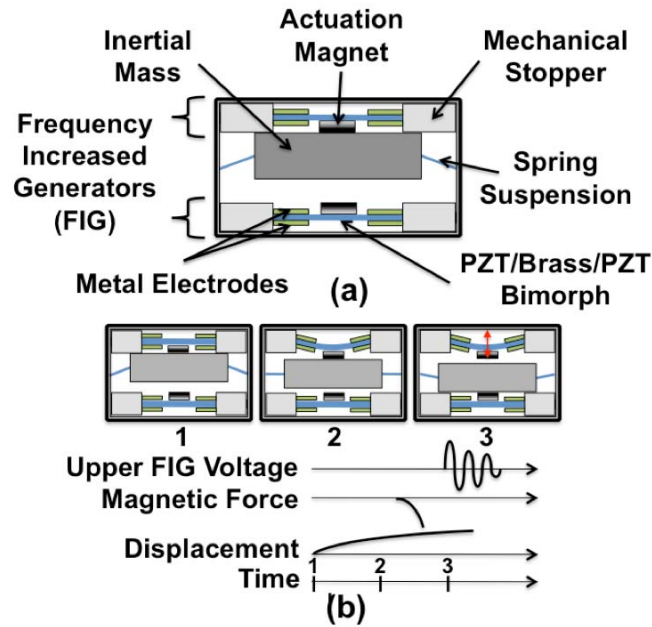
Figure 4-2. Conceptual illustration of the piezoelectric PFIG.

4.1.1 FIG DESIGN AND OPTIMIZATION

For the purposes of this study a readily available commercial lead zirconate titanate (PZT) bimorph is selected. The bimorph is made by Piezo Systems and it consists of two PZT-5A4E sheets bonded above and below a brass shim. Using thin film piezoelectric

material was considered because lithographically based fabrication would make the curved spiral shapes easier to manufacture. However, bulk PZT has markedly better piezoelectric properties than the best thin films reported in literature. For this reason, a bimorph based on bulk material was chosen.
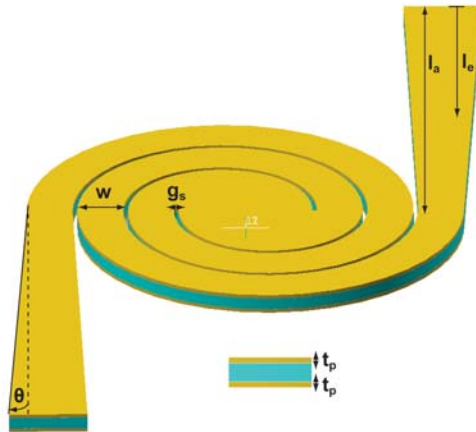
Figure 4-3. Illustration showing the FIG piezoelectric spiral parameters.

The spiral shape that was developed can be seen in Figure 4-1 and Figure 4-3. It has two arms that are fixed to the base. The two arms are designed with a linearly increasing cross-section, widening as the arms move from the spiral toward the clamped end. This way the high stress concentration at the clamped end is alleviated [94]. This improves the reliability, and the film stress is more evenly distributed across the spiral arms, allowing more of the PZT material to be utilized for energy conversion. The spiral PZT bimorph is a complex structure to analyze analytically. In order to design the FIG spiral, coupled field finite element modeling is performed using ANSYS. The structure is optimized to fit within the existing generator dimensions while generating the maximum amount of power per maximum force that can be applied by the inertial mass. In order to keep the dynamics of the PFIG system similar to the Gen 2 implementations, the stiffness of the PZT spiral should be in the range of 400-500N/m.
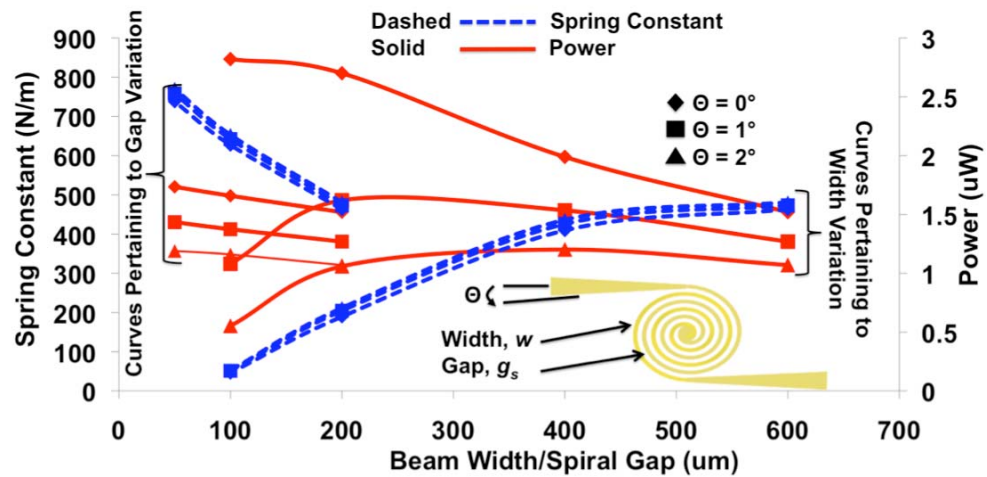
Figure 4-4. Simulated (ANSYS™) behavior of the PZT spiral FIG generator as a function of beam width, gap between the spirals, and arm theta (Θ). Right axis is used to show spring constant variation and left axis shows the predicted output power.

The influence of a number of geometric properties is investigated using FEM simulations. Those include the width, w, the arm length, l_a, the thickness of the PZT layers, t_p, the number of turns, n, the gap between adjacent spiral turns, g_s, and the electrode placement, l_e. An illustration of the geometry of the piezoelectric spiral is shown in Figure 4-3, which shows the various parameters. A fixed force in the center, mimicking the one applied by the inertial mass, is used to simulate FIG actuation. In these simulations all but one of the variables are held at a constant baseline while the influence of the variable under study is determined. In Figure 4-4, the influences of the spiral gap, g_s, and beam width, w, are shown. The solid red curves go with the power axis on the right hand side, and the dotted blue curves go with the spring constant axis on the left hand side. As the gap increases, the spring constant naturally decreases, because the overall spiral length increases (the number of turns is kept fixed). The power is shown to decrease with an increasing gap. The more compliant structure produces less stress in the arms where the electrodes are located, resulting in less charge. While deflection for a

129

constant force increases, most of the deflection occurs in the middle spiral area. The width, on the other hand, has a more complex effect. When the width is increased, the spring constant of the structure initially increases. The reason for this is that spring constant is linearly proportional to width for this particular type of bending moment. However, the spring constant plateaus with further increases to the width because the overall structure tends to become larger. The larger structure means the beams are longer, which counteracts the influence of the increased width. A wide range of values was studied; therefore one can observe that the compliance in the structure initially generated very low stress. Consequently, the stiffness and the power increased hand in hand in this regime. However, an optimum point exists, because the increasing spring constant ultimately limits the beam deflection. Therefore, further increases in stress are prevented, and the power begins to drop. The widening of the arm cross-section is modeled by Θ, the angle made by the spiral arm with its centerline. In all cases the power drops as Θ increases because of a reduction in the maximum stress in the beam.
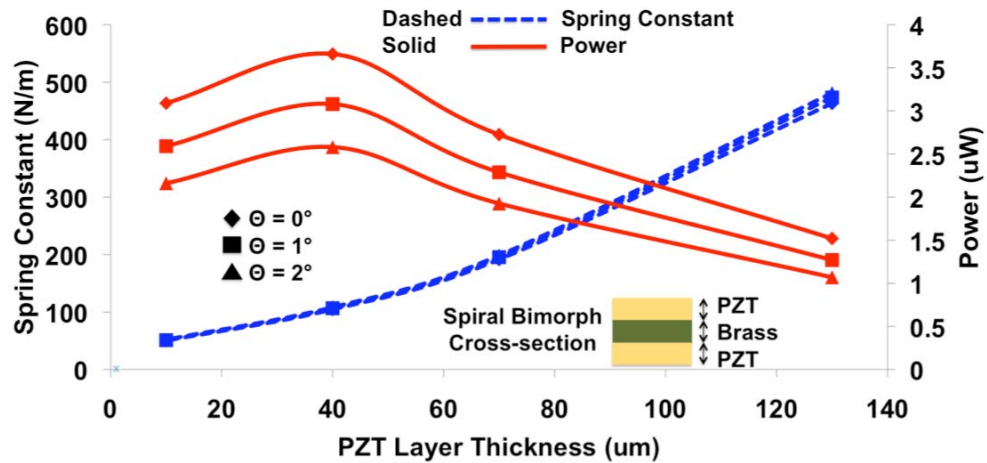
Figure 4-5. Simulated (ANSYS™) behavior of the PZT spiral FIG generator as a function of the PZT layer thickness. Right axis is used to show spring constant variation and left axis shows the output power

The thickness, t_p, of the PZT layer is a very important parameter and its influence is shown in Figure 4-5. One can see that an optimal thickness exists, once again caused by the interplay between the spring constant, the stress, and the deflection. When the structure is very compliant increasing the thickness helps to increase the power output by contributing to higher stress. However, this effect is eventually counteracted by the decreased deflection. Figure 4-6 shows the stress distribution along the two arms of the spiral as the cross section is changed. As expected, when the arm becomes gradually wider from center to base, the stress distribution becomes more uniform, making the FIG more reliable. The reliability in the arm is important, because the FIG is expected to have large deflections during operation, and alleviating the stress concentration at the base will help with the longevity of the device.
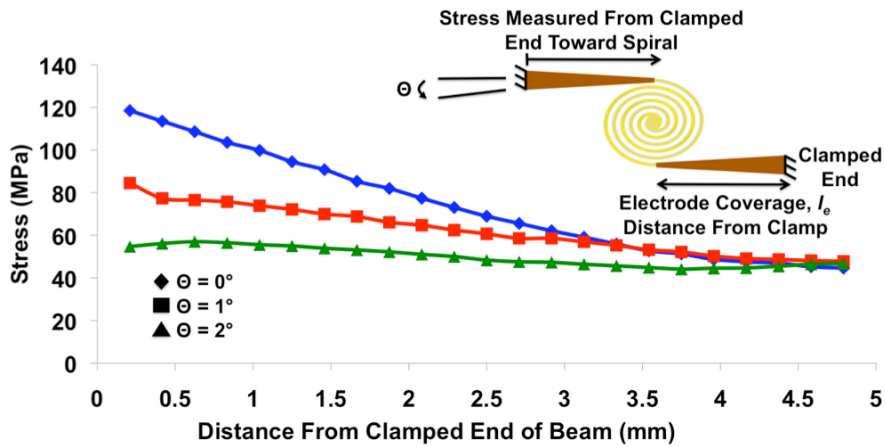
Figure 4-6. Simulated (ANSYS™) stress on the clamped ends of the PZT spiral FIG as a function of the distance from the clamp. A theta (Θ) of 1 is incorporated into the final design to reduce stress and to improve reliability.

A very important issue that needs to be considered when dealing with a spiral design is the stress/strain distribution within the structure. Figure 4-7a shows the simulated stress distribution within the PZT spiral, and Figure 4-7b shows the expected vertical strain distribution. It is apparent from the figure that the strain changes from positive to

negative at different locations along the structure. This can be explained by considering how a spiral structure will deflect. As the spiral moves the center region will act as a fixed support inducing bending in the arm. Additionally, there will be a torsional motion associated with the vertical deflection. The negative and positive strain values produce both negative and positive potentials along the surface of the structure. If an electrode were placed from the support all the way to the center in order to collect charge, this would lead to a charge cancelation, or averaging. That would ultimately reduce the power generated by the FIG. Due to the symmetric distribution of the negative and positive strain, conceivably electrodes could be patterned throughout the spiral to collect the entire negative charge in one location and the positive charge in a different location. Such an electrode placement scheme would complicate the fabrication and alignment process for benefits that are not necessarily justified. Most of the charge that is generated will occur at the base and along the long arm. For this reason an electrode was only placed along the straight arm such that $l_a=l_e$.
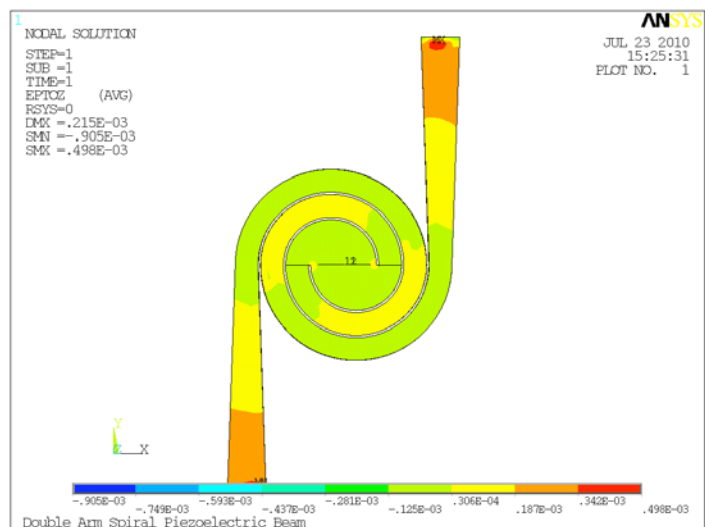
Figure 4-7. Simulated (ANSYS™) z-axis component of strain as the piezoelectric spiral deflects due to a force applied at the center.

Taking into account the modeling results, and making adjustments in order to fit the required area, the final spiral design has two turns, w=300μm and a gap of g_s=250μm. The gap is dictated by fabrication considerations, in that sufficient space needs to be left to machine the structure. In order to keep stress linear, and for structural rigidity reasons, the arm length is set to 5mm and a moderate tapper is added, where Θ=1.5°.

4.2 DEVICE FABRICATION AND ASSEMBLY

Since most of the PFIG components are exactly the same as the Gen 2 design their detailed fabrication will not be covered in this section. Rather, the manufacturing of the FIGs will be discussed. As was shown in Figure 4-5, the optimal thickness of the PZT layer for these FIGs is 40μm. In order to thin down the 130μm original PZT layer thickness, a lapping tool is used. The piezoelectric material is diced into squares that can fit within the PFIG enclosure. These samples are adhered to a metal disk using hot wax. This disk is then placed directly on the grinding tool. A 3μm diamond slurry is used for lapping. There are a few points of emphasis regarding this process. The first is that during the wax-based mounting, the PZT pieces have to be weighed down while the wax solidifies. If the surface of the PZT is not parallel to the surface of the metal disk the lapping can be very non-uniform. Other mounting options were also explored, including first bonding the PZT sample on a wafer using photoresist, and then mounting the wafer on the retention jig. However, photoresist, using various recipes, was found to have inadequate strength to retain the sample on the jig during the lapping process. The second point of emphasis is that regardless of the uniformity of the bond, the PZT sample will typically still be ground down non-uniformly. The retention jig is much larger, intended

133

for silicon wafers, and it cannot distribute the force well over the small piece in the center. Many alternatives have been explored including lapping bigger pieces, multiple pieces, etc. While this process is not controllable to the desired degree, it was the only best one available at the time of fabrication.

After the lapping process is complete the samples need to be thoroughly cleaned. They are first wiped using IPA while the wax, which is heated to release the sample, is still liquid. After removing them from the retention jig, they are soaked in acetone and in IPA for several hours in each. The PZT samples are finally rinsed in DI water and dehydrated on a hot plate. Next, metal has to be deposited for the electrodes. Metals do not adhere well to PZT. It was found that a thick combination of evaporated Cr/Au 500/5000Å would provide sufficient strength and adhesion.

The piezoelectric bimorph is then machined using a Ti-Sapphire femto-second laser in order to create the spiral pattern. The laser has a wavelength of 780nm, with a 150fs pulse duration and a 1kHz repetition rate. In order to enable complex shape patterning and automated machining of several samples in a serial process, the pieces are placed on a computer controlled XYZ-Φ motion stage, on which the laser beam is focused through a shutter. Compared to other bulk PZT substrate patterning technologies, femto-second laser machining provides a smaller feature size with a high aspect ratio, minimum undercut, and less damage to the material.

NdFeB magnets are adhered to the spiral center using cyanoacrylate. Electrical connections are made to the spiral arms by first isolating a pad at the base of the beam by physically severing the connection to the remaining metal on the surface of the sample. Wires are then bonded to this pad using conductive silver epoxy. In order to isolate the

spiral arms and to define the metal electrode, the diagnostic laser on a Suss Microtec probe station is used to trim the spiral arm and sever the metal connection where needed. The FIGs are isolated on either side from the metal PFIG casing by placing a specially machined styrene spacer. Holes machined in the FIG PZT substrate are used to align the spiral and to clamp it along with the PFIG lid. Figure 4-8 shows photographs of the assembled PFIG as well as the machined PZT spiral FIGs.
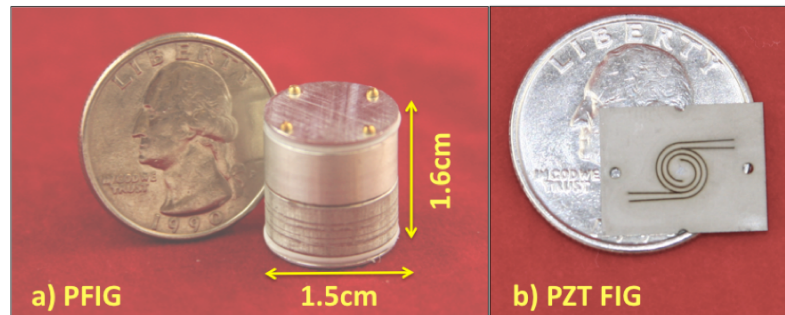
Figure 4-8. a) Photograph of the assembled PFIG generator. b) A photograph of a single PZT spiral Frequency Increased Generator (FIG).

4.3 GEN 3 TEST RESULTS

A summary of the fabricated devices is shown in Table 4-1. As was shown in Figure 4-5, the thickness of the PZT layer plays an important role in terms of increasing the power. Two FIGs are built, one where a 40μm thickness was targeted, and one with a full thickness bimorph in order to have a control sample. A minimum feature size of 250μm was expected from the fabrication and the laser ablation. In order to accommodate this feature size, a gap of 250μm was built into the design. The laser ablation process leaves a damaged area at the edge of the sample. The extent of this damaged area was not known, and it is important that this area not constitute a majority of the beam. Considering the structural integrity of the spiral, a 300μm width value was considered safe and was

designed into the FIG. However, it turned out that a much smaller gap could be achieved using the laser cutting process. In fact, the gap achieved was 50μm. This means that the width of the spiral beams increased by 200μm. Width measurements were taken at a few locations and they were in the range of 470-500μm. Unfortunately, these dimensions resulted in much stiffer structures for both the thick and the thin spiral PZT FIGs. The second fabrication related complication, which was already touched upon, was the uniformity of the lapping process. While a thickness of 40μm was sought for each side of the bimorph, the thicknesses that were achieved were in the range of 40-70μm, and they varied within the spiral itself. The combination of increased width and variable thickness contributed to a 2-3x increase in the resulting stiffness of the FIG.

Table 4-1: Summary of Gen 3 piezoelectric PFIG configurations

FIG Parameters			
Thick PZT Layer Spiral FIG		*Thin PZT Layer Spiral FIG*	
Spring Constant, k_f	4637N/m	Spring Constant, k_f	1370N/m
Mass, m_f	0.137g	Mass, m_f	0.093g
Natural Frequency, f_n	926Hz	Natural Frequency, f_n	611Hz
PZT layer thickness, t_p	130μm	PZT layer thickness, t_p	45-65μm
Spiral turns, n	2	Spiral turns, n	2
Spiral arm width, w	500μm	Spiral arm width, w	500μm
Spiral arm length, l_a	5mm	Spiral arm length, l_a	5mm
Spiral electrode length, l_e	5mm	Spiral electrode length, l_e	5mm
Spiral gap, g_s	50μm	Spiral gap, g_s	50μm
Shim Thickness	130μm	Shim Thickness	130μm
Impedance	232kΩ	Impedance	190kΩ
Q_T	64	Q_T	103
Q_e	379	Q_e	511
Q_m	77	Q_m	128
PFIG			
Inertial Mass, m_i		9.3g	
Spring Constant, k_i		150N/m[*]	
Actuation Gap, gap_T/gap_B (ST1)		0.86mm	
Internal Volume		1.2cm^3	
Total Volume		2.8cm^3	

*Simulated Value
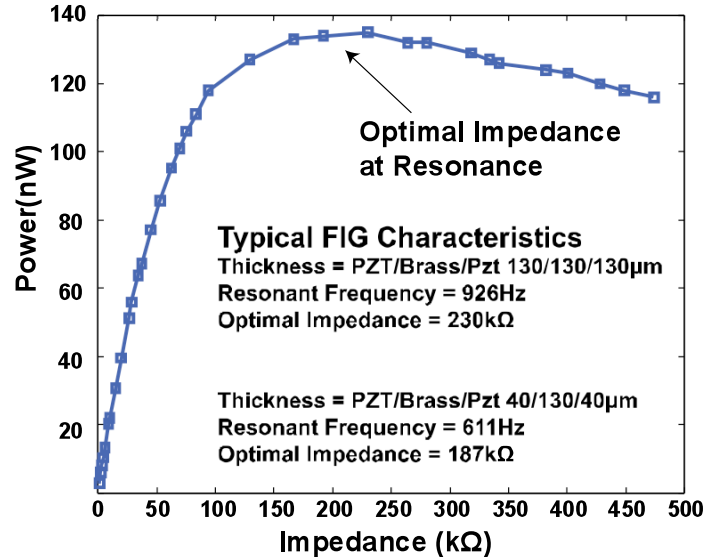
Figure 4-9. Measurement of optimal impedance.

Impulse response tests were carried out in order to determine the quality factors and the corresponding damping ratios. First the optimal load resistance had to be found. The output impedance of the FIG is complex; however, a resistive load is used. The FIG is actuated at its resonance frequency and the input load is varied until power is maximized. The procedure is illustrated for the thick film layer FIG in Figure 4-9. While performing this measurement it is important to take into account any incident impedance, for example from the measurement equipment. In this case since the voltage is measured using an oscilloscope, the 1MΩ input impedance of the device has to be accounted for. After the optimal input impedance is determined, the impulse response tests can be carried out. The results are summarized in table Table 4-1. The total quality factor for the thick layer FIG is exactly in the range of the published maximum quality factor for this material. When the PZT layer is thinned down for the other FIG variant, the quality factor increases slightly because there is less PZT material to cause friction and damping. The

137

measured electrical quality factors for both versions of the spiral FIG are very high. This is partly caused by the fabrication related changes to the design. The electrical quality factor for the thinned down FIG was expected to be lower than the bulk one: however, this is not the case. The reasons for this observation are explored in the discussion section.
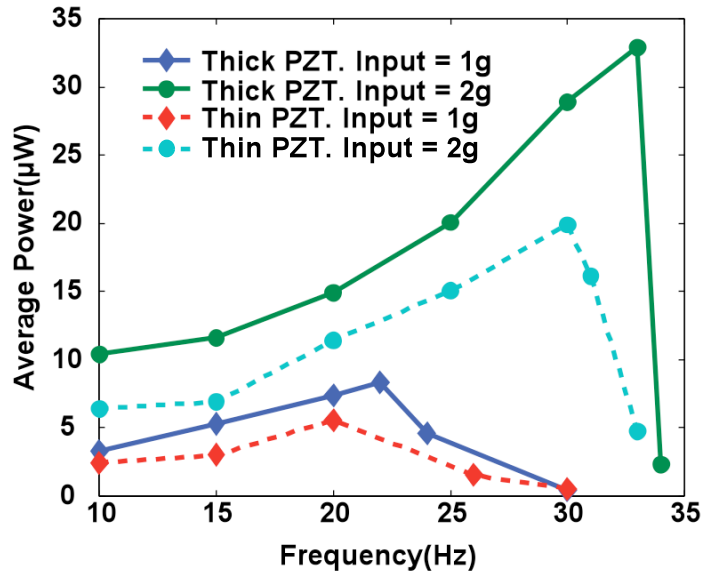
Figure 4-10. Frequency response of the Gen 3 PFIG generator at different vibration amplitudes.

The PFIG was assembled and the frequency response of the device to accelerations of both 1g and 2g were determined. The measurements are shown in Figure 4-10. The full thickness FIGs generated 3.25μW of average power when actuated at 1g with a frequency of 10Hz. The thinned down samples produced 2.44μW from the same input. As mentioned previously, the underperformance of the thin FIGs was unexpected and possible causes will be suggested in the discussion section. If the frequency response characteristics of the Gen 3 PFIG were compared with those of the Gen 2 device, one would quickly notice key differences. The middle operational band that occurs after the combined FIG/inertial mass resonance is exceeded, which was referred to as the "force

limited region" in the previous chapter, is not present. The dynamics of the Gen 3 device are altered because of the increased stiffness of the FIGs. This can be seen in the voltage waveforms shown in Figure 4-11. First there is an uncharacteristically large peak each time the inertial mass makes contact with the FIG. Because of the high stiffness the impact of the inertial mass is more pronounced, and the device does not move immediately. Instead, the inertial mass ricochets and causes the ringing seen in the plot. In fact, looking closely at the plot corresponding to FIG 2 in Figure 4-11, one can see that the inertial mass essentially bounces off the FIG, and that there is a secondary latching even when it comes back down. Secondly, the inertial mass does not actuate the devices well, as seen by the big discrepancy in the voltage between the initial spike and that where the inertial mass unlatches from the FIG. Most of these effects are a result of the increased spring constants of the FIGs. The FIG dynamics are altered in such a way that essentially the inertial mass is just impacting the FIGs and most of the energy is generated in the initial spike. The modified dynamics mean that the PFIG is highly influenced by the inertial mass/spring system, and so the frequency at which the output power begins to decrease is logically coincident with the natural frequency of that resonator. With an increase in acceleration, there is more velocity and the inertial mass can surmount the gap even at higher frequencies, so when tested at 2g, the cut-off frequency is higher.
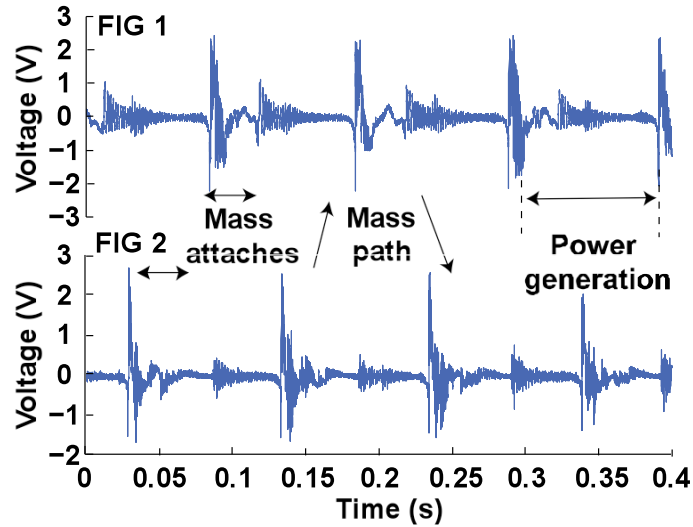
Figure 4-11. Oscilloscope trace showing the parametric generator operation (1g at 10 Hz) as the inertial mass moves from FIG to FIG and actuates each successively. Out of 4 electrode pairs (two on each spiral FIG), only 2 are plotted.

4.4 DISCUSSION

The challenges that arose with this third implementation of the PFIG generator were mainly related to issues caused by the fabrication process. This led to the dimensions and properties of the FIGs to be significantly different from their designed values. Additionally, it was expected that thinning down the PZT FIGs could increase the generated power significantly. However, in this first attempt the FIGs containing the thinned bimorphs produced less power. This is also likely to be due to the fabrication process. Unexpected effects such as micro-cracks could have developed during lapping, the surface could be rough and there may be consequently poor electrical contact, and/or excessive heating during laser machining could be causing degradation of the material properties. These possible reasons for underperformance were investigated using in-depth structural characterization of the samples through scanning electron microscopy and x-ray diffraction studies.

140

4.4.1 SURFACE QUALITY OF THE PZT BIMORPHS

During the testing of some of the thinned down FIGs, some erratic electrical behavior was noticed. This was especially noticeable when sweeping the impedance to find the optimal load. Instead of obtaining a smooth curve some dips were observed. These electrical problems point to problems along the surface of the PZT, where roughness and cracks could lead to instable electrical contacts. It was further important to study the surface, because that is where the major modifications took place.

| (a) | (b) |
| (c) | (d) |
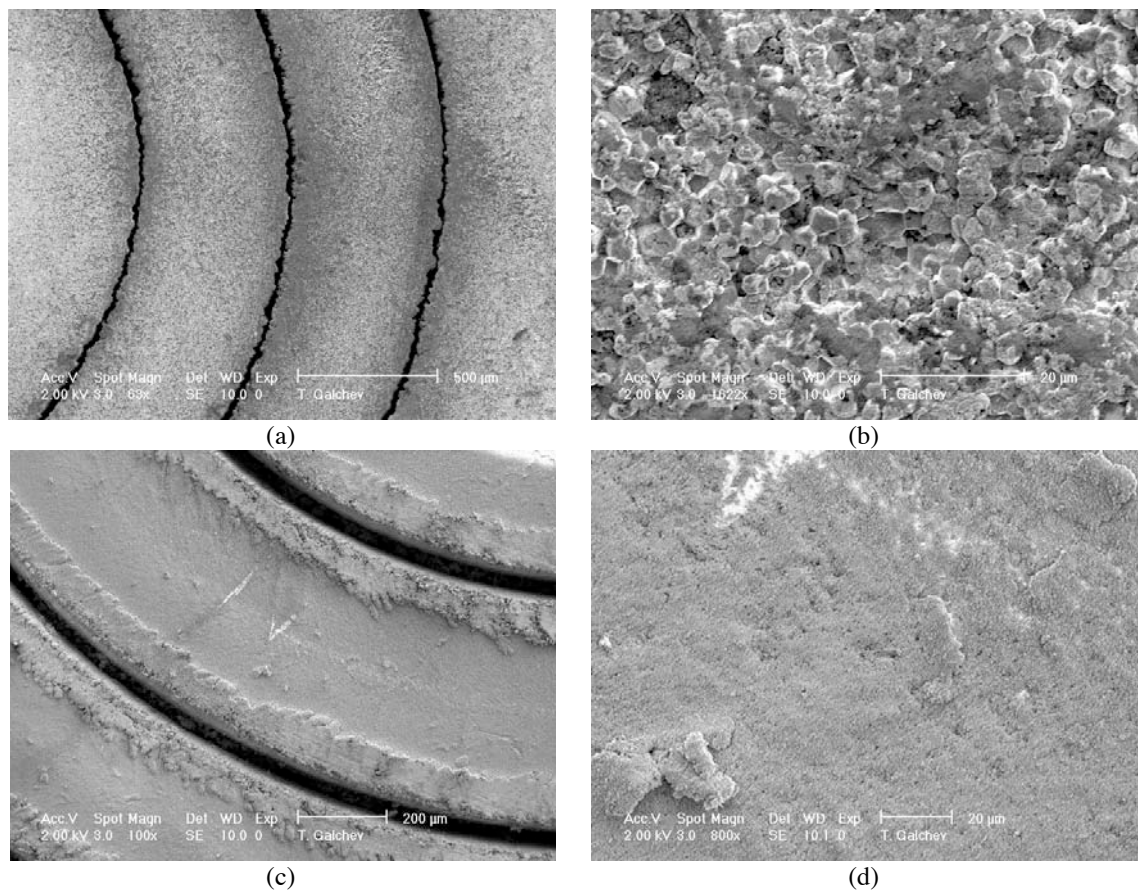
Figure 4-12. SEMs of the PZT FIGs. a-b) show the full thickness spiral and associated close-up showing the granularity in the material. c-d) show SEMs of the thinned spiral and associated close-up. The lapping smoothes the surface.

First the surface is examined visually. Scanning electron micrographs are taken of both the full thickness spiral and the thinned spiral. The results are shown in Figure 4-12. The top two SEMs, a and b, show the surface of the full thickness bimorph. No significant damage is seen from the laser machining. The surface is quite granular which explains the poor maximum quality factor. The bottom two SEMs, c and d, show the surface of a thinned spiral. One can see that the lapping process smoothes the surface quite a bit. If anything, this should be beneficial to metal uniformity during deposition, better conformity, and improved electrical contact. In Figure 4-12c what appears to be damage from the laser machining is actually metal that has been melted and re-deposited.

The surface quality was verified to be appropriate through the visual inspection. Next, x-ray diffraction studies were carried out on the PZT substrates pre- and post-processing, in order to understand the crystalline quality of the substrates, and the effect of processing on them. A wide-range theta-2theta scan was used, in order to observe all relevant peaks. While the scan was carried out in the range theta=0-120°. The figures included plot the scan in the 20-80° range, because no peak above the noise level was observed in the outer ends of the scan window.

Figure 4-13a shows that the bulk PZT substrate that is used for the Gen 3 device is polycrystalline, with no preferential orientation. The x-ray diffraction pattern of the bare substrate shows multiple peaks belonging to the PZT crystal, and confirms the polycrystalline structure. All of the observed peaks were of the perovskite phase, which lacks centrosymmetry. The perovskite phase is the desired structure for this design because it is the optimal phase that possesses piezoelectric properties. Undesirable (centrosymmetric, nonfunctional) phases of PZT were not observed in the structural

142

characterization. The x-ray diffraction scans were repeated after each step of the process and are shown in Figure 4-13b-d. Lapping, patterning, and metallization of the PZT substrates were found to have no deleterious effects on the structural characteristics. Each plane still yielded the same diffraction peak at a similar intensity as pre-processing. The structure was unharmed by the elevated temperature during laser machining and the physical abrasion applied during processing. Additionally, the electrodes, both sputtered and evaporated, yielded a single peak, denoting that a well-formed metal was deposited on the PZT.
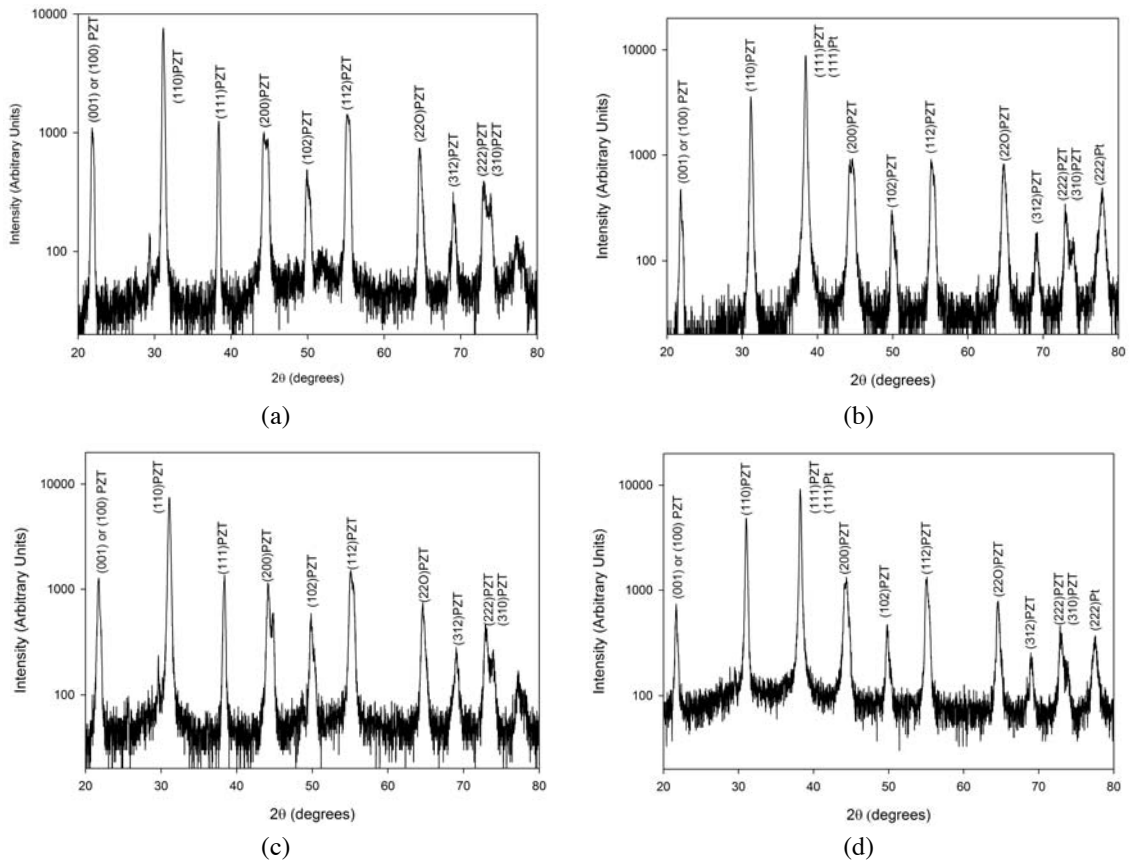
Figure 4-13. X-ray diffraction studies of the pzt bimorph along different points in the process including a) original bulk material, b) after lapping, c) after laser ablation, and d) after metallization.
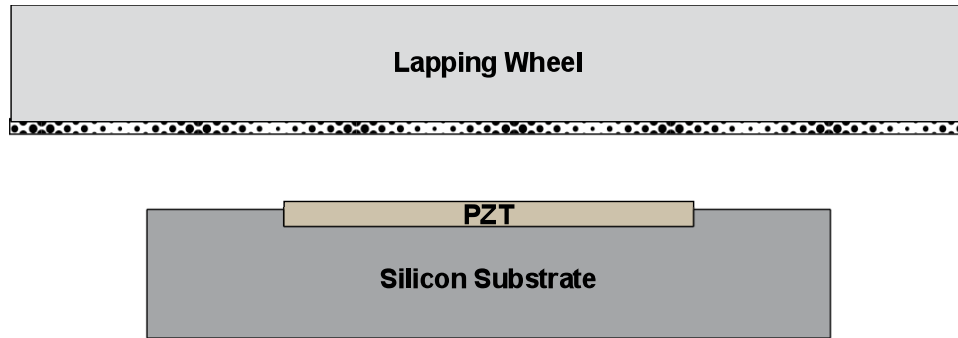
Figure 4-14. Modified lapping process where PZT sample is placed within a silicon cavity and lapped until the two surfaces are even. The silicon acts as a mask protecting the PZT from non-uniformity.

4.4.2   FABRICATION PROCESS EHANCEMENT

Since no materials related problem was discovered during the investigation, the underperformance of the thinned spirals is likely related to a processing issue. One of the likely scenarios is that the non-uniform lapping of the PZT is causing the stress gradients within the bending bimorph to shift both through the thickness and along the lateral directions as well. The biaxial stress gradients can cause averaging of the charge to take place, which would reduce the output voltage.

In order to improve the uniformity of the lapping process, a modified methodology can be used. One alternative is to create a lapping 'mask.' The approach is illustrated in Figure 4-14. A cavity is etched into silicon using a highly anisotropic etch such as DRIE. The PZT sample is then adhered inside the cavity. The entire structure is then lapped. When the PZT surface becomes even with that of the silicon wafer, the wafer will act as a mask, protecting the PZT from further lapping and preventing non-uniformities from occurring. Silicon has a much slower lapping rate than PZT. This process has already yielded much more uniform results. PZT samples as big as 31x63mm have been lapped down with a uniformity of +/-10μm. This is a significant improvement over previous

144

lapping attempts. This process uses an IPEC-472 CMP tool that has a secondary pad for lapping. Additionally, the change in lapping tools allows for the wafer to be adhered using photoresist, which is a much more uniform bond than wax.

The elimination of the wax bonding from the process is also important on its own. Wax residue remaining on the FIGs after lapping and cleaning could be to blame for the poor metal adhesion visually observed from time to time, as well as the erratic electrical behavior during impedance measurements.

The remaining fabrication related issues all had to do with a change in the geometry because of too high expectations regarding the minimum feature size achievable with the laser machining, and a very cautious design. Having now calibrated this process, and armed with realistic expectation for the design rules, these issues can easily be resolved.

4.5 PERFORMANCE

A number of challenges have been encountered during the development of the Gen 3 piezoelectric PFIG, which while resulting in a suboptimal device, have not prevented the generator from exceeding the performance of previously reported efforts in the low-frequency space. The Volume Figure of Merit and Bandwidth Figure of Merit are shown in Figure 4-15a-b, comparing the performance of the second and third generation PFIGs. The fabricated device generated a peak power of 100μW and an average power of 3.25μW from an input acceleration of 9.8m/s2 at 10Hz. The Gen 3 PFIG operates over a frequency range of 20Hz. The reduced volume of the generator, enabled by the use of piezoelectric transduction, helps in increasing its efficiency. The internal volume of the generator is 1.2cm^3.
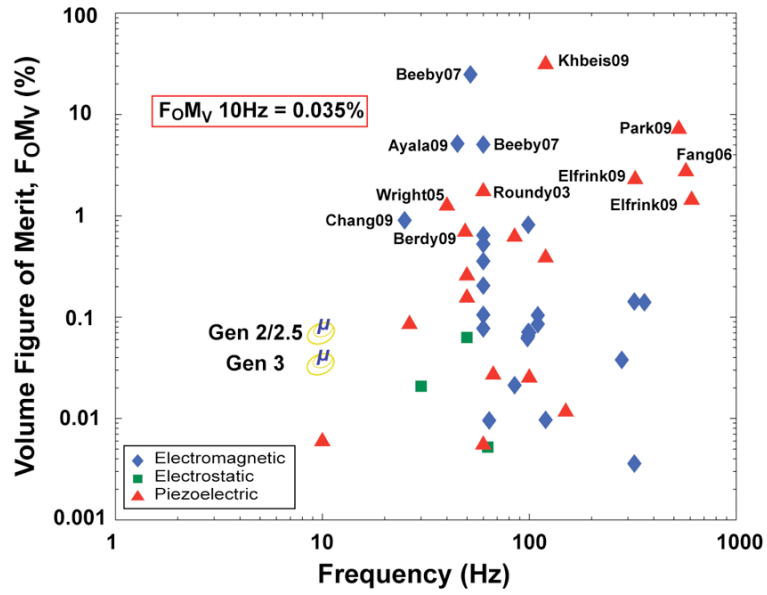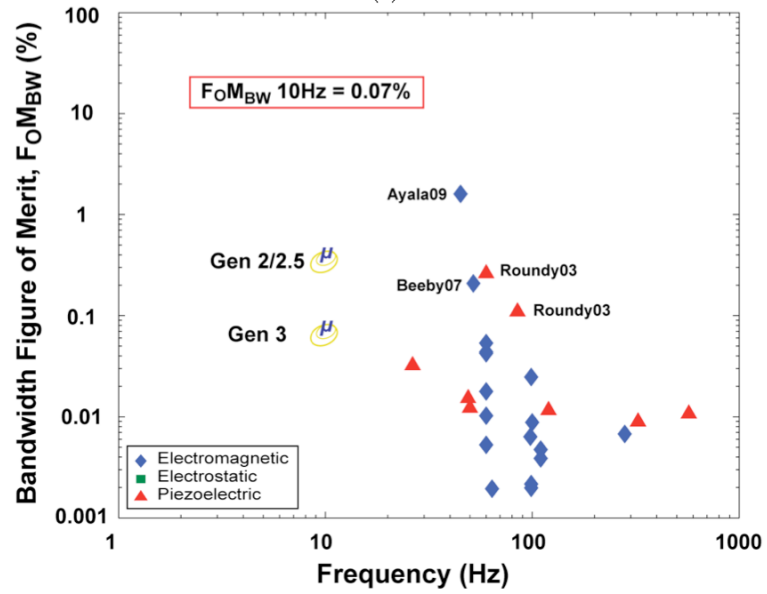
Figure 4-15. a) Volume Figure of Merit (FoMv) comparison of the PFIG generator to the state-of-the-art in vibration scavengers. b) Bandwidth Figure of Merit (FoMBW) comparison of the PFIG generator to the state-of-the-art in vibration scavengers.

4.6 CONCLUSION

This chapter demonstrated that the PFIG architecture could be implemented using piezoelectric transduction. There are a number of benefits that go along with this type of

implementation including a reduced volume, a large rectifiable voltage, and the possibility of combining piezoelectric and electromagnetic transduction mechanisms into a single generator. The scalability of the PFIG architecture was also demonstrated. The PFIG architecture is excellent for the micro scale where displacements are limited because all of the motion inside the PFIG is predetermined and designed into the system. This property is highlighted with the use of the brittle piezoelectric ceramic. This is the lowest frequency and highest acceleration generator implemented using piezoelectrics.

Chapter 5

VIBRATION SCAVENGING FOR CRITICAL INFRASTRUCTURE MONITORING

One application area that can benefit greatly form energy harvesting technology, making it more cost effective, is the monitoring of large engineered structures. Our societies function with the aid of vast networks of infrastructure such as buildings, highways, bridges, dams, railways, as well as by using large engineered tools such as ships, airplanes, and locomotives. The health and performance of some of these systems are monitored more closely than others, but in all cases they are severely undermanaged especially when it comes to civil infrastructure. Civil infrastructure is taken for granted in many respects even as the age of most of these technical structures predates 5 or more ancestral generations of their users at any given time. One category of civil structures that typically features ambitious engineering challenges is bridges. In the United States highway bridges undergo a visual inspection every two years [126]. This constitutes gross mismanagement in the face of other statistics. For example, as of December 2009 the US Department of Transportation rates 71,179 bridges as structurally deficient and 78,468 as functionally obsolete [127], which constitutes 25% of the 603,254 bridges in total. Of course, epic failures in these structures such as the 2007 I-35W bridge collapse in Minnesota garner a great deal of media attention. However, it is not widely known that

148

between 1989-2000 there have been 503 bridge collapses in the United States [128].

Closer monitoring of these structures is mainly limited by economics. Monitoring 600,000 bridges by humans is prohibitively expensive. Efforts to develop automated monitoring systems have been ongoing for quite sometime [129]. For example, accelerometers have been suggested to monitor changes to mode shapes or damping characteristics. Other methods are also under consideration. However, even these automated systems are quite costly. One of the main challenges rests in the wires used to route power and data from the sensors to the processing point, because wires are physically vulnerable and expensive to install and to maintain [130]. In fact, wires can cause a tenfold increase in the cost of a sensor [5]. For this reason interest in wireless sensing systems has grown, because such systems offer the promise of improved structural health monitoring and management. However, wireless sensors need wireless power to make them economically viable. This makes energy harvesting technology very important in these systems. Batteries and other stored energy means can be used, however multiple replacements will be needed through the lifetime of the system. Each replacement will carry with it a significant cost mainly due to labor. Since hundreds to thousands of sensors would be needed on typical bridges, the cost of non-renewable energy sources is a formidable barrier to the adoption of wireless monitoring systems.

This chapter explores the development and testing of an electromagnetic inertial power generation system for scavenging the very low-amplitude, low frequency, and non-periodic vibrations that can be found on typical bridges. While the characteristics of the vibrations make it challenging to harvest them and to convert their energy to electricity, they can be found in abundance on many bridges due to passing traffic. The

PFIG architecture is well suited towards scavenging these types of vibrations due to a number of reasons, the leading one being their non-periodic nature.
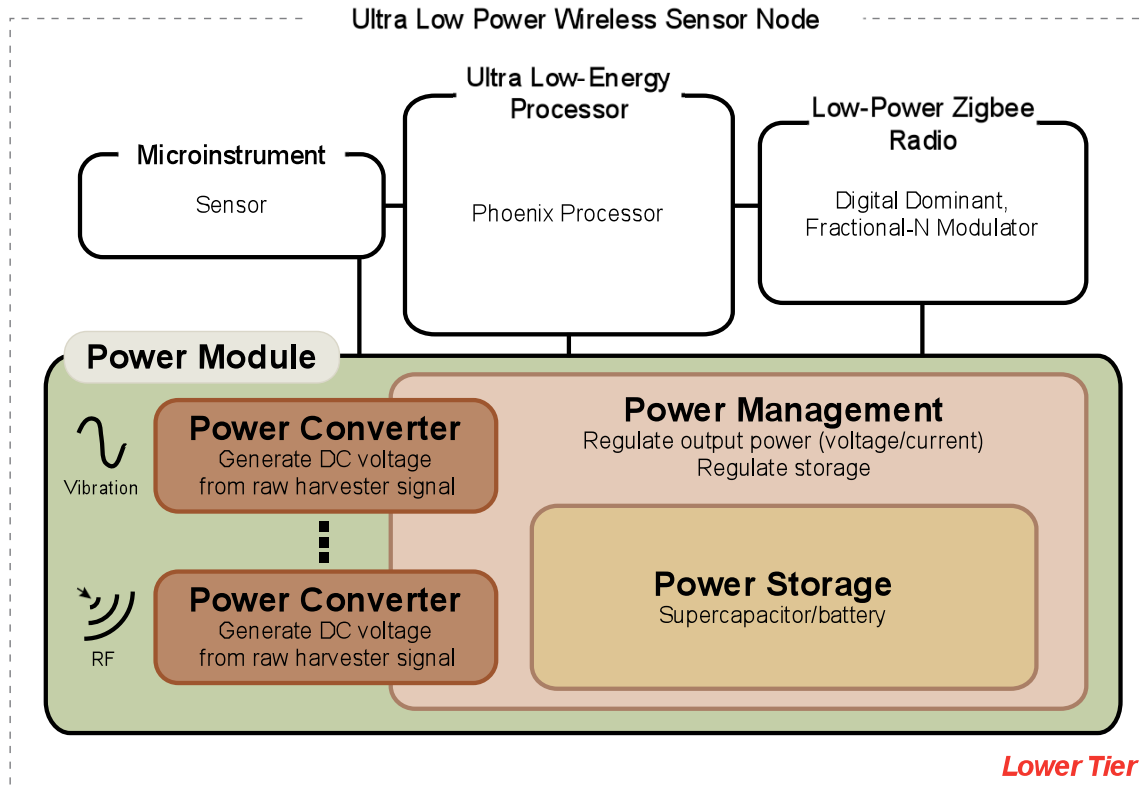
Figure 5-1. Architecture of the lower tier wireless sensor node for bridge monitoring.

5.1 WIRELESS MONITORING SYSTEM ARCHITECTURE

In order to reduce the transmit distance and to increase the spatial density of the sensors on the bridge so that better monitoring can be achieved, a two tiered system is being implemented [131]. The higher tier is essentially a hub that will aggregate the data, perform data processing, and transmit to a central location where the data can be utilized. This is a high-powered device that will be wired to a power source. The lower tier, on the other hand, will consist of many wireless sensor nodes spread out on the bridge. This node will feature the sensor, a low-power processor to control its operation, a radio

150

complying with the Zigbee standard, and a power module. The architecture is shown in Figure 5-1. The sensor node is being developed to consume as little energy as possible and to dissipate virtually no standby power. It is expected that the sensor node will draw <20mW of maximum power and less than 40pW of standby power. While the exact duty cycle is yet to be determined and depends on many system level considerations, one can estimate 200µW for a 1% duty cycle every 100 seconds, 100µW every 200 seconds, and so on. A target of 50µW is therefore set as the desired output from a vibration harvesting system.

The power module consists of a number of energy harvesting power sources, including vibration, RF, and possibly, others to be explored. Each source is interfaced using a power converter stage and depending on the source energy, this stage will comprise different schemes. For the vibration harvester the converter stage includes a means of rectifying the output voltage and increasing it to a useful level so that a battery or other storage element can be charged. This power conversion is controlled by a power management system, which also controls the energy storage and the power supply to the electronics of the sensor. The power module has to be as efficient as possible so as to add minimal additional power draw to the sensor node.

5.2   AVAILABILITY AND CHARACTERISTICS OF BRIDGE VIBRATIONS

The vibration responses of two different types of bridges were measured in order to determine the technical specifications for the vibration harvester. Data from a typical highway flyover steel girder-concrete deck composite structure, Figure 5-2, and from a nearly kilometer-long suspension bridge, Figure 5-3, were collected and analyzed. A tri-axial accelerometer (Crossbow CXL02TG3) was sampled at 100Hz. The girder bridge is

the Grove Street (GS) I-94 flyover in Ypsilanti, Michigan. There were 20 measurement points on the bridge. The suspension bridge is the New Carquinez Bridge (NC) in Valejo, California and it had 11 sensor locations. Acceleration recordings were made for several minutes on each node under routine traffic loads. Figure 5-2 shows two very typical acceleration waveforms from the GS bridge. Although there was less vibration directly in the middle and in the ends where the bridge is anchored, the remaining locations resembled the ones in the plot. The peak accelerations were all in the range of 10-35mg. The figure also shows zoomed in plots revealing the arbitrary nature of the vibration. This is confirmed by taking the discrete Fourier transform of the data. The results for two sensor locations are shown in the bottom of the figure. There is no identifiable peak, and in addition the frequency response of the two locations looks different. The energy is spread out in the 2-30Hz range. Data from the NC bridge is similar in that from sensor to sensor the frequency response is different, as shown in Figure 5-3. The difference is that significantly larger vibrations occur on the NC bridge. The measured accelerations span the range 10-130mg. The lowest vibration is measured in the middle and around the support columns, where the typical peaks are in the 5-10mg range.
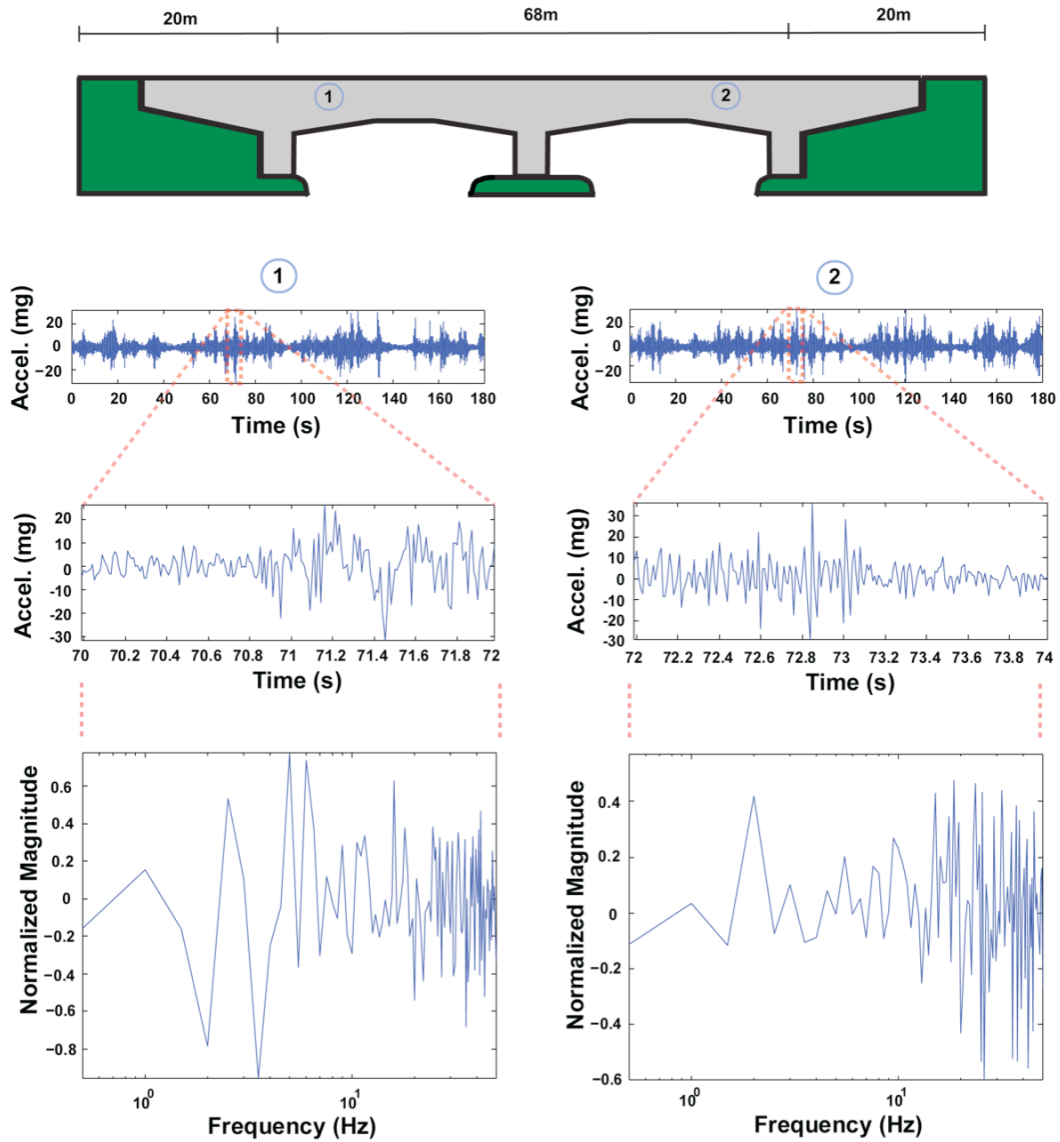
Figure 5-2. Acceleration data measured on a typical T-beam bridge. The circled number represents the sensor number and its location. Three-minute recordings were taken. A zoomed in acceleration waveform is shown in order to see details about its amplitude and periodicity. The bottom pictures show the frequency response of the data sample not only is there no clearly identifiable peak, but the frequency response is different at each sensor location. The acceleration data are courtesy of Masahiro Kurata and Jerome Lynch from the Grove Street bridge in Ypsilanti, Michigan.
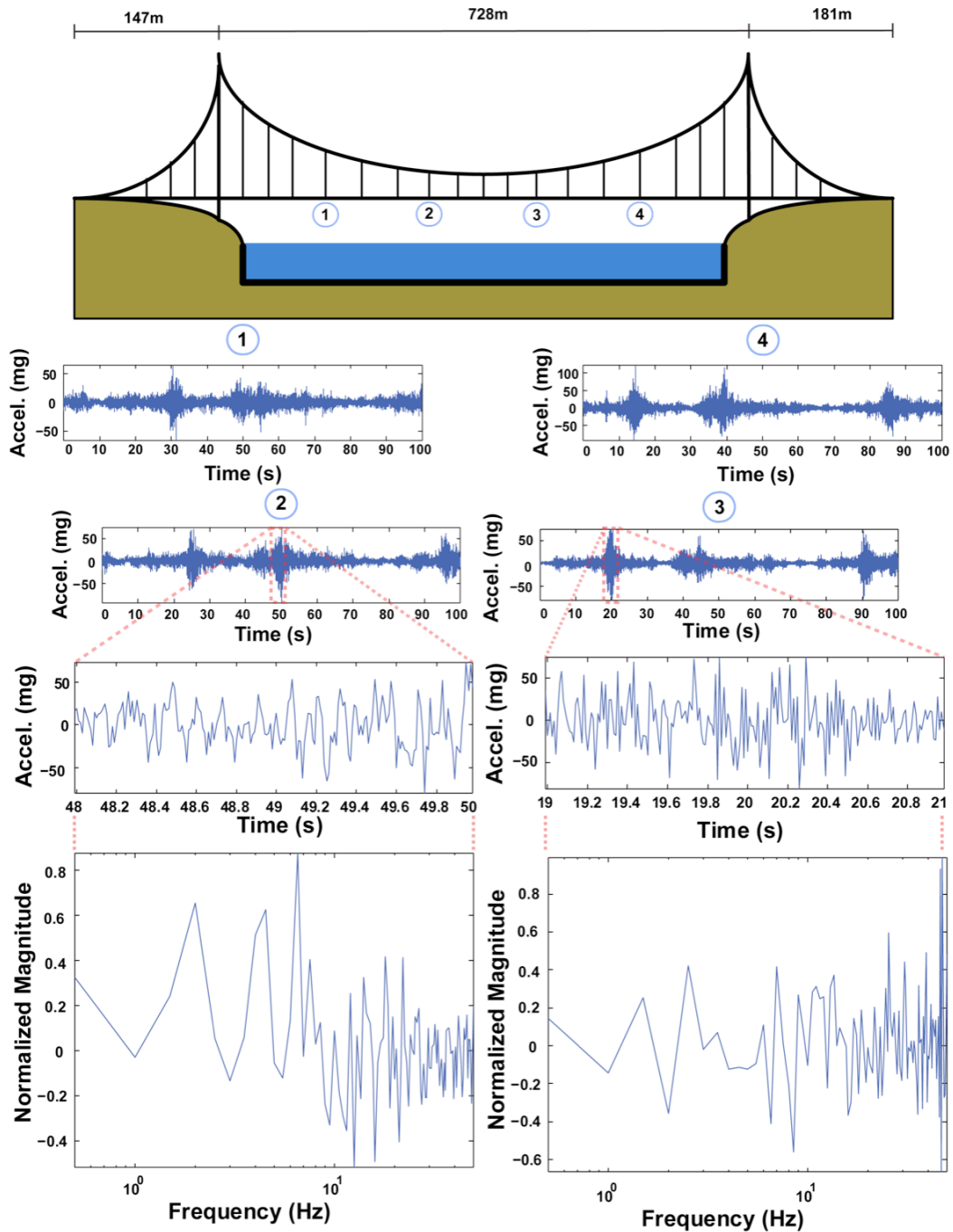
Figure 5-3. Acceleration data measured on a suspension bridge. The circled number represents the sensor number and its location. Three-minute recordings were taken. A zoomed in acceleration waveform is shown for two of the sensors in order to see details about its amplitude and periodicity. The bottom pictures show the frequency response of the data sample not only is there no clearly identifiable peak, but the frequency response is different at each sensor location. The acceleration data are from the New Carquinez Bridge in Valejo, California courtesy of Masahiro Kurata and Jerome Lynch.
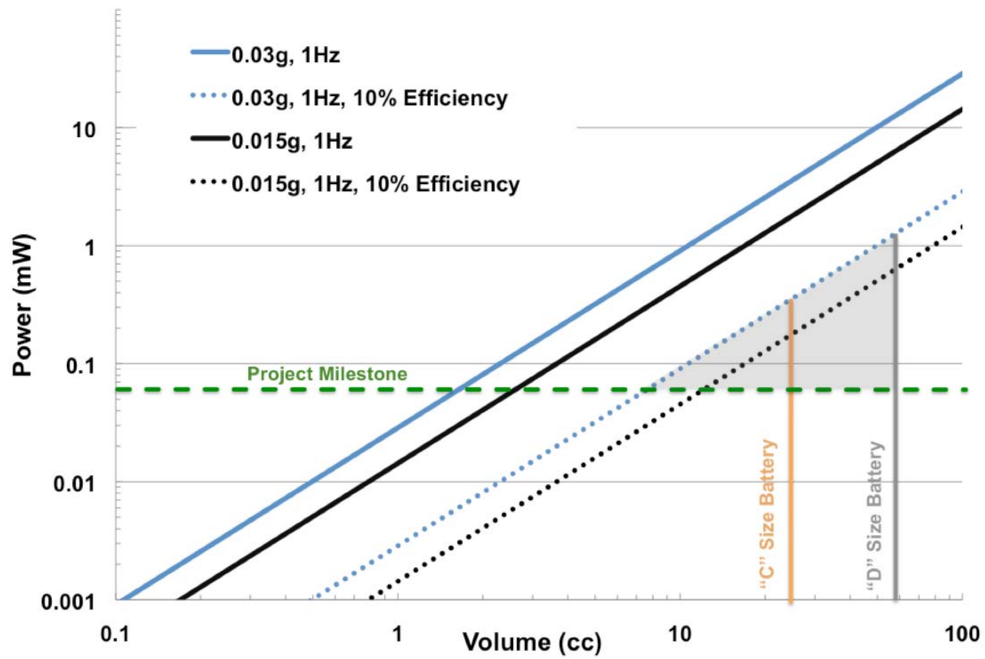
Figure 5-4. Plot showing the maximum possible power that can be converted by an inertial power generator as a function of volume from a vibration at 15mg and 30mg both occurring once per second.

The target minimum acceleration level for the bridge harvester is set to 30mg. While this is not the bottom of the vibration range found on the two bridges, it is sufficient for functionality in many of the locations that were measured, and as such provides a good starting point. Due to the low frequencies involved, this would become the lowest acceleration and the lowest frequency generator ever developed. Therefore, there was no need to add further complications on the first design cycle. The energy harvester should be able to function in the frequency range of 0-10Hz, and it would be a benefit if the bandwidth could be extended to 20Hz or even 30Hz to capture more of the vibration energy. A straightforward approach can be used to calculate the maximum power that can be converted by an inertial micro power generator such as the generic system shown in Figure 1-14. If a sinusoidal input is assumed to have amplitude Y_o and frequency ω, then the damping force can be set equal to the maximum inertial force $m\omega^2 Y_o$. Assuming that

work is extracted in both directions, then the distance over which this force acts is $4Z_{max}$.

Therefore one can write a simple equation for maximum power neglecting all parasitics

and complications as

$$Power_{max} = \frac{2}{\pi} Y_o Z_{max} \omega^3 m. \tag{5.1}$$

This simple relationship is used to make the plot in Figure 5-4, which shows the power

availability for a vibration scavenger as a function of volume for accelerations of 15-

30mg occurring with a frequency of 1Hz. Lines denoting 10% efficiency are also shown.

In Figure 5-4, half of the generator volume is occupied by the mass (density of $20g/cm^3$)

while the rest of the space is used for deflection. Using this simple calculation it is clear

that a significant window of opportunity exists to meet the project specification of 50μW

within a reasonable volume from the vibration conditions found on both the GS and NC

bridges.
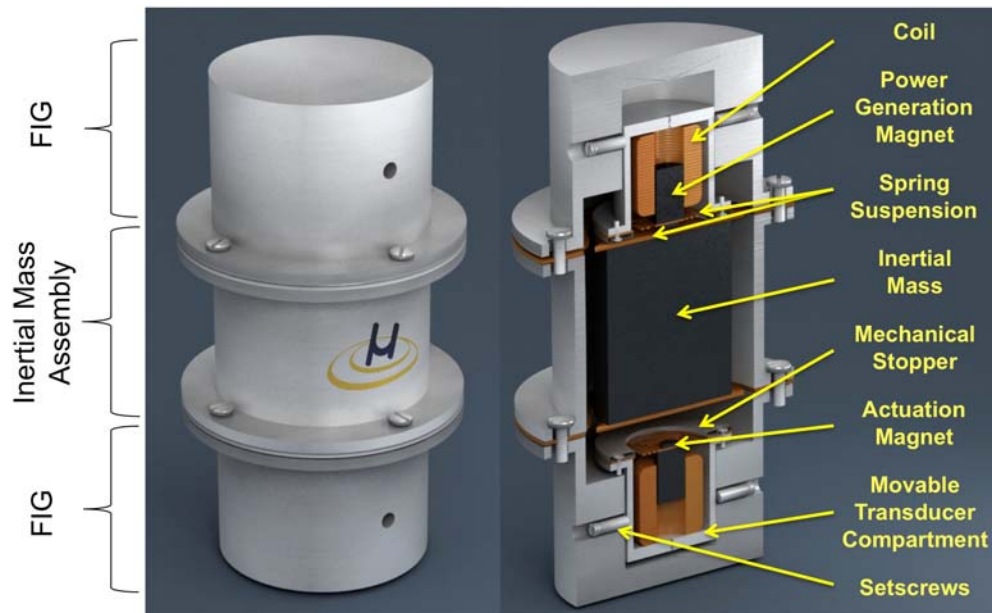
Figure 5-5. Conceptual diagram of the bridge harvester.

5.3 BRIDGE VIBRATION HARVESTING SYSTEM DESIGN

The bridge vibration harvester, while needing to comply with certain technical specifications, is in general an evolutionary iteration of the previous PFIGS. It incorporates a number of enhanced features from the previous generations. It follows that it be referred to as the fourth generation PFIG (Gen 4).

The Gen 4 device is being designed as an electromagnetic PFIG. The main consideration that was taken into account was the need for a robust system that can be utilized in the field with reliability and longevity. A piezoelectric implementation would require more involved fabrication and optimization and was a more complex solution. Additionally, it was not immediately obvious that large enough forces could be generated such that a piezoelectric FIG could be utilized effectively.

5.3.1 HARVESTER STRUCTURE

The overall generator structure can be seen in Figure 5-5. The large tungsten carbide inertial mass can be seen in the middle, with the two electromagnetic FIGs positioned above and below it. One of the first enhancements that have been incorporated into the design is a direct result of the lessons learned during the previous implementations. The inertial mass is suspended from the top and the bottom, rather than from the center. This implementation is expected to make the inertial mass less susceptible to out of axis motion. Preventing this unwanted torsional movement is very important in this particular design, because it will have to work in non-ideal field conditions.

The second non-ideality that needs to be addressed is gravity. The previous generations were tested in the laboratory in a manner such that the vibration was applied in the horizontal direction, allowing them to be free of gravitational acceleration along

the axis of motion. This option does not exist on a bridge, where the vibration of interest is vertical. Removing the bias due to gravity can be done in a number of ways. The simplest way is to build the PFIG system around a new equilibrium position, which takes into account the deflection of the various components due to gravity. In other words, Z_{lt} and Z_{lb} are altered to account for gravity. The only complication is that the relationship between the three system coordinates u, s, and z might be altered. In the generic PFIG implementation u is above z, which is above s. This relationship now strongly depends on gravity and the equilibrium position of the inertial mass. Indeed, it depends on all three, but the influence of gravity on the FIGs is expected to be negligible in comparison. In the Gen 4 system the anchoring position of the inertial mass is above both FIGs, because of the large deflection caused by gravity. To work around this for the purposes of simulation the system is modeled around a new set of coordinates $u'(t)$, $z'(t)$, and $s'(t)$, which have their zero position around this new equilibrium. Gravity is not considered in the dynamics of the system because it is a constant force that is balanced out by the suspension spring static deflection.
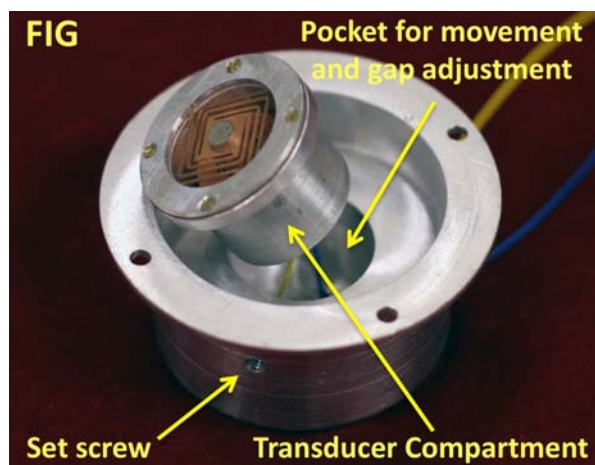
Figure 5-6. Photograph showing a close-up of the FIG and movable transducer.

As far as the physical implementation is concerned, as shown in Figure 5-6, the FIG consists of an outer case with a hole bored though the middle, where a secondary enclosure containing the transduction components is able to move in the z direction. This enclosure is held in place using setscrews from the sides and from the bottom. This way the position of u, s, and z can be adjusted. While it is possible to calculate what the bias is and to simply build it in, because of the large weight of the inertial mass, small manufacturing errors in the springs can lead to large changes in position. Since the ambient acceleration is very small, the inertial mass deflections will also be quite limited, thus mispositioning caused by gravity can have serious consequences. The second consideration that needs to be taken into account is that the coordinates of the three devices can switch their relationship. To allow for u and z to switch positions, the inner enclosure that houses the electromechanical transducer components, is designed to have a diameter that is smaller than the spring arms supporting the inertial mass. This way the fixed location of the inertial mass suspension does not affect positioning of the FIG transducer.

A variety of further enhancements are made in the Gen 4 design. For example the spring assembly that carries the power generation magnet is positioned relative to the coil and clamped using a ring that is screwed into the movable fixture. Having this ring be screwed in from the top enhances the alignment capabilities and reduces the parasitic effects of misplacing the moving magnet. In general the internal enclosure that houses the transducer has approximately the same dimensions as the Gen 2 FIG. The inner diameter is 3mm wider and it is 3mm taller than the Gen 2 FIG. This extra space was allotted to aid in making a more robust design and to alleviate some of the space related problems of

the previous devices.

5.3.2   HARVESTER COMPONENT DESIGN

As a starting point for the dynamics of the Gen 4 system, the previous two implementations are used. There is not a great deal of flexibility available for changing the interrelationships between the various system components. They are simply dictated by cost, manufacturing process and precision, as well as design cycle considerations. For example, while the system can be optimized for a lower inertial force, this would dictate other latching force requirements, requiring either a reduction in the displacement of the FIG or more sensitive and less robust FIG components. Additionally, lower FIG displacements mean that much more complex optimizations need to be carried out with respect to the transduction system for a given force or displacement. While keeping much of the system dynamics intact allows for a less complicated design, it means that the overall volume of the PFIG will increase significantly. To generate a similar inertial force to the Gen 2 and 3 devices that worked with a minimum acceleration of 1g, one must increase the mass by the same magnitude as the reduction in the minimum acceleration. From here the system was further developed numerically using Matlab. The extracted damping coefficients from the previous generations were used as a starting point to approximate the parasitic and electrical forces on the system. The final configuration of the system will be summarized in the results section and so the reader is referred to Table 5-1.

Upon finalizing a mechanical configuration for the system, the physical components were designed using a combination of analytical calculations and fine-tuning using FEM. The springs were modeled in ANSYS. In order to save space the supporting arms were

curved which made their analytical design very complicated. Figure 5-7 shows the two types of springs that were modeled for the FIG and inertial mass suspensions.

(a)   (b)
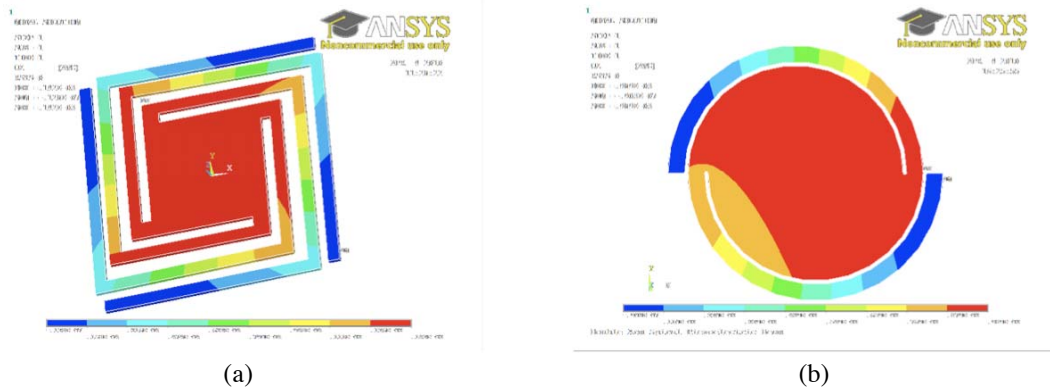
Figure 5-7. Simulated deflection in response to 0.1N is used to calculate the spring constant for a) FIG spring and b) inertial mass spring.

5.3.3   ENERGY CONVERSION ELECTRONICS

The vibration harvesters discussed in this thesis thus far have been incomplete. While the mechanical energy is converted to electrical energy, this energy is not in a form usable by most electronic devices. The alternating (AC) voltage has to, at a minimum, be converted to a constant (DC) value in order to be of practical use. However, the voltages produced by most energy harvesting devices are relatively low compared to those required for powering many contemporary electronic devices. Therefore, during AC to DC conversion, a circuit that boosts the voltage to an appropriate value should follow the rectification stage. In order to directly power some of the more advanced integrated circuits an appropriate voltage value means ~1V: for charging a super capacitor or rechargeable battery that value is ~3-4V. Depending on the load, a boost circuit with appropriate current delivery capability should be selected.

The efficiency of the energy conversion circuitry should be as high is possible,

because it directly impacts the total efficiency of the power harvesting system. While it may seem surprising, considering the now decade-old field of energy harvesting, complete systems consisting of both the harvester and the power conditioning electronics have rarely been demonstrated and constitute a very small fraction of all energy harvesting publications. A few of the most noteworthy ones can are referenced here [100, 132-141] so that the interested reader can pursue this topic in greater detail.

The goal of this effort was to demonstrate a complete energy harvesting system including the power conversion circuit. Increasing the efficiency of the electronic interface is an involved process and it was beyond the scope of this project. In order to make the system robust enough to easily be placed in the field, the electronic interface should be as simple as possible. The most noteworthy challenge here was to utilize as much of the decaying FIG output waveform as possible.

While the standard implementation would call for a rectifier followed by a DC-DC conversion circuit, this is not easy to implement in a passive system. The DC-DC conversion would typically contain complex switching in the most efficient implementations, for which timing signals need to be generated. In order to avoid this, a charge pumping circuit could be utilized, for which the switching is less complex and could be done with as little as one timing signal. It makes sense when pursuing a charge pump approach to incorporate the rectification in a single circuit. This type of circuit is typically referred to as a voltage multiplier and at its core is simply a cascade of single wave rectifiers.
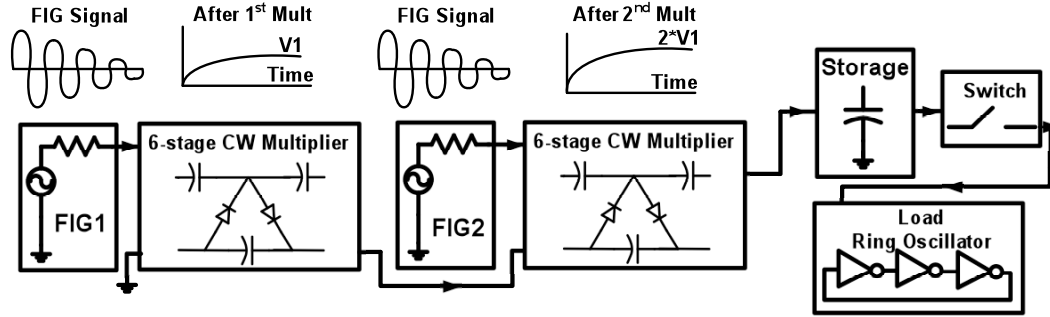
Figure 5-8. Energy conversion circuitry

The design of the full energy harvesting system is shown in Figure 5-8. A Cockcroft-Walton (CW) multiplier was attached to each of the two FIGs. The output of the two multipliers was cascaded to further increase the voltage and to combine the two outputs into one. The resulting charge was stored on a capacitor and it was available for powering various electronics. The feasibility of attaching a load and powering it using scavenged energy was demonstrated using a ring oscillator.
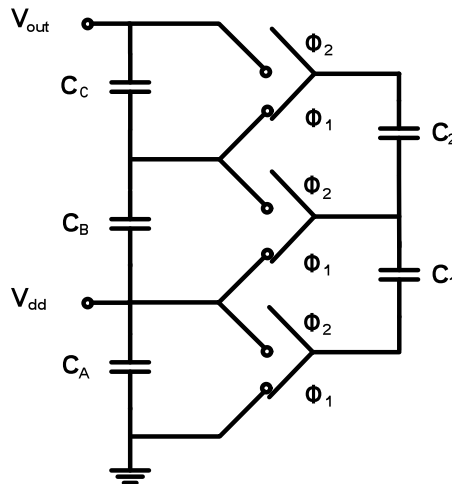
Figure 5-9. Cockcroft-Walton multiplying circuit.

The basic CW multiplier circuit is shown in Figure 5-9. There are two clock phases Φ_1 and Φ_2 that control the multiplier switches. In the most basic configuration all capacitors have the same capacitance C. During the first phase, capacitor C_A and C_1 are connected

and charged to V_{dd}. During the next switching cycle, Φ_2, the switches change position and C_1 is connected in parallel to C_B, sharing its charge and resulting in a potential of $V_{dd}/2$ on each capacitors. In the next cycle C_2 and C_B will be connected and will share a potential of $V_{dd}/4$, while at the same time C_1 is once again pre-charged to V_{dd}. This charge sharing will go on for a number of cycles until finally V_{out} reaches $3V_{dd}$. In the simplest passive implementation of this circuit, the switches are simply replaced by diodes, while the clocking is provided by the AC input waveform. The result is that the voltage is doubled after every stage so that $V_{out} = 2 \times n \times V_{peak}$, where n is the number of stages, and V_{peak} is the positive peak of the AC input signal. Of course, this equation assumes ideal conditions. To get efficient multiplication, the capacitor values should be much greater than the parasitic capacitances at each node. Additional reduction in the output voltage will be observed due to the turn on voltage associated with the diodes as well as due to the capacitance division effect at each node. The output impedance of the CW multiplier rapidly increases with the number of stages and reduces the current driving capability.
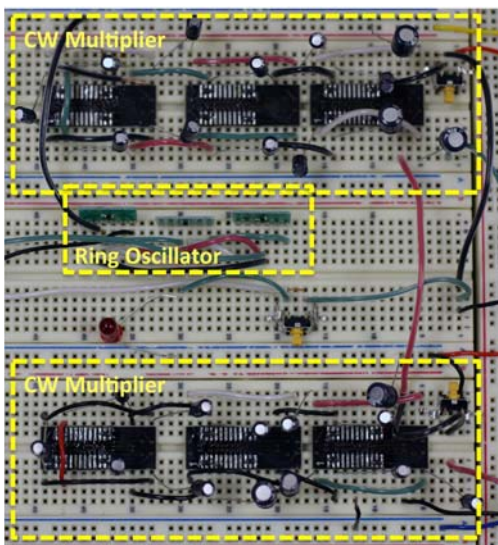
Figure 5-10. Photograph of the prototype power conversion circuit, courtesy of James McCullagh.

A picture of the entire system, built on a standard breadboard, is shown in Figure 5-10. BAT54WS Schottky diodes are used because of their low turn on voltage of 180-200mV. Electrolytic capacitors (10μF) are used for the multiplier and a 47μF capacitor is used to store the resultant charge. The ring oscillator load can be connected using a manual single pole single throw switch. The oscillator itself is made out of 3 NC7SP04 inverters.
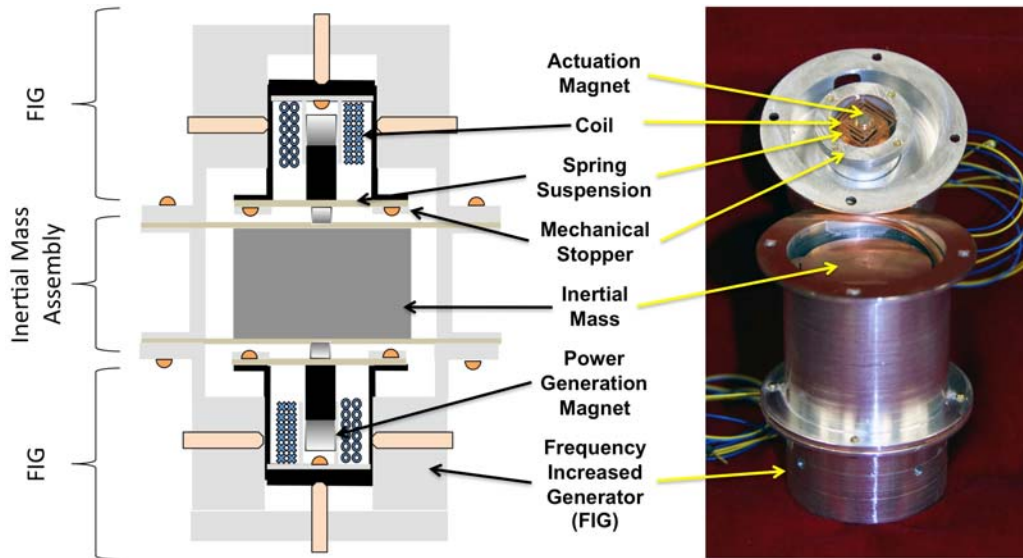
Figure 5-11. Gen 4 concept on the left side, along with a finished and partially opened device on the right.

5.4 GEN 4 FABRICATION AND ASSEMBLY

The fourth generation PFIG was fabricated and assembled in a very similar manner to its predecessors, save for a few points of enhancement. The finished device along with an illustration describing the placement and relationship of all the components is shown in Figure 5-11. The FIGs were located on the top and on the bottom. The electromagnetic core of the FIG was housed in an internal casing, which can slide up and down inside the FIG. This internal enclosure was held in place using 5 set screws, 4 on each side, and one pushing on it either on the top or on the bottom, depending on the orientation. The motion

165

of the internal FIG housing allowed the gap between the inertial mass and the FIGs to be changed. One reason for allowing this flexibility was to remove the bias of gravity as was previously discussed. The inertial mass was held in place by two springs (top and bottom) within a separate enclosure. When the FIGs were fastened above and below the inertial mass enclosure they also served to clamp the springs in place.

5.4.1 PFIG CASING

The casing and all of the hardware that hold the PFIG components together were milled out of aluminum. This casing had less intricate design and details then the previous one designed for the Gen 2 and 3 devices. The bigger pieces were held together using 1-72 bolts, while the FIG transducer assembly used 000-120 bolts as before. The area that was milled out inside of the FIG cap, where the internal transducer enclosure was able to move in and out, had a diameter that was precisely machined to be 25μm larger than that of the FIG enclosure. This way the transducer enclosure can slide freely without the danger of getting stuck due to twisting inside the recess. The FIG spring was fixed in place from the top using an aluminum ring that was screwed into the transducer enclosure. The holes where this ring was fixed in place had to be countersunk so as not to influence the gap between the FIG and the inertial mass.

5.4.2 INERTIAL MASS ASSEMBLY

The inertial mass was machined out of a 2.54cm diameter tungsten carbide rod. Electro discharge machining (EDM) was used to cut the appropriate piece off. This piece had to be ground down after the EDM step because a small chip was created at the end. For this reason the thickness that was cut off needed to be slightly larger than the final

desired thickness. The inertial mass was fixed to the spring suspensions using cyanoacrylate. In order to position it directly in the center of the spring, an alignment jig similar to the one used for the Gen 2 device (Figure 3-13) was used. The springs that were used had two arms on either side. This configuration left the inertial mass susceptible to torsion in the axis perpendicular to the one along which the spring arms are clamped. To alleviate this problem, the top and bottom springs were rotated exactly 90° from each other. This way the inertial mass had at least one set of supports providing resistance in both the x- and y-axes.

5.4.3   SPRING FABRICATION AND ASSEMBLY

The spring suspensions were once again made out of copper, similar to the previous designs. However this time they were made out of a thicker, 254μm copper sheet. This was done mainly to be able to meet the specifications for the inertial mass suspensions. However, because all of the springs were made in bulk out of the same lithographic mask, the same thickness was used for the FIGs as well. Additionally, instead of using immersion etching as was previously done, the spring manufacturing was outsourced to Kemac Technology for spray etching. The double sided process that Kemac Technology used, along with the precision of spray etching, allowed better feature and profile control, resulting in more reproducible results.

Photographs of the manufactured springs are shown in Figure 5-16a-b. The FIG spring assembly was made in the same way as the Gen 2.5 device. An alignment jig was used to align the magnet to the center of the spring. The power generation magnet was adhered to the spring on top of an aluminum spacer. An NdFeB N42 grade (4.75mm diameter and 2.4mm thickness) magnet was used for power generation. A smaller 3mm diameter

magnet NdFeB magnet was adhered to the top of the spring for magnetic latching. The finished spring assembly is shown in Figure 5-12c.

<table>
<tr><td>(a)</td><td>(b)</td></tr>
</table>
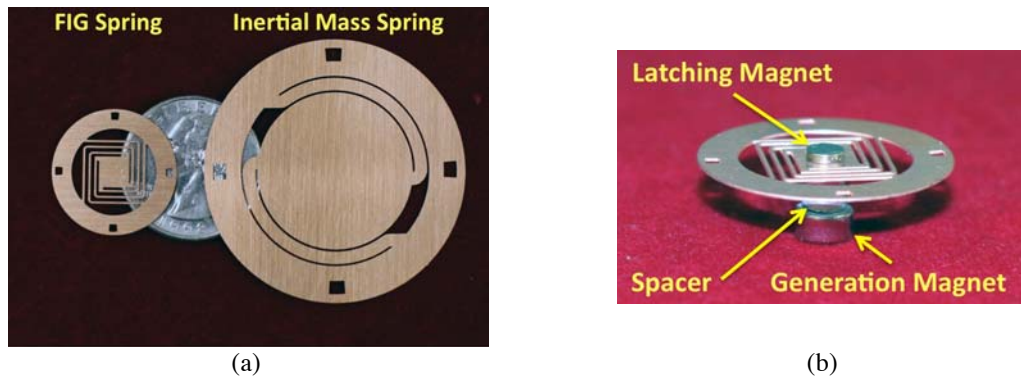
Figure 5-12. Photographs of a) FIG spring and inertial mass springs, and b) FIG spring assembly.

5.4.4   COILS

The coils were made in a similar manner to the Gen 2.5 generator. Acrylic and aluminum bobbins were first milled out of a solid material base. Afterwards, 50μm diameter enameled copper wire was wound around the bobbin. There were two types of coils that were designed and manufactured as will be discussed in the next section. One of them had two windings with opposite directions. In order to avoid making connections post-winding, both windings were made at the same time. The wound coils are shown in Figure 5-13a-b. The coil bobbin was once again aligned and fixed to the transducer enclosure using a 00-120 bolt in the center. The assembled transducer is shown in Figure 5-13c.

(a)   (b)   (c)
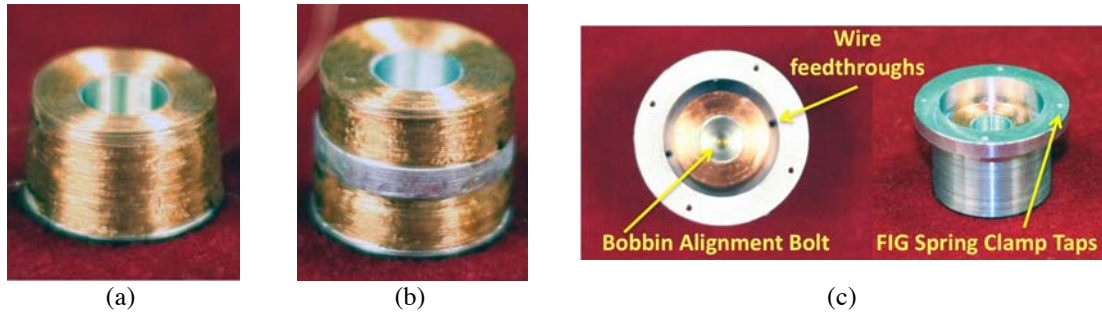
Figure 5-13. Photographs of a) coil type 1, b) coil type 2, and c) assembled transducer enclosure.

The finished PFIG measured 3.3cm in diameter and was 7.3cm tall. The internal volume of the device, featuring all of the transduction mechanisms, the inertial mass, and all of the space needed for the components to move, was $43cm^3$ ($68cm^3$ including the casing). The finished device is shown in Figure 5-14 and is compared to the size of a standard "D" size battery.

Figure 5-14. Photograph of the completed Gen 4 PFIG alongside a "D" size battery.

Table 5-1: Summary of Gen 4 bridge PFIG configurations

FIG Parameters			
Coil Type 1 (CT1)		*Coil Type 2 (CT2)*	
Coil Turns, N	6000	Coil Turns, N	7000
Coil Resistance	1.5kΩ	Coil Resistance	1.7kΩ
Spring Type 1 (ST1)		*Spring Type 2 (ST2)*	
Spring Constant, k_f	535N/m	Spring Constant, k_f	524N/m
Mass, m_f	0.587g	Mass, m_f	0.678g
Natural Frequency, f_n	152Hz	Natural Frequency, f_n	140Hz
Magnet Types	NdFeB	Magnet Types	NdFeB
Actuation Magnet Diameter	3.175mm	Actuation Magnet Diameter	3.175mm
Actuation Magnet Thickness	0.78mm	Actuation Magnet Thickness	0.78mm
Generation Magnet Diameter	4.76mm	Generation Magnet Diameter	4.76mm
Generation Magnet Thickness	2.4mm	Generation Magnet Thickness	2.4mm
Q_T	25	Q_T	10
Q_e	75	Q_e	23.3
Q_m	38	Q_m	17.5
PFIG			
Inertial Mass, m_i		250g	
Spring Constant, k_i		1140N/m[*]	
Actuation Gap, gap_T/gap_B (ST1)		0.66mm	
Actuation Gap, gap_T/gap_B (ST2)		0.66mm	
Internal Volume		43cm^3	
Total Volume		68cm^3	

*Simulated Value

5.5   TESTING GEN 4 AND RESULTS

A summary of the Gen 4 PFIG configurations is shown in Table 5-1. Two coils were designed and tested. Coil Type 1 (CT1) was a basic winding of 6,000 turns. It worked together with Spring Type 1 (ST1), which had a similar assembly as was seen in the Gen 2.5 parametric generator. The magnet was positioned using a spacer to rest directly above the beginning of the coil bobbin. Coil Type 2 (CT2) had two 3,500-turn windings, separated by a barrier, and wound in opposite directions. The goal of this configuration was to take advantage of the flux change associated with both poles of the moving magnet, as it translated up and down. The two windings were connected serially in accordance with the right hand rule, such that the generated voltages add. Spring Type 2 (ST2) is the nomenclature used to identify the spring assembly designed for use with CT2. The two spring assemblies were nearly identical in geometry. The main difference was that ST2 had a thicker spacer in order to position the power generation magnet directly in the middle of the two windings in CT2. The FIG mass change associated with the thicker aluminum spacer is the only difference in the configuration parameters in Table 5-1. Since the springs are identical, the two different FIG designs will be referred to simply as CT1 and CT2.

Impulse response tests were performed as before to determine the parasitic and electrical damping of the two FIG configurations. Voltage traces of the open circuit and loaded devices were collected and their spectral content was analyzed. The results are presented in Table 5-1. The electrical damping of CT2 is nearly a 3x improvement as compared to CT1. Unfortunately, the parasitic mechanical damping also increased by a factor of 2. This was almost certainly caused by airflow friction and squeeze film

damping inside the center of the bobbin. The 175μm margin left on either side of the moving magnet was not enough to alleviate the squeeze force. Due to the added parasitic damping CT2 generated a peak voltage of 4V and CT1 generated 3.85V in an open circuit configuration, and 1.65V and 1.42V respectively, when loaded. The marginal net improvement of using CT2 was deemed insufficient, considering the extra precision for alignment and assembly that is necessary to utilize this configuration appropriately. For this reason, the remaining test results form the Gen 4 PFIG were all achieved by using CT1.
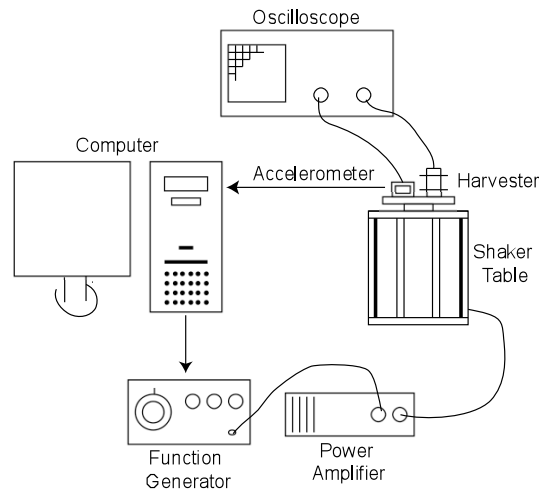
Figure 5-15. Test setup for Gen 4 characterization.

5.5.1 PERFORMANCE OF GEN 4 UNDER HARMONIC EXCITATION

Due to the low accelerations needed for characterization of the Gen 4 system, the Unoltz-Dickie shaker and associated control hardware could not be used. A new test setup was devised. It was based on an APS Dynamics APS113 long stroke linear shaker. The full test set-up is shown in Figure 5-15. An Agilent 33250A signal generator was used to generate the driving waveform. This waveform was then amplified using an APS Model 124 amplifier and fed into the shaker table. The resultant acceleration is monitored

using an Agilent ADXL203 accelerometer. While automated feedback control was not implemented, the signal from the accelerometer can be analyzed using LabView and corrections can be sent automatically to the signal generator. In the developed system, the accelerometer output was monitored using an oscilloscope and corrections were made manually using the signal generator. This had to be performed every time the desired acceleration level or frequency needed to be altered.
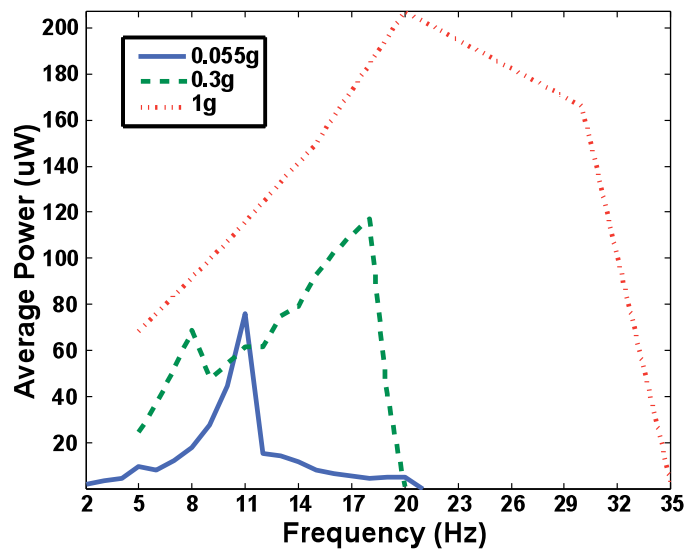
Figure 5-16. Acceleration and frequency response of the Gen 4 PFIG under harmonic excitation.

The performance of the Gen 4 PFIG was analyzed under sinusoidal excitation and the results are presented in Figure 5-16. The targeted minimum acceleration level was 0.03g. However, the possible latching forces were discrete, relaying on the availability of stock magnet sizes. As a result, a minimum of 0.05g was achieved. This was within the range of acceleration found on typical bridges. Further tuning of the generator to lower this acceleration level is a trivial matter and does not significantly alter the majority of the design. The frequency response to an acceleration range of 0.055-1g was measured. This is a span of almost two full orders of magnitude. These measurements were performed

without any modifications or tuning to the PFIG. This is an unprecedented operational span. A resonant generator cannot possibly be expected to perform over such a range. Due to its quality factor it will either result in structural failure, or most of the energy will be spent in colliding with motion-limiting structures. At low accelerations (0.05g) the Gen 4 device reaches the end of the velocity-limited region of operation rather quickly and its power output quickly drops. The operation of the Gen 4 PFIG under low accelerations will be analyzed in more detail in Section 5.6. At higher accelerations (and consequently higher velocities) the operational range was extended significantly. Figure 5-16 clearly shows how the force-limited region of operation extends the frequency range by a factor of 2 for 0.3g acceleration and a factor of 3 at 1g.

5.5.2   TESTING UNDER BRIDGE VIBRATION CONDITIONS

By utilizing the new test setup shown in Figure 5-15, it is possible to mimic the ambient conditions found on bridges in the laboratory. Ideally an automated system should be used to both generate the driving signal for the shaker table, and to compare it with the feedback accelerometer data. The necessary gain corrections would be made that way. Since this acceleration data varies in both amplitude and frequency, a linear gain factor may not be sufficient to reproduce it correctly. However, for the purposes of this study, the acceleration rendered by the shaker table was accurate enough to test the PFIG under non-periodic conditions.

A 20 second sample from the GS bridge data shown in Figure 5-2 was extracted and stored in the signal generator memory. The arbitrary function has the capability of reproducing the signal, and of repeating it with a certain period. This signal was then used to drive the shaker table. Figure 5-17 - Figure 5-19 show the output voltage of the

174

two FIGs in response to the acceleration signal recorded from the Grove Street bridge. In Figure 5-17 the signal was amplified by 3x, in Figure 5-18 by 1.5x, and in Figure 5-19 the acceleration was nearly identical to that felt on the bridge. In each of those cases the PFIG was able to generate an average power over the 20sec interval of 4.4μW, 1.9μW, and 0.5μW respectively. Since the anticipated standby power of the sensor node is 300nW, in all three cases enough energy was generated to satisfy this requirement, and extra energy was left over to charge up a storage element and to prepare it for the next transmit/receive cycle. In order to really make the Gen 4 PFIG compatible with both types of bridges discussed in the beginning of the chapter, the minimum acceleration needed for operation will have to be lower, in the range of 0.01-0.02g. Additionally, a better conversion efficiency, even by a moderate factor of 5-10 times increase, will make the system viable on almost any type of bridge.
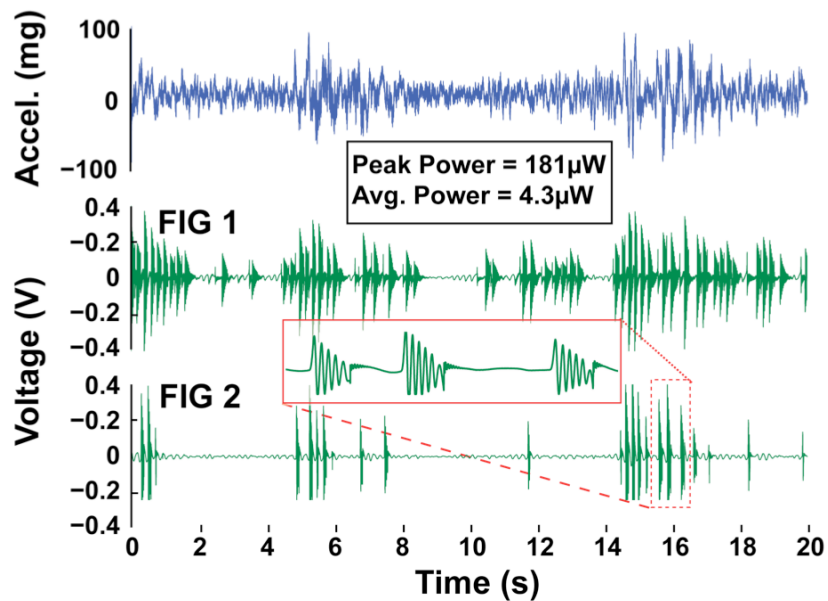
Figure 5-17. Gen 4 PFIG response when excited by a non-periodic vibration. The top plot shows the acceleration signal felt by the PFIG. It is an amplified 20 second extract from the data presented in Figure 5-2. The acceleration signal has been amplified such that the peaks occur at 100mg (~3x original). The bottom two traces show the voltage from the two FIGs.
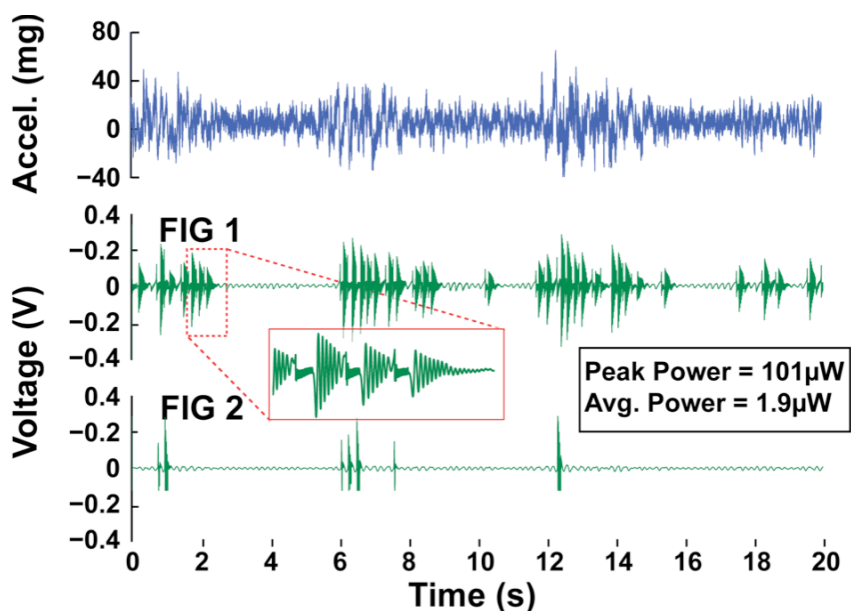
Figure 5-18. Gen 4 PFIG response when excited by a non-periodic vibration. The top plot shows the acceleration signal felt by the PFIG. It is an amplified 20 second extract from the data presented in Figure 5-2. The acceleration signal has been amplified such that the peaks occur at 80mg (~1.5x original). The bottom two traces show the voltage from the two FIGs.
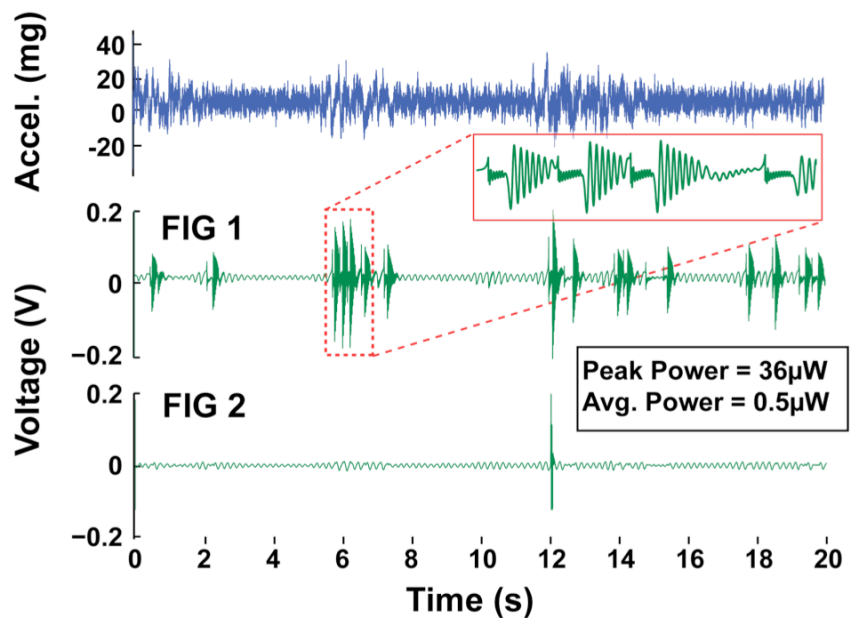
Figure 5-19. Gen 4 PFIG response when excited by a non-periodic vibration. The top plot shows the acceleration signal felt by the PFIG. It is an amplified 20 second extract from the data presented in Figure 5-2. The acceleration signal has been amplified such that the peaks occur at 40mg. The bottom two traces show the voltage from the two FIGs.

176

5.5.3 HARVESTER SYSTEM RESULTS

In order to show the viability of scavenging and using the vibration energy found on bridges, the Gen 4 device was interfaced with the multiplier circuit discussed in Section 5.3.3. The generator was subjected to bridge-like vibrations in a similar manner as the previous Section 5.5.2. The acceleration signal is shown in Figure 5-20a. This was once again a slightly amplified version of the original data (shown in the figure insert). The voltage on the storage capacitor at the end of the multiplier tree is shown in Figure 5-20b. Some ripples can be seen on the rising voltage. The ripples were caused by the parasitics associated with the circuit discharging the capacitor in the portions of time where there was a gap between acceleration spikes. Of course, in future iterations of the interface circuitry, parasitics can be minimized by a cleaner implementation on a printed circuit board, and even integration on chip. Also, the stored energy will not be on a device with such a large leak rate as an electrolytic capacitor. The most promising solution is to use a rechargeable battery. Figure 5-20c shows the output of the ring oscillator, which was connected to the multiplier via a push-button switch. The oscillation of the load device decays since the voltage output from the storage capacitor was not regulated. The system test has also been carried out using less amplified signals such as the ones in Figure 5-18 and in Figure 5-19. These resulted in much slower capacitor charging. When the acceleration is nearly identical to that on the bridge, the parasitics in the circuit overwhelm incoming energy because of the less frequent actuation in the FIGs. Nonetheless, this power conversion system showed for the first time that the decaying voltage produced by PFIG operation could be rectified, boosted, and stored.
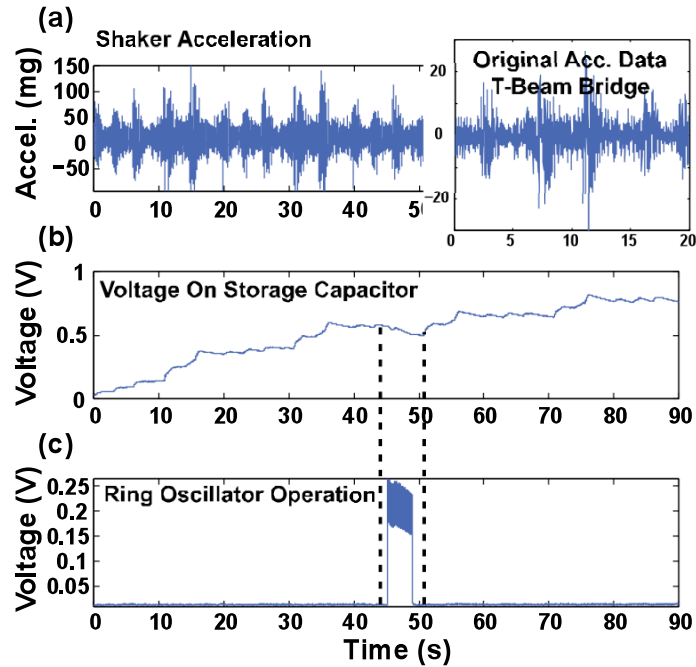
Figure 5-20. PFIG energy harvesting system test showing the Gen 4 device converting bridge-like vibrations and converting them into stored usable energy via the multiplier circuit. a) A recording of the acceleration used to drive the PFIG. b) Voltage on the storage capacitor rising over time. c) Unregulated power is used to drive the ring oscillator.

5.6 DISCUSSION

In a rewarding way, the fourth generation PFIG was the first to operate exactly as the generator architecture was originally envisioned. In the original concept, the latching magnets on the FIGs had a dual purpose of: 1) making a physical connection between the inertial mass and the FIG, and 2) assisting the inertial mass in leaving the FIG and accelerating away. In the Gen 2 and Gen 3 devices, the second of these functions, while present, is much less pronounced. The large inertial mass to magnetic field ratio allows the Gen 4 device to exploit this effect more freely.

Essentially, at the lowest points in the frequency and acceleration ranges of the PFIG, the inertial mass exists in a bi-stable state created by the two magnetic forces pulling it from either end. Small perturbations in its equilibrium can push it one way or the other.

178

Even when latched to one FIG or the other, the stability is not improved greatly since the inertial mass never really leaves the influence of the opposing magnetic field. This bi-stability has one major advantage and one major disadvantage. The advantage is that the inertial force needed to cause the mass to actuate the FIGs is reduced, relative to the force that would be needed if the opposing magnetic field were not present. In other words, a greater magnetic latching force (greater magnetic field) results in a lower minimum acceleration needed for the PFIG to operate. This is counterintuitive, because one would assume that the higher magnetic force would make it more difficult for the actuation to occur. The concept is best illustrated by simulating the PFIG response to an acceleration profile such as the one found on a typical bridge, because the different amplitudes that exist can be used to illustrate the bi-stability. Figure 5-21 shows the simulated behavior of the PFIG in response to the acceleration profile shown in the top of the figure. Comparing the top two plots showing the deflection in the FIGs with the bottom two, one can see that the device on the bottom undergoes more actuation cycles. By tripling the magnetic force, the acceleration threshold that would induce the inertial mass to leave the FIG is lowered. Upon close examination of the displacement profile in each case, one can see that the movement of the FIGs in the high magnetic field scenario has been distorted. The movement of the non-attached FIG is influenced by the position of the inertial mass, through the magnetic force of attraction between them.
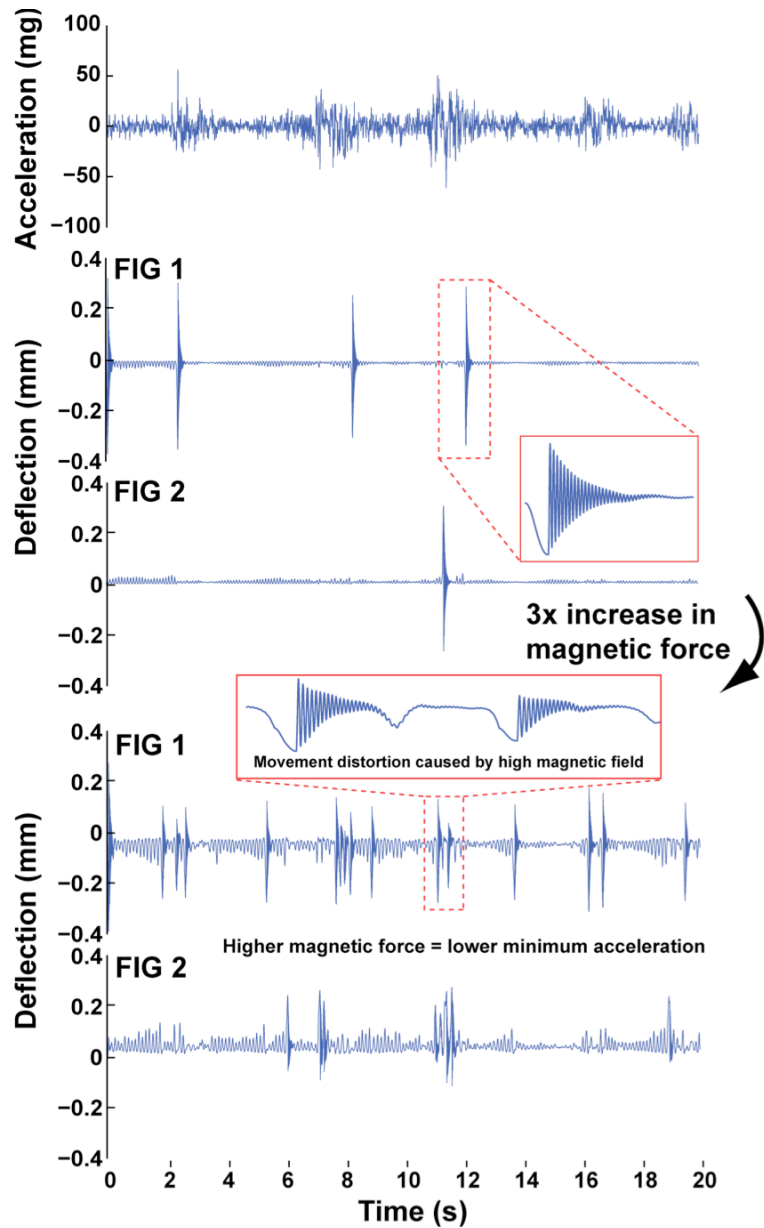
Figure 5-21. Simulated deflection in both FIGs in response to the acceleration shown in the top plot demonstrating the bi-stability of the inertial mass. Between the first two waveforms (FIG 1 and FIG 2) and the bottom two (FIG1 and FIG2) everything is kept constant, except the magnetic field caused by the latching magnets is increased by a factor of 3. The greater magnetic field, counter-intuitively, allows the PFIG to operate at lower accelerations.

The previous discussion leads directly to the main disadvantage of utilizing this instability. There is an ever-present magnetic force strongly affecting the motion of the FIG, which manifests itself as parasitic mechanical damping during the power generation cycle. The magnetic force causes the FIG motion to decay quickly. The augmented

180

motion of the FIG can be seen in the close-up shown in Figure 5-21. A related issue is that by increasing the magnetic field, the amplitude at which the FIG is released has been made smaller. This acts in combination with the increased mechanical damping to ultimately lower the energy converted per actuation cycle. Because of this, it is not immediately clear if the increased actuation cycles ultimately lead to the extraction of more energy. This effect needs to be studied and optimized numerically in greater detail.

The bi-stable operation of the PFIG and the increased influence of the latching magnets can be observed in practice, as well. Figure 5-22 shows the voltages generated by the FIGs when actuated periodically at the minimum acceleration of 55mg. Voltage traces from operation at 2, 5, and 10Hz can be seen. At the lower frequency when the velocity is limited and the inertial mass movement is reduced, the influence of the magnetic field on the FIG motion can be seen in the voltage profile. As the frequency increases to 10Hz, which is close to the natural frequency of the inertial mass/suspension system, and the velocity and displacement are increased, the FIG motion is influenced less. The higher velocity results in the inertial mass latching to the opposing FIG and pushing both devices further away to positions where they cannot influence the other FIG. There is sufficient room for this, because the magnetic forces cause the FIGs to operate at different equilibrium points within $gap_{T,B}$. This can be seen by closely observing Figure 5-21, which shows that the FIGs do not oscillate around zero. The PFIG system is heavily reliant on the inertial mass response and the interaction with the magnetic forces imposed by the FIG magnets. This explains the limited frequency response as seen in Figure 5-16. At the lowest acceleration, the dependence on the inertial mass velocity and the momentum dictate the operation of the PFIG, amplified by the

181

magnetic bi-stability. As the acceleration increases, these effects become less relevant, and the dynamic behavior of the PFIG, as observed in previous generations of the device, takes over.
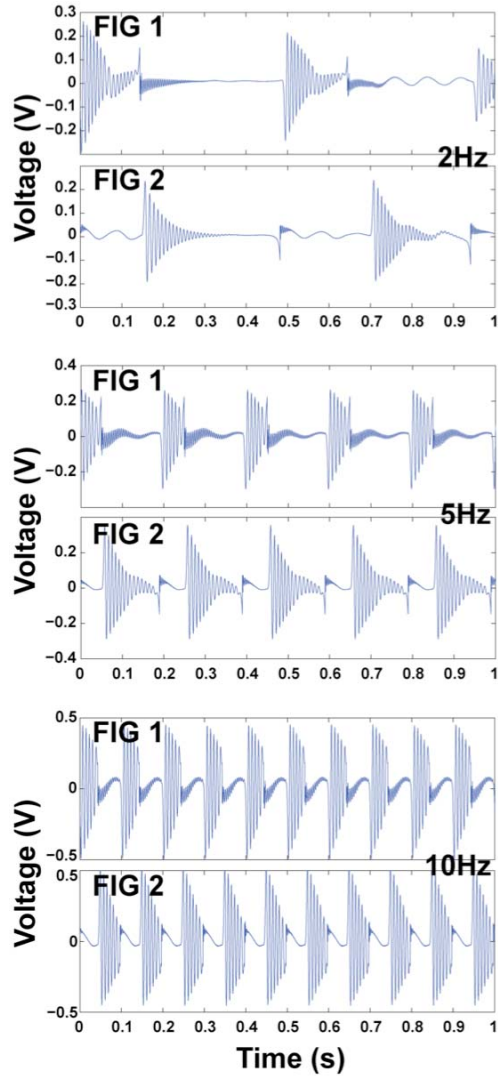
Figure 5-22. FIG voltage during actuation from a 55mg sinusoidal acceleration at 2, 5, and 10Hz.

5.7 GEN 4 PERFORMANCE

A performance comparison for the Gen 4 device can be seen in Figure 5-23. The Volume Figure of Merit (FoMv) of the PFIG generator was on par with the previous two

generations when calculated at the extreme low operating frequency of 2Hz, and it is increased significantly when all three devices are compared at 10Hz. It had a FoMv of 0.04% at the lowest end of its operating range. The Gen 4 PFIG significantly outperforms other efforts in the low end of the frequency spectrum (<10Hz). In fact, its efficiency would be significantly higher was in not for its increased volume. The Gen 4 device was designed for testing in a real application, and the space needed to make it sufficiently robust led to a large volume. For example, space exists inside the device for an energy conversion interface printed circuit board to be attached to each FIG, however, this interface has not yet been implemented. The FIGs themselves are about 25% larger than they need to be for the particular transduction design in use. Lastly, there is a great deal of spaced designed to be able to manipulate the FIG/mass gap for testing purposes, and this is not necessary for operation.

The bandwidth performance of the PFIG generator remains close to the previous electromagnetic implementation. The FoMv-BW for the Gen 4 device is 0.19%. However, more important than this metric of efficiency is having shown, for the first time, the efficient and robust operation of a vibration harvesting system in ambient conditions with non-periodic arbitrary vibrations.
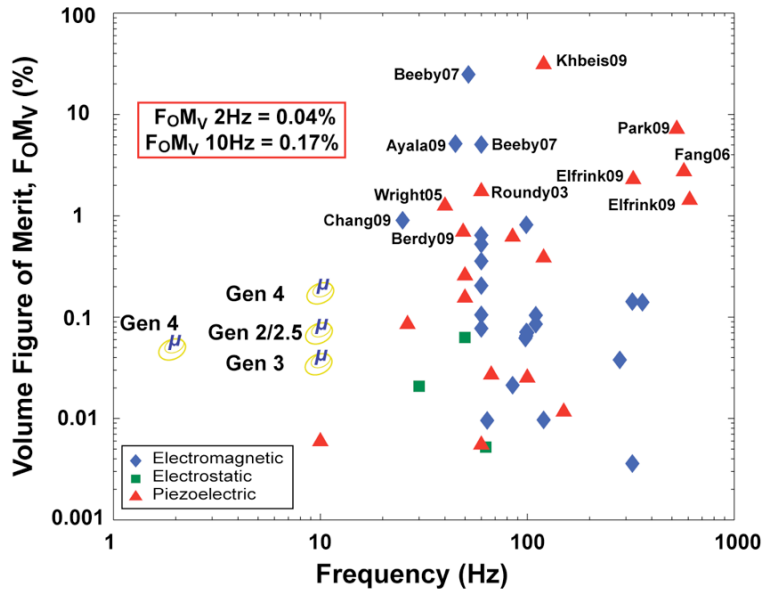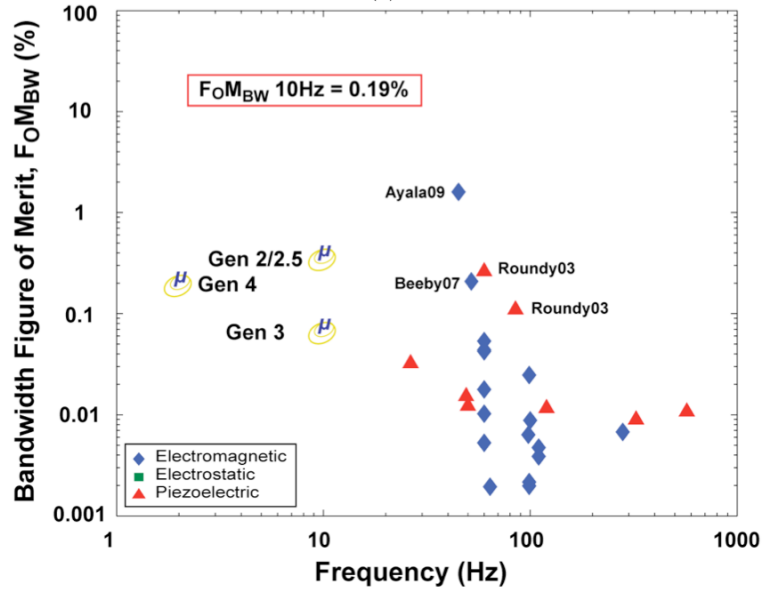
Figure 5-23. a) Volume Figure of Merit (FoMv) comparison of the PFIG generator to the state-of-the-art in vibration scavengers. b) Bandwidth Figure of Merit (FoM_BW) comparison of the PFIG generator to the state-of-the-art in vibration scavengers.

5.8 CONCLUSION

This chapter presented the design, fabrication, and testing of an electromagnetic inertial micro power generation system for scavenging the very low-amplitude, low

frequency, and non-periodic vibrations present on bridges. The design of the system was based on the analysis of the ambient environment found on two popular bridge types. The fabricated device generated a peak power of 57µW and an average power of 2.3µW from an input acceleration of 0.54m/s^2 (55mg) at only 2Hz. The device bandwidth at 55mg is 18Hz. The internal volume of the generator is 43cm^3 (68cm^3 including casing). The generator is capable of operating over an unprecedentedly large acceleration range (0.54-9.8m/s^2) and frequency range (up to 30Hz) without any modifications or tuning. Scavenging energy from arbitrary vibrations was demonstrated by using an acceleration recording from the Grove Street bridge, and by reproducing the ambient environment on the shaker table. Enough energy was generated to overcome the standby power of the wireless sensing system being developed, as well as to have extra power to accumulate for data transmission.

Chapter 6

CONCLUSION

The past several years have seen dramatic advancements in the size and energy efficiency of electronics. The considerable progress has enabled the development of portable wireless devices for various applications such as sensing, data collection, and data transmission. In the mass media and society, this has spawned great expectations for 'smart' homes, factories, grids, and cities. Automation systems employing millions of networked wireless sensors are expected to lead to unparalleled process and energy efficiency, comfortable living, security, and safety. While much work remains in developing the technologies to manage, process, and store the massive amount of data that will result from these information gathering technologies, the single greatest hurdle to the realization of 'smart' systems that exists on the physical (device) layer is the availability of cheap, long-lasting energy. Currently the majority of "wireless" sensors are still hardwired to external power sources. Tethering a wireless sensor to a hard-wire significantly limits its utility and practicality, and it can bring about a near tenfold markup in the cost of installation.

One of the most abundant energy sources is ambient motion, and over the past few years a great deal of research has gone into developing ways to use it effectively. In particular, ambient vibrations are of great interest because they exist in many settings

186

where self-powered long lifetime electronics will find highly desirable applications. Vibrations can provide abundant energy, and they can be transferred through many media, making this form of kinetic energy very useful. A vast majority of research efforts to date are aimed at utilizing resonant systems to scavenge high frequency periodic vibrations from machines or other man made sources. However, there are many applications where the available vibrations do not fit this mold. Low frequency motion is prevalent in applications such as wearable and implantable devices, environmental monitoring, agricultural applications, and security uses. Little work had been reported in this realm prior to this thesis. This type of kinetic energy poses a number of challenges. Low-frequency scavengers suffer from a decrease in the expected power density because 1) the required spatial displacement (and thus volume) is increased, 2) low frequency vibrations will produce weaker electromechanical coupling in the conversion mechanism, and 3) these types of vibrations are predominantly non-periodic. The non-periodicity of the vibrations necessitates the invention of scavenger architectures that do not rely on resonant operation.

6.1 THESIS CONTRIBUTIONS

This thesis discussed the development of a newly invented architecture for scavenging low frequency and non-periodic vibrations called the Parametric Frequency Increased Generator (PFIG). Three different implementations of the PFIG generator were developed and demonstrated. They have a combined operating range covering two orders of magnitude in acceleration and a frequency span of 0-60Hz, making them some of the most versatile generators in existence. The performance and the operating range of the developed harvesters is illustrated by Figure 6-1, where it is overlaid on top of the

vibration characteristics found in a number of different energy scavenging applications. This figure is best able to summarize the performance of the PFIG generators, showing how their operating range spans multiple different application areas in comparison to resonant devices, which are optimized for very specific vibration criteria. The achieved Volume Figure of Merit (FoMv) for the three devices is also included in Figure 6-1, in comparison to all other reported works.
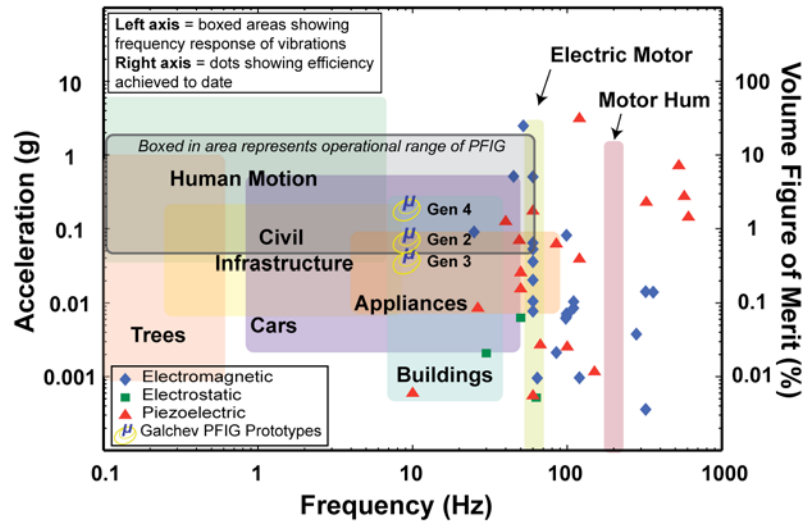
Figure 6-1. Composite plot showing the frequency response of the vibrations in typical environments with where energy harvesting applications may be found, along with the F_oM_v of vibration scavengers reported to date, including the PFIG harvesters developed in this thesis.

This thesis provided contributions that span a number of realms including the design and theory of vibration harvesters, technology and process development, and system level implementation and integration. With respect to the first category, design and theory of vibration harvesters, significant contributions include:

- Invention of a new vibration harvester architecture called the Parametric Frequency Increased Generator (PFIG)

- Development of a theoretical framework for analyzing, designing, and optimizing PFIG generators

- A software-based tool developed for simulating the dynamic behavior of the PFIG in response to periodic and arbitrary stimuli.

- Presentation of the environmental vibration characteristics vs. type of harvester tradeoffs and ideal operating range.

- Discussion of the design trade-offs including power vs. bandwidth, volume vs. power, etc

Validating the design and theory of the PFIG was achieved by manufacturing three generations of harvesters. The implementation of these devices led to a number of contributions on both technology and process development including:

- Design and implementation of an electromagnetic PFIG for large displacement, low-frequency vibrations

- Optimization of single magnet/coil electromagnetic transducer layout

- Development of a hybrid manufacturing and assembly process for producing the electromagnetic PFIG out of both lithographic and conventional processing means

- Design and implementation of a piezoelectric PFIG for large displacement, low-frequency vibrations

- Design and optimization of a spiral clamped-clamped piezoelectric bimorph transducer

The work in developing the PFIG architecture led to the development of an energy harvesting system for critical infrastructure monitoring. Contributions related to the system level implementation include:

- Design of an electromagnetic PFIG that can be broadly used in different bridge

environments. The design was based on the analysis of the vibrations on two fundamentally different bridge types.

- Development of a method to effectively bias the PFIG and eliminate the effect of gravity

- Demonstration of how magnetically induced bi-stability can be used to reduce the minimum acceleration needed for operation

- Development of an energy harvesting system including a discrete component power conversion electronic system

- Demonstration of the effective and efficient conversion of arbitrary bridge vibrations into electricity

In addition to the broad contributions attained during the development of the three PFIG generators, the devices themselves have set a number of records in terms of performance. The first electromagnetic PFIG harvester (Gen 2) generated a peak power of 163μW and an average power of 13.6μW from an input acceleration of $9.8/s^2$ at 10Hz. The device can generate energy from vibrations up to 60Hz. The internal volume of the generator is $2.12cm^3$. It sets the state-of-the-art in efficiency for vibration harvesters operating in the <20Hz range. The volume figure of merit is 0.068%, which is an order of magnitude improvement over other published works. The Gen 2 PFIG has the highest bandwidth figure of merit (0.375%) of all existing vibration harvesters that do not utilize active tuning. A subsequent piezoelectric PFIG implementation (Gen 3) produced 3.25μW of average power from an input acceleration of $9.8/s^2$ at 10Hz. The piezoelectric transduction mechanism allowed for a more compact implementation and the volume of the generator was halved ($1.2cm^3$) compared to Gen 2. This device also has a wide band

190

response with a maximum cutoff frequency of 24Hz. The second electromagnetic PFIG (Gen 4) that was developed for infrastructure monitoring generated a peak power of 57μW and an average power of 2.3μW from an input acceleration of 0.54m/s^2 (55mg) at only 2Hz. The internal volume of the generator is 43cm^3. It is capable of operating over an unprecedentedly large acceleration range (0.54-9.8m/s^2) and frequency range (up to 30Hz) without any modifications or tuning.

6.2 SUGGESTIONS FOR FUTURE WORK

While the work described in this thesis has contributed significantly to the state-of-the-art in vibration harvesters, a number of challenges and interesting research topics still exist.

To make the PFIG generators commercially viable, their performance has to be improved by a further order of magnitude in terms of efficiency. As a first step toward achieving this a more sophisticated numerical modeling tool needs to be developed. Due to the dynamic behavior of the PFIG, the only way to truly design and optimize it is further numerical modeling. A more complete model needs to be developed incorporating all of the energy loss and transfer mechanisms, especially during the latching. Once this is done, numerical optimization techniques need to be incorporated in order to design the PFIG mechanically. Second, an efficiency improvement will require at least a factor of 10 increase in the electrical damping ratio. For electromagnetic harvesters this will entail creating a transducer that prevents the magnetic flux from spreading out, but rather contains it within a magnetic circuit, while at the same time not significantly increasing the mass or impacting the mechanical performance of the FIG.

Analysis and design for reliability goes hand in hand with future advanced engineering

efforts to make the PFIG commercially viable. One of the inherent specifications for all energy harvesters is a long operating lifetime: 10-20 years and perhaps several hundred million to a few billion cycles. The academic community, most commercial efforts, as well as this thesis project have not focused on the topic of reliability. Instead, harvesters are built for performance and result in overstressing materials and choosing inappropriate materials whose longevity is not well understood. Almost no long term testing has been performed and demonstrated. With respect to the PFIG, the most important reliability issues have to do with the moving components: fatigue in the springs (particularly in the inertial mass suspension) and wear in the latching mechanism due to the occurrence of impact strain. Another aspect that is closely related to reliability is the design for operation in inhospitable environments and temperatures. Energy harvesters need to achieve similar performance to MIL-SPEC (US military specification) even for most applications that would not normally be considered harsh-environment. Even a harvester designed for operating on a typical bridge will likely be exposed to very harsh elements including direct sun exposure, rain, snow, etc. Future design efforts need to investigate the physics of failure and perform parts stress modeling. Additionally, well designed accelerated life tests need to be used to demonstrate reliability. Lastly, because there are significant unknowns, component and parts derating will need to be used to reduce the probability of failure.

It was shown that the PFIG is an excellent candidate for efficient operation over an even bigger range of ambient conditions as compared with resonant devices. This is especially true when considering implementation in the micro scale, where the volume and internal displacement are severely limited. Developing a MEMS PFIG generator is a

fascinating research area that poses a number of technology and processing challenges. New technologies will have to be developed to incorporate dense materials for making the inertial mass in wafer-level fabrication processes while providing precision and large deflection capability. The most likely transduction mechanism for MEMS PFIGs will be piezoelectric, because of the volume advantage piezoelectrics offer. Vacuum encapsulation can help minimize parasitic mechanical damping and can allow more mechanical energy to be converted to electrical energy. A MEMS PFIG will have to effectively integrate magnetic material for the latches, or new electrostatic or mechanical latching mechanisms will have to be developed.

Lastly, a very important area of future research will be in converting and managing the electrical energy coming out of the PFIG. These types of generators provide a significant challenge to power electronics because of their decaying output signal and intermittent operation. A much more efficient power conversion system will have to be designed. The initial circuit presented in Chapter 5 can be integrated and modified to use active components rather than passive diodes. An active rectification scheme eliminates the loss associated with the turn on voltage of the diodes at the expense of minimal power consumption. A more sophisticated energy management circuit can also incorporate feedback control of the PFIG generator itself.

Energy harvesting technology will enable many 'smart' technologies that can have a great impact on society in facilitating the gathering and use of information to live healthier and more content lives while utilizing resources more efficiently. However, further work is needed to reduce harvester cost, and to improve harvester utility and reliability.

APPENDIX A

The first Parametric Frequency Increased Generator (PFIG) was developed to validate the proposed system architecture. To this end, the prototype was designed with the highest flexibility in order to be able to manipulate the various mechanical parameters and study their influence. The Gen 1 PFIG was developed as three separate pieces, the two FIGs and the inertial mass. The three pieces are combined on a bench-top hybrid assembly to form the complete PFIG generator. Two of the three components are mounted on movable micropositioners so that their relative positions can be changed in the z-axis. The test setup is shown in Figure A-1. Additionally, this hybrid approach gives flexibility in interchanging components, characterizing the influence of and optimizing various parameters, and validating theoretical modeling of the system.
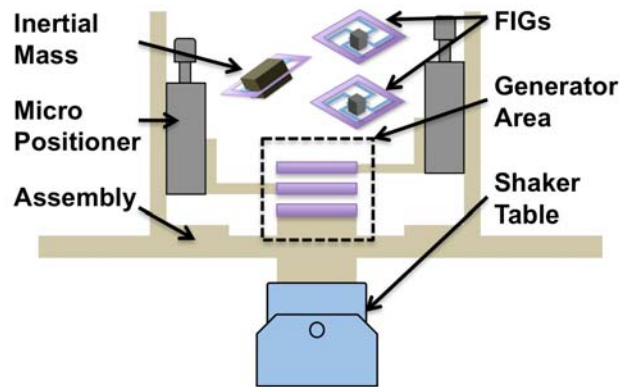
Figure A-1. PFIG hybrid assembly and test setup illustration.

FABRICATION

The generator consists of a number of discrete components that are used to hold the FIGs and inertial mass in place. All of this hardware, including the L-brackets that hold the micropositioners, the metal frame that extends from the micropositioner and holds the generator component in place, and the base plate, are machined out of aluminum. Spring suspensions for both the FIG and the inertial mass are fabricated out of 127μm thick copper alloy 110. The copper sheets are mounted on carrier silicon wafers using photoresist, lithographically patterned, and immersion etched in $FeCl_2$ at 45°C. NdFeB latching magnets are bonded to the inertial mass and FIG springs using cyanoacrylate. Small 2x2mm pieces of stainless steel comprise the ferromagnetic actuation area. Coils are wound from 50μm diameter enameled copper wire. The FIG components are mounted within a specially machined acrylic housing. The FIG housing is attached to the metal supporting structure using 4-40 screws, while the inertial mass spring is clamped in place using a screwed-in aluminum ring. The fabricated test setup and mounted PFIG are shown in Figure A-2a. Figure A-2b shows a close-up of one of the FIG cases revealing the coils, magnet, and assembled device. The entire test jig is mounted on a shaker system for vibration testing.
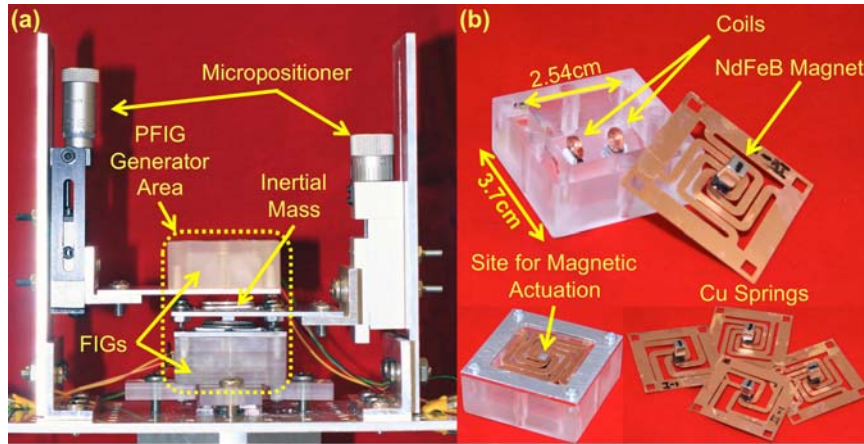
Figure A-2. a) Photograph of the assembled parametric generator and test setup. The top Frequency Increased Generator (FIG) and the inertial mass are mounted on micropositioners to freely tune the displacement gap. b) Detailed view of one of FIG components.

TEST RESULTS

Initial testing was performed to characterize the FIG devices. Each FIG was mounted on the test setup and actuated by providing an impulse using the area for magnetic actuation. Waveform traces of the generated output voltage are used to determine the natural frequency of the device, as well as to investigate the parasitic damping and electromechanical coupling of the system. These parameters can be extracted by processing the waveform to determine the frequency response. The frequency response is computed by taking the Discrete Fourier Transform of the voltage signal. Open circuit and loaded impulse response measurements are made, and they are used to determine the electromechanical coupling quality factor Q_e. Table A-1 shows a summary of the measured parameters for the FIGs. Four springs with different spring constants were fabricated, and Table A-1 shows results from each spring.

Table A-I. Gen 1 FIG Summary

Mass	1.2g			
Disp. Limit	1mm			
Coil Turns	2000			
Coil Resistance	295Ω			
Magnet	NdFeB 4.5x4.5x4.5mm			
	k^* (N/m)	f_o (Hz)	Q_p	Q_e
Spring 1	559	103	61	94
Spring 2	787	115	66	96
Spring 3	1053	137	61	138
Spring 4	1169	145	54	148

*Denotes Simulated Value

The PFIG is assembled on the test setup. Nominally FIG spring 1 is used for testing. The PFIG is designed for a minimum acceleration of 1g and it is characterized at that level. The minimum frequency at which the generator can be tested accurately is 10Hz due to limitations associated with the vibration test system. However nothing prevents the generator from functioning at lower frequencies, albeit at a reduced power level. Each FIG is loaded with a 270Ω resistor. Figure A-3 shows the operation of the PFIG. The top two plots show the voltage generated by each FIG across the load and the bottom plot shows the instantaneous power from FIG 2. One can discern from the voltage plots where the inertial mass attaches to each FIG, and where the mass detaches and travels to the opposing device. It is apparent from this plot that the two FIG devices are not operating symmetrically. Part of this non-symmetry is due to the fact that the top FIG device is suboptimal. The main reason for this is that due to hand assembly of the FIG casing, a larger gap has resulted between the coils and the magnet, decreasing the electromechanical coupling. However, asymmetry in the FIGs cannot be entirely avoided and mainly results from the complex interaction between the lathing magnet and the FIG just prior to lathing and immediately after release.
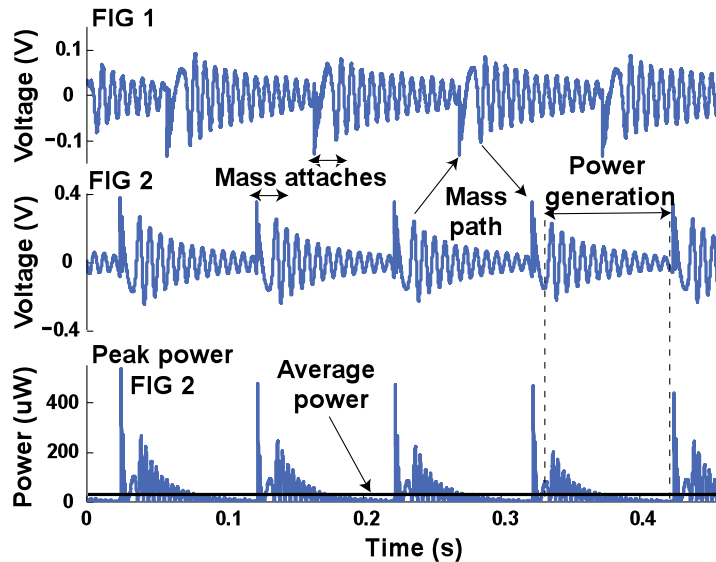
Figure A-3. Oscilloscope trace showing the parametric generator operation from an external acceleration of 1g at 10 Hz. The top and bottom voltage waveforms correspond to the top and bottom FIG devices as the inertial mass snaps back and forth between them. The bottom plots shows instantaneous power from FIG 2.

The PFIG generator consists of three spring-mass-damper systems. Many parameters have complex interactions and are of critical importance. The inertial mass size, coupled with the distance between each of the FIGs and the magnetic force of attraction, determine the minimum external vibration level needed for operation. For a certain actuation gap and inertial mass, an optimal FIG spring stiffness exists. Figure A-4 shows a simulation of the optimal spring stiffness. Four FIG springs are fabricated to validate this simulation. Measured results using each of those springs are also shown. After determining an optimal spring constant, the FIG mass can be reduced to increase the FIG frequency, thus further enhancing the power generating capability (frequency up-conversion). Since power $\sim mY^2\omega^3$, for a fixed displacement Y, mass can be reduced to increase ω. The simulated increase in power when the mass is cut in half is also shown in Figure A-4.
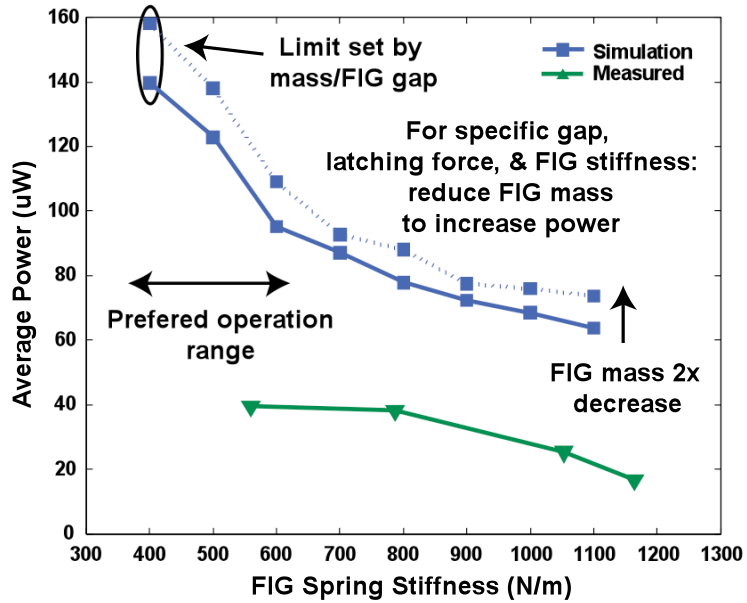
Figure A-4. Measured vs. simulated performance of the PFIG generator as a function of the FIGs spring constants (all other parameters constant). Input acceleration is 1g at 10 Hz.

The bandwidth of the Gen 1 PFIG device is mainly influenced by the resonant frequency of the inertial mass and its spring suspension. Above this frequency the inertial mass cannot respond fast enough to the input motion. Complex interactions that have been shown to increase the operating range of the later PFIG generations are not present in the Gen 1 device because of the large gap that is used. The device can be designed to operate up to a specific frequency by increasing the spring constant of the inertial mass. Figure A-5 shows the measured performance of the PFIG as the input frequency is increased. By increasing the spring constant of the inertial mass by 2, the PFIG cutoff frequency is increased by a factor of 1.4; from 22Hz to 31Hz.
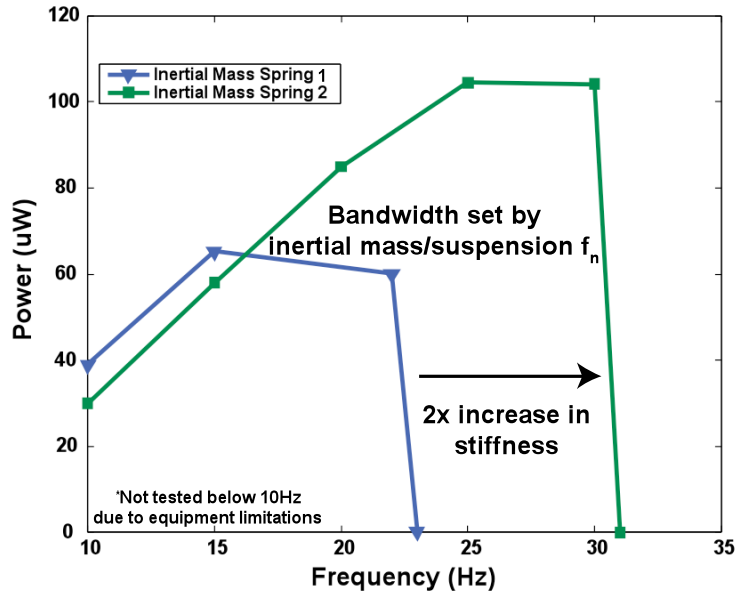
Figure A-5. Measured frequency response of the PFIG generator. The cut-off frequency is determined by the inertial mass/spring suspension natural frequency. By altering the suspension stiffness the bandwidth can be increased to a suitable value. Input acceleration is 1g at 10 Hz.

A summary of the PFIG performance is shown in Table A-2. The device is able to generate an average power of 39μW (combined FIG 1&2). A functional volume of 3.7cm^3 is calculated for the PFIG device: this includes the volume of all of the components (springs, mass, magnets, and coils) as well as the 'air' volume needed for displacement during operation.

Table A-2. Gen 1 PFIG Summary

Inertial Mass	9.63g
Suspension Spring	67 N/m*
Actuation Gap	2mm
Actuation Magnet	NdFeB, Dia. 1.15mm, Thk. 0.5mm
Actuation Area	2mm x 2mm
Peak Power (1g, 10Hz)	558.2 (μW)
Avg. Power (1g, 10Hz)	39.45 (μW)
Functional Volume	3.68 cm^3
Average Power Density	10.7 μW/ cm^3

*Denotes Simulated Value

CONCLUSION

A bench-top PFIG is developed and tested. The purpose of the Gen 1 PFIG is to validate and demonstrate the new architecture. The Gen 1 electromagnetic implementation is assembled on a hybrid test setup that can be modified and reconfigured. The fundamental operation of the PFIG, wherein a bi-stable mechanical structure is used to initiate high-frequency mechanical oscillations in an electromagnetic scavenger, is demonstrated. The Gen 1 PFIG is able to demonstrate the basic interactions between the inertial force, latching strength, FIG spring, and FIG natural frequency. A fundamental result is that for a specific latching force, the spring constant should be minimized to maximize the transferred mechanical energy from the inertial mass to the FIG. The Gen 1 device also demonstrates the first-order PFIG operational range dependence on the inertial mass resonator natural frequency.

REFERENCES

[1]   M. Seok, S. Hanson, Y. Lin, Z. Foo, D. Kim, Y. Lee, N. Liu, D. Sylvester, and D. Blaauw, "The Phoenix Processor: A 30pW platform for sensor applications," in *IEEE Symposium on VLSI Circuits*, Honolulu, HI, 2008, pp. 34-35.

[2]   R. Salot, S. Bancel, S. Martin, G. Savelli, C. Salvi, and M. Plissonnier, "Thermoelectric and microvibratory hybrid system with its power management," in *DTIP of MEMS and MOEMS*, Stresa, Italy, 2006.

[3]   S. Roundy, E. S. Leland, J. Baker, E. Carleton, E. Reilly, E. Lai, B. Otis, J. M. Rabaey, V. Sundararajan, and P. K. Wright, "Improving power output for vibration-based energy scavengers," *Pervasive Computing, IEEE,* vol. 4, pp. 28-36, 2005.

[4]   J. A. Paradiso and T. Starner, "Energy scavenging for mobile and wireless electronics," *IEEE Pervasive Computing,* vol. 4, pp. 18-27, 2005.

[5]   M. Hatler, D. Gurganious, and M. Ritter, "Perpetual power solutions for wireless sensor networks," ON World Inc., 2008.

[6]   H. Chisholm, "Encyclopedia Britannica " 11th ed. Cambridge University Press.

[7]   C. Ohl, "Light-sensitive electric device," US Patent 2402662, 1941.

[8]   A. Luque and A. Marti, "Ultra-high efficiency solar cells: the path for mass penetration of solar electricity," *Electronics Letters,* vol. 44, pp. 943-5, 2008.

[9]   D. K. A. Barnett, C.B. Honsberg, et. al., "Milestones toward 50% efficient solar cell modules," in *22nd European Photovoltaic Solar Energy Conference*, Milan, Italy, 2007, pp. 95-100.

[10]   M. Kishi, H. Nemoto, T. Hamao, M. Yamamoto, S. Sudou, M. Mandai, and S. Yamamoto, "Micro thermoelectric modules and their applications to wristwatches as an energy source," in *18th International Conference on Thermoelectrics*, 1999, pp. 301-307.

[11]   N. Ghafouri, H. Kim, M. Atashbar, and K. Najafi, "A micro thermoelectric energy scavenger for a hybrid insect," in *IEEE Sensors*, Lecce, Italy, 2008, pp. 1249-1252.

[12]   Thermo Life Energy Corp., January, 2009. [Online]. Available: http://www.poweredbythermolife.com.

[13]   E. Yeatman, "Advances in power sources for wireless sensor nodes," in *International Workshop on Wearable and Implantable Body Sensor Networks*, Imperial College, London, 2004, pp. 20-21.

[14]   J. Schuder, "Powering an artificial heart: birth of the inductively coupled-radio frequency system in 1960," *Artificial Organs,* vol. 26, pp. 909-915, 2002.

[15]   N. Tesla, "System of transmission of electrical energy," USPTO Patent 645576, 1897.

[16] A. Kurs, A. Karalis, R. Moffatt, J. D. Joannopoulos, P. Fisher, and M. Soljacic, "Wireless power transfer via strongly coupled magnetic resonances," *Science,* vol. 317, pp. 83-86, July 6 2007.

[17] S. Roundy, "Energy Scavenging for wireless sensor nodes with a focus on vibration to electricity conversion," PhD Thesis, UC Berkeley 2003.

[18] F. Liu, A. Phipps, S. Horowitz, N. Khai, L. Cattafesta, T. Nishida, and M. Sheplak, "Acoustic energy harvesting using an electromechanical Helmholtz resonator," *Journal of the Acoustical Society of America,* vol. 123, pp. 1983-90, 2008.

[19] S. Roundy, J. Bryzek, C. Ray, M. Malaga, and D. Brown, "Power generation utilizing tire pressure changes," WIPO Patent WO/2007/044443, 2005.

[20] J. A. Potkay and K. Brooks, "An arterial cuff energy scavenger for implanted microsystems," in *2nd International Conference on Bioinformatics and Biomedical Engineering ICBBE* 2008, pp. 1580-1583.

[21] A. Lal and J. Blanchard, "Daintiest dynamos " *IEEE Spectrum,* vol. 41, pp. 36-41, 2004.

[22] A. Lal, R. Duggirala, and H. Li, "Pervasive power: a radioisotope-powered piezoelectric generator," *Pervasive Computing, IEEE,* vol. 4, pp. 53-61, 2005.

[23] R. Duggirala, R. Polcawich, E. Zakar, M. Dubey, H. Li, and A. Lal, "MEMS radioisotope-powered piezoelectric u-power generator (RPG)," in *19th IEEE International Conference on Micro Electro Mechanical Systems MEMS'06*, Istanbul, Turkey, 2006, pp. 94-97.

[24] P. D. Mitcheson, E. M. Yeatman, G. K. Rao, A. S. Holmes, and T. C. Green, "Energy Harvesting From Human and Machine Motion for Wireless Electronic Devices," *Proceedings of the IEEE,* vol. 96, pp. 1457-1486, 2008.

[25] A. Betz, "*Introduction to the theory of Flow Machines,*" Oxford Pergamon Press, 1966.

[26] C. Federspiel and J. Chen, "Air-powered sensor," in *IEEE Sensors*, 2003, pp. 22-25

[27] A. S. Holmes, H. Guodong, and K. R. Pullen, "Axial-flux permanent magnet machines for micropower generation," *Journal of Microelectromechanical Systems,* vol. 14, pp. 54-62, 2005.

[28] R. Myers, M. Vickers, K. Hyeoungwoo, and S. Priya, "Small scale windmill," *Applied Physics Letters,* vol. 90, pp. 54106-1, 2007.

[29] A. S. Holmes, G. Hong, K. R. Pullen, and K. R. Buffard, "Axial-flow microturbine with electromagnetic generator: design, CFD simulation, and prototype demonstration," in *17th IEEE International Conference on Micro Electro Mechanical Systems MEMS'04*, Piscataway, NJ, USA, 2004, pp. 568-71.

[30] D. Rancourt, A. Tabesh, and L. G. Frechette, "Evaluation of centimeter-scale micro wind mills: Aerodynamics and electromagnetic power generation," in *PowerMEMS*, Freiburg, Germany, 2007, pp. 93-96.

[31] N. S. Shenck and J. A. Paradiso, "Energy scavenging with shoe-mounted piezoelectrics," *IEEE Micro,* vol. 21, pp. 30-42, 2001.

[32] J. Kymissis, C. Kendall, J. Paradiso, and N. Gershenfeld, "Parasitic power harvesting in shoes," in *Second International Symposium on Wearable Computers*, 1998, pp. 132-139.

[33]   J. Paradiso and M. Feldmeier, "A compact, wireless, self-powered pushbutton controller," in *Ubicomp 2001*, 2001, pp. 299-304.

[34]   E. E. Aktakka, H. Kim, M. Atashbar, and K. Najafi, "Mechanical energy scavenging from flying insects," in *Solid-State Sensors, Actuators, and Microsystems Workshop (Hilton Head 2008)*, Hilton Head, SC, 2008, pp. 382-382.

[35]   EnOcean, February, 2009. [Online]. Available: www.enocean.com.

[36]   R. Guigon, J. J. Chaillout, T. Jager, and G. Despesse, "Harvesting raindrop energy: experimental study," *Smart Materials and Structures,* vol. 17, pp. 015039-1, 2008.

[37]   R. Guigon, J. J. Chaillout, T. Jager, and G. Despesse, "Harvesting raindrop energy: theory," *Smart Materials and Structures,* vol. 17, pp. 015038-1, 2008.

[38]   T. Starner, "Human-powered wearable computing.," *IBM Systems Journal,* vol. 35, pp. 618-629, 1996.

[39]   E. M. Yeatman, P. D. Mitcheson, and A. S. Holmes, "Micro-engineered devices for motion energy harvesting," in *IEEE International Electron Devices Meeting IEDM*, 2007, pp. 375-378.

[40]   T. Sterken, K. Baert, C. Van Hoof, R. Puers, G. Borghs, and P. Fiorini, "Comparative modelling for vibration scavengers," in *IEEE Sensors*, 2004, pp. 1249-52.

[41]   P. D. Mitcheson, E. K. Reilly, T. Toh, P. K. Wright, and E. M. Yeatman, "Performance limits of the three MEMS inertial energy generator transduction types," *Journal of Micromechanics and Microengineering,* 2007.

[42]   S. P. Beeby, M. J. Tudor, and N. M. White, "Energy harvesting vibration sources for microsystems applications," *Journal of Measurement Science and Technology,* vol. 17, pp. 175-95, 2006.

[43]   P. D. Mitcheson, T. C. Green, E. M. Yeatman, and A. S. Holmes, "Architectures for vibration-driven micropower generators," *Journal of Microelectromechanical Systems,* vol. 13, pp. 429-40, 2004.

[44]   S. P. Beeby, R. N. Torah, M. J. Tudor, P. Glynne-Jones, T. O'Donnell, C. R. Saha, and S. Roy, "A micro electromagnetic generator for vibration energy harvesting," *Journal of Micromechanics and Microengineering,* vol. 17, p. 1257, 2007.

[45]   S. Roundy, "On the effectiveness of vibration-based energy harvesting," *Journal of Intelligent Material Systems and Structures,* vol. 16, pp. 809-23, 2005.

[46]   C. Shearwood and R. B. Yates, "Development of an electromagnetic micro-generator," *Electronics Letters,* vol. 33, pp. 1883-1884, 1997.

[47]   C. B. Williams, C. Shearwood, M. A. Harradine, P. H. Mellor, T. S. Birch, and R. B. Yates, "Development of an electromagnetic micro-generator," *IEEE Proceedings: Circuits, Devices and Systems,* vol. 148, pp. 337-342, 2001.

[48]   C. B. Williams, R. C. Woods, and R. B. Yates, "Feasibility study of a vibration powered micro-electric generator," in *IEEE Colloquium on Compact Power Sources* London, UK, 1996, pp. 7-1.

[49]   C. B. Williams and R. B. Yates, "Analysis of a micro-electric generator for microsystems," *Sensors and Actuators A (Physical) and International Solid-State Sensors and Actuators Conference - TRANSDUCERS '95,* vol. A52, pp. 8-11, 1996.

[50]   S. Roundy, P. K. Wright, and J. Rabaey, "A study of low level vibrations as a power source for wireless sensor nodes," *Computer Communications,* vol. 26, pp. 1131-1144, 2003.

[51]   E. S. Leland and P. K. Wright, "Resonance tuning of piezoelectric vibration energy scavenging generators using compressive axial preload," *Smart Materials and Structures,* vol. 15, p. 1413, 2006.

[52]   Y. B. Jeon, R. Sood, J.-h. Jeong, and S.-G. Kim, "MEMS power generator with transverse mode thin film PZT," *Sensors and Actuators A: Physical,* vol. 122, pp. 16-22, 2005.

[53]   W. Choi, Y. Jeon, J. H. Jeong, R. Sood, and S. Kim, "Energy harvesting MEMS device based on thin film piezoelectric cantilevers," *Journal of Electroceramics,* vol. 17, pp. 543-548, 2006.

[54]   M. Renaud, T. Sterken, A. Schmitz, P. Fiorini, C. Van Hoof, and R. Puers, "Piezoelectric harvesters and MEMS technology: Fabrication, modeling and measurements," in *IEEE International Conference on Solid-State Sensors, Actuators and Microsystems TRANSDUCERS'07*, 2007, pp. 891-894.

[55]   R. Elfrink, M. Renaud, T. M. Kamel, C. de Nooijer, M. Jambunathan, M. Goedbloed, D. Hohfeld, S. Matova, and R. van Schaijik, "Vacuum packaged MEMS piezoelectric vibration energy harvesters," in *PowerMEMS*, Washington DC, 2009, pp. 67-70.

[56]   R. Elfrink and et al., "Vibration energy harvesting with aluminum nitride-based piezoelectric devices," *Journal of Micromechanics and Microengineering,* vol. 19, p. 094005, 2009.

[57]   R. Amirtharajah and A. P. Chandrakasan, "Self-powered signal processing using vibration-based power generation," *IEEE Journal of Solid-State Circuits,* vol. 33, pp. 687-695, 1998.

[58]   S. Meninger, J. O. Mur-Miranda, R. Amirtharajah, A. Chandrakasan, and J. H. Lang, "Vibration-to-electric energy conversion," *IEEE Transactions on Very Large Scale Integration (VLSI) Systems,* vol. 9, pp. 64-76, 2001.

[59]   S. Meninger, T. O. Mur-Miranda, R. Amirtharajah, A. Chandrakasan, and J. Lang, "Vibration-to-electric energy conversion," in *International Symposium on Low Power Electronics and Design*, 1999, pp. 48-53.

[60]   T. Sterken, P. Fiorini, K. Baert, R. Puers, and G. Borghs, "An electret-based electrostatic u-generator," in *IEEE International Solid-State Sensors and Actuators Conference*, 2003, pp. 1291-4.

[61]   R. A. Steven and A. S. Henry, "A review of power harvesting using piezoelectric materials " *Smart Materials and Structures,* 2007.

[62]   P. Miao, P. D. Mitcheson, A. S. Holmes, E. M. Yeatman, T. C. Green, and B. H. Stark, "MEMS inertial power generators for biomedical applications," *Microsystem Technologies,* vol. 12, p. 1079, 2006.

[63]   W. J. Li, T. C. H. Ho, G. M. H. Chan, P. H. W. Leong, and W. Hiu Yung, "Infrared signal transmission by a laser-micromachined, vibration-induced power generator," in *43rd IEEE Midwest Symposium on Circuits and Systems*, 2000, pp. 236-239.

[64]   N. N. H. Ching, H. Y. Wong, W. J. Li, P. H. W. Leong, and Z. Wen, "PCB Integrated micro-generator for wireless systems," in *International Symposium on*

Smart Structures, Hong Kong SAR, 2000.

[65]   W. J. Li, Z. Wen, P. K. Wong, G. M. H. Chan, and P. H. W. Leong, "A micromachined vibration-induced power generator for low power sensors and robotic systems," in *World Automation Congress 8th International Symposium on Robotic Applications*, Maui, HI, 2000.

[66]   M. El-hami, P. Glynne-Jones, N. M. White, M. Hill, S. Beeby, E. James, A. D. Brown, and J. N. Ross, "Design and fabrication of a new vibration-based electromechanical power generator," *Sensors and Actuators A: Physical,* vol. 92, pp. 335-342, 2001.

[67]   N. N. H. Ching, H. Y. Wong, W. J. Li, P. H. W. Leong, and Z. Wen, "A laser-micromachined vibration to electrical power transducer for wireless sensing systems," in *11th International conference Solid-State Sensors and Actuators*, Munich, Germany, 2001.

[68]   N. N. H. Ching, H. Y. Wong, W. J. Li, P. H. W. Leong, and Z. Wen, "A laser-micromachined multi-modal resonating power transducer for wireless sensing systems," *Sensors and Actuators A: Physical,* vol. 97-98, pp. 685-690, 2002.

[69]   M. Mizuno and D. G. Chetwynd, "Investigation of a resonance microgenerator," *Journal of Micromechanics and Microengineering,* vol. 13, p. 209, 2003.

[70]   J. M. H. Lee, S. C. L. Yuen, W. J. Li, and P. H. W. Leong, "Development of an AA size energy transducer with micro resonators," in *International Symposium on Circuits and Systems ISCAS*, Bangkok, Thailand, 2003, pp. 876-9.

[71]   P. Glynne-Jones, M. J. Tudor, S. P. Beeby, and N. M. White, "An electromagnetic, vibration-powered generator for intelligent sensor systems," *Sensors and Actuators A: Physical,* vol. 110, pp. 344-349, 2004.

[72]   S. P. Beeby, M. J. Tudor, E. Koukharenko, N. M. White, T. O'Donnell, C. Saha, S. Kulkarni, and S. Roy, "Design and performance of a microelectromagnetic vibration powered generator," in *13th International Solid-State Sensors, Actuators and Microsystems TRANSDUCERS '05 Conference on*, 2005, pp. 780.

[73]   S. Beeby, J. Tudor, R. Torah, E. Koukharenko, S. Roberts, T. O'Donnell, and S. Roy, "Macro and micro scale electromagnetic kinetic energy harvesting generators," in *DTIP MEMS MOEMS*, Stresa, Italy, 2006.

[74]   C. R. Saha, T. O'Donnell, N. Wang, and P. McCloskey, "Electromagnetic generator for harvesting energy from human motion," *Sensors and Actuators A (Physical),* vol. 147, pp. 248-53, 2008.

[75]   T. von Buren and G. Troster, "Design and optimization of a linear vibration-driven electromagnetic micro-power generator," *Sensors and Actuators, A: Physical,* vol. 135, p. 765, 2007.

[76]   C. Serre, A. Pérez-Rodríguez, N. Fondevilla, J. Morante, J. Montserrat, and J. Esteve, "Vibrational energy scavenging with Si technology electromagnetic inertial microgenerators," *Microsystem Technologies,* vol. 13, p. 1655, 2007.

[77]   W.-S. Huang, K.-E. Tzeng, M.-C. Cheng, and R.-S. Huang, "A silicon MEMS micro power generator for wearable micro devices," *J. of Chinese Institute of Engineering,* vol. 30, pp. 133-140, 2007.

[78]   Perpetuum PMG17 Datasheet, February, 2009. [Online]. Available: www.perpetuum.com.

[79]   Ferro Solutions VEH360, February, 2009. [Online]. Available: www.ferrosi.com.

[80] I. Ayala, D. Zhu, M. Tudor, and S. Beeby, "Autonomous tunable energy harvester," in *PowerMEMS*, Washington DC, 2009, pp. 49-52.

[81] S. C. Chang, F. M. Yaul, A. Dominguez-Garcia, F. O'Sullivan, D. M. Otten, and J. Lang, "Harvesting energy from moth vibrations during flight," in *PowerMEMS*, Washington DC, 2009, pp. 57-60.

[82] N. Wang and D. P. Arnold, "Fully batch fabricated MEMS magnetic vibrational energy harvesters," in *PowerMEMS*, Washington DC, 2009, pp. 348-351.

[83] D. Hoffman, C. Kallenbach, M. Dobmaier, B. Folkmer, and Y. Manoli, "Flexible polyimide film technology for vibration energy harvesting," in *PowerMEMS*, Washington Dc, 2009, pp. 344-347.

[84] E. Bouendeu, A. Greiner, P. J. Smith, and J. G. Korvink, "An efficient low cost electromagnetic vibration harvester," in *PowerMEMS*, Washington DC, 2009, pp. 320-323.

[85] P. Wang, X. Dai, X. Zhao, and G. Ding, "A micro electromagnetic vibration energy harvester with sandwitched structure and air channel for high energy conversion," in *PowerMEMS*, Washington DC, 2009, pp. 296-299.

[86] P. Glynne-Jones, M. El-hami, S. Beeby, E. James, A. D. Brown, C. Hill, and N. M. White, "A vibration-powered generator for wireless microsystems," in *International Symposium on Smart Struct. Microsyst.*, Hong Kong, 2000.

[87] K. Hammond, E. Lai, E. Leland, S. Mellers, D. Steingart, E. Carleton, B. Reilly, J. Baker, B. Otis, J. Rabaey, D. Culler, and P. Wright, "An integrated node for energy-scavenging, sensing, and data-transmission: applications in medical diagnostics," in *2nd International Workshop on Wearable and Implantable Body Sensor Networks*, London, UK, 2005, pp. 58.

[88] E. Lefeuvre, A. Badel, C. Richard, L. Petit, and D. Guyomar, "A comparison between several vibration-powered piezoelectric generators for standalone systems," *Sensors and Actuators A: Physical,* vol. 126, pp. 405-416, 2006.

[89] S. Tanaka, "Power micro-electromechanical systems (Power MEMS)," *Transactions of the Institute of Electrical Engineers of Japan, Part E,* vol. 122-E, pp. 1-9, 2002.

[90] F. Hua-Bin, L. Jing-Quan, X. Zheng-yi, D. Lu, W. Li, C. Di, C. Bing-chu, and L. Yue, "Fabrication and performance of MEMS-based piezoelectric power generator for vibration energy harvesting," *Microelectronics Journal,* vol. 37, pp. 1280-4, 2006.

[91] M. Ferrari, V. Ferrari, D. Marioli, and A. Taroni, "Modeling, fabrication and performance measurements of a piezoelectric energy converter for power harvesting in autonomous microsystems," *IEEE Transactions on Instrumentation and Measurement,* vol. 55, pp. 2096-2101, 2006.

[92] T. H. Ng and W. H. Liao, "Sensitivity analysis and energy harvesting for a self-powered piezoelectric sensor," *Journal of Intelligent Material Systems and Structures,* vol. 16, pp. 785-797, October 1, 2005 2005.

[93] V. R. Challa, M. G. Prasad, S. Yong, and F. T. Fisher, "A vibration energy harvesting device with bidirectional resonance frequency tunability," *Smart Materials and Structures,* vol. 17, p. 015035, 2008.

[94] N. M. White, P. Glynne-Jones, and S. P. Beeby, "A novel thick-film piezoelectric micro-generator," *Smart Materials and Structures,* p. 850, 2001.

[95]   Mide PEH20W Datasheet, February, 2009. [Online]. Available: www.mide.com.

[96]   A. Bayrashev, W. P. Robbins, and B. Ziaie, "Low frequency wireless powering of microsystems using piezoelectric-magnetostrictive laminate composites," *Sensors and Actuators A: Physical,* vol. 114, pp. 244-249, 2004.

[97]   M. Marzencki, S. Basrour, and B. Charlot, "Design, modelling and optimisation of integrated piezoelectric micro power generators," in *NSTI Nanotechnology Conference and Trade Show*, Anaheim, CA, USA, 2005, pp. 545.

[98]   D. Zhu, S. Beeby, M. Tudor, and N. R. Harris, "A self powered tag for wireless structure health monitoring in aeronautical applications," in *PowerMEMS*, Washington DC, 2009, pp. 201-204.

[99]   D. Berdy, P. Srisungsitthisunti, X. Xu, J. Rhoads, B. Jung, and D. Peroulis, "Compact low frequency meandered piezoelectric energy harvester," in *PowerMEMS*, Washington DC, 2009, pp. 71-74.

[100]   P. Woias, M. Wischke, C. Eichhorn, and B. Fuchs, "An energy autonomous wireless temperature monitoring system powered by piezoelectric energy harvesting," in *PowerMEMS*, Washington DC, 2009, pp. 209-212.

[101]   G. A. Ardila Rodriguez, H. Durou, A. Ramond, P. Dubreuil, D. Belharet, C. Rossi, and D. Esteve, "A PZT energy harvester MEMS for low amplitude accelerations: fabrication and characterization," in *PowerMEMS*, Washington DC, 2009, pp. 197-200.

[102]   J. C. Park, D. H. Lee, J. Y. Park, Y. S. Chang, and Y. P. Lee, "High performance piezoelectric MEMS energy harvester based on D33 mode of PZT thin film on buffer-layer with PBTIO3 inter-layer," in *International Solid-State Sensors, Actuators and Microsystems Conference TRANSDUCERS'09*, 2009, pp. 517-520.

[103]   M. Wischke, M. Masur, and P. Woias, "A hybrid generator for virbration energy harvesting applications," in *International Solid-State Sensors, Actuators and Microsystems Conference TRANSDUCERS'09*, 2009, pp. 521-524.

[104]   M. Khbeis, J. McGee, and R. Ghodssi, "Development of a simplified hybrid ambient low frequency, low intensity vibration energy scavenger system," in *International Solid-State Sensors, Actuators and Microsystems Conference TRANSDUCERS'09*, 2009, pp. 525-528.

[105]   M. Renaud, P. Fiorini, R. van Schaijk, and C. van Hoof, "An impact based piezoelectric harvester adapted to low frequency environmental vibrations," in *International Solid-State Sensors, Actuators and Microsystems Conference TRANSDUCERS'09*, 2009, pp. 2094-2097.

[106]   M. Miyazaki, H. Tanaka, G. Ono, T. Nagano, N. Ohkubo, T. Kawahara, and K. Yano, "Electric-energy generation using variable-capacitive resonator for power-free LSI: efficiency analysis and fundamental experiment," in *International Symposium on Low Power Electronics and Design*, 2003, pp. 193.

[107]   Y. Arakawa, Y. Suzuki, and N. Kasagi, "Micro seismic power generator using electret polymer film," in *Power MEMS* Kyoto, Japan, 2004.

[108]   T. Tsutsumino, Y. Suzuki, N. Kasagi, and Y. Sakane, "Seismic power generator using high-performance polymer electret," in *IEEE International Conference on Micro Electro Mechanical Systems MEMS'06*, 2006, pp. 98-101.

[109]   R. Tashiro, N. Kabei, K. Katayama, E. Tsuboi, and K. Tsuchiya, "Development of an electrostatic generator for a cardiac pacemaker that harnesses the ventricular

wall motion," *Journal of Artificial Organs,* vol. 5, pp. 0239-0245, 2002.

[110] G. Despesse, T. Jager, J. J. Chaillout, J. M. Leger, and S. Basrour, "Design and fabrication of a new system for vibration energy harvesting," in *Research in Microelectronics and Electronics, 2005 PhD* Lausanne, Switzerland, 2005, pp. 225.

[111] T. Sterken, P. Fiorini, G. Altena, C. Van Hoof, and R. Puers, "Harvesting energy from vibrations by a micromachined electret generator," in *International Solid-State Sensors, Actuators and Microsystems Conference TRANSDUCERS'07,* 2007, pp. 129-132.

[112] Y. Chiu, C.-T. Kuo, and Y.-S. Chu, "Design and fabrication of a micro electrostatic vibration-to-eectricity energy converter," in *DTIP* Stresa, Italy, 2006.

[113] D. Miki, M. Honzumi, Y. Suzuki, and N. Kasagi, "MEMS electret generator with eectrostatic levitation," in *PowerMEMS*, Washington DC, 2009, pp. 169-172.

[114] J. Z. Wong, J. Yan, K. Soga, and A. Seshia, "A multi-degree-of-freedom electrostatic MEMS power harvester," in *PowerMEMS*, Washington DC, 2009, pp. 300-303.

[115] D. Paci, M. Schipani, V. Bottarel, and D. Miatton, "Optimization of a piezoelectric energy harvester for environmental broadband vibrations," in *15th IEEE International Conference on Electronics, Circuits and Systems (ICECS 2008)*, 2008, pp. 177-81.

[116] E. Reilly, L. Miller, R. Fain, and P. K. Wright, "A study of ambient vibrations for piezoelectric energy conversion " in *PowerMEMS*, Washington, DC, 2009, pp. 312-315.

[117] T. von Buren, P. Lukowicz, and G. Troster, "Kinetic energy powered computing - an experimental feasibility study," in *7th IEEE International Symposium on Wearable Computing*, 2003.

[118] S. Roundy and Y. Zhang, "Toward self-tuning adaptive vibration-based microgenerators," in *Smart Structures, Devices, and Systems II*, Sydney, Australia, 2005, pp. 373-384.

[119] C. Eichhorn, F. Goldschmidtboeing, Y. Porro, and P. Woias, "A piezoelectric harvester with an integrated frequency-tuning mechanism " in *PowerMEMS*, Washington, DC, 2009.

[120] I. Sari, T. Balkan, and H. Kulah, "An electromagnetic micro power generator for wideband environmental vibrations," *Sensors and Actuators A (Physical),* vol. 145-146, pp. 405-13, 2008.

[121] H. Kulah and K. Najafi, "Energy scavenging from low-frequency vibrations by using frequency up-conversion for wireless sensor applications," *IEEE Sensors Journal,* vol. 8, pp. 261-8, 2008.

[122] H. Kulah and K. Najafi, "An electromagnetic micro power generator for low-frequency environmental vibrations," in *MEMS '04*, 2004, pp. 237-240.

[123] T. von Buren and G. Troster, "Design and optimization of a linear vibration-driven electromagnetic micro-power generator," *Sensors and Actuators A: Physical,* vol. 135, pp. 765-775, 2007.

[124] D. Spreemann, D. Hoffmann, B. Folkmer, and Y. Manoli, "Numerical optimization approach for resonant electromagnetic vibration transducer designed for random vibration," *Journal Of Micromechanics And Microengineering,* vol.

18, p. 104001, 2008.

[125] W. T. Thomson, "Theory of vibration with applications," *Prentice-Hall,* 1988.

[126] J. P. Lynch, "An overview of wireless structural health monitoring for civil structures," *Philosophical Transactions of the Royal Society London, Series A (Mathematical, Physical and Engineering Sciences),* vol. 365, pp. 345-72, 2007.

[127] Our Nation's Highways: 2010, [Online]. Available: http://www.fhwa.dot.gov/policyinformation/pubs/pl10023/fig7_3.cfm.

[128] M. Kurata, J. P. Lynch, T. Galchev, M. Flynn, P. Hipley, V. Jacob, G. van der Linden, A. Mortazawi, K. Najafi, R. L. Peterson, S. Li-Hong, D. Sylvester, and E. Thometz, "A two-tiered self-powered wireless monitoring system architecture for bridge health management," in *Proceedings of the SPIE*, USA, 2010, pp. 76490.

[129] H. Sohn, C. R. Farrar, F. M. Hemez, D. D. Shunk, S. W. Stinemates, B. R. Nadler, and J. J. Czarnecki, "Review of structural health monitoring literature from 1996-2001," Los Alamos National Laboratory, Los Alamos, 2004.

[130] J. P. Lynch, K. H. Law, A. S. Kiremidjian, E. Carryer, C. R. Farrar, H. Sohn, D. W. Allen, B. Nadler, and J. R. Wait, "Design and performance validation of a wireless sensing unit for structural monitoring applications," South Korea, 2004, pp. 393-408.

[131] J. P. Lynch, V. Kamat, V. C. Li, M. Flynn, D. Sylvester, K. Najafi, T. Gordon, M. Lepech, A. Emami-Naeini, A. Krimotat, M. Ettouney, S. Alampalli, and T. Ozdemir, "Overview of a cyber-enabled wireless monitoring system for the protection and management of critical infrastructure systems," in *Proceedings of the SPIE*, USA, 2009, pp. 72940L.

[132] R. J. M. Vullers, R. van Schaijk, I. Doms, C. Van Hoof, and R. Mertens, "Micropower energy harvesting," *Solid-State Electronics,* vol. 53, pp. 684-93, 2009.

[133] T. H. Ng and W. H. Liao, "Sensitivity analysis and energy harvesting for a self-powered piezoelectric sensor," *Journal of Intelligent Material Systems and Structures,* vol. 16, pp. 785-97, 2005.

[134] C. Peters, D. Spreemann, M. Ortmanns, and Y. Manoli, "A CMOS integrated voltage and power efficient AC/DC converter for energy harvesting applications," *Journal Of Micromechanics And Microengineering,* vol. 18, p. 104005 2008.

[135] T. T. Le, H. Jifeng, A. von Jouanne, K. Mayaram, and T. S. Fiez, "Piezoelectric micro-power generation interface circuits," *IEEE Journal of Solid-State Circuits,* vol. 41, pp. 1411-20, 2006.

[136] G. K. Ottman, H. F. Hofmann, and G. A. Lesieutre, "Optimized piezoelectric energy harvesting circuit using step-down converter in discontinuous conduction mode," *IEEE Transactions on Power Electronics,* vol. 18, pp. 696-703, 2003.

[137] G. K. Ottman, H. F. Hofmann, and G. A. Lesieutre, "Optimized piezoelectric energy harvesting circuit using step-down converter in discontinuous conduction mode," in *Power Electronics Specialists Conference PESC*, Cairns, Qld., Australia, 2002, pp. 1988-94.

[138] G. K. Ottman, H. F. Hofmann, A. C. Bhatt, and G. A. Lesieutre, "Adaptive piezoelectric energy harvesting circuit for wireless remote power supply," *IEEE Transactions on Power Electronics,* vol. 17, pp. 669-76, Sept. 2002.

[139] E. Lefeuvre, D. Audigier, C. Richard, and D. Guyomar, "Buck-boost converter for

sensorless power optimization of piezoelectric energy harvester," *IEEE Transactions on Power Electronics,* vol. 22, pp. 2018-2025, 2007.

[140] C. Xinping, C. Wen-Jen, K. Ya-Chin, and L. Yi-Kuen, "Electromagnetic energy harvesting circuit with feedforward and feedback DC-DC PWM boost converter for vibration power generator system," *IEEE Transactions on Power Electronics,* vol. 22, pp. 679-685, 2007.

[141] Y. K. Ramadass and A. P. Chandrakasan, "An efficient piezoelectric energy-harvesting interface circuit using a bias-flip rectifier and shared inductor," in *IEEE International Solid-State Circuits Conference (ISSCC 2009)*, 2009, pp. 296-7.